



Current Perspectives on Chemical Sciences

Vol. 2



Book Publisher
International


Current Perspectives on Chemical Sciences

Vol. 2

Current Perspectives on Chemical Sciences

Vol. 2

India ■ United Kingdom


**Book Publisher
International**

Editor(s)

Dr. Harekrushna Sutar

Assistant Professor,
Chemical Engineering Department, Indira Gandhi Institute of Technology, Sarang,
District-Dhenkanal, Odisha, India.
Email: h.k.sutar@gmail.com, harekrushna.sutar@igitsarang.ac.in;

FIRST EDITION 2020

ISBN 978-93-90431-43-4 (Print)
ISBN 978-93-90431-51-9 (eBook)
DOI: 10.9734/bpi/cpcs/v2



Contents

Preface	i
Chapter 1 The Thermodynamic Coordinate Transformations and the Thermodynamic Covariance Principle Giorgio Sonnino and Alberto Sonnino	1-20
Chapter 2 Synthesis and Structural Features of Indanone, Tetralone and Naphthone Derivatives: Selective Fluorination and Condensation Products Paul D. Boyle, David Breaud, Matthew Churley, Patrick Coppock, Jr., Elvia Encarnacion-Thomas, Chloe Fernandes, Augustus W. Fountain, Cristina Gomez, Alejandro Guzman, James L. Jackson, Linh Lam, Ajay Mallia, Samantha Moseley, Sang H. Park, William F. Pearman, Robert D. Schmidt, Joseph C. Sloop, Roger D. Sommer, Stephanie Stalker, Jonathan Weyand, Karla Wilmott and Jonathan Yi	21-36
Chapter 3 Investigating the Influence of the Transport of Sea Spray on the Salinization of the Semiarid Region Waters (Bahia, Brazil) Adriana M. C. Silva, Vânia P. Campos, Rafaela S. Domingues, Lícia P. S. Cruz and Franciele O. Santana	37-53
Chapter 4 Focusing on Organocatalytic Asymmetric Michael Addition of Ketones to α, β-unsaturated Nitro Compounds Jae Ho Shim, Si Hun Nam, Byeong-Seon Kim and Deok-Chan Ha	54-66
Chapter 5 High Photocatalytic Activity of the TiO₂/ZnO Mesoporous Composites Obtained by Solution Combustion Method A. Luna-Flores, I. Niño-Flores, M. A. Morales, A. D. Hernández-de la Luz, J. A. Luna-López, R. Portillo, D. Cruz-González, R. Agustín-Serrano and M. P. Sampedro	67-89
Chapter 6 A Study on Thermal Degradation of Hydrazinated Transition Metal Acetamido Benzoates E. Helen Pricilla Bai and S. Vairam	90-106
Chapter 7 Studies on the Formulation of Sustained Release Zolpidem Tartrate Matrix Tablets through Optimization and Their Evaluation Masheer Ahmed Khan and S. C. Chaturvedi	107-124
Chapter 8 Solution Behavior and Optical Properties of Platinum Complexes Featuring “Pt(pq)(C\equivC^tBu)” Units Connected by <i>N</i>-donor Ligands Elena Lalinde, M. Teresa Moreno, Santiago Ruiz and Sergio Sánchez	125-142
Chapter 9 Investigation of the Anatomical Variability of the Trunk and Root Tissues of <i>Rhizophora racemosa</i> (G. Mey) and <i>Avicennia germinans</i> (Linné): A Bioaccumulation of Heavy Metals and Pollution Effects on Mangrove Trees Study S. B. Mabicka Iwangou, P. Soulounganga, A. Besserer, R. Safou Tchiama, C. Ndoutoume, T. Andzi Barhé and P. Gerardin	143-162

Preface

This book covers key areas of Chemical Sciences. The contributions by the authors include Thermodynamics of irreversible processes, Lie algebras and Lie groups, covariance principles, transport processes in Tokamak-plasmas, Thermodynamical Field Theory, 2-trifluoroacetyl-1, 3-diketone, 1,3,5-triketone, tautomerism, chalcone, 4H-chromone, pyrazole, Selective Fluorination, Sea spray, rainwater, particulate matter, stable isotopes, Semiarid Region, Salinization, Organocatalyst, enantioselectivity, yield, thiourea catalyst, asymmetric, β -unsaturated Nitro Compounds, Combustion solution method, composite, photocatalysis, mesoporosity, TiO/ZnO₂, IR, simultaneous TG-DT88A, acetamido benzoate, electronic spectra, Hydrazinated Transition Metal, Zolpidem tartrate, matrix tablets, sustained release, HPMC, polymer, factorial design, Alkynyl, cyclometalated, luminescence, platinum, N-donor ligand, Mangrove, parenchyma bands, sclerous cells, bioremediation, heavy metals, Rhizophora racemosa, Avicennia germinans, Bioaccumulation of Heavy Metals etc. This book contains various materials suitable for students, researchers and academicians in the field of Chemical Sciences.

The Thermodynamic Coordinate Transformations and the Thermodynamic Covariance Principle

Giorgio Sonnino^{1*} and Alberto Sonnino²

DOI: 10.9734/bpi/cpcs/v2

ABSTRACT

The concept of *equivalent systems* from the thermodynamic point of view was originally introduced by Th. De Donder and I. Prigogine. However, the De Donder-Prigogine definition of thermodynamic invariance based only on the invariance of the entropy production is not sufficient to guarantee the equivalence character between two sets of thermodynamic forces and conjugate thermodynamic fluxes. In addition, it is known that there exists a large class of flux-force transformations such that, even though they leave unaltered the expression of the entropy production, they may lead to certain paradoxes.

Main objective of this series of works is to determine the non-linear closure equations (i.e. the flux-force relations), valid for thermodynamic systems outside the Onsager region, which do not contain inconsistencies. To this aim, a thermodynamic theory for irreversible processes [referred to as the *Thermodynamical Field Theory* (TFT)] has been developed. The TFT rests upon the concept of equivalence between thermodynamic systems. More precisely, the equivalent character of two alternative descriptions of a thermodynamic system is ensured if, and only if, the two sets of thermodynamic forces are linked with each other by the so-called *Thermodynamic Coordinate Transformations* (TCT). In this work, we describe the Lie group associated to the TCT. The TCT guarantee the validity of the so-called *Thermodynamic Covariance Principle* (TCP): “*The nonlinear closure equations, i.e., the flux-force relations, everywhere and in particular outside the Onsager region, must be covariant under TCT*”. In other terms, the fundamental laws of thermodynamics should be manifestly covariant under transformations between the admissible thermodynamic forces, i.e., under TCT. The TCP ensures the validity of the fundamental theorems for systems far from equilibrium. We shall see that the requirement of the validity of the TCP will impose strict restrictions allowing determining, for example, the expression of the collisional operator for magnetically confined plasmas.

Keywords: Thermodynamics of irreversible processes; Lie algebras and Lie groups; covariance principles; transport processes in Tokamak-plasmas.

1. INTRODUCTION

The objective of this Chapter is to investigate and revise the concept of *equivalent systems from the thermodynamic point of view*, originally introduced by Th. De Donder and I. Prigogine. According to our definition, two systems are thermodynamically equivalent if, under transformation of the thermodynamic forces, both the entropy production and the Glansdorff-Prigogine dissipative quantity (see the definition in the forthcoming Section (55)) remain unaltered. This kind of transformations may be referred to as the *Thermodynamic Coordinate Transformations* (TCT). In Section (55) we determine the general class of transformations satisfying the TCT. As known, the Noether theorem establishes that the symmetries underlying a physical system are intimately related to the conservation laws characterizing the system. So, the invariance of a system under TCT is intimately

¹Department of Theoretical Physics and Mathematics, Université Libre de Bruxelles (ULB), Campus Plaine CP 231, Boulevard de Triomphe, 1050 Brussels, Belgium.

²Faculty of Engineering Sciences, University College London, Gower Street, London WC1E 6BT, UK.

*Corresponding author: E-mail: Giorgio.Sonnino@ulb.ac.be, gsonnino@ulb.ac.be;

linked to the existence of a group, which we refer to as the *TCT-group*. The equivalent character of two transformations under TCT naturally leads to the concept of the *Thermodynamic Covariance Principle* (TCP). This principle states that all thermodynamic equations involving the relation between thermodynamic forces and fluxes (e.g. the flux-force closure relations) must be covariant under TCT. The Lie group representations associated to the TCT- group is described in Section (3) and the formulation of the Thermodynamic Covariance Principle is reported in Section (4). In Section (5) we can find an example of application of the TCP to magnetically confined plasmas. We derive in a rigorous way the expression for the collisional operator for Tokamak-plasmas which is currently largely used in the numerical simulations. We mention that the TCP is the milestone for constructing the nonlinear closure equations for thermodynamic systems out of Onsager's region. This task has been accomplished by means of three hypotheses: two constraints (A) and (B), and one assumption (C) [1].

- (A) The thermodynamic principles and the theorems valid for systems far from equilibrium must be satisfied.
- (B) The validity of the thermodynamic covariance principle (TCP) must be ensured.
- (C) Close to the steady states, the nonlinear closure equations can be derived by the principle of least action.

This theory, based on (A), (B), and (C), is referred to as the *Thermodynamical Field Theory* (TFT). In Section (6) we confront the electron heat loss in fully collisional Frascati Tokamak Upgrade (FTU)-plasmas estimated by the TFT against the experimental data and the linear (Neoclassical) predictions. We show that (contrarily to Onsager's prediction) the TFT theoretical predictions are in fairly good agreement with experimental data in the expected region of validity. To perform this comparison, the Shafranov shift has also been taken into account¹.

2. THE DE DONDER-PRIGOGINE THERMODYNAMIC INVARIANCE

Onsager's theory is based on three assumptions [2,3]: i) *The probability distribution function for the fluctuations of thermodynamic quantities* (Temperature, pressure, degree of advancement of a chemical reaction etc.) *is a Maxwellian*, ii) *Fluctuations decay according to a linear law*, and iii) *The principle of the detailed balance* (or the microscopic reversibility) *is satisfied*. Onsager showed the equivalence of the assumptions i)-iii) with the equations

$$J_\mu = \tau_{0\mu\nu} X^\nu \quad ; \quad \frac{\partial \tau_{0\mu\nu}}{\partial X^\lambda} = 0 \quad (1)$$

where $\tau_{0\mu\nu}$ are the transport coefficients and X^μ and J_μ denote the thermodynamic forces and the conjugate fluxes, respectively. Assumption iii) allows deriving the *reciprocity relations* $\tau_{0\mu\nu} = \tau_{0\nu\mu}$. Note that in Eq. (1), as well as in the sequel, the summation convention on the repeated indexes is understood. The Onsager theory of fluctuations starts from the Einstein formula linking the probability of a fluctuation, \mathcal{W} , with the entropy change, ΔS , associated with the fluctuations from the state of equilibrium

$$\mathcal{W} = W_0 \exp[\Delta S/k_B] \quad (2)$$

In Eq. (2), k_B is the Boltzmann constant and W_0 is a normalization constant, which ensures that the sum of all probabilities equals to one. Prigogine generalized Eq. (2), which applies only to adiabatic or isothermal transformations, by introducing the entropy production due to fluctuations. Denoting by ξ_i ($i = 1 \dots m$) the m deviations of the thermodynamic quantities from their equilibrium value, Prigogine

¹In Tokamak-plasmas, the plasma pressure leads to an outward shift of the center of the magnetic flux surfaces. The direction of the electric current that flows inside the plasma J is perpendicular to both the magnetic field and the shift displacement of the circular magnetic lines. Note that the poloidal magnetic field increases and the magnetic pressure will, then, balance the outward force. This effect is referred to as the Shafranov shift.

proposed that the probability distribution of finding a state in which the values ξ_i lie between ξ_i and $\xi_i + d\xi_i$ is given by [4]

$$W = W_0 \exp[\Delta_I S/k_B] \quad \text{where} \quad \Delta_I S = \int_E^F d_I s \quad ; \quad \frac{d_I s}{dt} \equiv \int_{\Omega} \sigma dv \quad (3)$$

Here, dv is a (spatial) volume element of the system, and the integration is over the entire space Ω occupied by the system in question. E and F indicate the equilibrium state and the state to which a fluctuation has driven the system, respectively. Note that this probability distribution remains unaltered for flux-force transformations leaving invariant the entropy production. Concrete examples of chemical reactions, equivalent from the thermodynamic point of view, have also been analyzed in literature. As an example, among these, we choose the simplest of all. Let us consider, for example, a chemical system in which

a) two *isomerisations* $A \rightarrow B$ and $B \rightarrow C$ take place [4].

From the macroscopic point of view, the chemical changes could be equally well described by the

b) two *isomerisations* $A \rightarrow C$ and $B \rightarrow C$.

It can be checked that, under a linear transformation of the thermodynamic forces (which in this case corresponds to a linear transformation of the chemical affinities) the entropy productions for the two chemical reactions a) and b), are equal. Indeed, the corresponding affinities of the reactions a) read: $A^1 = \mu_A - \mu_B$, and $A^2 = \mu_B - \mu_C$, with A^i and μ_i ($i = A, B, C$) denoting the affinities and the chemical potentials, respectively. The change per unit time of the mole numbers is given by

$$\frac{dn_A}{dt} = -v_1 \quad ; \quad \frac{dn_B}{dt} = v_1 - v_2 \quad ; \quad \frac{dn_C}{dt} = v_2 \quad (4)$$

with v_i ($i = 1, 2$) denoting the chemical reaction rates. In this case the thermo-dynamic forces and the flows are the chemical affinities (over temperature) and the chemical reaction rates, respectively *i.e.*, $X^\mu = A^\mu/T$ and $J_\mu = v_\mu$. Hence, the corresponding entropy production reads $d_I S/dt = A^1/T v_1 + A^2/T v_2 > 0$. The affinities corresponding to reactions b) are related to the old ones by

$$A'^1 = \mu_A - \mu_C = A^1 + A^2 \quad ; \quad A'^2 = \mu_B - \mu_C = A^2 \quad (5)$$

By taking into account that

$$\frac{dn_A}{dt} = -v'_1 \quad ; \quad \frac{dn_B}{dt} = -v'_2 \quad ; \quad \frac{dn_C}{dt} = v'_1 + v'_2 \quad (6)$$

we get

$$v_1 = v'_1 \quad ; \quad v_2 = v'_1 + v'_2 \quad (7)$$

where the invariance of the entropy production is manifestly shown. Indeed,

$$d_I S/dt = (A^1/T)v_1 + (A^2/T)v_2 = (A'^1/T)v'_1 + (A'^2/T)v'_2 = d_I S'/dt \quad (8)$$

or $J_\mu X^\mu = J'_\mu X'^\mu$ (where the Einstein summation convention on the repeated indexes is adopted). On the basis of the above observations, Th. De Donder and I. Prigogine formulated, for the first time, the concept of *equivalent systems from the thermodynamical point of view*. For Th. De Donder and I.

Prigogine, *thermodynamic systems are thermodynamically equivalent if, under transformation of fluxes and forces, the bilinear form of the entropy production remains unaltered, i.e., $\sigma = \sigma'$* [5].

2.1 Remarks on De Donder-Prigogine's Thermodynamic Invariance Formulation

The Thermodynamic Invariance Principle formulated by De Donder-Prigogine, based only on the invariance of the entropy production, is not sufficient to guarantee the equivalence character of the two descriptions (J_μ, X^μ) and (J'_μ, X'^μ) . Indeed, we can easily convince ourselves that there exists a large class of transformations such that, even though they leave unaltered the expression of the entropy production, they may lead to certain paradoxes to which J. E. Verschaffelt and R. O. Davies have called attention [6,7]. This obstacle can be removed if one takes into account one of the most fundamental and general theorems valid in thermodynamics of irreversible processes: the *Universal Criterion of Evolution*. In general, Glansdorff and Prigogine have shown that: *For time-independent boundary conditions, a thermodynamic system, even in strong non-equilibrium conditions, relaxes to a stable stationary state in such a way that the following Universal Criterion of Evolution is satisfied* [8,9]:

$$\int_{\Omega} J_\mu \frac{\partial X^\mu}{\partial t} dv \leq 0 \quad (9)$$

Here, Ω is the volume occupied by the system and dv the volume-element, respectively. In addition

$$\int_{\Omega} J_\mu \frac{\partial X^\mu}{\partial t} dv = 0 \quad \text{At the steady state} \quad (10)$$

Quantity $P \equiv \int_{\Omega} J_\mu \frac{\partial X^\mu}{\partial t} dv$ may be referred to as *the Glansdorff-Prigogine dissipative quantity*.

Let us check the validity of this theorem by considering two, very simple, examples. Let us consider, for instance, a closed system containing m components ($i = 1 \dots m$) among which chemical reactions are possible. The temperature, T , and the pressure, p , are supposed to be constant in time. The change in the number of moles n_i , of component i , is

$$\frac{dn_i}{dt} = \nu_i^j v_j \quad (11)$$

with ν_i^j denoting the stoichiometric coefficients. By multiplying both members of Eq. (11) by the time derivative of the chemical potential of component i , we get

$$\dot{\mu}^i \frac{dn_i}{dt} = \left(\frac{\partial \mu^i}{\partial n_\kappa} \right)_{pT} \frac{dn_i}{dt} \frac{dn_\kappa}{dt} = \nu_i^j \dot{\mu}^i v_j \quad (12)$$

By taking into account the De Donder law between the affinities A^i and the chemical potentials *i.e.*, $A^i = -\nu_i^j \mu^j$, we finally get

$$P \equiv J_\mu \frac{dX^\mu}{dt} = v_j \frac{d}{dt} \left(\frac{A^j}{T} \right) = -\frac{1}{T} \left(\frac{\partial \mu^i}{\partial n_\kappa} \right)_{pT} \frac{dn_i}{dt} \frac{dn_\kappa}{dt} \leq 0 \quad (13)$$

where the negative sign of the term on the right-hand side is due to the second law of thermodynamics. Hence, the Glansdorff-Prigogine dissipative quantity P is always negative, and it vanishes at the stationary state.

As a second example, we analyze the case of heat conduction in non-expanding solid. In this case the thermodynamic forces and the conjugate flows are the (three) components of the gradient of the inverse of the temperature, $X^\mu = [\text{grad } (1/T)]^\mu$ and the (three) components of the heat flow, $J_\mu = \mathbf{J}_{q\mu}$ (with $i = 1,2,3$), respectively. Hence,

$$P \equiv \int_{\Omega} J_\mu \frac{\partial X^\mu}{\partial t} dv = \int_{\Omega} \mathbf{J}_{q\mu} \frac{\partial}{\partial t} [\text{grad } (1/T)]^\mu dv \quad (14)$$

With partial integration, and by taking into account the energy law

$$\rho c_v \frac{\partial T}{\partial t} = -\text{div } \mathbf{J}_q \quad (15)$$

after simple calculations, we get

$$P = - \int_{\Omega} \frac{\rho c_v}{T^2} \left(\frac{\partial T}{\partial t} \right)^2 dv \leq 0 \quad (16)$$

with $P = 0$ at the steady state. In Eqs. (15) and (16), ρ and c_v are the mass density and the specific heat at volume constant, respectively. By summarizing, without using the Onsager reciprocal relations and without assuming that the transport coefficients are constant (i.e. independent of the thermodynamic forces), the dissipative quantity P is always a negative quantity. This quantity vanishes at the stationary state. In the two above-mentioned examples, the thermodynamic forces are the chemical affinities (over temperature) and the gradient of the inverse of temperature, respectively. However, we could have adopted a different choice of the thermodynamic forces. If we analyze, for instance, the case of heat conduction in non-expanding solid, where chemical reactions take place simultaneously, we can choose as thermodynamic forces a combination of the (dimensionless) chemical affinities (over temperature) and the (dimensionless) gradient of the inverse of temperature. Clearly, this representation is thermodynamically equivalent to the previous one (where the thermodynamic forces are simply the chemical affinities over temperature and the gradient of the inverse of temperature) only if the negative sign of the dissipative quantity P is preserved. In particular, the equations providing the stationary states (i.e. Eq. (10)) must admit *exactly the same solutions*.

3. THE THERMODYNAMIC COORDINATE TRANSFORMATIONS (TCT)

One of the central aspects of a theory is the concept of invariance of physics' laws. This invariance can be described in many ways, for example, in terms of local covariance or covariance of diffeomorphism. A more explicit description can be given through the use of tensors. The characteristic of the tensors that proves to be crucial, used in this approach, is the fact that (once given the metric) the operation of contracting a tensor of rank r on all indices r provides a number-an *invariant*, which is independent of the set of coordinates used to perform the contraction. Physically, this means that the invariant calculated by adopting a specific coordinate system (i.e., a specific set of thermodynamic forces) will have the same value if calculated in another -thermodynamically equivalent-coordinate system (i.e. in another equivalent set of thermodynamic forces), suggesting some independent meaning.

According to our approach, we say that in thermodynamics of irreversible processes two set of thermodynamic forces are equivalent if the following two conditions are satisfied [1,10]:

- (i) The entropy production σ should be invariant under transformation of the thermodynamic forces $\{X^\mu\} \rightarrow \{X'^\mu\}$.

- (ii) The Glansdorff-Prigogine dissipative quantity P should also remain invariant under the force transformations $\{X^\mu\} \rightarrow \{X'^\mu\}$.

Condition ii) stems from the fact that a steady state should be transformed into a steady state, and a stable steady state should be transformed into a stable steady-state, with the same degree of stability. In mathematical terms, this implies that $t = t'$ and

$$\sigma = J_\mu X^\mu = J'_\mu X'^\mu = \sigma' ; P = P' \rightarrow J_\mu \delta X^\mu = J'_\mu \delta X'^\mu \quad (17)$$

Eqs. (17) are satisfied iff the transformed thermodynamic forces and conjugate fluxes read as [1]

$$X'^\mu = \frac{\partial X'^\mu}{\partial X^\nu} X^\nu \quad , \quad J'_\mu = \frac{\partial X^\nu}{\partial X'^\mu} J_\nu \quad (18)$$

Transformations (18) are referred to as the *Thermodynamic Coordinate Transformations* (TCT) [1].

3.1 Transformation Rules of Entropy Production, Forces and Flows

Under TCT, the expression of entropy production transforms as

$$\sigma = J_\mu X^\mu = \tau_{\mu\nu} X^\mu X^\nu = g_{\mu\nu} X^\mu X^\nu = g'_{\mu\nu} X'^\mu X'^\nu = \sigma' \quad (19)$$

From Eqs (18) and (19) we derive

$$g'_{\lambda\kappa} = g_{\mu\nu} \frac{\partial X^\mu}{\partial X'^\lambda} \frac{\partial X^\nu}{\partial X'^\kappa} \quad (20)$$

Moreover, inserting Eqs (18) and Eq. (20) into relation $J_\mu = (g_{\mu\nu} + f_{\mu\nu})X^\nu$, we obtain

$$J'_\lambda = \left(g'_{\lambda\kappa} + f'_{\mu\nu} \frac{\partial X^\mu}{\partial X'^\lambda} \frac{\partial X^\nu}{\partial X'^\kappa} \right) X'^\kappa \quad (21)$$

or

$$J'_\lambda = (g'_{\lambda\kappa} + f'_{\lambda\kappa})X'^\kappa \quad \text{with} \quad f'_{\lambda\kappa} = f_{\mu\nu} \frac{\partial X^\mu}{\partial X'^\lambda} \frac{\partial X^\nu}{\partial X'^\kappa} \quad (22)$$

Hence, the transport coefficients transform like a *thermodynamic tensor of second order*². It is easily checked that transformations (18) preserve the validity of the reciprocal relations for transport coefficients *i.e.*, if $g_{\mu\nu} = g_{\nu\mu}$ then $g'_{\mu\nu} = g'_{\nu\mu}$ (and, if $f_{\mu\nu} = -f_{\nu\mu}$ then $f'_{\mu\nu} = -f'_{\nu\mu}$).

3.2 The TCT-Symmetry Group

3.2.1 Topological structure the TCT-group

The invariance of a system under TCT is intimately linked to existence of a group, which we refer to as the *TCT-group* or, briefly, G^n [11,12]. The TCT- group with its properties can be identified by analyzing the solution of Eq. (18). The solution of Eq. (18) reads [1]

²We may qualify as *thermodynamic tensor* or, simply *thermo-tensor*, (taken as a single noun) a set of quantities where only transformations Eqs. (18) are involved. This is in order to qualify as a tensor, a set of quantities, which satisfies certain laws of transformation when the coordinates undergo a general transformation. Consequently, every tensor is a thermodynamic tensor but the converse is not true.

$$X'^{\mu} = X^1 F^{\mu} \left(\frac{X^2}{X^1}, \frac{X^3}{X^2}, \dots, \frac{X^n}{X^{n-1}} \right) \quad (23)$$

where F^{μ} are arbitrary functions of variables X^j/X^{j-1} with $(j = 2, \dots, n)$. We demand that the n functions F^{μ} be smooth, so that the TCT preserve equations satisfied by the derivatives of thermodynamic quantities, and also that the transformation be non-degenerate with a smooth inverse, so that the transformed theory contain all of the information of the original theory. The non-degenerate property is also a necessary and sufficient condition for the finiteness of the transformed transport coefficients, even though it implies that the F^{μ} themselves may sometimes diverge. For example, from the transformation

$$X'^1 = X^2, \quad X'^2 = X^1 \quad (24)$$

one obtains

$$F^1(X^2/X^1) = X^2/X^1, \quad F^2(X^2/X^1) = 1 \quad (25)$$

showing that $F^1(X^2/X^1)$ diverges at $X^1 = 0$, whereas the X'^{μ} are always finite. Eq. (32) is the most general class of transformations expressing the equivalent character of two descriptions $\{X^{\mu}\}$ and $\{X'^{\mu}\}$. Hence, the TCT may be *highly nonlinear coordinate transformations* but, in the Onsager region, we may (or we must) require that they have to reduce to

$$X'^{\mu} = c_{\nu}^{\mu} X^{\nu} \quad (26)$$

where c_{ν}^{μ} are constant coefficients (i.e., independent of the thermodynamic forces). The linear and homogeneous transformations (26) are largely used in literature because, besides their simplicity, they are *nonsingular* transformations. From Eq. (18) we get the following important identities

$$X^{\nu} \frac{\partial^2 X'^{\mu}}{\partial X^{\nu} \partial X^{\kappa}} = 0 \quad ; \quad X'^{\nu} \frac{\partial^2 X^{\mu}}{\partial X'^{\nu} \partial X'^{\kappa}} = 0 \quad (27)$$

Moreover

$$\begin{aligned} dX'^{\mu} &= \frac{\partial X'^{\mu}}{\partial X^{\nu}} dX^{\nu} \\ \frac{\partial}{\partial X'^{\mu}} &= \frac{\partial X^{\nu}}{\partial X'^{\mu}} \frac{\partial}{\partial X^{\nu}} \end{aligned} \quad (28)$$

i.e., dX^{μ} and $\partial/\partial X^{\mu}$ transform like a thermodynamic contra-variant and a thermodynamic covariant vector, respectively. According to Eq. (28), thermodynamic vectors dX^{μ} define the *tangent space* to Ts . It also follows that the operator $P(X)$, i.e. the dissipation quantity, and in particular the definition of steady states, are invariant under TCT. Parameter ζ , defined as

$$d\zeta^2 = g_{\mu\nu} dX^{\mu} dX^{\nu} \quad (29)$$

is a scalar under TCT. The operators \mathcal{O} and \square^2 defined as

$$\begin{aligned} \mathcal{O} &\equiv X^{\mu} \frac{\partial}{\partial X^{\mu}} = X'^{\mu} \frac{\partial}{\partial X'^{\mu}} = \mathcal{O}' \\ \square^2 &\equiv g_{\mu\nu} \frac{\partial}{\partial X^{\mu}} \frac{\partial}{\partial X^{\nu}} = g'_{\mu\nu} \frac{\partial}{\partial X'^{\mu}} \frac{\partial}{\partial X'^{\nu}} = \square'^2 \end{aligned} \quad (30)$$

are also invariant under TCT. These operators play an important role in the formalism TFT [1].

The coordinates $\mathbf{X} = \{X^1, \dots, X^n\}$ of the *Space of Thermodynamic Forces* (or, simply referred to as the *Thermodynamic Space*), take values on \mathbb{R}^n . However, the ratios $X^\mu/X^{\mu-1}$ are the coordinates for a different space, the real projective space \mathbb{RP}^{n-1} , which is defined to be the quotient of \mathbb{R}^n minus the origin by the scaling map $X^\mu \rightarrow \alpha X^\mu$ where α is any nonzero real number. Note that some of the X^μ may vanish; removing the origin simply implies that not all of the X^μ vanish simultaneously. Fig. 1 illustrates a space, which is diffeomorphic to the \mathbb{RP}^{n-1} . Observe that X'^μ is an arbitrary smooth, degree 1 function of the X 's with the property that $X \rightarrow X'$ is invertible. This implies that $X'^\mu/X'^{\mu-1}$ is an arbitrary degree 0 function with these same properties. Now, $\{X'^\mu/X'^{\mu-1}\}$ are again coordinates of \mathbb{RP}^{n-1} . The fact that $X'^\mu/X'^{\mu-1}$ is degree 0 implies that it is invariant under the transformation $X^\mu \rightarrow \alpha X^\mu$ and so the map $X'^\mu/X'^{\mu-1}$ is in fact a map from $\mathbb{RP}^{n-1} \rightarrow \mathbb{RP}^{n-1}$:

$$\mathbb{RP}^{n-1} \rightarrow \mathbb{RP}^{n-1} : \frac{X^\mu}{X^{\mu-1}} \mapsto \frac{X'^\mu}{X'^{\mu-1}} = \frac{F^\mu \left(\frac{X^2}{X^1}, \frac{X^3}{X^2}, \dots, \frac{X^n}{X^{n-1}} \right)}{F^{\mu-1} \left(\frac{X^2}{X^1}, \frac{X^3}{X^2}, \dots, \frac{X^n}{X^{n-1}} \right)} \quad (31)$$

So, we have learned that the TCT yields a map from \mathbb{RP}^{n-1} to itself. Furthermore, the invertibility condition implies that this map is invertible and the smooth inverse condition implies that this map is a diffeomorphism. Thus, every TCT defines a diffeomorphism of \mathbb{RP}^{n-1} to itself.

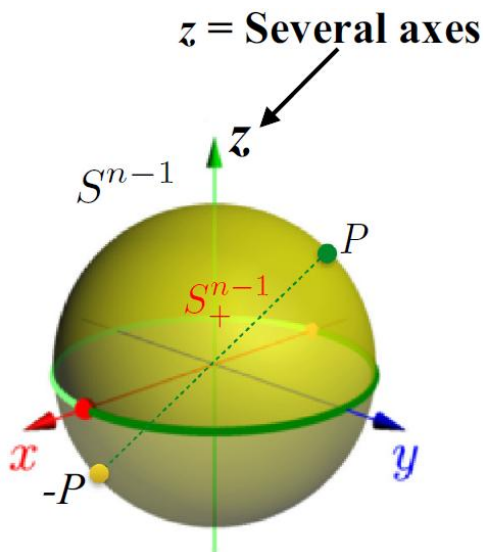


Fig. 1. The projective space. The Projective space \mathbb{RP}^{n-1} is diffeomorphic to S_+^{n-1} made by the upper hemisphere + half equator (without the red and yellow points) + the red point

At this point, we are tempted to conclude that the group of TCTs is just the group $\text{diff}(\mathbb{RP}^{n-1})$ of such diffeomorphisms. However, this is not quite true because the ratios $X'^\mu/X'^{\mu-1}$ do not contain all the information in the X'^μ .

To reconstruct all the X'^μ from the ratios, one also needs to know, for example, X'^1 or equivalently the real-valued function $F^1: \mathbb{RP}^{n-1} \rightarrow \mathbb{R}$, which intuitively gives the overall scale dependence of the TCT. Therefore, the TCT-group is a product of $\text{diff}(\mathbb{RP}^{n-1})$ with the multiplicative group of maps from \mathbb{RP}^{n-1} to the non-vanishing reals \mathbb{R}^x where the non-vanishing condition is needed to ensure non-degeneracy (see see Fig. (2)) [11,12]. Let us illustrate the structure of the group G^n with two simple examples. The simplest example is the case $n = 1$, where there is only one force X^μ . Now, \mathbb{RP}^{n-1} is just a point. The group of diffeomorphisms of the point is a trivial group, consisting of only the identity element. Any bundle over a point is trivial, so in this case the total space of the bundle is just \mathbb{R}^x itself and so the group of TCTs is the group of maps from the point to \mathbb{R}^x which is just \mathbb{R}^x itself, the multiplicative group of non-vanishing real numbers α . The action of this group on the force

X^μ is just multiplication by α . So, there is a one to one correspondence between TCTs and nonzero real numbers α . Therefore, we find that if there is only one thermodynamic force, then the TCTs are linear.

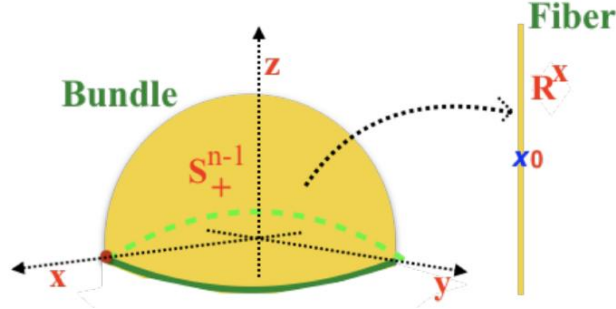


Fig. 2. The TCT-group. The TCT-group G^n is the application F^μ , from the *bundle* (the projective space \mathbb{RP}^{n-1}) to the *fiber* (\mathbb{R}^x)

The case $n = 2$ shows the full structure of the group. The projective space \mathbb{RP}^1 is a semicircle with both extremes identified, which topologically is just the circle S^1 . Therefore, the group of TCTs is locally the product of the group of diffeomorphisms of the circle, which physically describes the mixing between X^1 and X^2 , with the group of scalings $S^1 \rightarrow \mathbb{R}^x$. Now, a rotation of the (X^1, X^2) plane by 180° is a rotation of \mathbb{RP}^1 all the way around and so it acts trivially on \mathbb{RP}^1 . However, it corresponds to the element -1 of the maps from \mathbb{RP}^1 to \mathbb{R}^x . So indeed, the group G^2 is not simply a product of the groups of scalings and rotations; the scalings are nontrivially fibered over the rotations.

3.2.2 Algebraic structure of the TCT-group

In the previous Subsection, we have seen the TCT group, denoted by G^n , is a specific subgroup of the homogeneous diffeomorphisms from $\text{diff}(\mathbb{R} \setminus \{0\})$. In this Subsection, we describe the algebraic properties of the group G^n . Let S^{n-1} be the $(n - 1)$ -dimensional unit sphere ($|\mathbf{X}| = 1$), represented as a C^∞ differentiable manifold, as a submanifold embedded in \mathbb{R}^n . Define the equivalent relation \mathcal{R} as follows: $\mathbf{X}, \mathbf{Y} \in S^{n-1}$ are equivalent iff $\mathbf{Y} = \pm \mathbf{X}$. Denote by \mathcal{G}_p^n the subgroup of $\text{diff}(\mathbb{R} \setminus \{0\})$ and let $\mathbf{Y} \in \mathcal{G}_p^n$ iff $\mathbf{Y}(-\mathbf{X}) = -\mathbf{Y}(\mathbf{X})$ where $S^{n-1} \ni \mathbf{X} \rightarrow \mathbf{Y}(\mathbf{X}) \in S^{n-1}$. The TCT group, denoted by G^n , is the subgroup of homogeneous diffeomorphisms from $\text{diff}(\mathbb{R} \setminus \{0\})$ i.e., $\text{diff}(\mathbb{R} \setminus \{0\}) \ni \mathbf{X} \mapsto \mathbf{Y}_g(\mathbf{X}) \in \text{diff}(\mathbb{R} \setminus \{0\})$. Hence, $\mathbf{Y}_g \in G^n$ iff

$$\mathbf{Y}_g(\mathbf{X}) = \lambda \mathbf{Y}_g(\mathbf{X}) \quad \lambda \in \mathbb{R}, g \in G^n \quad (32)$$

It is possible to demonstrate that the TCT-group, G^n , may be split in a semidirect product of two subgroups where the first one is a *normal*, Abelian, subgroup, denoted by N^n , and the second one is the *reflection* subgroup denoted by H^n [11]. More specifically, let us introduce two subgroups N^n and H^n defined as follows. Let N^n denote the subset *normal subgroup* of G^n defined as

$$N^n : \mathbf{Y}_g(\mathbf{X}) = \mathbf{X} r_g(\mathbf{X}) \quad g \in N^n \subset G^n \quad (33)$$

with $\lambda \in \mathbb{R}$. Here, $r_g(\mathbf{X})$ is a positive $C^\infty(\mathbb{R} \setminus \{0\})$ homogeneous function i.e.

$$r_g(\lambda \mathbf{X}) = r_g(\mathbf{X}) > 0 \quad \text{with } \lambda \in \mathbb{R} \quad (34)$$

Let H^n denote the *reflection* subgroup of G^n defined as

$$H^n : \|\mathbf{Y}_h(\mathbf{X})\| = \|\mathbf{X}\| ; \mathbf{Y}_h(-\mathbf{X}) = -\mathbf{Y}_h(\mathbf{X}) \quad \text{with } h \in H^n$$

then the following theorem is valid [11]

$$G^n = N^n \times H^n \quad (35)$$

The interested reader can find in the Appendix the proof of this Theorem. A consequence of (35) is that the irreducible representations of the group G^n are related to the irreducible representations of the subgroups N^n and H^n .

4. THE THERMODYNAMIC COVARIANCE PRINCIPLE (TCP)

The thermodynamic equivalence principle leads, naturally, to the following *Thermodynamic Covariant Principle* (TCP) [1,10]:

All thermodynamic equations involving the thermodynamic forces and flows (e.g., the closure equations) must be covariant under (TCT).

The essence of the TCP is the following. The equivalent character between two representations is warranted iff the fundamental thermodynamic equations (e.g. the transport equations) are covariant under the Thermodynamic Coordinate Transformations (TCT). From this principle, it is possible to obtain the (non- linear) closure equations by truncating the equations (obtained, for instance, by kinetic theory) relating the thermodynamic forces with the conjugate flows in such a way that the resulting expressions satisfy the TCP. A concrete example is briefly mentioned in the forthcoming Section (4).

5. A PHYSICAL APPLICATION OF THE TCP: DERIVATION OF THE COLLISIONAL OPERATOR FOR MAGNETICALLY CONFINED PLASMAS

The aim of this section is to derive the expression of the collisional operator for magnetically confined plasmas, which guarantees that the thermodynamic covariance principle (TCP) is satisfied by the closure transport relations (i.e., the flux-force relations). Let us consider a two-component system of charged particles. The statistical state is represented by two reduced distribution functions f^α corresponding to ions i and electrons e [13] (no Einstein's convention on index α):

$$\begin{aligned} \frac{\partial}{\partial t} f^\alpha(\mathbf{q}, \mathbf{v}, t) = & -\mathbf{v} \cdot \frac{\partial}{\partial \mathbf{q}} f^\alpha(\mathbf{q}, \mathbf{v}, t) - \frac{e_\alpha}{m_\alpha} \left[\mathbf{E}(\mathbf{q}, t) + \frac{1}{c} \mathbf{v} \wedge \mathbf{B}(\mathbf{q}) \right] \cdot \frac{\partial}{\partial \mathbf{v}} f^\alpha(\mathbf{q}, \mathbf{v}, t) \\ & + C^\alpha(f, f) \end{aligned} \quad (36)$$

Here, $\alpha = e, i$ and c is the speed of light in vacuum. Moreover, e_α and m_α are the charge and the mass of species α , \mathbf{q} and \mathbf{v} denote the generalized coordinates and the velocity of the particle, and \mathbf{E} and \mathbf{B} the electric and the magnetic fields, respectively. Note that the first term on the right-hand side of Eq. (36) represents the *free flow*, the second term corresponds to the *electromagnetic contribution*, and the last term is the contribution due to *collisions*. In many applications in plasmas physics (including those involving the radio-frequency waves), collisions dominate the thermal particles. Therefore, the distribution function can conveniently be expanded about a Maxwellian

$$f^\alpha(\mathbf{x}, \mathbf{v}, t) = f_{eq.}^\alpha(\mathbf{x}, \mathbf{v}, t) [1 + \chi(\mathbf{x}, \mathbf{v}, t)] \quad (37)$$

where \mathbf{x} denotes the *position of the particle*. In Eq. (37) we have introduced the *reference state* $f_{eq.}^\alpha(\mathbf{x}, \mathbf{v}, t)$, i.e., the local plasma equilibrium (L.P.E.), and the *deviation from the reference state* χ . The local plasma equilibrium is defined in the following way. The electron-electron and ion-ion collisions bring the plasma in a short time to a state of local plasma equilibrium satisfying the equations

$$C^{ee} = C^{ii} = 0 \quad (38)$$

with C^{ee} and C^{ii} denoting the electron-electron and ion-ion collisions, respectively (see below the expression of the collisional operator). The L.P.E. is the solution of Eqs. (38)

$$f_{eq}^\alpha(\mathbf{x}, \mathbf{v}, t) = (2\pi)^{-3/2} n_\alpha(\mathbf{x}, t) \left[\frac{m_\alpha}{T_\alpha(\mathbf{x}, t)} \right]^{3/2} \exp(-\mathbf{c}_n \cdot \mathbf{c}_n) \quad (39)$$

$$\mathbf{c}_n \equiv \left(\frac{m_\alpha}{T_\alpha} \right)^{1/2} [\mathbf{v} - \mathbf{u}(\mathbf{x}, t)]$$

where \mathbf{u}^α , n^α , T^α are the *mean velocity*, the *number density*, and *temperature*, respectively. The deviation χ may be developed in terms of the Hermite polynomials $H_{r_1 r_2}^{(m)} \dots$:

$$\begin{aligned} \chi(\mathbf{x}, \mathbf{c}_n, t) = & \sum_{n=0}^{\infty} q^{\alpha(2n)}(\mathbf{x}, t) H^{(2n)}(\mathbf{c}_n) + \sum_{n=0}^{\infty} q_r^{\alpha(2n+1)}(\mathbf{x}, t) H_r^{(2n+1)}(\mathbf{c}_n) \\ & + \sum_{n=0}^{\infty} q_{rs}^{\alpha(2n)}(\mathbf{x}, t) H_{rs}^{(2n)}(\mathbf{c}_n) + \dots \end{aligned} \quad (40)$$

with $q^{\alpha(m)}(\mathbf{x}, t)$ denoting the Hermitian moments [13]. The Landau collisional operator can be brought into the form [14,15]

$$C^\alpha(f, f) = \sum_{\beta=e,i} C^{\alpha\beta}$$

$$C^{\alpha\beta}(f^\alpha(1), f^\beta(2)) = 2\pi e_\alpha^2 e_\beta^2 \ln \Lambda \int d\mathbf{v}_2 \tilde{\partial}_r G_{rs}(\mathbf{v}_1 - \mathbf{v}_2) \tilde{\partial}_s f^\alpha(1) f^\beta(2) \quad (41)$$

with r, s identifying the components of a vector, and indices (1) and (2) the colliding particles (1) and (2), i.e., (1) $\equiv (\mathbf{x}_1, \mathbf{v}_1, t)$ and (2) $\equiv (\mathbf{x}_2, \mathbf{v}_2, t)$. Here, $\ln \Lambda$ and G_{rs} are the *Coulomb logarithm* (linked to the *Debye length* λ_D) and the *Landau tensor*, respectively, i.e.,

$$\begin{aligned} \ln \Lambda = & \ln \frac{3(T_e + T_i)\lambda_D}{2Ze^2} \\ \lambda_D = & \left[\frac{4\pi Ze^2(n_e T_e + n_i T_i)}{T_e T_i (1 + Z)} \right]^{-1/2} \\ G_{rs}(\mathbf{a}) = & \frac{a^2 \delta_{rs} - a_r a_s}{a^3} \end{aligned} \quad (42)$$

with \mathbf{a} denoting the relative velocity of two particles, i.e., $\mathbf{a} \equiv \mathbf{v}_1 - \mathbf{v}_2$. The operator $\tilde{\partial}_r$ is defined as follows:

$$\tilde{\partial}_r \equiv m_\alpha^{-1} \partial_{v_{1r}} - m_\beta^{-1} \partial_{v_{2r}} \quad (43)$$

By inserting Eqs. (37) - (40) into Eq. (36), and by truncating the expansion up to the second order of the (small) *drift parameter* ϵ (defined as the Larmour radius over a macroscopic length), we get the *vector moment equations* [14]

$$\begin{aligned}
 & \Omega_\alpha \tau_\alpha \epsilon_{rmn} q_m^{\alpha(1)} b_n + \tau_\alpha Q_r^{\alpha(1)} + g_r^{\alpha(1)} + \bar{g}_r^{\alpha(1)} + O(\epsilon^2) \\
 & \Omega_\alpha \tau_\alpha \epsilon_{rmn} q_m^{\alpha(3)} b_n + \tau_\alpha Q_r^{\alpha(3)} + g_r^{\alpha(3)} + \bar{g}_r^{\alpha(3)} + O(\epsilon^2) \\
 & \Omega_\alpha \tau_\alpha \epsilon_{rmn} q_m^{\alpha(5)} b_n + \tau_\alpha Q_r^{\alpha(5)} + g_r^{\alpha(5)} + \bar{g}_r^{\alpha(5)} + O(\epsilon^2) \\
 & Q_r^{\alpha(m)} = n_\alpha^{-1} \int d\mathbf{v} H_r^m [(m_\alpha/T_\alpha)^{1/2} (\mathbf{v} - \mathbf{u}^\alpha)] C^\alpha
 \end{aligned} \tag{44}$$

where the Einstein convention is adopted on the repeated indices m and n , but not on the index α . Here, \mathbf{b}_n is a unit vector along the magnetic field \mathbf{B} , i.e., $\mathbf{b}_n \equiv \mathbf{B}_n/B$, ϵ_{rmn} is the completely antisymmetric Levi-Civita symbol, Ω_α is the Larmor frequency of species α , and τ_α is the *relaxation time of species α* , respectively. Moreover, $g_r^{\alpha(n)}$, $\bar{g}_r^{\alpha(n)}$, and $Q_r^{\alpha(n)}$ are the *dimensionless source terms related to the thermodynamic forces*, the *additional sources terms in the long mean free path transport regime*, and the *dimensionless friction terms*, respectively (the exact definitions of these quantities may be found in Ref. [14]).

For collision-dominated plasmas (i.e., in absence of turbulence), the entropy production \sum^α of the plasma for species α may be brought into the form [14]

$$\sum^\alpha = -\tau_\alpha \sum_{n=0(1)}^N q_r^{\alpha(n+1)} Q_r^{\alpha(2n+1)} \tag{45}$$

The lower limit for n is 0 for the electrons and 1 for the ions. Hence, thanks to this theorem, $Q_r^{\alpha(n)}$ and $q_r^{\alpha(n)}$ are the *thermodynamic forces* and the *thermodynamic fluxes* for magnetic confined plasmas, respectively. Equation (45) tells us that the last equation of Eqs. (44) is the closure equation (flux-forces relation) for tokamak plasmas, derived by kinetic theory. As mentioned in Section (55), the region where the transport coefficients do not depend on the thermodynamic forces is referred to as *Onsager's region* or the *linear thermodynamic regime*. Out of Onsager's regime, the transport coefficients may depend on the thermodynamic forces. This happens when the above-mentioned assumption (i) and/or assumption (ii) are/is not satisfied (see Section (55)). Magnetically confined tokamak plasmas are a typical example of thermodynamic systems out of Onsager's region. In this case, even in absence of turbulence, the local distribution functions of species (electrons and ions) deviate from the (local) Maxwellian [see Eq. (37)]. After a short transition time, the plasma remains close to (but, it is not in) a state of local equilibrium (see, for example, [14,16]). The neoclassical theory is a linear transport theory (see, for example, [14]) meaning by this, a theory where the moment equations are coupled to the closure relations (i.e., flux-force relations), which have been linearized with respect to the generalized frictions (see, for example, Ref. [13]). This approximation is clearly in contrast with the fact that the distribution function of the thermodynamic fluctuations is not a Maxwellian and it could be a possible cause of disagreement between the theoretical predictions and the experimental profiles [16,17]. However, it is important to mention that it is well accepted that the main reason of this discrepancy is attributed to turbulent phenomena existing in tokamak plasmas. Fluctuations in plasmas can become unstable and therefore amplified, with their nonlinear interaction, successively leading the plasma to a state, which is far away from equilibrium. In this condition, the transport properties are supposed to change significantly and to exhibit qualitative features and properties that could not be explained by collisional transport processes, e.g., size scaling with machine dimensions and nonlocal behaviors that clearly point at turbulence spreading, etc. (see, for example, Ref. [18]). Hence, the truly complete transport theory of plasmas must self-consistently incorporate the instability theory that includes the influence of nonlinear transformations on fluctuations. This global approach is the purpose of the so-called anomalous transport theory (still far from a complete and comprehensive theory). This type of problem is, however, far beyond the scope of this work. Here, more modestly, we deal with plasmas in the collisional-dominated transport regime, characterized by a time scale which is much longer than one involved in the so-called fluctuation-induced turbulence transport. Our aim is to determine the simplest expression of the

collisional operator such that the resulting closure equation satisfies the TCP (without, of course, violating the energy, mass, and momentum conservation laws). Concretely, in mathematical terms, we need to identify an operator able to kill the terms that do not satisfy the TCP and, in order not to violate the conservation laws, which commutes with the operator $\tilde{\delta}_r$. The last equation in Eq. (44) will satisfy the TCP if

$$\text{when } C^{\alpha\beta} \rightarrow \lambda C^{\alpha\beta} \quad \text{then } Q_r^{\alpha(m)} \rightarrow \lambda Q_r^{\alpha(m)} \quad (46)$$

with λ denoting a constant parameter. We introduce now the operator \mathcal{O}_{TCT} defined as follows:

$$\mathcal{O}_{TCT} \equiv \left[2 - \chi^{\alpha(1)} \frac{\partial}{\partial \chi^{\alpha(1)}} - \chi^{\beta(2)} \frac{\partial}{\partial \chi^{\beta(2)}} \right] \quad (47)$$

It is easily checked that this operator possesses the following properties:

$$\begin{aligned} \mathcal{O}_{TCT}(\chi^\alpha) &= \chi^\alpha & ; & \quad \mathcal{O}_{TCT}((\chi^\alpha)^2) = 0 \\ \mathcal{O}_{TCT}(\chi^{\alpha(1)}\chi^{\beta(2)}) &= 0 & ; & \quad [\mathcal{O}_{TCT}, \tilde{\delta}_r] = 0 \end{aligned} \quad (48)$$

where the square brackets denote the *Lie brackets*. The last equation of Eq. (44) (the closure equation) satisfies the TCP iff

$$C_{TCT}^\alpha = C^{\alpha\beta} [\mathcal{O}_{TCT}(f(1)f(2))] \quad (49)$$

or

$$\begin{aligned} C_{TCT}^{\alpha\beta} &= 2\pi e_\alpha^2 e_\beta^2 \ln \Lambda \int d\mathbf{v}_2 \tilde{\delta}_r G_{rs}(\mathbf{v}_1 - \mathbf{v}_2) \tilde{\delta}_s \\ &\quad \times \{ (f^\alpha(1)_{eq.} f^\beta(2)_{eq.} [\chi^\alpha(1) + \chi^\beta(2)] \} \end{aligned} \quad (50)$$

Equation (50) can conveniently be written in the form

$$\begin{aligned} C_{TCT}^{\alpha\beta} &= 2\pi e_\alpha^2 e_\beta^2 \ln \Lambda \int d\mathbf{v}_2 \tilde{\delta}_r G_{rs}(\mathbf{v}_1 - \mathbf{v}_2) \tilde{\delta}_s (f^\alpha(1) f^\beta(2))_+ \quad \text{with} \\ (f^\alpha(1) f^\beta(2))_+ &\equiv f^\alpha(1) f_{eq.}^\beta(2) + f_{eq.}^\alpha(1) f^\beta(2) \end{aligned} \quad (51)$$

Thanks to the last relation in Eqs, (48), we also get

$$\int d\mathbf{v} C_{TCT}^\alpha = 0 \quad (\alpha = e, i) \quad \text{number of particles conservation.} \quad (52)$$

$$\sum_\alpha m_\alpha \int d\mathbf{v} v_r C_{TCT}^\alpha = 0 \quad (r = 1, 2, 2) \quad \text{momentum conservation.} \quad (53)$$

$$\sum_\alpha \frac{1}{2} m_\alpha \int d\mathbf{v} v^2 C^\alpha = 0 \quad \text{energy conservation.} \quad (54)$$

with $C_{TCT}^\alpha = \sum_{\beta=e,i} C_{TCT}^{\alpha\beta}$. Equation (51) is the linearized TCT collision operator used in existing literature [19,20]. However, it should be noted that in previous literature the quadratic contributions in the distribution functions are ignored without any physical justification. Here, on the contrary, the linearization process of the collisional operator rests upon the validity of a fundamental principle, that is, the thermodynamic covariance principle. Notice that to linearize the collisional operator does not mean that we are in the Onsager regime. As known, this regime is attained by performing two operations: (1) the transport phenomena is evaluated by determining a finite number of Hermitian moments of the distribution functions, and (2) the truncated set of moment equations is linearized in some appropriate way [13,14].

6. SUMMARY OF THE CHAPTER AND CONCLUDING REMARKS

If one requires that only the entropy production is invariant under the flux-force transformation, without imposing the auxiliary condition that also the Glansdorff-Prigogine dissipative quantity P must be invariant under TCT, we enter into contradiction. Indeed, let us consider a thermodynamic system where the transport coefficients satisfy the reciprocity relations. Then, it is easily checked that there exists a larger class of thermodynamic transformations, leaving invariant the entropy production, which violates the validity of the reciprocity relations [21]. In addition, as rightly pointed out by Verschaffelt and Davies, *to impose that only the entropy production must be invariant under flux-force transformations may lead to paradoxes or inconsistencies* [6,7]. The correct way to overcome this *impasse* is to require that both the entropy production and the Glansdorff-Prigogine dissipative quantity P must remain unaltered under the TCT (with the supplementary condition that $t = t'$). In this chapter, we determined the class of thermodynamic transformations leaving invariant both the entropy production and the Glansdorff-Prigogine dissipative quantity. This class of admissible transformations, referred to as the Thermodynamic Coordinate Transformations (TCT), is the most general class of force-transformations able to warrant the equivalence between thermodynamic systems. Successively, we studied the Lie group associated to the TCT. More in particular, also the Lagrangian of a thermodynamic system must be invariant under TCT. The TCT form a group (referred to as the G^n group). In particular, we have seen that the TCT group is a bundle whose base is $diff(\mathbb{R}^{n-1})$ and the fiber is the space of maps $\mathbb{R}^{n-1} \rightarrow \mathbb{R}^x$. We have also seen, that the TCT group may be split as semidirect product of an Abelian normal subgroup and another subgroup of TCT. The irreducible representations of the TCT group are then related to the irreducible representations of these two subgroups. The invariance under TCT leads naturally to the formulation of the Thermodynamic Covariance Principle (TCP). This principle affirms that the thermodynamic equations, including the nonlinear closure relations, must be covariant under the TCT. The Nonlinear closure relations theory for transport processes in non-equilibrium systems (referred to as the *Thermodynamic Field Theory* (TFT)), reported in Ref. [1], is based on the validity of the Thermodynamic Covariance Principle. This assumption allows truncating, at the lowest order, the (highly nonlinear) equations relating the thermodynamic forces with the conjugate fluxes. For example, in the case of Tokamak-plasmas, these relations are obtained by kinetic theory and are expressed by highly nonlinear integral equations [13]. In this specific case, the generalized frictions are the thermodynamic forces whereas the conjugate fluxes correspond to the Hermitian moments [14]. The Hermitian moments are linked to the deviation of the distribution function from the (local) Maxwellian, whereas the generalized frictions are linked to the collision term. According to the TCP, these integral equations may be truncated in such a way that the resulting expressions satisfy the covariance under TCT.

In the second part of this chapter we have derived the collisional operator for fully ionized Tokamak-plasmas that ensures, at the lowest order, the covariance under TCT of the closure transport equations [11]. Fig. 3 shows a comparison between experimental data for fully collisional FTU (Frascati Tokamak Upgrade) – plasmas and the theoretical predictions. In the vertical axis, we have the (surface magnetic-averaged) radial electron heat flux and in the horizontal axis the minor radius of the Tokamak. The lowest dashed profile corresponds to the Onsager (neo-classical) theory and the bold line to the nonlinear theory (i.e. the Thermodynamical Field Theory (TFT)) satisfying the TCP, respectively. The highest profile is the experimental data provided by the C.R. ENEA EUROfusion [22]. As we can see, the TCP is well satisfied in the core of the plasma where plasma is in the collisional transport regime. Towards the edge of the Tokamak, transport is dominated by

turbulence. The theoretical predictions are fairly in line with the preliminary experimental data obtained for FTU-plasmas. In Ref. [23], we report, for the first time, the explicit form of the nonlinear partial differential equations (PDEs) subject to the correct boundary conditions that have to be satisfied by transport coefficients having a vanishing skew-symmetric piece. We also report, for the first time, the nonlinear PDEs, with the appropriate boundary conditions, for transport coefficients when the thermodynamic system is subject to two thermodynamic forces (e.g. the gradient of pressure and the gradient of temperature). Since the proposed PDEs have been derived without neglecting any term of the dynamical equations (i.e., the energy, mass and momentum balance equations), we propose them as a good candidate for describing transport processes in thermodynamic systems also for systems in turbulent regime. The main objective of our research is to apply our approach to the Divertor Tokamak Test (DTT) facility, to be built in Italy, and to the International Thermonuclear Experimental Reactor (ITER).

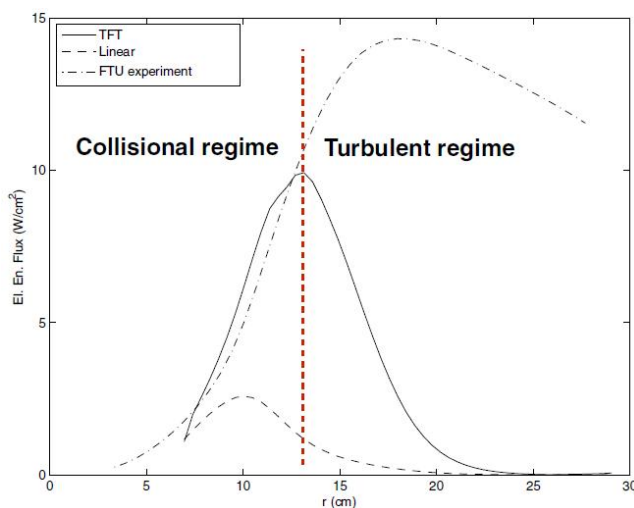


Fig. 3. Electron heat loss in FTU-plasmas vs the minor radius of the Tokamak. The highest dashed line is the experimental profile. These data have been provided by Marinucci from the C.R. ENEA EUROfusion in Frascati [22]. The bold line is the theoretical profile obtained by the nonlinear theory satisfying the TCP (TFT) and the lowest dashed profile corresponds to the theoretical prediction obtained by Onsager's theory (i.e., by the neoclassical theory)

For the sake of completeness, we conclude this chapter by mentioning that attempts to derive a *Generally Covariant Thermodynamic Field Theory* (GTFT) can be found in refs [24,25,26]. In Refs [24,25], the general covariance has been assumed to be valid for general transformations in the space of the thermodynamic configurations, whereas in Ref. [26] it is assumed that the entropy production rate must be invariant under *General Spatial Coordinate Transformations*³. However, it is now well established that that the GTFT is in disagreement with experiments and it is valid only for a very limited class of thermodynamic processes. So, at a best of our knowledge, a correct theory of transport processes in non-equilibrium systems must respect the TCP, i.e. the TFT.

COMPETING INTERESTS

Authors have declared that no competing interests exist.

REFERENCES

1. Sonnino G. Nonlinear closure relations theory for transport processes in nonequilibrium systems. *Phys. Rev. E.* 2009;79:051126.

³Notice that in [26] the invariance of the Prigogine-Glansdorff dissipation is not satisfied.

2. Onsager L. Reciprocal relations in irreversible processes, I. *Phys. Rev.* 1931;37:405.
3. Onsager L. Reciprocal relations in irreversible processes, II. *Phys. Rev.* 1931;38:2265.
4. Prigogine I. *Thermodynamics of irreversible processes.* John Wiley & Sons; 1954.
5. Prigogine I. *Etude Thermodynamique des Phénomènes Irréversibles, Thèse d'Aggrégation de l'Enseignement Supérieur de l'Université Libre de Bruxelles (U.L.B.);* 1947.
6. Verschaffelt JE. The thermomechanical effect. *Bull. Classe Sci. Acad. Roy. Belg.* 1951;37:853.
7. Davies RO. Transformation properties of the Onsager relation. *Physica.* 1952;18:182.
8. Glandsdorff P, Prigogine I. *Thermodynamic theory of structure, stability and fluctuations.* John Wiley & Sons, London, New York; 1971.
9. Glandsdorff P, Prigogine I. Sur Les Propriétés Différentielles de La Production d'Entropie. *Physica.* 1954;20:773.
10. Sonnino G, Sonnino A. The thermodynamic covariance principle. *Journal of Thermodynamics & Catalysis.* 2014;5:129.
11. Sonnino G, Evslin J, Sonnino A, Steinbrecher G, Tirapegui E. Symmetry group and group representations associated with the thermodynamic covariance principle. *Phys. Rev. E.* 2016;94:042103.
12. Sonnino G. Geometry and symmetry in non-equilibrium thermodynamic systems. American Institute of Physics (AIP), Conference Proceedings. 2017;1853:030002.
DOI: 10.1063/1.498535.
Workshop: MaxEnt. 36 International Workshops on Bayesian Inference and Maximum Entropy Methods in Science and Engineering, Ghent (Belgium), July 10-15; 2016.
13. Balescu R. *Transport Processes in Plasmas, Vol 1. Classical Transport,* Elsevier Science Publishers B.V., Amsterdam, North-Holland; 1988.
14. Balescu R. *Transport Processes in Plasmas, Vol 2. Neoclassical Transport,* Elsevier Science Publishers B.V., Amsterdam, North-Holland; 1988.
15. Lifshitz EM, Pitaevskii LP. *Physical Kinetics: Course of Theoretical Physics, Vol. 10 - 1st Ed.,* British Library Cataloguing in Publication Data, Oxford London Boston Munich New Delhi Singapore Sidney Tokyo Toronto Wellington; 1981.
16. Sonnino G, Peeters P. Nonlinear transport processes in tokamak plasmas. I. The collisional regimes. *Physics of Plasmas.* 2008;15:062309/1-062309/23.
17. Sonnino G. Losses and nonlinear steady-state particle distribution functions for fully ionized tokamak-plasmas in the collisional transport regimes. *Eur. Phys. J.* 2011;D62:81.
18. Diamond PH, Itoh SI, Itoh K, Hahm TS. Zonal flows in plasma - A review. *Plasma Phys. Controlled Fusion.* 2005;47:R35.
19. Hinton FL, Hazeltine RD. Theory of plasma transport in toroidal confinement systems. *Rev. Mod. Phys.* 1976;48:239.
20. Karney CFF. Fokker-Planck and Quasilinear codes. *Comput. Phys. Rep.* 1986;4:183.
21. De Groot SR, Mazur P. *Non-equilibrium thermodynamics.* Dover Publications, Inc., New York; 1984.
22. Marinucci M. Experimental data for electron heat loss in FTU-plasmas. Private Communication, C. R. ENEA EUROfusion (Frascati- Italy); 2015.
23. Sonnino G, Nardone P, Peeters P, Tirapegui E. Nonlinear transport in nonequilibrium systems (with an Application to Tokamak-plasmas). *Chaos.* 2020;30:063110.
DOI: <https://doi.org/10.1063/5.0006213>
24. Sonnino G, Evslin J. Geometrical thermodynamic field theory. *Int. J. Quantum Chem.* 2007;107:968.
25. Sonnino G, Evslin J. The minimum rate of dissipation principle. *Physics Letters A.* 2007;365:364.
26. Poletini M. Theory and experiments. *J. Stat. Mech.* 2013;P07005.
DOI: 10.1088/1742-5468/2013/07/P07005
27. Available:https://en.wikipedia.org/wiki/Semidirect_product
28. Robinson DJS. *A course in the theory of groups.* Springer, New York; 1982.
29. Weisstein EW. Semidirect Product, From MathWorld, Wolfram Web Resource.
Available:<http://mathworld.wolfram.com/SemidirectProduct.html>
30. Semi-direct product. *Encyclopedia of Mathematics.*
Available:http://www.encyclopediaofmath.org/index.php_title=Semi-direct-productoldid=35135

APPENDIX: SPLITTING OF THE TCT-GROUP

In this Appendix, we shall prove the validity of Eq. (35). Denote with S^{n-1} the $(n-1)$ -dimensional unit sphere represented as a C^∞ differentiable manifold, which in our case is a submanifold embedded in \mathbb{R}^n of the form

$$\|\mathbf{X}\| = 1 \quad (55)$$

Here the function $\mathbb{R}^n \ni \mathbf{X} \mapsto \|\mathbf{X}\| \in \mathbb{R}^+$ is some $C^\infty(\mathbb{R}^n)$ function having also the properties of a norm. For instance

$$\|\mathbf{X}\| = \left[\sum_{j=1}^n (X_j)^{2k} w_j \right]^{\frac{1}{2k}} ; \quad w_j > 0, \quad k = 1, 2, \dots \quad (56)$$

Let $G_n^S = \text{Diff}(S^{n-1})$ be the group of diffeomorphisms of S^{n-1} and let $G_n^P \subset \text{Diff}(S^{n-1})$ be the subgroup of G_n^S that preserves the equivalence relation \mathcal{R} induced on S^{n-1} by $\mathbf{X}, \mathbf{Y} \in S^{n-1}$ are equivalent iff $\mathbf{Y} = \pm \mathbf{X}$.

Remark 1 *The quotient space S^{n-1}/\mathcal{R} is a diffeomorphism with the $n-1$ dimensional projective space \mathbb{P}^{n-1} , so G_n^P is isomorphic to $\text{Diff}(\mathbb{R}\mathbb{P}^{n-1})$. For all map $\mathbf{X} \rightarrow \mathbf{Y}(\mathbf{X})$ where $\mathbf{Y} \in G_n^S$ we have $\mathbf{Y} \in G_n^P$ iff*

$$\mathbf{Y}(-\mathbf{X}) = -\mathbf{Y}(\mathbf{X}) \quad (57)$$

We denote by N^n the abelian group generated by all $C^\infty(S^{n-1})$ positive functions where the group operation is defined by multiplication, with the additional symmetry property

$$f(\mathbf{X}) \in N^n \quad \text{if} \quad f(-\mathbf{X}) = f(\mathbf{X}) \quad (58)$$

We also denote by $G^n \subset \text{Diff}(\mathbb{R}^n \setminus \{0\})$ the TCT-group: the subgroup of the group of diffeomorphisms of $\mathbb{R}^n \setminus \{0\}$ having the additional homogeneity property

$$\begin{aligned} \mathbb{R}^n \setminus \{0\} \ni \mathbf{X} &\mapsto \mathbf{Y}_g(\mathbf{X}) \in \mathbb{R}^n \setminus \{0\} \\ \mathbf{Y}_g(\lambda \mathbf{X}) &= \lambda \mathbf{Y}_g(\mathbf{X}); \quad \lambda \in \mathbb{R}, \quad g \in G^n \end{aligned} \quad (59)$$

We denote by N^n the subset (normal subgroup, see below) of G^n having the form

$$\mathbf{Y}_g(\mathbf{X}) = \mathbf{X} r_g(\mathbf{X}); \quad g \in N^n \subset G^n \quad (60)$$

where $r_g(\mathbf{X})$ is a positive $C^\infty(\mathbb{R}^n \setminus \{0\})$ homogeneous function

$$r_g(\lambda \mathbf{X}) = r_g(\mathbf{X}) > 0; \quad \lambda \in \mathbb{R} \quad (61)$$

We have the following *proposition*

Proposition 2 *N^n is a normal abelian subgroup, and for all $g, g_1, g_2 \in N^n$ we have*

$$\begin{aligned} r_{g_1 g_2}(\mathbf{X}) &= r_{g_1}(\mathbf{X}) r_{g_2}(\mathbf{X}) \\ r_{g^{-1}}(\mathbf{X}) &= \frac{1}{r_g(\mathbf{X})} \end{aligned} \quad (62)$$

Proof. The group properties Eqs. (62, 2) results immediately, by direct calculation from the general definition of the group product in G^n

$$\mathbf{Y}_{g_1 g_2}(\mathbf{X}) := [\mathbf{Y}_{g_1} \circ \mathbf{Y}_{g_2}](\mathbf{X}); \quad g_1, g_2 \in G^n \quad (63)$$

and by from the definition Eq. (60). The abelian character results from Eq. (62). In order to prove that N^n is a normal subgroup, let $h \in N^n$ and let be $g \in G^n$ an arbitrary element of the TCT-group. We have to prove that

$$u := ghg^{-1} \in N^n \quad (64)$$

or equivalently, to prove that

$$Y_u(\mathbf{X}) = Y_{ghg^{-1}}(\mathbf{X}) = [Y_g \circ Y_h \circ Y_{g^{-1}}](\mathbf{X}) = \mathbf{X} r(\mathbf{X}) \quad (65)$$

where

$$Y_h(\mathbf{x}) = \mathbf{X} r_h(\mathbf{X}) \quad (66)$$

with $r_h(\mathbf{X})$ denoting a positive $C^\infty(\mathbb{R}^n \setminus \{0\})$ homogeneous function. Let us also denote

$$Y_z(\mathbf{X}) = [Y_g \circ Y_h](\mathbf{X}) \quad (67)$$

From Eqs. (59, 66), we get

$$Y_z(\mathbf{X}) = r_h(\mathbf{X}) Y_g(\mathbf{X}) \quad (68)$$

and from Eqs. (65, 68, 59) we find

$$\begin{aligned} Y_u(\mathbf{X}) &= [Y_z \circ Y_{g^{-1}}](\mathbf{X}) = [r_h Y_g \circ Y_{g^{-1}}](\mathbf{X}) \\ &= [r_h \circ Y_{g^{-1}}](\mathbf{X}) [Y_g \circ Y_{g^{-1}}](\mathbf{X}) = r [Y_{g^{-1}}(\mathbf{X})] \mathbf{X} \end{aligned} \quad (69)$$

Observe that $r[Y_{g^{-1}}(\mathbf{X})]$ possesses all the properties required by Eq. (61) which proves Eq. (65). ■

Let us now denote by H^n the subgroup of G^n having the properties

$$\begin{aligned} \|\mathbf{Y}_h(\mathbf{X})\| &= \|\mathbf{X}\| \\ \mathbf{Y}_h(-\mathbf{X}) &= -\mathbf{Y}_h(\mathbf{X}) \quad h \in H^n \end{aligned} \quad (70)$$

Remark 3 Setting in Eq. (70) $\|\mathbf{X}\| = 1$ and by using the second equation of Eqs. (70), we note that the diffeomorphism group H^n is isomorphic to the $\text{Diff}(\mathbb{R}\mathbb{P}^{n-1})$ where \mathbb{P}^{n-1} is the $(n-1)$ -dimensional projective space, since \mathbb{P}^{n-1} can be represented as S^{n-1} with identified antipodal points.

We have the following proposition

Proposition 4 For all $g \in G^n$ we have the unique representation

$$\begin{aligned} g &= h g_N; \quad g_N \in N^n, \quad h \in H^n \\ \mathbf{Y}_g(\mathbf{x}) &= [\mathbf{Y}_h \circ \mathbf{Y}_{g_N}](\mathbf{X}) \end{aligned} \quad (71)$$

Proof. Existence of the representation. Notice that by setting

$$\begin{aligned} \mathbf{Y}_h(\mathbf{X}) &= \frac{\mathbf{Y}_g(\mathbf{X}) \|\mathbf{X}\|}{\|\mathbf{Y}_{g_N}(\mathbf{X})\|} \\ \mathbf{Y}_{g_N}(\mathbf{X}) &= \mathbf{X} r_N(\mathbf{X}) \\ r_N(\mathbf{X}) &= \frac{\|\mathbf{Y}_g(\mathbf{X})\|}{\|\mathbf{X}\|} \end{aligned} \quad (72)$$

Eq. (71) is verified and $r_N(\mathbf{x})$ has the property Eq. (61). In order to prove uniqueness, we consider that in Eq. (71) $\mathbf{Y}_h \in N^n$, with property Eqs. (70), but otherwise arbitrary and $\mathbf{Y}_{g_N}(\mathbf{X}) = \mathbf{X} r(\mathbf{X})$ with $r(\mathbf{X})$ an arbitrary smooth, homogenous function of zero degree. We rewrite Eq. (71), by using Eq. (59)

$$\mathbf{Y}_g(\mathbf{X}) = \mathbf{Y}_h [\mathbf{X} r(\mathbf{X})] = r(\mathbf{X}) \mathbf{Y}_h(\mathbf{X}) \quad (73)$$

Since $r(\mathbf{X}) > 0$ we have

$$\|\mathbf{Y}_g(\mathbf{X})\| = |r(\mathbf{X})| \|\mathbf{Y}_{g_N}(\mathbf{X})\| = r(\mathbf{X}) \|\mathbf{X}\| \quad (74)$$

which leads to

$$r(\mathbf{X}) = r_h(\mathbf{X}) = \frac{\|\mathbf{Y}_g(\mathbf{X})\|}{\|\mathbf{X}\|} \quad (75)$$

From Eqs. (75,74) we obtain Eq. (72) so the proof of uniqueness of the representation Eq. (71). ■

Irrespective to the choice of the norm in the definition of the subgroup H^n , we may easily convince ourselves that they are all equivalent up to a group isomorphism. For easy reference, we recall the semidirect product definition and properties [27,28,29,30].

Theorem 5 Let N, H subgroups of the group G , where N is a normal sub-group. Then the following statements are equivalent:

- a) $G = NH$ and $N \cap H = \{e\}$.
- b) For all $g \in G$ there exists a unique representation $g = nh$ with $n \in N$ and $h \in H$.
- c) For all $g \in G$ there exists a unique representation $g = hn$ with $n \in N$ and $h \in H$.
- d) The natural embedding $i: H \rightarrow G$, composed with the natural projection $p: G \rightarrow G/N$, yields an isomorphism $\psi: H \rightarrow G/N$, $\psi = p \circ i$ with inverse $\hat{\chi}: G/N \rightarrow H$.
- e) There exists a homomorphism $\chi: G \rightarrow H$ that is the identity on H and whose kernel is N .

If one of the above properties are verified, G is said to split in a semidirect product of the subgroups H and normal subgroup N . In this case the representations of the group G are related to the representations of the subgroups H and N . By using the Theorem 5 and Propositions 4, 2, we finally get

Theorem 6 The TCT-group G^n is a semidirect product of the abelian normal subgroup N^n and the subgroup H^n

$$G^n = N^n \rtimes H^n \quad (76)$$

Biography of author(s)



Prof. Dr. Giorgio Sonnino

Department of Theoretical Physics and Mathematics, Université Libre de Bruxelles (ULB), Campus Plaine CP 231, Boulevard de Triomphe, 1050 Brussels, Belgium.

He is a Senior Scientific Researcher at the Université Libre de Bruxelles (ULB), Department of Theoretical Physics and Mathematics. He is also Scientific Adviser on “*Sinergy between Scientific Research and Higher Education*” at the European Union - Directorate General for “*Education, Youth, Sport and Culture*”. He has co-authored more than 90 scientific papers published in international scientific peer reviewed journals. He is a referee of several International peer reviewed International Scientific Journals (e.g. Phys. Rev., The Royal Society, Physics Letters, Physics of Fluids, Nuclear Fusion, MPDI etc.) and Editor of several International peer reviewed International Scientific Journals (e.g. MPDI, JMP, Science Publishing Group etc.). He was appointed as a Professor at the Università degli Studi di Genova – Italy and at the University of Tor Vergata, Rome – Italy in the framework of the European GOTIT programme. He was awarded with several scientific prizes. He received his Diploma “Habilitation to Supervise Research” (HDR Diploma – “*Thèse d’Habilitation à Diriger des Recherches*”) in 2002 at the Institut Nonlinéaire de Nice (INLN), Nice - France on “*Thermodynamical Field Theory*”. He got two post-doctorate positions: the first one in 1992 at the Institut Nonlinéaire de Nice (INLN) – France on “*Pattern formations in parametrically forced reaction diffusion chemical systems with nearly degenerate bifurcations*” and the second one in 1993 at the CENOLI (Centre for Nonlinear Systems and Complex Phenomena) on “*The role of hydrodynamic fluctuations near the critical bifurcation points*”. He received his Ph.D. (with end grade *Summa cum Laude*) in 1992 at the *Service de Chimie Physique II*, Université Libre de Bruxelles (ULB), Brussels - Belgium on “*Theory on Hydrodynamic Fluctuations*”. He received his Master Degree in Physics (with end grade *110/110 cum Laude*) in 1985 at the Physics Department, Università degli Studi di Genova, Genova - Italy, with a Master thesis on “*Study of relaxation of hydrodynamic systems far from equilibrium toward the thermodynamic equilibrium*”.



Dr. Alberto Sonnino

Faculty of Engineering Sciences, University College London, Gower Street, London WC1E 6BT, UK.

He was a co-founder and researcher at chainspace.io, which built a scalable smart contract platform. He is now a Research Scientist at Facebook Novi, based in London. His research interests are in distributed systems, blockchains, and privacy enhancing technologies. He has a special interest in cryptography. In the past, he worked on numerical calculations and simulations for physics-related problems (plasma physics, category theory, symmetry groups).

© Copyright (2020): Author(s). The licensee is the publisher (Book Publisher International).

DISCLAIMER

This chapter is an extended version of the article published by the same author(s) in the following journal.
Journal of Thermodynamics & Catalysis, 5(2), 2014.

Synthesis and Structural Features of Indanone, Tetralone and Naphthone Derivatives: Selective Fluorination and Condensation Products

Paul D. Boyle¹, David Breaud², Matthew Churley², Patrick Coppock, Jr.², Elvia Encarnacion-Thomas², Chloe Fernandes², Augustus W. Fountain³, Cristina Gomez⁴, Alejandro Guzman², James L. Jackson⁵, Linh Lam², Ajay Mallia², Samantha Moseley², Sang H. Park², William F. Pearman⁴, Robert D. Schmidt⁶, Joseph C. Sloop^{2*}, Roger D. Sommer⁷, Stephanie Stalker², Jonathan Weyand⁴, Karla Wilmott² and Jonathan Yi²

DOI: 10.9734/bpi/cpcs/v2

ABSTRACT

The present study aims to investigate the synthesis and structural features of Indanone, Tetralone and Naphthone derivatives. Indanone, tetralone and naphthone derivatives and fused-ring heterocycles have been prepared via Claisen condensations, arylhydrazine condensations, Baker-Venkataraman rearrangements, Claisen-Schmidt reactions, selective fluorinations and trifluoroacetylations in yields ranging from 22-92%. Of particular interest is the regiochemistry and stereochemistry observed in these products and their utility as scaffolds for the preparation of heterocyclic derivatives. We also note unusual transformations including a novel one-pot, dual trifluoroacetylation, trifluoroacetylnaphthone synthesis via a deacetylation as well as an acetyl-trifluoroacetyl group exchange. Solid-state structural features exhibited by these compounds were investigated using crystallographic methods. Moreover, Selective incorporation of fluorine and fluorine-containing groups into these heterocyclic products will be a focus of this work. We anticipate reporting these findings in the near future.

Keywords: 2-trifluoroacetyl-1; 3-diketone; 1,3,5-triketone; tautomerism; chalcone; 4H-chromone; pyrazole.

1. INTRODUCTION

Molecules which have medicinal, industrial and herbicidal properties are of continued interest to the pharmaceutical, chemical and agrochemical communities. Substantial investment and research in the field of anti-infectives are now desperately needed if a public health crisis is to be averted. The causes of antimicrobial resistance are multifactorial. In case of an antibiotic, it has been well documented that resistance is mainly caused by continued overreliance on and imprudent use of these antibacterial agents [1,2]. For example, indanone derivatives have anticoagulant properties and are used in elaborating latent fingerprints, bindone variants comprise components of near infrared dyes while certain tetralones and naphthones, ketones similar in structure to those shown in Fig. 1, have demonstrated bioactive properties [3-8]. Since bioactivity is known to be enhanced in many classes of

¹Department of Chemistry, Western University, 1151 Richmond St., London, Ontario, N6A 5B7, Canada.

²School of Science and Technology, Georgia Gwinnett College, 1000 University Center Lane, Lawrenceville, GA 30043, USA.

³Department of Chemistry and Biochemistry, University of South Carolina, 631 Sumter Street Columbia, SC 29208, USA.

⁴Department of Chemistry and Life Science, United States Military Academy, 646 Swift Road, West Point, NY 10996, USA.

⁵US Army Corps of Engineers, 101 West Oglethorpe Avenue, Savannah, GA 31401, USA.

⁶Department of Chemistry, North Carolina State University, P.O. Box 8204, Raleigh, NC 27695, USA.

⁷Molecular Education, Technology, and Research Innovation Center, North Carolina State University, 2620 Yarbrough Dr., Raleigh, NC 27695, USA.

*Corresponding author: E-mail: jsloop@ggc.edu;

fluorinated molecules [6,9], it is desirable to prepare fluorine-containing molecules with similar architecture and gain a better understanding of their structure-property relationships. An examination of the role of fluorine in medicinal chemistry reveals that substitution of an organic compound with even a single fluorine atom or trifluoromethyl group located in a key position of a biologically active molecule can result in a profound pharmacological effect [10,11].

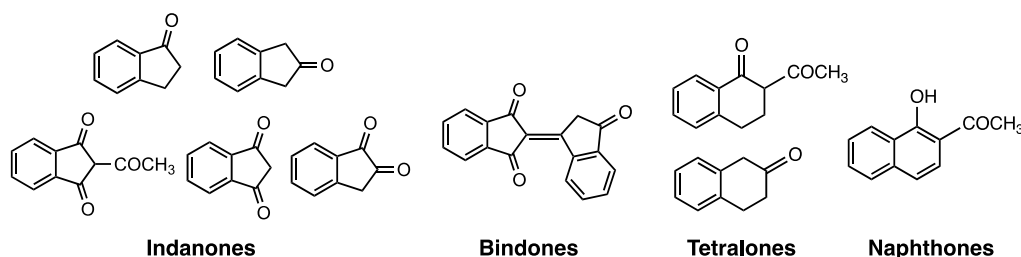


Fig. 1. Medicinally and industrially important ketones

Previously, we reported the preparation and structure-property relationships of acyclic fluorinated and trifluoromethylated β -diketones [12,13]. While the syntheses and properties of these molecules have been investigated thoroughly [14-16], the preparation and study of selectively fluorinated, cyclic ketones containing the structural features of the molecules depicted in Fig. 1 remain relatively limited [17-22]. Currently, many fluorinated compounds are synthesized routinely in pharmaceutical research and are widely used in the treatment of diseases. Fluorine substitution has been extensively investigated in drug research as a means of enhancing biological activity and increasing chemical or metabolic stability [23].

The molecules of interest in this study, shown in Scheme 1, provide this sort of molecular architecture. This paper addresses the design and synthetic approach to prepare these novel molecules, the interesting synthetic results, unique solid-state structural features that differentiate these molecules and the use of selected indanone, bindone, tetralone and naphthone scaffolds in the preparation of fused-ring pyrazoles [24-28], 4*H*-chromones [29-40] and chalcones [41,42], species known to have bioactive properties.

2. EXPERIMENTAL

2.1 Instrumentation

Melting points were obtained on a Mel-Temp or SRS Digimelt MPA160 melting point apparatus and are uncorrected. NMR data were collected in CDCl_3 with TMS as an internal standard using a Varian VXR-400 spectrometer with a broad band probe operating at 400.0 MHz for ^1H , 376.2 MHz for ^{19}F (C_6F_6 as an internal standard) and 100.3 MHz for ^{13}C , an Anasazi-90 spectrometer operating at 90.51 MHz for ^1H , 84.8 MHz for ^{19}F (CFCl_3 as an external standard) and 22.7 MHz for ^{13}C , a Varian VXR-200 spectrometer with a broad band probe operating at 200.0 MHz for ^1H , 188.2 MHz for ^{19}F and 50.3 MHz for ^{13}C , and/or a Bruker Avance 300 spectrometer operating at 300.0 MHz for ^1H , 282.0 MHz for ^{19}F and 75.4 MHz for ^{13}C . Gas chromatographic and mass spectral data were collected on a Shimadzu QP 20105 GC-MS instrument. IR data were collected on a Thermo Scientific Nicolet iS5 FT-IR spectrometer (iD5 ATR) with resolutions of 2 cm^{-1} . Unless otherwise noted, CDCl_3 was used as the solvent and internal standard for ^1H and ^{13}C NMR experiments while CFCl_3 served as the internal standard for ^{19}F NMR experiments. Temperature control for conventional reactions was provided by a J-Kem 210 temperature controller. Radial chromatography was performed on a Chromatotron using 4 mm gypsum/silica gel plates (Analtech) with a gradient elution of 10-30% ethyl acetate in hexane unless otherwise noted. Flash chromatography was performed using a 2" diameter glass column loaded with 60 mesh silica gel (Sigma-Aldrich) using a gradient elution of 10-30% ethyl acetate in hexane unless otherwise noted. All X-ray measurements were made on a Bruker-Nonius X8 Apex2 diffractometer.

2.2 Preparative Procedures

2.2.1 General procedure for the preparation of trifluoromethyl- β -diketones and triketones [19]

A 100 mL round bottom flask equipped with a magnetic stirrer is charged with 50 mL diethyl ether and 60 mmol of sodium methoxide is added slowly. Then, 1 eq (60 mmol) of trifluoromethyl ethyl acetate is added dropwise slowly while stirring. After 5 minutes, 1 eq (60 mmol) of the ketone is added dropwise and stirred overnight at room temperature under a calcium chloride drying tube. The resulting solution is evaporated to dryness under reduced pressure and the solid residue dissolved in 30 mL 3M sulfuric acid. This solution is extracted with ether, and the organic layer dried over Na₂SO₄. The solvent is evaporated under reduced pressure and the crude diketone purified by radial chromatography.

2.2.2 General procedure for the preparation of selectively fluorinated ketones [13,19]

A 100 mL round bottom flask equipped with a magnetic stirrer is charged with 40 mL CH₃CN and the ketone (1 eq: 1-10 mmol). Then, Selectfluor[®] (1-3 eq (3-30 mmol)) dissolved in 30 ml CH₃CN is added slowly while stirring. The solution is either allowed to stir at room temperature or refluxed as required. Times range from 10-30 h. The resulting solution is evaporated to dryness under reduced pressure and the solid residue taken up in distilled water. This solution is extracted with CH₂Cl₂ and the organic layer dried over Na₂SO₄. The solvent is evaporated under reduced pressure and the crude fluorinated ketone purified by radial chromatography.

2.2.3 General procedure for the preparation of pyrazoles [24-28]

A 50 mL round bottom flask equipped with a magnetic stirrer is charged with 25 mL ethanol, the ketone (2 mmol) and 4-trifluoromethylphenylhydrazine (2 mmol). Then, 1 drop concentrated sulfuric acid is added while stirring. A reflux condenser is affixed and the reaction mixture refluxed for 48 h. The resulting solution is evaporated to dryness under reduced pressure and the solid residue is neutralized with 15 mL saturated sodium carbonate. This solution is extracted with 3X5 mL CH₂Cl₂, and the organic layer dried over Na₂SO₄. The solvent is evaporated under reduced pressure and the pyrazole purified by column chromatography (10-30% ethyl acetate/hexane).

2.3 Physical and Spectral Data of Synthesized Compounds

2.3.1 2-fluoro-1,3-indanedione (1b) [19]

This compound was obtained in 60% yield as pale, yellow crystals (EtOH), m.p. 97-99°C. NMR: ¹H (90.5 MHz) δ 5.4 (d, ¹J_{H-F}=51.0Hz, 1H), 7.65-8.22 (m, 4H). ¹³C (22.7 MHz) δ 90.1 (d, ¹J_{C-F}=211.2Hz, CF), 125.3, 138.9, 141.9, 193.5 (d, ²J_{C-F}=24.0Hz, C-CF). ¹⁹F (84.8 MHz) δ -207.3 (d, ¹J_{F-H}=51.1Hz, 1F). HRMS (ESI+) Calcd. for C₉H₅FO₂: 164.02740. Found: 164.027580.

2.3.2 2,2-difluoro-1,3-indanedione (1c) [19]

This compound was obtained in 60% yield from fluorination of 1b as described in the general procedure above as yellowish-brown crystals (EtOH), m.p. 116-117°C. NMR: ¹H (90.5 MHz) δ 8.0-8.15 (m, 4H). ¹³C (22.7 MHz) δ 104.0 (t, ¹J_{C-F}=264Hz, CF₂), 128.8, 138.2, 139.3 (t, ³J_{C-F}= 4.3 Hz), 185.8 (t, ²J_{C-F}=24.0Hz, C-CF₂). ¹⁹F(84.8 MHz) δ -125.9 (s, 2F).

2.3.3 [Δ 1,2'-Biindan]-1',3,3'-trione (1d) [19]

This compound was obtained in 72% yield as orange crystals (EtOH), m.p. 207-209°C. NMR: ¹H (300 MHz) δ 4.17 (s, 2H), 7.74-8.04 (m, 8H), 9.50 (d, J=7.8Hz, 1H). ¹³C (75.5 MHz) δ 43.4, 123.0, 123.4, 123.5, 125.8, 131.7, 134.2, 135.3, 135.4, 140.4, 141.2, 141.6, 145.9, 155.4, 189.5, 191.0, 201.2.

2.3.4 [Δ 1,2'-Biindan]-2-fluoro-1',3,3'-trione (1e) [19]

This compound was obtained in 85% yield from fluorination of 1d as described in the general procedure above as orange crystals (EtOH), m.p. 165-168°C (dec). NMR: ^1H (300 MHz) δ 6.45 (d, $^1J_{\text{H-F}}=46.1\text{Hz}$, 1H), 7.75-8.20 (m, 7H), 9.50 (d, $J=7.7\text{Hz}$, 1H). ^{13}C (75.5 MHz) δ 70.8 (d, $^1J_{\text{C-F}}=194\text{Hz}$, CF), 125.4, 126.6, 129.3, 130.1, 132.0, 137.7, 138.5, 166.3, 189.3, 191.2, 204.1 (d, $^2J_{\text{C-F}}=24\text{Hz}$, C-CF). ^{19}F (282 MHz) δ -182.4 (d, $^1J_{\text{F-H}}=46.0\text{Hz}$, 1F). Analysis calcd for $\text{C}_{18}\text{H}_9\text{FO}_3$: C, 73.97, H, 3.10. Found: C, 74.06, H, 3.21.

2.3.5 2-fluoro-2-(2'-fluoro-3'-oxoindeny)-1,3-indanedione (1f) [19]

This compound was obtained in 92% yield from fluorination of 1e as described in the general procedure above as yellow crystals (EtOH), m.p. 126-129°C. NMR: ^1H (300 MHz) 7.8-8.25 (7H, m), 9.53 (1H, d, $J=6.9\text{Hz}$). ^{13}C (75.5 MHz) δ 89.9, 125.1, 126.3, 129.5, 130.0, 132.2, 137.1, 138.0 (d, $^1J_{\text{C-F}}=254\text{Hz}$, CF), 166.1, 185.9, 189.1. ^{19}F (282 MHz) δ -137.3 (s, 1F), -176.7 (s, 1F). HRMS (ESI+) calcd for $\text{C}_{18}\text{H}_8\text{F}_2\text{O}_3$: 310.04415. Found: 310.04415.

2.3.6 1-trifluoroacetyl-2-indanone (2b) [19]

This compound was obtained in 52% yield as a brown oil. NMR: ^1H (300 MHz) δ 3.73 (2H, s), 7.29 (2H, m), 7.60 (2H, m), 14.19 (1H, bs), ^{13}C (75.5 MHz) δ 40.9, 111.5, 120.4 (CF₃, q, $^1J_{\text{C-F}}=277\text{Hz}$), 122.9, 123.0, 124.9, 127.7, 128.1, 128.8, 129.6, 154.5 (C-CF₃, q, $^2J_{\text{C-F}}=37\text{Hz}$), 203.0. ^{19}F (282 MHz) δ -68.59 (s, 3F). Analysis calcd for $\text{C}_{11}\text{H}_7\text{F}_3\text{O}_2$: C, 57.90, H, 3.09. Found: C, 58.04, H, 3.02.

2.3.7 1,3-ditrifluoroacetyl-2-indanone (2c) [19]

This compound was obtained in 42% yield as yellow crystals (cyclohexane), m.p. 111-113°C. NMR: ^1H (300 MHz) δ 7.34 (2H, m), 7.65 (2H, m), 13.50 (2H, bs). ^{13}C (75.5 MHz) δ 111.5, 118.4 (CF₃, q, $^1J_{\text{C-F}}=273\text{Hz}$), 119.6, 122.9, 126.7, 128.4, 128.9, 130.2, 168.5 (C-CF₃, q, $^2J_{\text{C-F}}=35\text{Hz}$), 177.0. ^{19}F (282 MHz) δ -68.53 (s, 3F). HRMS (ESI+) calcd for $\text{C}_{13}\text{H}_6\text{F}_6\text{O}_3$: 324.02211, Found: 324.02158.

2.3.8 (\pm)1-fluoro-2-indanone (2d) [17]

This compound was obtained in 70% yield as a racemic mixture of enantiomers as a brown oil. NMR: ^1H : δ 3.58 (s, 2H), 5.7 (d, $^2J_{\text{H-F}}=52.5\text{Hz}$, 1H), 7.0-7.6 (m, 4H). ^{19}F : δ -180.8 (d, $^2J_{\text{F-H}}=52.5\text{Hz}$, 1F).

2.3.9 3-trifluoroacetyl-2-tetralone (3b) and 1-trifluoroacetyl-2-tetralone (3c) [19]

These compounds were obtained as a 4:3 mixture of 3b:3c. Radial chromatography afforded two product fractions. Fraction 1: 3b as orange crystals (hexane), in 40% yield, m.p. 123-126°C. NMR: ^1H : (300 MHz) δ 3.76 (2H, s), 3.81 (2H, s), 7.25-8.05 (4H, m), 15.01 (1H, bs). ^{13}C (75.5 MHz) δ 27.8, 38.3, 103.7, 117.5 (CF₃, q, $^1J_{\text{C-F}}=281\text{Hz}$), 127.1, 127.3, 127.8, 127.9, 130.5, 133.4, 157.3, 174.8 (C-CF₃, q, $^2J_{\text{C-F}}=35\text{Hz}$), 191.0. ^{19}F (C₆F₆ ext. std.) (282 MHz) δ -70.62 (s, 3F). HRMS (ESI+) calcd for $\text{C}_{12}\text{H}_9\text{F}_3\text{O}_2$: 242.04470, found: 242.04436. Fraction 2: 3c (30%) as an orange solid, m.p. 88-89°C. 3c: NMR: ^1H (300 MHz) δ 2.72 (2H, t, $^2J=1.9\text{Hz}$), 3.01 (2H, t, $^2J=1.9\text{Hz}$), 7.25 (4H, m), 14.98 (1H, bs). ^{13}C (75.5 MHz) δ 25.0, 30.3, 102.9, 118.6 (CF₃, q, $^1J_{\text{C-F}}=282\text{Hz}$), 126.6, 126.9, 127.3, 128.1, 130.2, 133.8, 158.1, 175.4 (C-CF₃, q, $^2J_{\text{C-F}}=35\text{Hz}$), 189.1. ^{19}F (C₆F₆ ext. std.) (282 MHz) δ -67.70 (s, 3F). HRMS (ESI+) calcd for $\text{C}_{12}\text{H}_9\text{F}_3\text{O}_2$: 242.04470, found: 242.04442.

2.3.10 3-trifluoroacetyl-2-naphthol (3d) [19]

A round bottom flask equipped with a magnetic stirrer containing 30 mL dry Et₂O is charged with 1 equivalent NaOCH₃. Then, 1 equivalent ethyl trifluoroacetate is added dropwise slowly and stirred for 15 min. To this solution is added a 4:3 mixture of compounds 3b:3c dissolved in 20 mL Et₂O. The reaction mixture is stirred overnight at room temperature under a calcium chloride drying tube. The solvent is removed under reduced pressure while heating at 60°C for 20 min. The solid residue is

acidified with 30 mL 3M sulfuric acid and extracted with 3-15 mL portions of Et₂O. The organic layers were combined, washed with deionized water, and the organic layer dried over Na₂SO₄. The solvent was evaporated under reduced pressure, providing a orange solid, which when subjected to radial chromatography, gave a fraction which upon recrystallization, yielded pale, orange crystals (CH₂Cl₂), 3d, in 45% yield, m.p. 80-83°C. 3d: NMR: ¹H (300 MHz) δ, 7.25-8.05 (6H, m), 14.83 (1H, bs). ¹³C (75.5 MHz) δ: 119.3 (CF₃, q, ¹J_{C-F}=284Hz), 124.9, 125.4, 126.9, 129.9, 130.1, 130.4, 131.4, 135.1, 139.1, 157.3, 184.6 (C-CF₃, q, ²J_{C-F}=35Hz). ¹⁹F (C₆F₆ ext. std.) (282 MHz) δ -74.25 (s, 3F). Analysis calcd for C₁₂H₇F₃O₂: C, 60.01, H, 2.94. Found: C, 60.13, H, 2.88.

2.3.11 4,4,4-trifluoro-1-(1-oxotetrahydronaphthyl)-1,3-butanedione (4b) [19]

A 100 mL round bottom flask is charged with 50 mL dry Et₂O, 5 mL dry diisopropylamine, equipped with a magnetic stir bar and placed under N₂ at 0°C. To this is added LDA (0.0120 mol) and stirred for fifteen minutes. Then, a solution of 4a (0.004 mol) in 15 mL dry Et₂O is added dropwise slowly via syringe. After 8 h, ethyl trifluoroacetate (0.008 mol) is delivered dropwise slowly via syringe, the reaction mixture is stirred overnight and allowed to warm to rt. A third equivalent of ethyl trifluoroacetate (0.004 mol) is added after 24 hours and the solution is left to stir again overnight. The reaction mixture is acidified with 30 mL 3M sulfuric acid. The organic layer was separated, washed with deionized water, and the organic layer dried over Na₂SO₄. The solvent was evaporated under reduced pressure, and subjected to radial chromatography. After recrystallization from cyclohexane, 4b was obtained as reddish-brown crystals in 27% yield, m.p. 133-135°C. 4b: NMR: ¹H (300 MHz) δ 2.85 (2H, t, 7.6 Hz), 2.93 (2H, t, 7.6 Hz), 6.76 (s, 1H), 7.37-7.77 (4H, m), 15.68 (2H, bs). ¹³C (75.5 MHz) δ 20.9, 22.7, 104.6, 118.4 (CF₃, q, ¹J_{C-F}=270 Hz), 125.9, 126.8, 127.3, 127.4, 128.2, 128.5, 128.6, 129.9, 133.9, 142.8, 177.0 (C-CF₃, q, ²J_{C-F}=36 Hz), 182.2. ¹⁹F (C₆F₆ ext. std.) (282 MHz) δ -72.04 (s, 3F). Analysis calcd for C₁₄H₁₁F₃O₃: C, 59.16, H, 3.90. Found: C, 58.99, H, 4.01.

2.3.12 2-trifluoroacetyl-1-tetralone (4c) [19]

This compound was obtained as off-white crystals, 4c, in 53% yield, m.p. 50-52°C. 4c: NMR: ¹H (300 MHz) δ 2.75 (2H, t, 9.0Hz), 2.88 (2H, t, 9.0Hz), 7.16-7.87 (4H, m), 15.62 (1H, bs). ¹³C (75.5 MHz) δ 21.0, 27.8, 38.3, 103.7, 117.5 (CF₃, q, ¹J_{C-F}=285Hz), 127.1, 127.3, 127.8, 127.9, 130.5, 133.4, 157.3, 174.8 (C-CF₃, q, ²J_{C-F}=35Hz), 185.0. ¹⁹F (C₆F₆ ext. std.) (282 MHz) δ -70.61 (s, 3F). HRMS (ESI+) calcd for C₁₂H₉F₃O₂: 242.04470, found: 242.04436.

2.3.13 naphtho[1,2-c]-N-4-trifluoromethylphenyl-5'-methylpyrazole (4d) [25,26]

This compound was obtained as orange crystals, 4d, in 62% yield, m.p. 127-129°C. 4c: NMR: ¹H (300 MHz) δ 2.22 (3H, s), 2.84 (2H, t, 8.1Hz), 2.95 (2H, t, 7.0Hz), 6.76-7.89 (8H, m). ¹³C (75.5 MHz) δ 11.4, 21.9, 23.8, 119.81, 122.5, 124.2 (CF₃, q, ¹J_{C-F}=281Hz), 125.8, 126.7 (C-CF₃, q, ²J_{C-F}=31Hz), 126.9, 127.7, 127.9, 128.9, 129.1, 132.2, 137.0, 137.7, 140.9, 143.5, 146.7. ¹⁹F (C₆F₆ ext. std.) (282 MHz) δ -60.76 (s, 3F). MS: m/z 328 (100%, M⁺), 313 (30%, M-CH₃⁺), 145 (40%, ⁺C₆H₄-CF₃). Analysis calcd for C₁₉H₁₅F₃N₂: C, 69.50, H, 4.61, N, 8.53. Found: C, 69.32, H, 4.54, N, 8.45.

2.3.14 4,4,4-trifluoro-1-(1-hydroxynaphthyl)-1,3-butanedione (5b) [19]

Using the method described for the preparation and isolation of 4b, the crude product was recrystallized from cyclohexane and 5b was obtained as brown crystals, in 22% yield, m.p. 154-157°C. 5b: NMR (300 MHz) ¹H: δ 6.90 (s, 1H), 7.51-8.50 (6H, m), 14.44 (1H, bs), 15.70 (1H, bs). ¹³C (75.5 MHz) δ 111.9, 115.7 (CF₃, q, ¹J_{C-F}=271Hz), 127.1, 127.3, 127.8, 127.9, 130.5, 133.4, 157.3, 174.8 (C-CF₃, q, ²J_{C-F}=35Hz), 185.0. ¹⁹F (C₆F₆ ext. std.) (282 MHz) δ -71.60 (s, 3F). Analysis calcd for C₁₄H₉F₃O₃: C, 59.59, H, 3.21. Found: C, 59.86, H, 3.16.

2.3.15 2-acetyl-4-fluoro-1-naphthol (5c) and 2-acetyl-3-fluoro-1-naphthol (5d) [19]

These compounds were obtained as a 5:1 mixture of 5c:5d. Radial chromatography (100% CH₂Cl₂ - 50/50 CH₂Cl₂/MeOH) afforded 5c as brown crystals (51%, m.p. 93-95°C) and 5d as a tan solid (13%,

m.p. 88-91°C). 5c: NMR: ^1H (300 MHz) δ 2.71 (3H, s), 7.31-8.48 (5H, m), 14.01 (1H, bs). ^{13}C (75.5 MHz) δ 26.9, 113.1, 118.3, 124.9, 126.0, 127.4, 130.1, 137.4, 150.5 (Ar-F, d, $^1J_{\text{C-F}}=243\text{Hz}$), 162.4, 204.2. ^{19}F (C_6F_6 ext. std.) (282 MHz) δ -134.0 (s, 1F). Analysis calcd for $\text{C}_{12}\text{H}_9\text{FO}_2$: C, 70.59, H, 4.44. Found: C, 70.77, H, 4.31. 5d: NMR: ^1H (300 MHz) δ 2.63 (3H, s), 7.40-8.00 (5H, m), 13.82 (1H, bs). ^{13}C (75.5 MHz) δ 27.6, 111.3, 120.3, 124.6, 125.1, 126.9, 128.6, 130.2, 130.3, 155.5 (Ar-F, d, $^1J_{\text{C-F}}=244\text{Hz}$), 158.7, 203.4. ^{19}F (C_6F_6 ext. std.) (282 MHz) δ -134.2 (s, 1F). Analysis calcd for $\text{C}_{12}\text{H}_9\text{FO}_2$: C, 70.59, H, 4.44. Found: C, 70.44, H, 4.49.

2.3.16 2-trifluoromethyl- β -naphthochromone (5e) [29]

A 10 mL round bottom flask equipped with a magnetic stirrer was charged with 5a (0.89 mmol) and TFAA (1.8 mmol). To this solution was added Pyr (0.89 mmol) and heated at 80°C for 3 h. The reaction mixture was allowed to cool to room temperature, neutralized with 1M HCl, extracted with EtOAc (2X5 mL) and washed twice with distilled water (2X5 mL). The organic layer was passed through a Na_2SO_4 -filled Pasteur filter-tip pipet, the solvent removed under reduced pressure and the residue dried in vacuo. Radial chromatography (gradient elution of 10-30% ethyl acetate in hexane) afforded 5e as colorless crystals (61%, m.p. 124-126°C). FT-IR (ATR) 1674 cm^{-1} (C=O). NMR: ^1H (400 MHz) δ 9.89 (1H, d, $J = 9$ Hz); 8.18 (1H, d; $J = 8$ Hz); 7.91 (1H, dd, $J = 7; 1$ Hz); 7.78 (1H, m); 7.69 (1H, m); 7.58 (1H, d, $J = 9$ Hz); 6.91 (1H, s); ^{13}C (100 MHz) δ 113.3, 113.7, 117.0, 118.4 (q, $^1J_{\text{C-F}} = 276$ Hz), 126.7, 127.4, 128.3, 129.1, 129.6, 131.0, 136.5, 149.6 (q, $^2J_{\text{C-F}} = 38$ Hz), 156.8, 178.2. ^{19}F (376 MHz) δ -70.5 (s, 3F); MS: m/z 264 (100%, M+), 236 (53%, M-CO+).

2.3.17 3-oxoindeno[1,2-c]-N-4-trifluoromethylphenyl-5'-methylpyrazole (6b) [25,26]

This compound was obtained as brown crystals, 6b, in 36% yield, m.p. 149-152°C. FT-IR (ATR): 1705 cm^{-1} (C=O), 1378 (CF_3). NMR: ^1H (300 MHz) δ 2.48 (3H, s), 7.20-7.59 (4H, m), 7.69-7.98 (4H, m). ^{13}C (75.5 MHz) δ 12.7, 121.1, 123.1, 124.1, 124.2 (CF_3 , q, $^1J_{\text{C-F}}=272\text{Hz}$), 124.6, 125.5, 127.0, 127.5, 127.6, 129.2 (C- CF_3 , q, $^2J_{\text{C-F}}=32\text{Hz}$), 130.9, 132.3, 134.2, 140.3, 147.2, 157.6, 183.5. ^{19}F (C_6F_6 ext. std.) (282.0 MHz) δ -61.00 (s, 3F). MS: m/z 328 (50%, M⁺), 327 (100%, M-H⁺), 258 (15%, M- CF_3 ⁺). Analysis calcd for $\text{C}_{18}\text{H}_{11}\text{F}_3\text{N}_2\text{O}$: C, 65.85, H, 3.38, N, 8.53. Found: C, 66.08, H, 3.42, N, 8.33.

2.3.18 E-2-(3,5-Dimethoxybenzylidene)indan-1-one (7b) [41]

A 25 mL beaker equipped with a stir bar was charged with 3,5-dimethoxybenzaldehyde (3.0 mmol) and warmed to 60°C. Then, 1-indanone (3.0 mmol) and solid NaOH (3.8 mmol) were added. The reaction mixture was stirred for 30 minutes at 60°C. The resulting reaction mixture was neutralized with 4 mL of 1M HCl, the resulting residue was washed with several 1 mL aliquots of distilled water and the crude product isolated via vacuum filtration. Recrystallization from 95% ethanol afforded 7b as colorless needles in 56% yield, m.p. 174-175°C. FT-IR (ATR): 1695 cm^{-1} (C=O). NMR: ^1H (300 MHz) δ 3.94 (6H, s), 6.6 (1H, t, 6Hz), 6.9 (1H, d, 6Hz), 7.50-7.67 (6H, m), 7.97 (1H, d, 10Hz). ^{13}C (75.5 MHz) δ 32.0, 55.1, 101.3, 108.4, 124.0, 125.8, 127.3, 133.5, 134.3, 134.8, 136.7, 137.6, 149.2, 160.6, 193.9. Analysis calcd for $\text{C}_{18}\text{H}_{16}\text{O}_3$: C, 77.12, H, 5.75. Found: C, 77.21, H, 5.79.

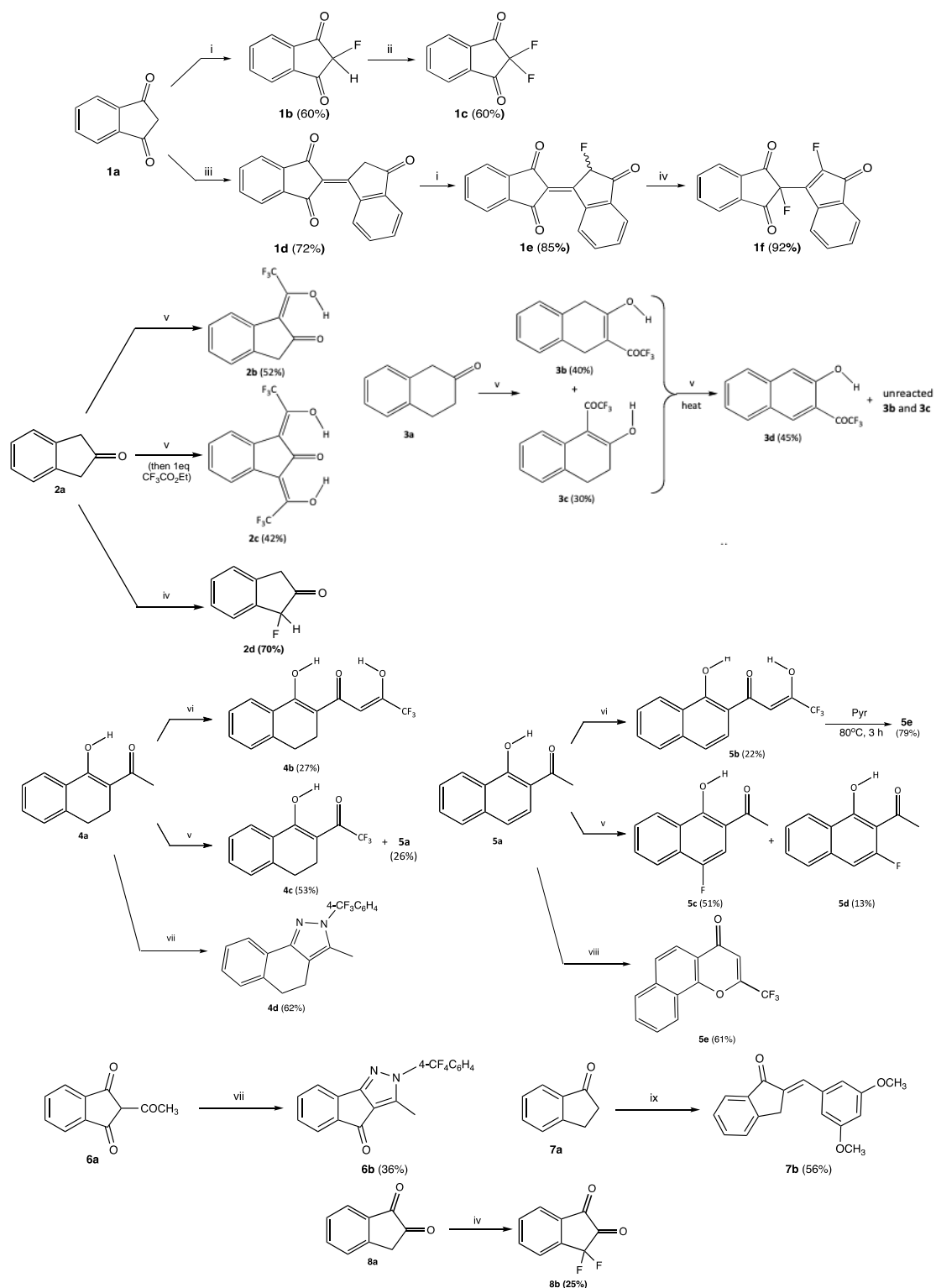
2.3.19 3,3-difluoro-1,2-indanedione (8b) [17]

This compound was obtained in 25% yield as yellow-brown crystals, m.p. 99-103°C, dec. NMR: ^1H : δ 7.1-8.6 (m, 4H). ^{19}F : δ -86.1 (s, 2F). Decomposition of the product occurred when subjected to column chromatography, so further characterization was not possible.

3. RESULTS AND DISCUSSION

3.1 Synthesis

Compounds 1a-8a are commercially available and were used without further purification. The remaining compounds were prepared using a variety of condensation/cyclodehydration methods, or direct fluorination with Selectfluor® [12,13-15,17,19,25,26,41]. See Scheme 1.



Conditions: i. 1.1 eq Selectfluor[®], MeCN, reflux, 10 h. ii. 1.5 eq Selectfluor[®], MeCN, RT, 18-30 h. iii. H₂SO₄, MeOH, reflux, 24 h. iv. 1.1 eq Selectfluor[®], MeCN, reflux, 16 h. v. CF₃CO₂Et, NaOMe, Et₂O, rt, 18 h. vi. (1) 3.0 eq LDA, Et₂O, 0°C; (2) 2 eq CF₃CO₂Et, 0°C→rt, 24 h; (3) 2 eq CF₃CO₂Et. vii. 4-CF₃C₆H₄NHNH₂, cat H₂SO₄, EtOH, reflux, 48 h. viii. 1 eq. pyridine, 2 eq. (CF₃CO)₂O, 80°C, 3 h. ix. 3,5-dimethoxybenzaldehyde, 1 eq. solid NaOH, 60°C, 0.5 h.

Scheme 1. Ketone and heterocycle synthesis

3.1.1 Ketone preparation

Our group showed that regioselective monofluorination and geminal difluorination of acyclic β -diketones could be effected with Selectfluor[®] under mild conditions without the necessity of specialized glassware or safety precautions [13,16,24]. The synthetic investigation herein sought to take advantage of these efforts by probing Selectfluor[®]'s efficiency and effectiveness in the mono- and difluorination of 1,3-indanedione and bindone. Our efforts revealed some unexpected findings. The monofluorination of 1a proceeded with little difficulty to give 2-fluoro-1,3-indanedione (1b) in the diketonic form (as evidenced by a doublet signal ($J_{F-H}=51.1\text{Hz}$) in the ^{19}F NMR at -207.3 ppm), albeit in slightly lower yield compared to fluorination achieved with 5% F_2 in N_2 [16]. Diketone 1b was also successfully fluorinated (as evidenced by a singlet signal in the ^{19}F NMR at -125.9 ppm), delivering the geminally difluorinated product 1c in good overall yield.

We also examined whether bindone (1d), the aldol self-condensation product of 1,3-indanedione, would react similarly to treatment with Selectfluor[®]. As expected, monofluorination was achieved in high yield to give 1e as an enantiomeric triketone pair (^{19}F NMR: -182.4 ppm , $J_{F-H}=46.0\text{Hz}$), but the site of fluorination was the α -carbon adjacent to the isolated ketone rather than fluorination between the 1,3-diketone residue. Subsequent fluorination of 1e likewise yielded interesting results. Particularly noteworthy were the fluorination regioselectivity and alkene rearrangement observed during the formation of triketone 1f. We expected an outcome similar to the fluorination of 1b, but the occurrence of two distinct signals in the ^{19}F NMR at -137.3 ppm and -176.7 ppm ruled out geminal difluorination. Evidently, the alkene in 1e retains sufficient nucleophilic nature to permit electrophilic fluorination between the β -dicarbonyl residue. This addition, coupled with a concomitant E1-like elimination leads to 1f, rather than formation of $[\Delta 1,2'$ -Biindan]-2,2-difluoro-1',3,3'-trione, shown in Scheme 1.

While preparing 2b and 2c, the one-pot, twin trifluoroacetylation of 2-indanone gave the dual exocyclic enol 2c in moderate yield (confirmed by the presence of a single, highly deshielded ^{19}F NMR resonance at -68.5 ppm) [20] and no 2c', Fig. 2. In this case, the ethoxide base present following the condensation apparently deprotonates the unsubstituted benzylic α -hydrogen (H_3) rather than the more acidic α -hydrogen H_1 .

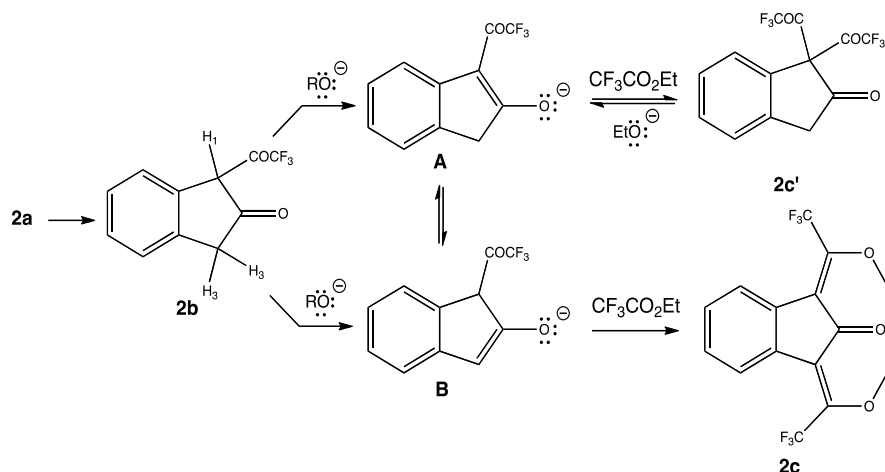


Fig. 2. Formation of 1,3-ditrifluoroacetyl-2-indanone (2c)

There are several possible explanations for the formation of 2c and the failure to obtain 2c'. The most plausible scenario involves initial formation of 2c'. Given the basic reaction conditions, however, we surmise that upon attachment of the second COCF_3 group, 2c' may undergo nucleophilic acyl substitution by ethoxide, reverting 2c' back to enolate A. A second possibility for the failure to obtain 2c' may be larger steric demands in the transition state leading to enolate A formation relative to that leading to enolate B. Finally, a base-promoted tautomerization from enolate A to enolate B could occur before formation of 2c', ultimately leading to 2c.

Monofluorination of 2a with Selectfluor® proceeded satisfactorily, providing 2d in 70% yield. Observations of a ^{19}F NMR doublet centered at $\delta_{\text{F}} = -180.7$ ppm ($^2J_{\text{F-H}} = 52.5$ Hz) and a ^1H NMR doublet centered at $\delta_{\text{H}} = 5.55$ ppm ($^2J_{\text{H-F}} = 52.5$ Hz) confirm monofluorination at the α -carbon [24]. We postulate that an enol form of the ketone might serve as nucleophile in this reaction. A proposed mechanism for the α -fluorination of 2a is shown in Fig. 3.

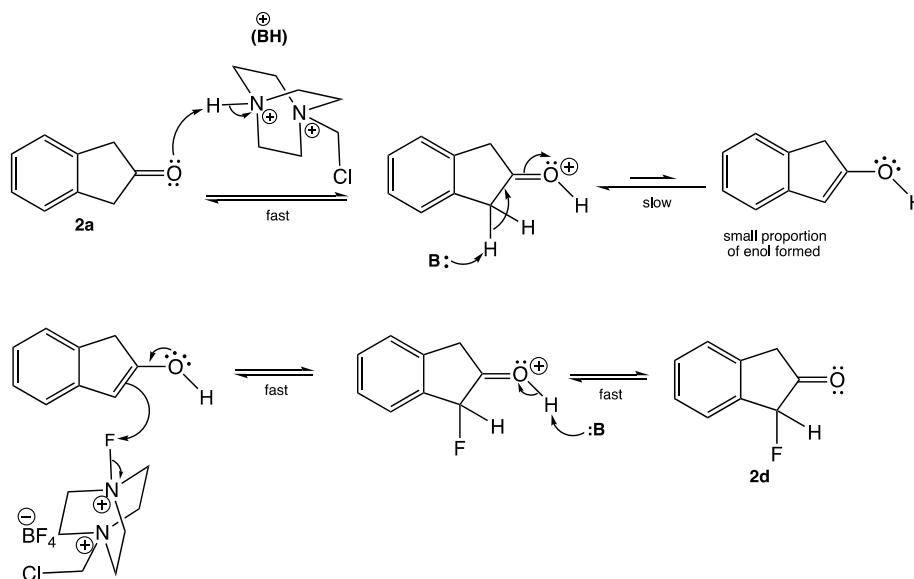


Fig. 3. Mechanism for the formation of 2d

We attempted a ditrifluoroacetylation methodology strategy similar to that employed enroute to 2c with β -tetralone (3a) to ascertain whether this could be generalized to other ketones with two acidic α -hydrogen sets. Sequential treatment of 3a with two equivalents of ethyl trifluoroacetate followed by neutralization at room temperature led to a mixture of the 3- and 1-trifluoroacetyl-2-tetralone endocyclic enols 3b and 3c, respectively; the formation of 1,3-ditrifluoroacetyl-2-tetralone was not observed. Assignment of the endocyclic enolic structures was based on the observation of a single ^{19}F NMR resonance at -70.6 ppm for 3b and -67.7 ppm for 3c. When the reaction workup conditions were modified by subjecting the enols 3b and 3c to an additional equivalent of base and ethyl trifluoroacetate followed by *in vacuo* removal of solvent at elevated temperature, we were surprised to find that aromatization occurred to give the trifluoroacetylated naphthol 3d in moderate overall yield. Fig. 4 depicts a plausible route to naphthol 3d. We surmise that deprotonation of the less sterically hindered α -hydrogen enroute to 3b occurs rather than abstraction of the more acidic, benzylic α -hydrogen. Detrifluoroacetylation of triketone I followed by tautomerization of diketone II under acidic workup provides naphthol 3d.

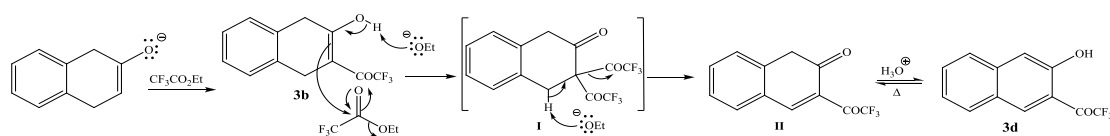


Fig. 4. Mechanism for the formation of 3b and 3d

Application of Light and Hauser's method to 4a and 5a produced the cross-conjugated, dienolic 1,3,5-triketones 4b and 5b in modest yields [14]. Assignment of the enolic structures was based on a combination of resonances found in their NMR spectra – (4b) ^1H : an alkene proton signal @ 6.76 ppm (1H), a broad, unresolvable singlet corresponding to the enol protons @ 15.68 ppm (2H) and ^{19}F : a singlet @ -72.0 ppm (3F); for (5b) ^1H : an alkene proton signal @ 6.90 ppm (1H), a singlet corresponding to the phenolic enol proton @ 14.44 (1H), a broader singlet @ 15.68 ppm (1H)

corresponding to the enol adjacent to the CF_3 group and ^{19}F : a singlet @ -71.6 ppm (3F). Addition of D_2O to the NMR samples of 4b and 5b resulted in rapid diminution of the exchangeable enolic protons in the ^1H NMR. Increasing the molar ratio of ethyl trifluoroacetate:diketone to > 2:1, although necessary for triketone product formation, also led to *O*-trifluoroacetylated by-products. Fortunately, these were easily separated by chromatography from the desired 1,3,5-triketones. Additionally, we found that when 4a was subjected to standard Claisen reaction conditions, an unintended acetyl-trifluoroacetyl group exchange occurred to give 2-trifluoroacetyl-1-tetralone (4c) in good yield along with, to our surprise, naphthol 5a. A process similar to the detrifluoroacetylation depicted in Fig. 2 may be operating in these cases as well.

Treatment of 5a with Selectfluor[®] demonstrated the fluorination preference of activated aromatic substrates over acetyl groups [27,43,44]. The fluorinated naphthols 5c and 5d were achieved in good overall yield and a 5:1 ratio of the *para:meta* isomers, respectively. Ring fluorination was confirmed by the observation of resonances in the ^{19}F NMR spectra as singlets: -134.0 ppm (1F) and -134.2 ppm (1F) for 5c and 5d, respectively. Preferential *para* fluorination is in accord with the *o-p* directing ability of the hydroxyl group. Use of up to 5 equivalents of Selectfluor[®] to effect fluorination at the acetyl carbon provided only the monofluorinated naphthols 5c and 5d.

3.1.2 Fused-ring tricyclic trifluoromethylheterocycle preparation

Ketones 4a and 6a served as scaffolds for the preparation of unique heterocyclic compounds. Treatment of 4a and 6a with 4-trifluoromethylphenylhydrazine under ethanolic, acidic conditions at 70°C for 48 hours provided the novel naphtho[1,2-*c*]-*N*-4-trifluoromethylphenyl-5'-methylpyrazole (4d) and 3-oxoindeno[1,2-*c*]-*N*-4-trifluoromethylphenyl-5'-methylpyrazole (6b), respectively, in moderate yields [24,25]. Small proportions of the complementary 3'-methylpyrazole regioisomers were also detected by ^{19}F NMR, but were not isolated.

In the case of 6a, the preference of initial nucleophilic attack at C_1 is supported by density functional theory [45]. Computations performed at the RB3LYP level using the 6-31G (D) basis set show that the LUMO of 6a (Fig. 5) contains a substantial orbital at C_1 allowing for better overlap with the $-\text{NH}_2$ group of the arylhydrazine HOMO at that site. Whereas, the minimal orbital density at C_2 supports a lower likelihood of initial nucleophilic attack at that position.

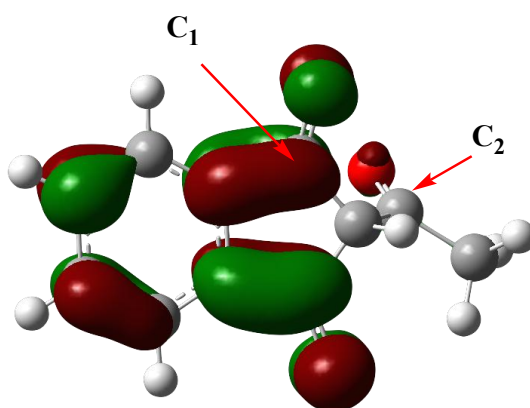


Fig. 5. 6a LUMO

Preliminary microwave-mediated syntheses of these and several other fused-ring pyrazoles have been performed and yields are comparable to the conventional processes reported in this work [26].

Using 5a as the scaffold, a solventless, pyridine-promoted Baker-Venkatarman (B-V) rearrangement with trifluoroacetic anhydride was conducted to prepare 2-trifluoromethyl- β -naphthochromone (5e) in good overall yield [29]. The rearrangement mechanism [30,40], shown in Fig. 6, features *O*-trifluoroacetylation, an intramolecular Claisen condensation and subsequent cyclodehydration enroute to the β -naphthochromone product.

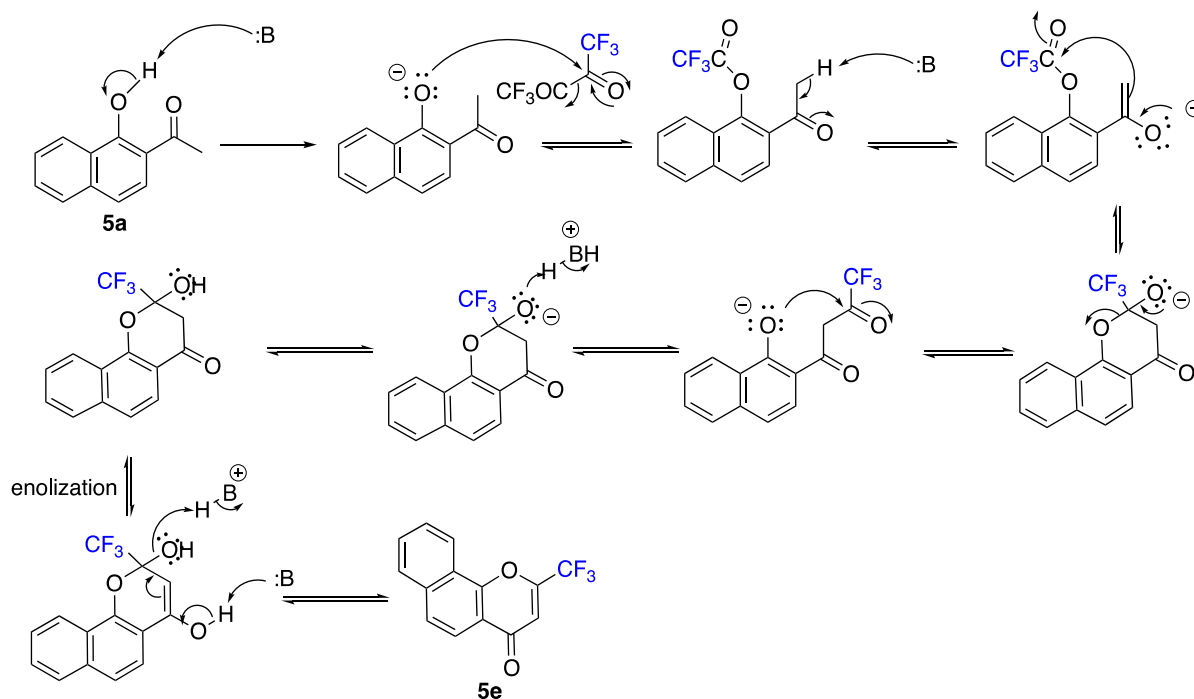


Fig. 6. B-V mechanism for the formation of 5e

Compound 5b was also induced to cyclodehydrate under solventless, pyridine-promoted conditions, providing 5e in 79% yield. A mechanism for this transformation is proposed in Fig. 7. Evidence in support of this mechanism is the observation of a ^{19}F NMR resonance @ δ -86.5 ppm, likely corresponding to the intermediate (Int) identified below when the reaction was quenched prior to completion.

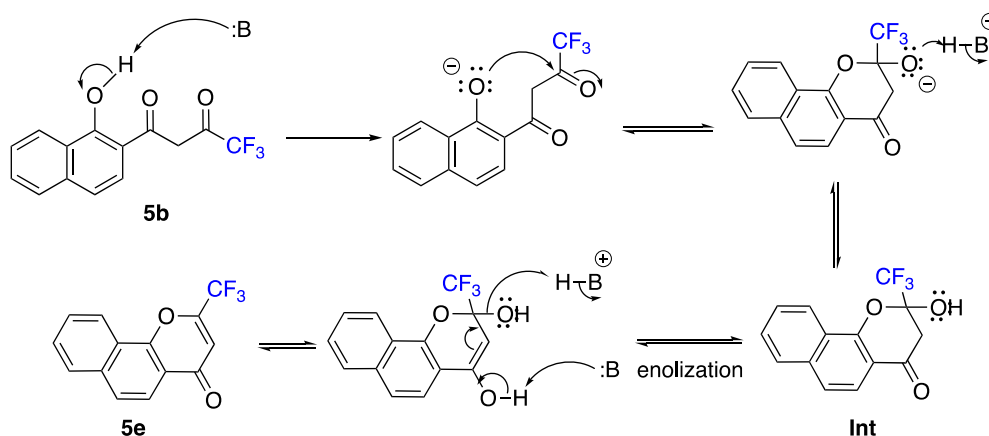


Fig. 7. Cyclodehydration mechanism for the formation of 5e

3.1.3 Chalcone synthesis

A green, based-promoted Claisen-Schmidt reaction was employed delivering the *E*-chalcone 7b in good overall yield. In this reaction, 3,5-dimethoxybenzaldehyde served as the solvent, which melts at $\sim 60^\circ\text{C}$ and solubilizes the 1-indanone (7a) starting material. Preparation of a series of functionalized indenochalcones is underway as a prelude for use of this scaffold in the preparation of heterocycles.

3.2 Solid State Structural Features: X-Ray Crystallography

Several of the target molecules (1d, 2c, 3c, 4c and 7b) were examined by x-ray crystallography and are depicted in Fig. 8 [19,41,46-51]. See references 15 and 36 for complete crystallographic parameters. Critical bond information is listed in Table 1. The crystallographic information files for these molecules have been uploaded to the Cambridge Crystallographic Data Center and have the following control numbers: 1d: 854704, 2c: 854697, 3d: 854705, 4c: 854706 and 7b: 1894469. Spectral data provided in the experimental section support the solid-state structural data presented herein [12-20,52-58].

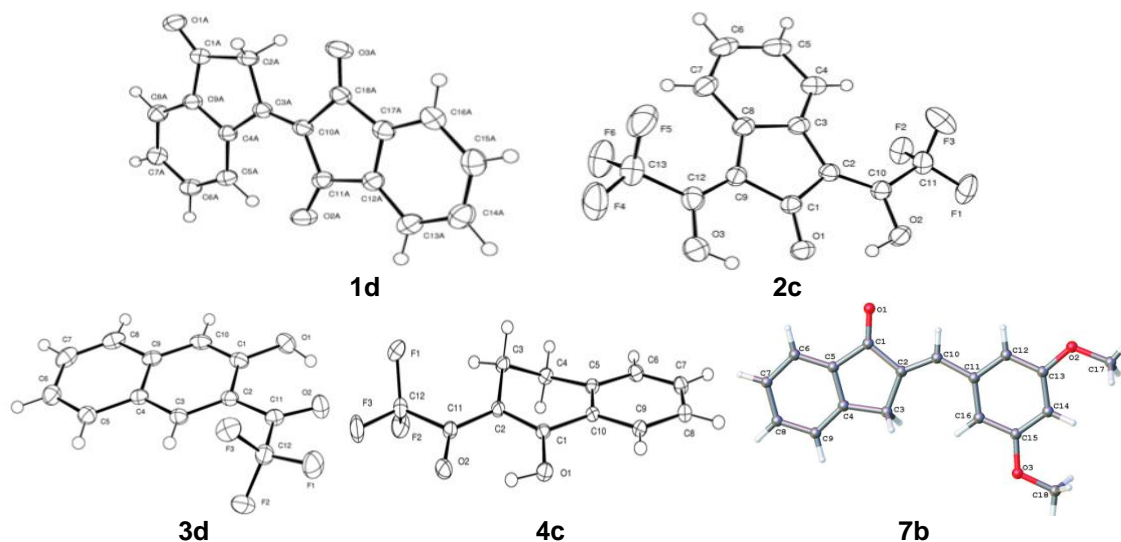


Fig. 8. Displacement drawings of 1d, 2c, 3d, 4c and 7b. Ellipsoids are at the 50% probability level and hydrogen atoms were drawn with arbitrary radii for clarity

In the case of compound 1d, the small $O_3-C_{10}-C_{18}-C_3$ dihedral angle of -2.4° shows the bridge to be nearly planar across the ring bridge. The C-O and C_3-C_{10} bond lengths are consistent with those of typical carbonyls and alkenes, respectively and identify 1d as a cross-conjugated triketone in the solid state. For 2c, x-ray crystallography confirms the planar, exocyclic dienolic molecular architecture shown in Fig. 8. The weak intramolecular H-bonding normally observed in cyclic triketones is clearly supported for 2c by the interatomic $O\cdots H-O$ distances of 1.75\AA and 1.81\AA and very short O-H bond lengths of 0.88\AA and 0.90\AA [18,32]. The small $O_1-C_1-C_2-C_{10}$ dihedral angle of -1.91° attests to the planar nature of the cyclopentanone residue.

Likewise, 3-trifluoroacetyl-2-naphthol (3d) and 2-trifluoroacetyl-1-tetralone (4c) show trends consistent with a single endocyclic *cis*-enol tautomer having weak intramolecular H-bonding, e.g. interatomic $O\cdots H-O$ distances $> 1.7\text{\AA}$, O-H bond lengths $< 1.0\text{\AA}$ and small $O_1-C_1-C_2-C_{11}$ dihedral angles. For 3d, the aromatic ring introduces an additional structural constraint that prohibits tautomerism to either the diketo form or any other enolic structure.

The chalcone 7b also shows interesting molecular architecture. Nearly planar, the indanone ring system and the 3,5-dimethoxyphenyl ring deviate from planarity by only 2.54° , comparable to that of 1d. Additionally, the C_1-O_1 and C_2-C_{10} bond lengths are consistent with conjugated carbonyl-alkene α,β -unsaturated systems. The *E* stereochemistry of 7b is confirmed by an $O_1\cdots C_{12}$ interatomic distance $> 4.2\text{\AA}$, in accord with other *E*-chalcones available in the Cambridge Structural Database [41].

Table 1. Selected interatomic distances and bond lengths of 1d, 2c, 3d, 4c and 7b

	Interatomic Distances (Å)		Bond Lengths (Å)			Dihedral \angle (°)
	O ¹ ...O(C)	O ¹ ...H	O-H	C-O	C-C	
1d	NA	NA	NA	C _{1A} -O _{1A} 1.2143(17) C _{11A} -O _{2A} 1.2212(17) C _{18A} -O _{3A} 1.2143(17)	C _{3A} -C _{10A} 1.3574(19)	O ₃ -C ₁₈ -C ₁₀ -C ₃ -2.4(11)
2c	O ₁ ...O ₂ 2.5781(13) O ₁ ...O ₃ 2.5926(14)	O ₁ ...H ₂ 1.75(2) O ₁ ...H ₃ 1.81(2)	O ₂ -H ₂ 0.90(2) O ₃ -H ₃ 0.88(2)	C ₁ -O ₁ 1.2576(15) C ₁₀ -O ₂ 1.3308(15) C ₁₂ -O ₃ 1.3242(17)	C ₁ -C ₂ 1.4547(15) C ₂ -C ₁₀ 1.3593(17) C ₉ -C ₁₂ 1.3602(17)	O ₁ -C ₁ -C ₂ -C ₁₀ -1.91(11)
3d	O ₁ ...O ₂ 2.6142(17)	O ₂ ...H 1.75(3)	O ₁ -H 0.97(3)	C ₁ -O ₁ 1.3588(19) C ₁₁ -O ₂ 1.2199(18)	C ₁ -C ₂ 1.438(2) C ₂ -C ₁₁ 1.459(2)	O ₁ -C ₁ -C ₂ -C ₁₁ 1.9(2)
4c	O ₁ ...O ₂ 2.5063(9)	O ₂ ...H 1.72(2)	O ₁ -H 0.855(19)	C ₁ -O ₁ 1.3215(9) C ₁₁ -O ₂ 1.2476(10)	C ₁ -C ₂ 1.3895(10) C ₂ -C ₁₁ 1.4193(10)	O ₁ -C ₁ -C ₂ -C ₁₁ -2.04(11)
7b	O ₁ ...C ₁₂ >4.2	NA	NA	C ₁ -O ₁ 1.2255(11)	C ₂ -C ₁₀ 1.3421(12)	C ₁ -C ₂ -C ₁₀ -C ₁₁ 178.55(9)

4. FUTURE DIRECTIONS

An expanded investigation of green synthesis methods incorporating sonication, μ wave irradiative, solvent-free reactions and ionic liquid mediated processes using several of the ketone scaffolds in this work is underway. Target molecules of interest are fused-ring heteroaromatic species: indeno- and naphthopyrazoles, tetracyclic quinolines as well as new examples of 2- and 3-acetylated chromones. In addition, selective incorporation of fluorine and fluorine-containing groups into these heterocyclic products will be a focus of this work. We anticipate reporting these findings in the near future.

5. CONCLUSION

This work has shown the versatility of the indanone, tetralone and naphthone molecular scaffolds towards functionalization enroute to trifluoroacetylated and selectively fluorinated derivatives in moderate yields to yields in excess of 90%. Many of these di- and triketone products have unique keto-enol structural features as exhibited by X-Ray crystallographic studies. In addition, this work has demonstrated that several of these novel ketones can serve as scaffolds to prepare fluorinated polycyclic heterocycles, such as indenopyrazoles, naphthopyrazoles and naphthochromones in moderate yields.

ACKNOWLEDGEMENTS

The authors wish to thank the NCSU Molecular Education, Technology, and Research Innovation Center (METRIC) for crystallographic support and NCSU Mass Spectrometry Facility for high resolution mass spectroscopic support of this work. J.C.S. thanks the SST Faculty Research Fund for providing financial support for this work. E.E-T. thanks NCSU METRIC for funding an X-Ray Analysis Grant in support of this work.

COMPETING INTERESTS

Authors have declared that no competing interests exist.

REFERENCES

- Davies J, Davies D. Origins and evolution of antibiotic resistance. *Microbiology and Molecular Biology Reviews*. 2010;74(3):417-433.
- Sharma V, Chitranshi N, Agarwal AK. Significance and biological importance of pyrimidine in the microbial world. *International Journal of Medicinal Chemistry*; 2014.
- Nauta WT, Rekker RF. Biological activities of 1,3-indandiones. *pharmacochemistry of 1,3-indanediones*. Eds.; Elsevier Scientific Publishing Co., New York. 1981;187-269.
- Wiesner S, Springer E, Sasson Y, Almog J. Chemical development of latent fingerprints: 1, 2-indanedione has come of age. *Journal of Forensic Science*. 2001;46(5):1082-4.
- Daehne S, Resch-Genger U, Wolfbeis OS. Proceedings of the NATO advanced research workshop on syntheses, optical properties and applications of near infrared (NIR) dyes in high technology fields. Eds.; Kluwer Academic Publishers, Dordrecht, Netherlands. 1997;52:363-364.
- van Klink JW, Larsen L, Perry NB, Weavers RT, Cook GM, Bremer PJ, MacKenzie AD, Kirikae T. Triketones active against antibiotic-resistant bacteria: Synthesis, structure–activity relationships and mode of action. *Bioorganic & Medicinal Chemistry*. 2005;13(24):6651-62.
- An TY, Hu LH, Chen RM, Chen ZL, Li J, Shen Q. Anti-diabetes agents---I: Tetralone derivative from *Juglans regia*. *Chinese Chemical Letters*. 2003;14(5):489-90.
- Jain R, Jain SC, Arora R. A new cholestane derivative of *Abutilon bidentatum* Hochst. and its bioactivity. *Pharmazie*. 1996;51(4).
- Mentré F, Pousset F, Comets E, Pland B, Diquet B, Montalescot G, Ankri A, Mallet A, Lechat P. *Clinical Pharmacology and Therapeutics*. 1998;63:64-78.
- Shah P, Westwell AD. The role of fluorine in medicinal chemistry. *Journal of Enzyme Inhibition and Medicinal Chemistry*. 2007;22(5):527-540.
- Kokuryo Y, Kawata K, Nakatani T, Kugimiya A, Tamura Y, Kawada K, Matsumoto M, Suzuki R, Kuwabara K, Hori Y, Ohtani M. Synthesis and evaluation of novel fluorinated methotrexate derivatives for application to rheumatoid arthritis treatment. *J Med Chem*. 1997;40:3280–3291.
- Sloop JC, Bumgardner CL, Washington G, Loehle WD, Sankar SS, Lewis AB. Keto–enol and enol–enol tautomerism in trifluoromethyl- β -diketones. *Journal of Fluorine Chemistry*. 2006;127(6):780-6.
- Sloop J, Boyle P, Fountain AW, Pearman W, Swann J. *Eur. J. Org. Chem*. 2011;5:936-941.
- Sloop JC, Boyle PD, Fountain AW, Pearman WF, Swann JA. Electron-deficient aryl β -diketones: Synthesis and novel tautomeric preferences. *European Journal of Organic Chemistry*. 2011;5:936-41.
- Light R, Hauser C. *J. Org. Chem*. 1960;25:538-546.
- Reid J, Calvin M. *J. Amer. Chem. Soc*. 1950;72:2948-2952.
- Sloop J. Synthesis of fluorinated pyrazoles and isoxazoles. The effect of 2-Fluoro and 2-Chloro substituents on the Keto-Enol Equilibria of 1,3-Diketones. DOD Technical Report, Defense Technical Information Center. 1990;1-32.
- Sloop J, Churley M, Guzman A, Moseley S, Stalker S, Weyand J, Yi J. *Amer. J. Org. Chem*. 2014;1:1-10.
- Bolvig S, Hansen PE. *Mag. Res. Chem*. 1996;34:467-478.
- Sloop J, Boyle P, Fountain AW, Gomez C, Jackson J, Pearman W, Schmidt Weyand R. *J. Appl. Sci. Special Edition: Organo-Fluorine Chemical Science*. 2012;2:61-99.
- Sloop J. *Reports in Organic Chemistry*. 2013;3:1-12.
- Stavber S, Sket B, Zajc B, Zupan M. *Tetrahedron*. 1989;45(18):6003-6010.
- Zajc B, Zupan M. *J. Org. Chem*. 1982;47:573-575.
- Kim CY, Chang JS, Doyon JB, Baird TT, Fierke CA, Jain A, Christianson DW. Contribution of fluorine to protein-ligand affinity in the binding of fluoroaromatic inhibitors to carbonic anhydrase II. *J Am Chem Soc*. 2000;122:12125–12134.
- Sloop J, Bumgardner C, Washington G, Loehle WD. *J. Fluorine Chem*. 2002;118:135-147.
- Sloop J. Synthesis and study of selectively fluorinated diketones, aromatics & heterocycles: Undergraduate organofluorine research progress. 69th SERMACS. Charlotte, NC; 2017.
- Sloop J, Mallia A. Synthesis and study of polyfunctional & fused-ring heterocycles: Research progress at Georgia Gwinnett College. 71st SERMACS, Savannah, GA; 2019.
- Sloop J, Jackson J, Schmidt R. *Heteroatom Chem*. 2009;20(6):341-345.

29. Sloop J, Holder C, Henary M. *Eur. J. Org. Chem.* 2015;16:3405-3422.
30. Fernandes C, Park SH, Sloop J, Wilmott K. *Chem. Methodologies.* 2020;4:554-564.
31. Castañeda I, Ulic S, Védova C, Metzler-Nolte N, Jiosz J. *Tetrahedron Lett.* 2011;52:1436-1440.
32. Patel M, Bhila V, Patel N, Patel A, Brahmabhatt D. *Med. Chem. Res.* 2012;21:4381-4388.
33. Tawfik H, Ewies E, El-Hamouly W. *Int. J. Res. Pharm. Chem.* 2014;4:1046-1085.
34. Dias T, Duarte C, Lima C, Proença M, Pereira-Wilson C. *Eur. J. Med. Chem.* 2013;65:500-510.
35. Xiang H, Zhao Q, Tang Z, Xiao J, Xia P, Wang C, Yang C, Chen X, Yang H. *Org. Lett.* 2017;19:146-149.
36. Yue Y, Peng J, Wang D, Bian Y, Sun P, Chen C. *J. Org. Chem.* 2017;82:5481-5486.
37. O'Leary E, Jones D, O'Donovan F, O'Sullivan T. *J. Fluorine Chem.* 2015;176:93-120.
38. Cui H, Ding M, Huang D, Zhang Z, Liu H, Huang H, She Z. *RSC Adv.* 2017;7:20128-20134.
39. Dofe V, Sarkate A, Lokwani D, Shinde D, Kathwate S, Gill C. *J. Het. Chem.* 2017;54:2678-2685.
40. Irgashev R, Safrygin A, Safrygin M, Ezhikova M, Kodess M, Röschenthaier GV, Sosnovich V. *Tetrahedron.* 2015;71(12):1822-1830.
41. Ameen D, Snape T. *Synthesis.* 2014;46:A-R.
42. Encarnacion-Thomas E, Sommer R, Mallia A, Sloop J. *IUCRData.* 2020;5:x200759.
43. Berthelette C, McCooye C, Leblanc Y, Trimble L, Tsou N. *J. Org. Chem.* 1997;62:4339-4342.
44. Rioski M, John J, Zheng M, Kirshner J, Colby D. *J. Org. Chem.* 2011;76:3676-3683.
45. Kirsch P. *Modern fluoroorganic chemistry: Synthesis, reactivity, applications.* Wiley-VCH Verlag GmbH & Co., Darmstadt, GE. 2004;78-79.
46. Frisch M, Trucks G, Schlegel H, Scuseria G, Robb M, Cheeseman J, Scalmani G, Barone V, Petersson G, Nakatsuji H, Li X, Caricato M, Marenich A, Bloino J, Janesko B, Gomperts R, Mennucci B, Hratchian H, Ortiz J, Izmaylov A, Sonnenberg J, Williams-Young D, Ding F, Lipparini F, Egidi F, Goings J, Peng B, Petrone A, Henderson T, Ranasinghe D, Zakrzewski V, Gao J, Rega N, Zheng G, Liang W, Hada M, Ehara M, Toyota K, Fukuda R, Hasegawa J, Ishida M, Nakajima T, Honda Y, Kitao O, Nakai H, Vreven T, Throssell K, Montgomery Jr. J, Peralta J, Ogliaro F, Bearpark M, Heyd J, Brothers E, Kudin K, Staroverov V, Keith T, Kobayashi R, Normand J, Raghavachari K, Rendell A, Burant J, Iyengar S, Tomasi J, Cossi M, Millam J, Klene M, Adamo C, Cammi R, Ochterski J, Martin R, Morokuma K, Farkas O, Foresman J, Fox D. *Gaussian 09, Gaussian, Inc., Wallingford CT; 2016.*
47. Bruker. *Instrument Service, APEX3 and SAINT.* Bruker AXS Inc., Madison, Wisconsin, USA; 2017.
48. Bruno I, Cole J, Kessler M, Luo J, Motherwell W, Purkis L, Smith B, Taylor R, Cooper R, Harris S, Orpen A. *J. Chem. Inf. Comput. Sci.* 2004;44:2133-2144.
49. Groom C, Bruno I, Lightfoot M, Ward S. *Acta Cryst.* 2016;B72:171-179.
50. Harada J, Harakawa M, Sugiyama S, Ogawa K. *Cryst Eng Comm.* 2009;11:1235-1239.
51. Krause L, Herbst-Irmer R, Sheldrick G, Stalke D. *J. Appl. Cryst.* 2015;48:3-10.
52. Macrae C, Sovago I, Cottrell S, Galek P, McCabe P, Pidcock E, Platings M, Shields G, Stevens J, Towler M, Wood P. *J. Appl. Cryst.* 2020;53:226-235.
53. Crouse D, Hurlbut S, Wheeler D. *J. Org. Chem.* 1981;46:374-378.
54. Murdock K. *J. Org. Chem.* 1959;24:845-849.
55. Forsen S, Nilsson M. *Acta Chemica Scandinavica.* 1959;13:1383-1394.
56. Hunig S, Hoch H. *Justus Liebigs Ann. Chem.* 1968;716:68-77.
57. Ebraheem K. *Monatshefte fur Chemie.* 1991;122:157-163.
58. Hansen P, Ibsen S, Kristensen T, Bolvig S. *Mag. Res. Chem.* 1994;32:399-408.
59. Dolbier W. *Guide to fluorine NMR for organic chemists.* John Wiley and Sons, Inc. Hoboken, New Jersey. 2009;70-81:152-158.

Biography of author(s)



Joseph C. Sloop

School of Science and Technology, Georgia Gwinnett College, 1000 University Center Lane, Lawrenceville, GA 30043, USA.

He was born in 1961 in Chapel Hill, North Carolina. In 1983 he received his B.S. with Special Attainments in Chemistry from Davidson College and began service in the U.S. Army. In 1990, he obtained his M.S. at North Carolina State University (NCSU) under the direction of Prof. Carl Bumgardner on the preparation of fluorinated heterocycles. After teaching at the United States Military Academy (USMA) at West Point and continued service in the military, he completed doctoral training at NCSU with Prof. David Shultz in the field of magnetochemistry and returned to West Point to teach and conduct research with the USMA Photonics Research Center. In 2009, he joined the faculty at Georgia Gwinnett College (GGC), where he presently serves as Chair of the Chemistry Faculty & Professor of Chemistry for the School of Science and Technology. He is the recipient of the Phi Kappa Phi Scholastic Achievement Award (2008), the GGC Award for Scholarship and Creative Activities (2012), a co-recipient of the Blackboard Catalyst Award (2012) and the Chronicle of Higher Education's Top 125 Tech Innovators on The Digital Campus (2013) and was named a Governor's Teaching Fellow and a GGC Center for Teaching Excellence Fellow in 2016. He has published more than thirty papers, three book chapters, two organic chemistry laboratory manuals and is the author of *Succeeding in Organic Chemistry: A Systematic Problem-Solving Approach to Structure, Function and Mechanism*. His research interests include selective fluorination methods of ketone and amine derivatives, solventless condensation reactions of indanones, green synthesis of fused-ring, fluorinated heterocyclic systems, as well as QSAR and computational studies of keto-enol tautomerism in diketones and their condensation reactions. He holds memberships in the American Chemical Society, the International Society of Heterocyclic Chemistry and the Georgia Academy of Science.

© Copyright (2020): Author(s). The licensee is the publisher (Book Publisher International).

DISCLAIMER

This chapter is an extended version of the article published by the same author(s) in the following journal. Applied Sciences, 2(1): 61-99, 2012.

Investigating the Influence of the Transport of Sea Spray on the Salinization of the Semiarid Region Waters (Bahia, Brazil)

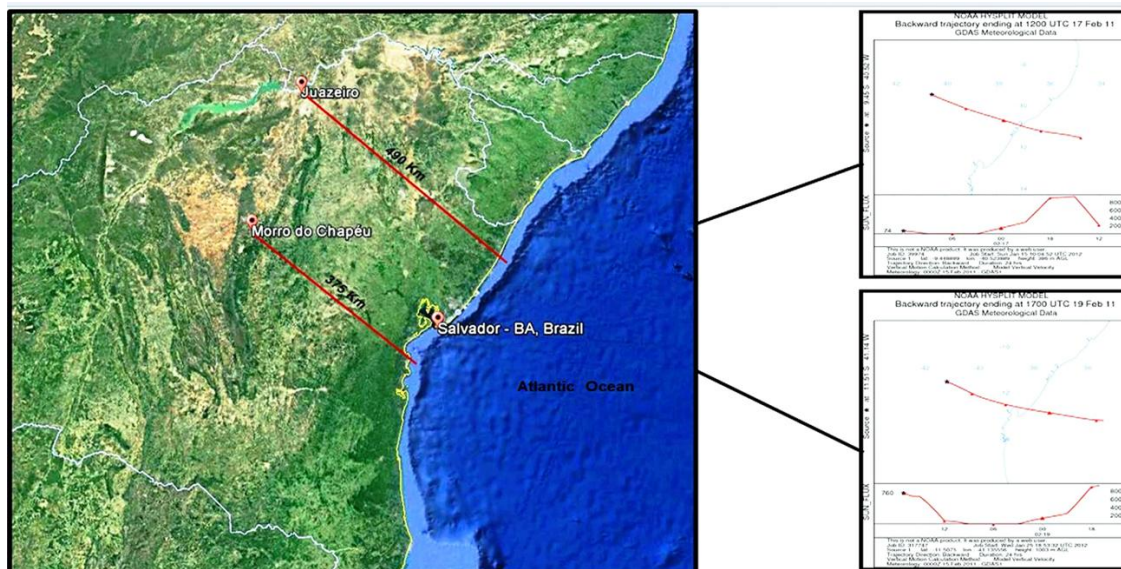
Adriana M. C. Silva¹, Vânia P. Campos^{2*}, Rafaela S. Domingues²,
Lícia P. S. Cruz² and Franciele O. Santana²

DOI: 10.9734/bpi/cpcs/v2

ABSTRACT

In this work, the rainwater and the atmospheric particulate matter were characterized by investigating the presence of sea spray in the atmosphere of the semiarid region of Bahia, Brazil, aiming to study the influence of its transport on the salinization of the waters of the region. Stable isotopes of deuterium and oxygen-18 were also determined in the rain as environmental tracers, evaluating the isotopic ratios $^{18}\text{O}/^{16}\text{O}$ and D/H. Atmospheric deposition is one of the main stages of the cycling and redistribution of the various chemical elements on the earth's surface. The atmosphere of the region suffers significant marine influence, as well as resuspended soil particles and anthropogenic sources. The results demonstrate that the amount of sea spray which reaches the region is insufficient to interfere at the groundwater composition and the cause of its salinization should be attributed to the local geology and the evaporation and salt concentration process due to the high temperatures found in the region.

GRAPHICAL ABSTRACT



Keywords: Sea spray; rainwater; particulate matter; stable isotopes; Semiarid Region.

¹Federal University of São Francisco Valley, Collegiate of Agricultural and Environmental Engineering 48902-300 Juazeiro-BA, Brazil.

²Federal University of Bahia/Chemistry Institute - Analytical Chemistry Department, 40170-290 Salvador-BA, Brazil.

*Corresponding author: E-mail: vaniaroc@ufba.br, vpalmeiracampos@gmail.com;

1. INTRODUCTION

The contribution of chemical species to the atmosphere represents an important mechanism of the hydrogeochemical processes, very significant in semiarid regions, that continuously suffers with a high frequency of dry periods. The problem of the salinization of surface waters in these regions certainly points to factors such as the recharging of water bodies with salinated water due to leaching of salts from the soil and to the salt concentration in the reservoirs because of the high evaporation rate typical in the Brazilian Northeast region [1]. A report by FAO in 2000 estimated that globally the area of salt-affected soils including saline and sodic soils was 831 million ha [2,3].

Atmospheric deposition is one of the main stages of the cycling and redistribution of the various chemical elements on the earth's surface. Atmospheric inputs can be evaluated through three depositional forms: Dry-only, wet-only and bulk deposition [4,5]. Therefore, their quantitative and qualitative knowledge is essentially important for the understanding of the biogeochemical cycles and anthropogenic influences on them. The wet deposition comprises the atmospheric particles and gases removal processes by the rain, fog or snow. The dry deposition includes all the particles and gases transferring processes to all types of surfaces in the absence of moisture [6]. Atmospheric deposition is an important component of the nutrient cycles of terrestrial ecosystems, but field measurements are especially scarce in tropical regions [7].

The sea spray can be transported to long distances, reaching the semiarid regions. The sea spray is a type of particulate matter produced naturally via the bubble-bursting process typically from whitecap generation. The bubbles scavenge organic matter as they rise to the surface. When they burst at the air-sea interface, they release a mixture of organic matter and inorganic sea salt, forming the sea spray aerosol, comprising the range of the submicrometre size and up to a few micrometres [8]. It constitutes one of the most important natural aerosol systems and contributes to the Earth's radiative budget, biogeochemical cycling, impacts on ecosystems and even to regional air quality [9]. Strongly dependent on the intensity of local winds, as shown Masiol et al. [10] the sea spray can be transported to long distances and deposited in a wet and / or dry way and it can reach the semiarid regions, distant from its emission source. Being these particles, if primary, basically composed of seawater (NaCl in carbonate/borate buffer), thus having an alkaline pH, they are able to neutralize rain acidity by gas to particle interaction [11,12].

The particulate phase of atmospheric aerosol is characterized by various physical parameters, with the distribution of its size as the most important one. Chemically, its composition reflects its emission sources [13]; their size is an important parameter for the evaluation of their impact on the global climate system [14].

The environmental isotopic ratios δ deuterium and δ oxygen-18 (δD and $\delta-O^{18}$) act as excellent natural tracers of air masses. They have been used very successfully as one of the unconventional tools in the study of the surface and underground water reserves [15]. The natural isotopes appear in the water in low concentrations that vary when they undergo processes of changing phase, such as evaporation. Thus, the environmental tracers are used to identify and separate the different salinity sources, as well as the effect of evapotranspiration in these processes [16] and it can be a useful tool in the study of the salinization processes [17], including salinization of the waters of the semiarid regions.

The processes of water and soil salinization, low rainfall rate and high evaporation rate of the water stored in reservoirs, contribute to the degradation of the quality of the water in the semiarid region of Brazil.

As a consequence of the vulnerability of water resources in semiarid areas, especially considering their scarcity, the study of the surface and underground water quality becomes important, aiming to provide water with better quality for more noble uses such as household supplies. There is a reasonable amount of data with results of analysis of legislated parameters in Brazil, which determine the quality of water in some parts of semiarid regions [1,18].

Some studies indicate differentiated causes to the salinization of water, among them are the high evaporation rates, that concentrate the salts in the surface waters and in the soils during the dry periods; this salt is transported to the aquifer in the wet period by the recharge waters [19]. Kovda [20] pointed as the main salinization source in the semiarid region, the aerosols coming from the marine atmosphere transported by the wind, which can be later leached from the soil and carried to the water bodies by runoff. On the other hand, according to Wetzel [21], the water conductivity values in tropical regions are related to the geochemical and climatic characteristics of the region.

In this work, rainwater and atmospheric particulate matter were characterized, investigating the presence of sea spray in the Semiarid of Bahia, Brazil, intending to study the influence of its transport in the salinization of waters in the region. The δD and δO^{18} were also evaluated in the rain as environmental tracers. Additionally, there was a secondary data research on the geological characteristics of the semiarid region of the Bahia State, associated with the salinity of groundwater.

2. EXPERIMENTAL

2.1 Sampling

The Semiarid of Bahia occupies most of the northeastern Brazil and nearly 2/3 of the state's territory. Among its main climatic characteristics, the high temperature average and extremely concentrated average annual rainfall of less than 800 mm stand out, creating long periods of drought (usually seven to nine months) and rainy periods restricted to few months of the year [22].

For the proposed study, two areas in the Semiarid of Bahia (Fig. 1) with different salinity characteristics of its natural waters were chosen: Juazeiro (9° 26' 56" S, 40° 31' 26" W), at 386 m of altitude, located in the north of the state, with groundwater that is often brackish, and it is characterized by the lack of rain and great irregularity in its distribution from 250 mm to 750 mm per year, low cloud cover, strong sunlight, high levels of evaporation, high average temperatures (~ 27°C) and low relative humidity; and Morro do Chapéu (11° 30' 27" S, 41° 08' 08" W), at 1,003 m above sea level, located in the northwest of the state, a region with typically sweet groundwater.

All rainy events were sampled for periods of 24 h during one year, in both locations (55 rain samples from Juazeiro and 35 from Morro do Chapéu), for the determination of the major ions, using an automatic "wet only" deposition collector, set to about 1.5 m from the ground, consisting of a funnel (598 cm²) and a collector flask (6 L), both made of polyethylene, protected in a metal box.

Sampling and storing rainwater samples for determination of hydrogen and oxygen isotopes were made according to the instructions of the International Atomic Energy Agency (IAEA) [23]. The main problems that should be avoided are the fractionization by evaporation or diffusion of water vapor and / or isotopic exchange with the environment as well as with the storage bottle. Thus, a collector was mounted in a 20 L flask containing 100 mL of mineral oil to prevent evaporation and wrapped in aluminum foil to prevent sample degradation; there was a sieve on the top, disallowing the entry of other materials. Most rainy events that occurred during one year was collected. Immediately after sampling aliquots in duplicate of the samples were transferred and stored in 100 mL amber glass bottles, fully completed and duly sealed, to avoid isotopic fractionation after collection. The samples were stored in a refrigerator and transported safely in thermal containers at low temperatures to the laboratory for measurement of stable isotopes.

The sampling of atmospheric particulate material was made in two intensive campaigns for 6 days, simultaneously, at the two sampling stations. The samplings were made for 24 h periods. The campaigns were scheduled for periods typically with predominant winds from the Atlantic and thus, based on the back trajectories study, it was observed that almost 100% of the sampling time of atmospheric particulate matter, the air masses arrived in both locations coming from the ocean.

Samples of suspended particles fractionated by size have been obtained with a Berner low-pressure impactor (BLPI) [24] with six stages: 0.06, 0.18, 0.55, 1.7, 5.0, and >14.5 μm . The particles were sampled on a Nucleopore membrane (47 mm, 0.2 μm) at air flow of 19.2 L min⁻¹ during 24 h.

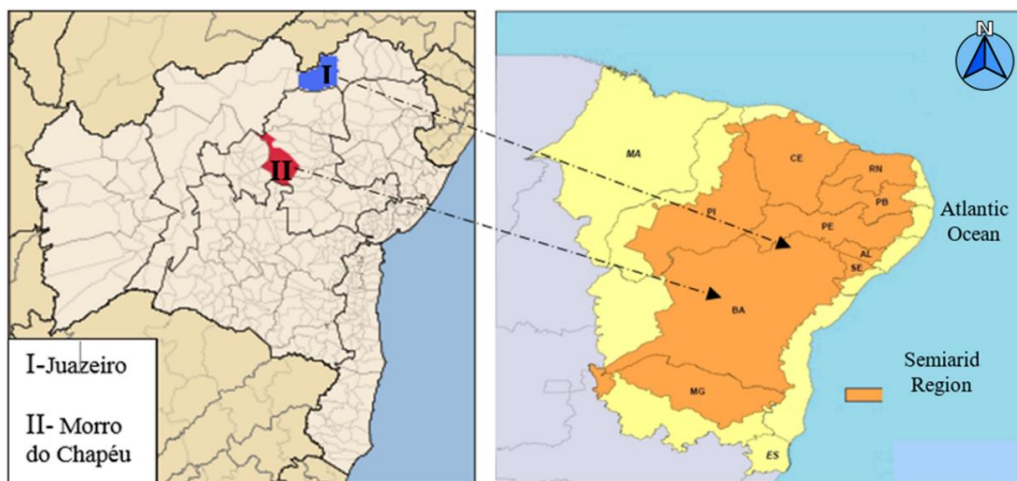


Fig. 1. Location of the sampling stations: (a) on the map of Brazil; (b) on the map of the Brazilian semiarid region

2.2 Analyses and Quality Control

The analytical methodology included ion chromatography for the determination of anions Cl^- , NO_3^- and SO_4^{2-} , with detection limits (LOD): 1.97, 0.322 and 1.25 $\mu\text{mol L}^{-1}$, respectively, in the rainwater and particulate matter, molecular spectrophotometry using the indophenol method ($\lambda = 630\text{nm}$) for the determination of NH_4^+ (LOD: 0.0944 $\mu\text{mol L}^{-1}$) flame photometry for Na^+ and K^+ (LOD: 2.61 and 0.246 $\mu\text{mol L}^{-1}$ respectively), and atomic absorption spectrometry with flame for Ca^{2+} and Mg^{2+} (LOD: 1.70 and 0.251 $\mu\text{mol L}^{-1}$ respectively). The atmospheric particulate matter on the membranes was extracted with 1.5 mL of deionized water in ultrasound bath for 15 min, followed by centrifugation and analysis, using the same above cited analytical methods. The LOD for Cl^- , NO_3^- , SO_4^{2-} and Na^+ in atmospheric particulate matter were: 0.107, 0.0174, 0.0678 and 3.91 nmol m^{-3} , respectively. Because it only had 1.5 mL of each sample of atmospheric particulate matter in the different stages of the cascade impactor, it was not possible to analyze the other ions in this matrix. The pH measurements of the rain samples were made with a pHmeter MPA 210 (MLABOR) Model AF 405 (accuracy of 0.02 pH units), using a combined glass electrode, calibrated with buffer solutions. Conductivity measurements were made with a conductivimeter Marconi Model MACA 150, provided with a platinum cell with a constant of 1.0 cm^{-1} , which allows thermostated measurements at $25 \pm 0.1^\circ\text{C}$.

The isotopic analyzes were performed using Finnigan equipments: a mass spectrometer (MS - MAT Delta Plus), an automatic reactor (H - Device Thermo Quest) specific for analysis of the ratio D/H and an online automatic sample preparation system (Gas Bench II) for the isotopic determination of the $\text{O}^{18}/\text{O}^{16}$ ratio. The standard water was a SMOW sample (standard mean ocean water), provided by the IAEA.

The quality control analysis was done using a standard reference rain, produced by the Canadian environmental agency (RAIN-97, lots 1107 and 407) containing all species determined in the rain and in the particulate matter. The quality of the data series was controlled by mass balance (total sum of cation equivalents *versus* ion equivalents) and comparing the calculated and measured conductivity values [25].

2.3 Statistical Analysis

The evaluation of possible correlations between the ions measured in the rain and in the atmospheric particulate matter was made using the Pearson correlation coefficient [26].

With the use of PCA, along with the hierarchical cluster analysis (HCA), the preview of the various ions in rainwater samples and particulate matter fractionated by size has become more rapid, objective and efficient. The program used for the application of this statistical tool was Statistica, version 10.0.

2.4 Air Mass Trajectories

A study of the trajectories of air masses for the sampling period was done using the NOAA HYSPLIT Model [27]. The back trajectories were simulated for each period and sampling station, taking into accounts their respective altitudes and georeference, allowing the determination of the air masses trajectory that comes to each site.

2.5 Study of the Geological Characteristics of the Water Basins of the Semiarid of Bahia

Chemical secondary data on the groundwaters of the Bahia State were used. The major ions in groundwater were thus compiled, which could come from the sea spray. The data come from the registration of the wells, made available by the Company of Rural Engineering of Bahia, CERB, on the official website of the Geological Survey of Brazil [28] through the Information System Groundwater (SIAGAS). Associations were made between the groundwater salinity of the region with the local geology, which will be discussed particularly in the two areas chosen for atmospheric studies of this work, that are part of the Salitre riverbasin, semiarid region of Bahia.

3. RESULTS AND DISCUSSION

3.1 Inorganic Characterization of the Rain

In the two sampling sites (Juazeiro and Morro do Chapéu) the conductivity of the rain ranged from 21.5 to 70.8 $\mu\text{S cm}^{-1}$ and 4.58 to 19.1 $\mu\text{S cm}^{-1}$, respectively. The molar concentrations and the percentage distribution of the ionic species decreased in the following order: $\text{Cl}^- > \text{Ca}^{2+} > \text{NO}_3^- > \text{NH}_4^+ > \text{Na}^+ > \text{K}^+ > \text{Mg}^{2+} > \text{SO}_4^{2-} > \text{H}^+$ in Juazeiro (Fig. 2a) and $\text{Cl}^- > \text{NH}_4^+ > \text{Na}^+ > \text{NO}_3^- > \text{Mg}^{2+} > \text{H}^+ > \text{SO}_4^{2-} > \text{K}^+ > \text{Ca}^{2+}$ in Morro do Chapéu (Fig. 2b). The presence of sea spray was detected by the ratio Cl^-/Na^+ in the rainwater, which also shows other sources of Cl^- in the atmosphere of the region, mainly in *Juazeiro*. As found by Gioda et al. [29] in Puerto Rican rainforest, despite the altitude and distance from the sea, the atmosphere of the Semiarid of Bahia represented by wet precipitation, is strongly influenced by marine sources rather than local antropogenic sources. NH_4^+ , one of the most abundant ions in the rain of the two localities, probably has its origin in the use of fertilizers in the vicinity of the rain sampling sites, which is more intense in Morro do Chapéu.

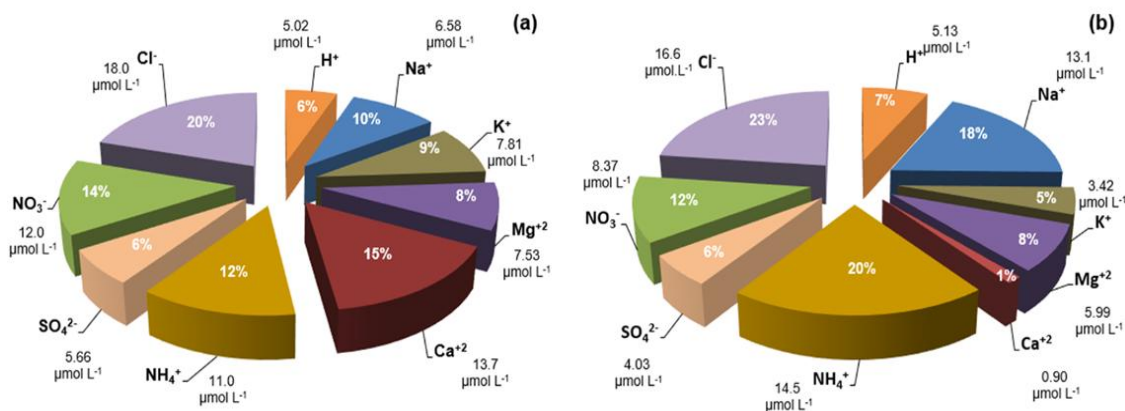


Fig. 2. Percentual distribution and volume-weighted mean ($\mu\text{mol L}^{-1}$) of ions in the rain of the Semiarid of Bahia, Brazil: (a) Juazeiro; (b) Morro do Chapéu

The results showed pH values of the rain in Juazeiro between 5.98 and 7.33, with 6.80 as volume-weighted mean (VWM); in Morro do Chapéu the pH values ranged from 6.40 to 7.24, with 6.75 as VWM. These values suggest a neutralization of the rain acidity by ammonia either by basic soil particles or by sea spray. The calculated average parcel of the rain acidity neutralization by sea spray, using Na^+ as tracer, calculated according to Campos et al. [12], was 26.3% and 27.6%, respectively, in those locations. The estimation of the influence of the sea spray in rain from both locations showed the following contribution of constituents: Cl^- (56% and 92%), SO_4^{2-} (38% and 81%), Mg^{2+} (14% and 26%), Ca^{2+} (25% and 57%) and K^+ (2.2% and 0%). Thus, it is observed that in the locality of Morro do Chapéu, the contribution of marine aerosol is virtually the only source of chloride.

3.2 Inorganic Characterization of the Atmospheric Particulate Matter (PM)

Considering the two locations, the concentration level of the major inorganic species in PM was in the range of 13.6 - 26.9 nmol m^{-3} Cl^- , 3.23 - 6.17 nmol m^{-3} NO_3^- , 2.87 - 11.0 nmol m^{-3} SO_4^{2-} and 11.5 - 37.0 nmol m^{-3} Na^+ . Fig. 3 shows the average percentage distribution of these ions in the two locations, which characterizes the atmospheric particulate matter in that semiarid region. It can be seen in this figure that Na^+ e Cl^- are the most abundant ions.

Fig. 3 shows the distribution percentage and average concentration of the ions, that were analyzed in the atmospheric particulate material. The apparent deficit in the chloride particle shown in these figure, can be attributed to atmospheric reactions on the surface of sea spray, producing gaseous HCl [24]. This does not happen in the rain, as previously discussed with reference to other sources of Cl^- in the region, which should be gas, since they are not represented in the particulate material.

The SO_4^{2-} _{nss} percentual (nss: non sea salt) comparing to total sulfate (SO_4^{2-} _T) in the atmosphere of both locations shows that the sea spray SO_4^{2-} contribution to the particulate material is only 3 and 2%, on average. Sievering et al. [30] calculated the SO_4^{2-} _{nss} of the region as:

$$[\text{SO}_4^{2-}]_{\text{nss}} = [\text{SO}_4^{2-}]_{\text{T}} - 0.06 [\text{Na}^+] \quad (1)$$

where $[\text{SO}_4^{2-}]_{\text{T}}$ and $[\text{Na}^+]$ are concentrations of the ions in the particulate material; 0.06 is the molar ratio $\text{SO}_4^{2-}/\text{Na}^+$ in the sea water.

Fig. 4 shows the distribution by size of these particles where Na^+ e Cl^- can be observed predominantly as particles > 1.7 μm . This is observed also in other works [8,9,31]. Since Na^+ and Cl^- are mainly originated by sea spray, their particles are mainly distributed in the micrometric fraction. However, as expected for long-range transport, the sea spray content in the sub-micrometric fraction is not negligible, as can be seen in this figure.

From Fig. 4 the chloride depletion seems to be high in both the stations, especially in the 0.55 μm fraction measured at Morro do Chapéu. Fig. 4 also shows that the predominance of NO_3^- and SO_4^{2-} as atmospheric fine particles ($\leq 1.7 \mu\text{m}$) suggests a secondary source by gas-particle or particle-particle conversion, according to Allen et al. [32] and Contini et al [33].

3.3 Isotopic Characterization of the Rain

Stable isotopes of oxygen-18 and deuterium were determined in the rain as environmental tracers, evaluating the isotopic ratios $^{18}\text{O}/^{16}\text{O}$ and D/H, which can vary in the rain according to the water source and the processes that occur during their displacement and its surface storage, such as climate of the local of the precipitation (rainfall and temperature), geographical features (distance from the coast, elevation) and evaporation degree. The quantitation of the isotope ratio is given in terms of its deviation ($\delta \text{‰}$) in the sample compared to a standard water (standard mean ocean water – IAEA), R_p , and the sample isotopic ratio $^{18}\text{O}/^{16}\text{O}$ (R_a) [34]:

$$\delta \text{‰} = [(R_a - R_p)/R_p] \times 10^3 \quad (2)$$

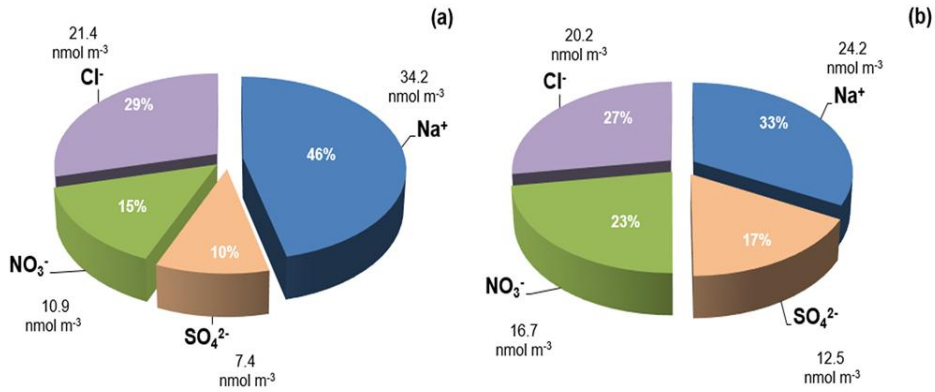


Fig. 3. Percentual distribution and average concentration of the major ions in the atmospheric particulate matter. Semi-arid of Bahia, Brazil: (a) Juazeiro; (b) Morro do Chapéu

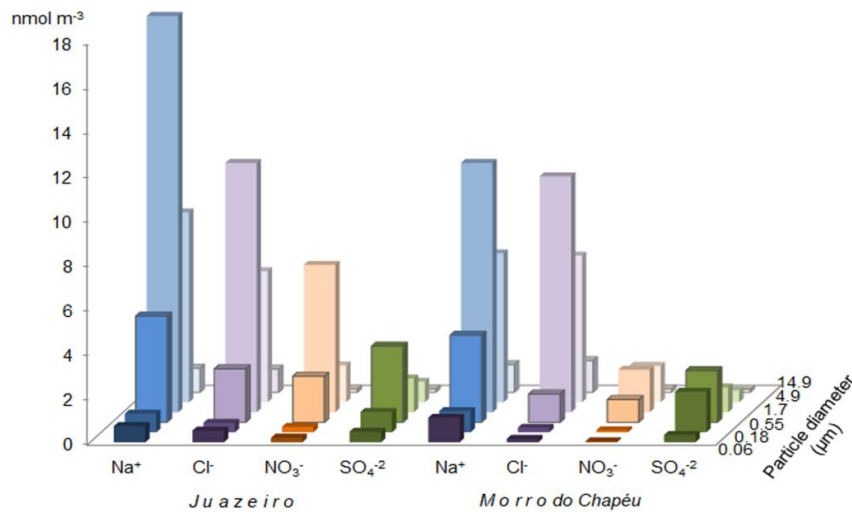


Fig. 4. Average concentrations of Cl^- , Na^+ , SO_4^{2-} and NO_3^- fractionated by size in the atmospheric particulate material in the Semi-arid of Bahia, Brazil. Juazeiro and Morro do Chapéu

The deuterium excess (d) is a function of the source of the water vapor as well as of the hydrologic recycling degree in the basin. Increases in d result from the additional contribution of the recycled water vapor from the surface water evaporation and from the captured water by interception during the climatic event [35]. According to Armengaud et al. [36], d provides information on the distance of the evaporative sources, which originated the rains, i.e. air masses subject to several consecutive episodes of condensation and evaporation produces precipitations with elevated values of the deuterium excess.

The excess of deuterium (d) is expressed by equation 3:

$$d = \delta D - 8 \delta O^{18} (\text{‰}) \tag{3}$$

The parameter d is also dependent on the location; the average value found by Craig [34] was 10‰.

The data relating to the environmental isotopes oxygen-18 and deuterium in the precipitation characterized the studied area, with maximum and minimum values of 28.8‰ and -58.5‰ for δD and -6.81‰ and 2.55‰ for δO^{18} in Juazeiro and 23.3‰ and -48.6‰ for δD and -9.49‰ and -0.02‰ for δO^{18} in Morro do Chapéu, respectively. The amounts of deuterium excess corroborate with the type of precipitation of air masses that represent the precipitation of the region maximum and minimum values were: 41.5 ‰ and -20.7‰ in Juazeiro and 43.7‰ and -1.1‰ in Morro do Chapéu, respectively. The more positive values found for *Morro do Chapéu* characterize waters from further afield. Fig. 5 shows the daily variation of precipitation at this location as an example of the semiarid region of Bahia, with their isotopic ratios and the calculated deuterium excess, enabling the characterization of the temporal and spatial variability compared with the analysis of the origin of the deposited water in the region.

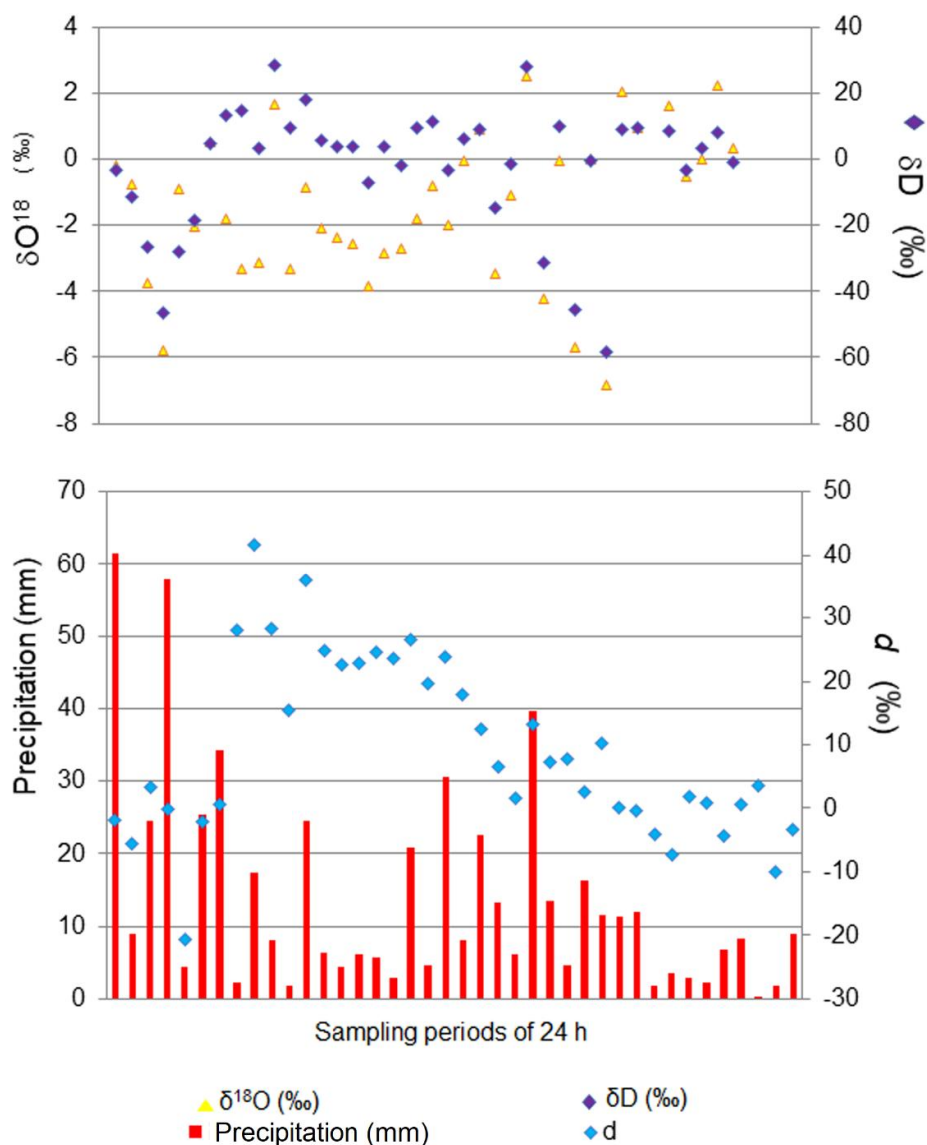


Fig. 5. Change in the daily total precipitation and corresponding isotopic ratios and deuterium excess (Juazeiro, Semiarid of Bahia, Brazil)

3.4 Air Mass Characterization

The study of the trajectories of air masses for each rain event and during the PM sampling period using the NOAA HYSPLIT Model [27] showed that, in the most of the atmospheric PM sampling days, the air mass that arrived in the region passed over the ocean: frequency of 83% for Juazeiro and 75% for Morro do Chapéu. In the case of the sampled rainy events, the frequency of air masses coming from the ocean was relatively low for Juazeiro (29%) and it was maintained at 75% for the locality Morro do Chapéu. It was possible to know because for each sampling day has been generated a backward trajectory graph, from the beginning of the 24 h of sampling until the end. The Fig. 6 shows examples of backward trajectories of air masses of sampling days.

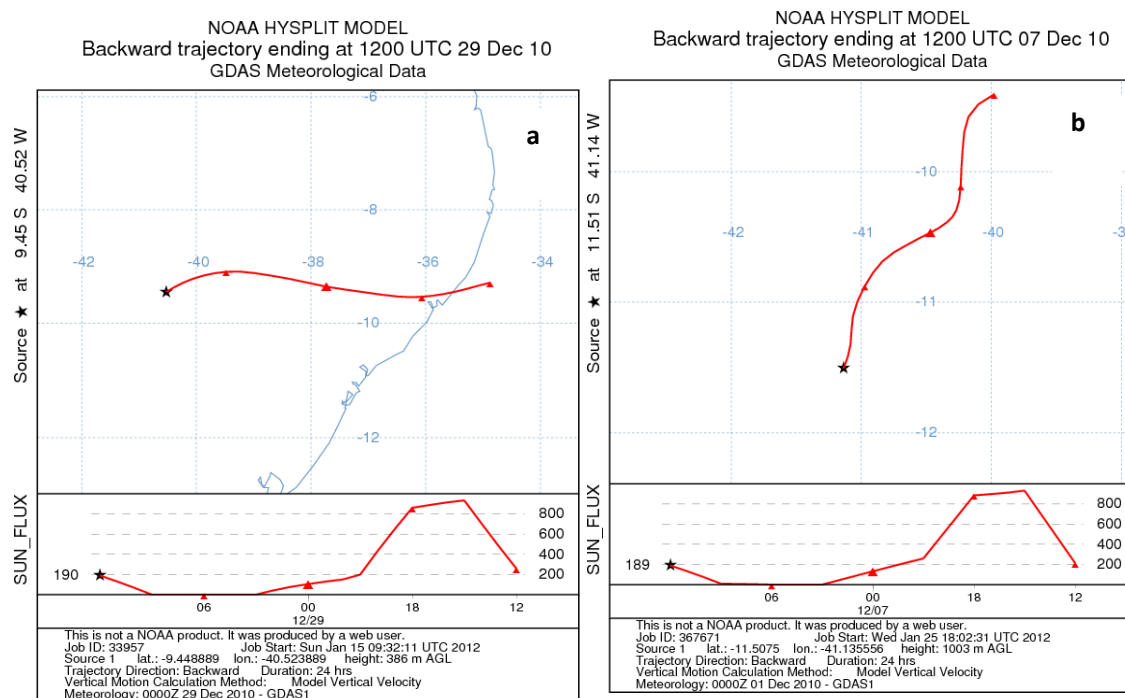


Fig. 6. Examples of backward trajectories of air masses that arrive in Semi-arid of Bahia, Brazil: (a) Juazeiro; (b) Morro do Chapéu

3.5 Statistical Analysis

The hierarchical cluster analysis (HCA) was applied to the data arrays of the rainwater samples for both seasons (Juazeiro and Morro do Chapéu) using the Statistica 10.0 program, aiming to complement the studies conducted to investigate the marine influence and other sources (natural continental and anthropogenic) in the waters salinization in the Semi-arid of Bahia. Analyzing the dendograms obtained (Fig. 7), one can see that for Juazeiro there is the division of five groups, showing strong similarities between (i) Cl^- and K^+ , what could indicate common origin from biomass burning; (ii) Na^+ and pH; (iii) NO_3^- and NH_4^+ ; (iv) SO_4^{2-} , $\text{SO}_4^{2-}_{\text{nss}}$; (v) Ca^{2+} , Mg^{2+} and conductivity, which seems that, in this station, the crustal contribution is dominant with respect to sea spray. For Morro do Chapéu, there was the formation of three groups with great similarity, the first of them shows similarities between Cl^- , Na^+ and Mg^{2+} , indicating the sea spray contribution; the second group shows similarities between SO_4^{2-} , $\text{SO}_4^{2-}_{\text{nss}}$ and pH; the third group shows similarities between NO_3^- , conductivity, NH_4^+ , Ca^{2+} and K^+ .

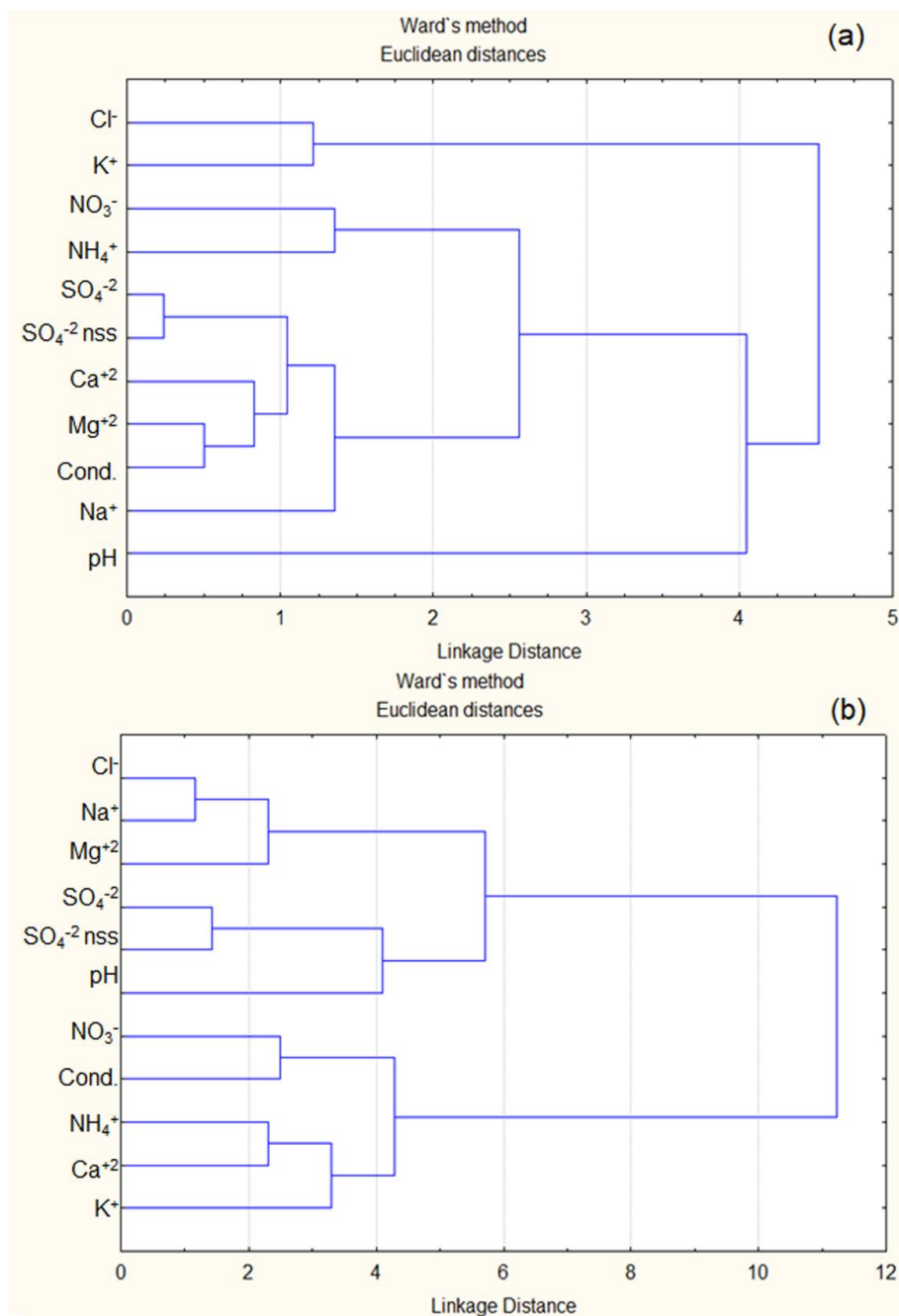


Fig. 7. Dendrogram obtained by HCA of the variables to rainwater samples: (a) Juazeiro; (b) Morro do Chapéu

The correlation matrix (Table 1) constructed with the data of the rain samples of the region, showed the following strong positive correlations: (i) Cl⁻, Na⁺ and Mg⁺² displayed high positive correlation coefficient in Morro do Chapéu and high similarity according to the dendrogram, supporting the marine influence in this place; (ii) between nitrogen species (NH₄⁺ and NO₃⁻) in both locations, related to human activities with emission of precursors: NO_x (NO + NO₂), by more intense emissions from biomass burning, being NO₃⁻ ion the major oxidation products of these compounds; NH₄⁺, by management of animal waste, disposal of sewage, landfills and dumps; (iii) SO₄⁻² and SO₄⁻² nss

correlates with NO_3^- in the rain of Juazeiro, showing common origin of these species and with ions derived from soil resuspension, such as Mg^{2+} and Ca^{2+} . Therefore, in this station, the main source of SO_4^{2-} could be the continental dust. On the other hand, in Morro do Chapéu the low correlation coefficient between SO_4^{2-} and NO_3^- and also the dissimilarity shown in the dendrogram indicates no common origin and also corroborates with the low percentual (19%) of anthropogenic contribution found to SO_4^{2-} in the rain this location.

Table 1. Correlation matrix with the data of the rain samples of the Juazeiro and Morro do Chapéu regions

Juazeiro											
	1	2	3	4	5	6	7	8	9	10	11
1- Cl^-	1.0										
2- NO_3^-	0.36	1.0									
3- SO_4^{2-}	0.62*	0.72*	1.0								
4- SO_4^{2-} nss	0.63*	0.70*	0.99**	1.0							
5- NH_4^+	0.42	0.76*	0.58	0.59	1.0						
6- Ca^{2+}	0.53	0.65*	0.93**	0.93**	0.51	1.0					
7- Mg^{2+}	0.51	0.70*	0.96**	0.95**	0.50	0.95**	1.0				
8- K^+	0.58	0.44	0.57	0.59	0.29	0.48	0.53	1.0			
9- Na^+	0.51	0.71*	0.92**	0.87**	0.48	0.84**	0.92**	0.42	1.0		
10- pH	-0.010	-0.025	0.086	0.052	-0.067	0.072	0.081	0.050	0.085	1.0	
11- Cond	0.53	0.68*	0.92**	0.90**	0.60*	0.92**	0.91**	0.51	0.86**	0.12	1.0

Morro do Chapéu											
	1	2	3	4	5	6	7	8	9	10	11
1- Cl^-	1.0										
2- NO_3^-	0.41	1.0									
3- SO_4^{2-}	0.67*	0.30	1.0								
4- SO_4^{2-} nss	0.41	0.13	0.93	1.0							
5- NH_4^+	0.30	0.65*	0.24	0.09	1.0						
6- Ca^{2+}	0.20	0.44	0.050	-0.090	0.46	1.0					
7- Mg^{2+}	0.63*	0.57	0.45	0.22	0.50	0.77*	1.0				
8- K^+	0.26	0.54	0.060	-0.040	0.35	0.54	0.51	1.0			
9- Na^+	0.88**	0.49	0.73	0.44	0.42	0.32	0.73*	0.23	1.0		
10- pH	-0.10	-0.30	0.11	0.22	-0.28	0.010	0.010	-0.020	0.00	1.0	
11- Cond	0.56	0.74*	0.29	0.069	0.57	0.64*	0.76*	0.57	0.62*	-0.048	1.0

r in bold: significant correlation ($p < 0.05$); *r* with *: Strong correlation ($0.60 \leq |r| < 0.80$);
r with **: Very strong correlation ($0.80 \leq |r| < 1.0$). Cond: conductivity

The principal component analysis technique (PCA) was applied to the data in the two sampling locations used in this study in the samples of atmospheric particulate matter. Samples were identified by a code that identifies the station (J: Juazeiro; M: Morro do Chapéu), the month of the collection (A: April; N: November), the initial date of sampling and identification of the particles (F: Fine particles; C: Coarse particles).

Fig. 8 shows the graphs of scores and loadings using two main components to explain the results that are associated with each variable (Cl^- , NO_3^- , SO_4^{2-} , Na^+) for fine and coarse particles. Looking at this figure, the PCA showed that the first and second main components explain 81 and 14%, respectively, of the total variance.

The ions Na^+ and Cl^- were the most abundant in the coarse fraction of the particles, suggesting a significant contribution by the sea spray in this size range of the particulate matter that comes to this region, especially in Morro do Chapéu.

The predominance of SO_4^{2-} in fine mode in both sampling stations, after a long period of drought, confirms its secondary source by particle - particle or gas - particle conversion through the SO_2 oxidation, emitted from burning local biomass. The main contribution of the ion NO_3^- in fine particulate material supports the existence of gas phase reactions between NH_3 , Cl^- from sea spray and nitric acid, with the formation of NH_4Cl and NH_4NO_3 , partially explaining the loss of chloride of the coarse particulate and, at the same time, nitrate gain for the fine particulate.

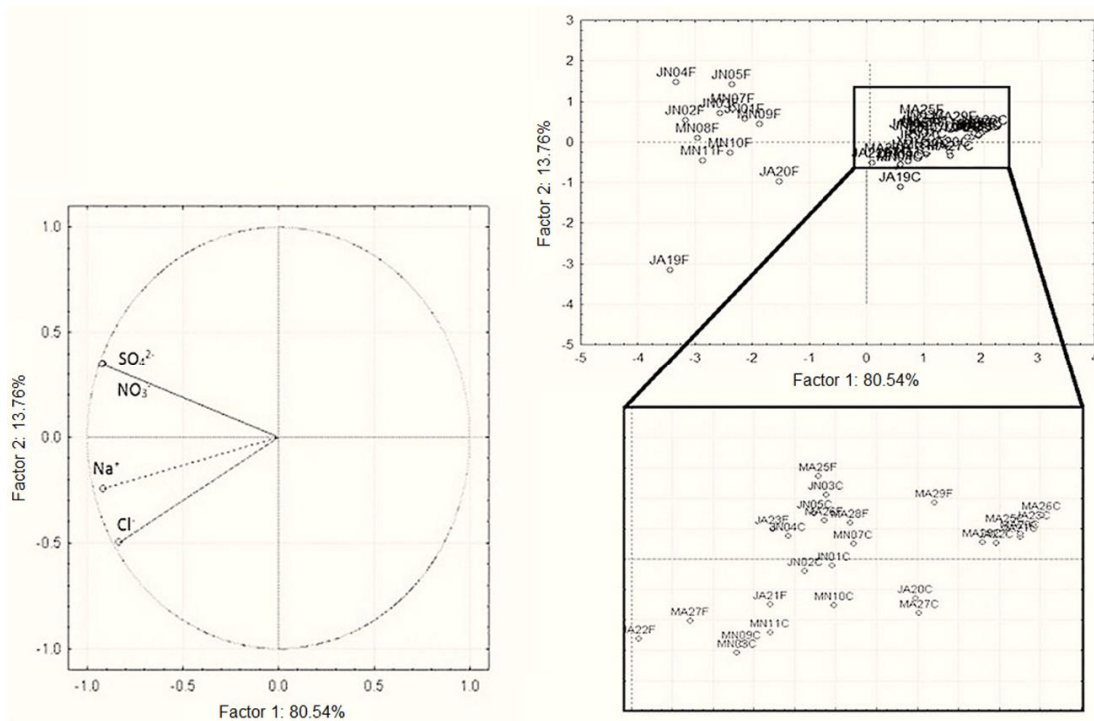


Fig. 8. (a) Graph of weights (projection of the variables in the space); (b) Graph of scores of PC1 versus PC2, obtained from all variables in the samples of atmospheric particulate matter with the projection of the variables in the space

3.6 Contribution of Sea Spray to the Groundwater of the Study Area

Table 2 presents the ranges of total concentration of the main ions in groundwater, which could originate from the sea spray, as well as nss (non sea salt) concentrations and the contribution of sea spray (ss) to those sampled waters from six wells in the region of Juazeiro and eight wells in the region of Morro do Chapéu.

The estimation of the sea spray in the groundwater from Juazeiro and Morro do Chapéu showed, respectively, the following maximal contribution of constituents (Table 2): 4.4% and 26% Cl^- , 38% and 11% SO_4^{2-} , 1.4% and 17% Ca^{2+} , 5.5% and 26% Mg^{2+} and 24% and 0.0% K^+ . These data show that the amount of sea spray that reaches the region is not sufficient to salinize the groundwaters.

The municipalities of Juazeiro and Morro do Chapéu, areas considered to the atmospheric study in this work, are located in the Salitre river basin in semi-arid region of Bahia. The research that was done in this work on the geological characteristics of these locations showed that this basin is under different hydrogeologic domains, which are entities resulting from the grouping of geologic units with hydrogeologic affinity, having the basis mainly the lithologic characteristics of the rocks [37]. These domains, in the case of the semi-arid region of the state of Bahia and its relation to the increasing salinity of the groundwater are: the coverage domain (freshwater), domain of the sediment and metasediments (freshwater and slightly brackish water), domain of the limestones (brackish water) and domain of the crystalline (very brackish water). The municipality Morro do Chapéu prevails largely in the metasediments domain, with freshwater, with a small part in the domain of the limestones, and few points with slightly brackish water, represented in Fig. 9 by the locality of Velame (0.72‰).

The municipality of Juazeiro, which also belongs to the domain of metasediments, but only a small part, has waters with low salinity, for example in the locality of Paredão, 0.41‰ (Fig. 9), the limestones domain predominates, imprinting a strong salinization of its groundwater (2.3 to 12‰, Fig.

9), with the salinity varying according to local rainfall and reflecting the mineralogical composition of the rock. Fig. 9 shows the salinity of the water in these and other cities of the Salitre river basin, highlighting the municipalities Morro do Chapéu and Juazeiro.

Table 2. Ranges of total concentration, nss (non sea salt) and sea spray contribution in the groundwater of the studied areas. Water basin of the Salitre river, Semiarid of Bahia, Brazil

Ion	Juazeiro			Morro do Chapéu		
	C _T	C _{nss}	Sea spray %	C _T	C _{nss}	Sea spray %
	μmol L ⁻¹ (%)			μmol L ⁻¹ (%)		
Na ⁺	0.261- 304	-	-	632-50870	-	-
Cl ⁻	253-406	253 - 388 (95.6 - 100)	0.0-4.4	1022-147242	761-143990 (74.5-98)	2.0-26
SO ₄ ²⁻	47.6-70.8	29.4-70,8 (61.7-100)	0.0-38	829-18229	829-17624 (88.6-100)	0.0-11
Ca ²⁺	151-1290	151-1274 (98.6-100)	0.0-1.4	1518-56000	1257-52918 (82.8-98)	2.0-17
Mg ²⁺	89.7-326	89.7-308 (94.5-100)	0.0-5.5	984-33210	723-30158 (73.5-92)	8.0-26
K ⁺	25.6-76.9	25.6-58.7 (76.3-100)	0.0-24	51,3-659	51.3-659 (100)	0.0

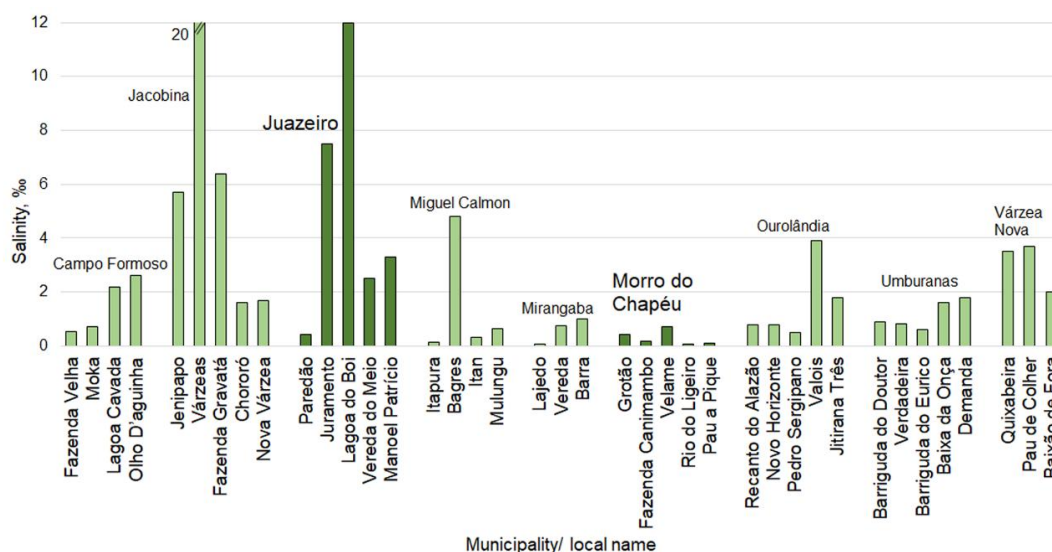


Fig. 9. Salinity levels of groundwater in different municipalities / locations of the Salitre river basin in the semiarid region of Bahia, Brazil, highlighting the municipalities of Morro do Chapéu and Juazeiro

4. CONCLUSIONS

The composition of rainwater in the two sampling stations, Juazeiro and Morro do Chapéu, in the Semiarid of Bahia, Brazil, showed that the atmosphere of both localities suffers significant marine influence, as well as resuspended soil particles and anthropogenic sources. The results demonstrate the potential of certain isotopic tracers in the rain, for the understanding of the hydrological cycle in the two localities in the semiarid region in the studied area: in Morro do Chapéu, waters of the precipitation are mostly coming from further afield sites, while in Juazeiro, they come from the region, although air masses often reach the coast, as shown by backward trajectories. The estimate of the contribution of sea spray in the rain in Juazeiro is much less (56%) than in Morro do Chapéu (92%), although the groundwater is sweet in this locality. The contribution of the sea spray for the groundwater at the study areas calculated using Na⁺ as tracer showed to be small in relation to the

main ions that could have this origin: Cl^- , SO_4^{2-} , Ca^{2+} , Mg^{2+} e K^+ . This allows to conclude that the amount of sea spray that interferes at the groundwater composition is insufficient to salinize waters. As showed by the study, the salinity of the groundwater is associated with the geological characteristics of these locations. Thus, the cause of the salinization of the waters in the Semiarid of Bahia, Brazil, must be attributed to the local geology and processes of evaporation and concentration of salts, due to the high temperatures to which the region is subjected.

ACKNOWLEDGEMENT

The authors acknowledge UNIVASF (Federal University of São Francisco Valley, Juazeiro-BA, Brazil); CAPES (Coordination for the Improvement of Higher Education Personnel); Prof. Maria Zucchi, Federal University of Bahia/Physics Institute.

COMPETING INTERESTS

Authors have declared that no competing interests exist.

REFERENCES

1. Brito L. T. de L, Srinivasan VS, Silva A. de S, Gheyi HR, Galvão C. de O, Hermes LC. *Rev. Bras. Eng. Agr. Amb.* 2005;9:596.
2. Martinez-Beltran J, Manzur CL. Overview of salinity problems in the world and FAO strategies to address the problem. In: *Proceedings of the International Salinity Forum, Riverside.* 2005;311–313.
3. Greene R, Timms W, Rengasamy P, Arshad M, Cresswell R. Soil and aquifer salinization: Toward an integrated approach for salinity management of groundwater. In *Integrated Groundwater Management.* Springer, Cham. 2016;377-412.
4. Dämmgen U, Erisman W, Cape N, Grünhage L, Fowler D. *Environ. Pollut.* 2005;134:535.
5. Araujo TG, Souza MF, Mello WZD, da Silva DM. Bulk atmospheric deposition of major ions and dissolved organic nitrogen in the lower course of a tropical river basin, Southern Bahia, Brazil. *Journal of the Brazilian Chemical Society.* 2015;26(8):1692-1701.
6. Finlayson-Pitts BJ, Pitts JN. *Chemistry of the upper and lower atmosphere: Theory, experiments and applications.* Academic Press: San Diego, USA; 2000.
7. Van Langenhove L, Verryckt LT, Bréchet L, Courtois EA, Stahl C, Hofhansl F, Penuelas J. Atmospheric deposition of elements and its relevance for nutrient budgets of tropical forests. *Biogeochemistry;* 2020.
8. Quinn PK, Collins DB, Grassian VH, Prather KA, Bates TS. *Chem. Rev.* 2015;115:4383.
9. D O'Dowd C, De Leeuw G. *Phil. Trans. R. Soc. A.* 2007;365:1753.
10. Masiol M, Squizzato S, Ceccato D, Rampazzo G, Pavoni B. *Atmos. Environ.* 2012;63:117.
11. Bruynseels F, Storms H, Tavares TM, Van Grieken R. *J. Environ. Anal. Chem.* 1985;23:1.
12. Campos VP, Costa ACA, Tavares TM. *J. Environ. Manage.* 2007;84:204.
13. Seinfeld JH, Pandis SN. *Atmospheric chemistry and physics: From air pollution to climate change.* John Wiley and Sons: New York, USA; 1998.
14. Vignati E, Facchini MC, Rinaldi M, Scannell C, Ceburnis D, Sciare J, Kanakidou M, Myriokefalitakis S, Dentener F, O'Dowd CD. *Atmos. Environ.* 2010;44:670.
15. Shamsi A, Kasemi GA. *J. Geope.* 2014;4:73.
16. Clark I, Fritz P. *Environmental isotopes in hydrogeology, 2nd Ed.;* Lewis Publishers: New York, USA; 1997.
17. Ghoshet P, Chakrabarti R, Bhattacharya SK. *India. Chem. Geol.* 2013;335:118.
18. Oliveira CN, Campos VP, Medeiros YDP. *Quim. Nova.* 2010;33:1059.
19. Whipkey CE, Capo RC, Chadwick OA, Stewart BW. *Chem. Geol.* 2000;168:37.
20. Kovda DA. *Irrigation, drainage and salinity: An international sourcebook.* FAO/UNESCO: Paris, France; 1973.
21. Wetzel RG. *Limnology – Lake and river ecosystems, 3rd Ed.;* Elsevier Academic Press: California, USA; 2001.

22. Giulietti AM, Queiroz LP de. IMSEAR: Millennium Institute of the Semi-Arid actions in its four years. In: Queiroz, L. P. de; Rapini, A.; Giulietti, A. M., (Ed.); Towards Greater Knowledge of the Brazilian Semi-Arid Biodiversity. Brasília, Brazil; 2006.
23. Available:http://www.iup.uniheidelberg.de/institut/studium/lehre/AquaPhys/docPAS/IEHC_Vol3.pdf
24. Wang HC, John W. *Aerosol Sci. Technol.* 1988;8:157.
25. World Meteorological Organization (WHO); Manual for the GAW Precipitation Chemistry Programme. No.160; GAW Precipitation Chemistry Science Advisory Group: New York, USA; 2004.
26. Callegari J, Sidia M. *Bioestatística: Princípios e aplicações.* Artemed: Porto Alegre, Brasil; 2003.
27. Available:<http://ready.arl.noaa.gov/HYSPLIT.php>
28. Available:<http://siagasweb.cprm.gov.br/layout>
29. Gioda A, Mayol-Bracero OL, Scatena FN, Weathers KC, Mateus VL, McDowell WH. *Atmos. Environ.* 2013;68:208.
30. Sievering H, Ennis G, Gorman E. *Global Biogeochem. Cy.* 1990;4:395.
31. Andreas EL, Edson JB, Monahan EC, Rouault MP, Smith SD. *Boundary-layer meteorology.* 1995;72:3.
32. Allen HM, Draper DC, Ayres BR, Ault A, Bondy A, Takaham S, Modini RL, Baumann K, Edgerton E, Knote C, Laskin A, Wang B, Fry JL, *Atmos. Chem. Phys.* 2015;15:10669.
33. Contini D, Cesari D, Genga A, Siciliano M, Ielpo P, Guascito MR, Conte M. *Sci. Total Environ.* 2014;472:248.
34. Craig H. *Science.* 1961;133:1702.
35. Rozanski K, Araguás-Araguás L, Gonfiantini R. *Climate change in continental isotopic records: Geophys. Monogr. Ser.* 1993;78:1.
36. Armengaud A, Kroster R, Jouzel J, Ciais P. *Geophys. Res.* 1998;103:8947.
37. Bomfim LFC, Jesus JDA. *Mapa de domínios / subdomínios hidrogeológicos da Bahia.* CPRM: Salvador-BA, Brasil; 2004.

Biography of author(s)



Adriana M. C. Silva

Federal University of São Francisco Valley, Collegiate of Agricultural and Environmental Engineering 48902-300 Juazeiro-BA, Brazil.

Research and Academic Experience: Ph.D. in Analytical Chemistry, she teaches classes at the Universidade Federal do Vale do São Francisco, inserted in the Colegiado de Agricultura e Engenharia Ambiental. In addition she develops research, extension and administrative activities at the university.

Research Area: Analytical Chemistry

Number of Published papers: 04 papers in international and national journals and 11 Abstracts published in conference proceedings.

Any other remarkable point(s): She has participation in teams of 7 research projects, two of which are currently.



Vânia P. Campos

Federal University of Bahia/Chemistry Institute - Analytical Chemistry Department, 40170-290 Salvador-BA, Brazil.

Research and Academic Experience: PhD in Chemistry, Full Professor at the Departamento de Química Analítica– Instituto de Química - UFBA, where she teaches classes and develops research on Atmospheric and Environmental Chemistry and on air and water sampling techniques.

Research Area: Environmental Analytical Chemistry, Hydrophere and Atmosphere Chemistry.

Number of Published papers: 37 papers in international and national journals, 5 Book Capters, 40 lectures/conferences presented at national and international congresses.

Special Award (If any): Highlight Award in Chemistry / Sociedade Brasileira de Química-Regional Bahia; Inventor Award / Núcleo de Inovação e Tecnologia-UFBA, Mandacaru Award Instituto Ambiental Brasil Sustentável.

Any other remarkable point(s): She is Full Member of the Academia de Ciências da Bahia.



Rafaela S. Domingues

Federal University of Bahia/Chemistry Institute - Analytical Chemistry Department, 40170-290 Salvador-BA, Brazil.

Research and Academic Experience: Graduated in Chemistry, Chemistry Institute/UFBA, with experience in underground water.

Research Area: Environmental Analytical Chemistry - Chemistry of the hydrophere.



Lícia P. S. Cruz

Federal University of Bahia/Chemistry Institute - Analytical Chemistry Department, 40170-290 Salvador-BA, Brazil.

Research and Academic Experience: She teaches subjects such as Separation Methods, Instrumental Analytical Chemistry, Water and Wastewater Chemistry Analysis and develops research in the areas of Analytical Chemistry and Environmental Chemistry, mainly addressing topics as environmental monitoring, air and water pollution, passive sampling, air and water sampling techniques, chromatographic techniques, organic and inorganic compounds in environmental matrices and health risk analysis.

Research Area: Analytical Chemistry and Environmental Chemistry

Number of Published papers: 16 published papers, 2 book chapters and more than 60 abstracts at congresses

Any other remarkable point(s): She participated as researcher in teams of 15 research projects and is reviewer of some international journals



Franciele O. Santana

Federal University of Bahia/Chemistry Institute - Analytical Chemistry Department, 40170-290 Salvador-BA, Brazil.

Research and Academic Experience: PhD in Chemistry (Universidade Federal da Bahia - UFBA - Brazil, 2019), Junior Postdoctoral Researcher at the SENAI CIMATEC, supported by Conselho Nacional de Desenvolvimento Científico e Tecnológico (CNPq). She is also a collaborator researcher at the Laboratório de Química Analítica Ambiental - LAQUAM/UFBA, since 2011, where conducts research in environmental chemistry area.

Research Area: Environmental Analytical Chemistry, Atmospheric chemistry, especially in urban air pollution, passive sampling, microplastic pollution and chromatographic techniques

Number of Published papers: 7 complete paper published in journals in the last three years, 28 Abstracts published in conference proceedings.

Special Award (If any): "Mention Distinction" for the PhD thesis (2019) by the Programa de Pós-Graduação em Química - UFBA and "Highlight Student Award" (2014) by the Congregação do Instituto de Química - UFBA.

Any other remarkable point(s): Currently, develops research on microplastic pollution in the Todosos Santos Bay, a coastal area of the South Atlantic.

© Copyright (2020): Author(s). The licensee is the publisher (Book Publisher International).

DISCLAIMER

This chapter is an extended version of the article published by the same author(s) in the following journal.
J. Braz. Chem. Soc, 28(12): 2402-2411, 2017.

Focusing on Organocatalytic Asymmetric Michael Addition of Ketones to α , β -unsaturated Nitro Compounds

Jae Ho Shim¹, Si Hun Nam¹, Byeong-Seon Kim^{2*} and Deok-Chan Ha^{1*}

DOI: 10.9734/bpi/cpcs/v2

ABSTRACT

An organic catalyst "(*R, R*)-1,2-diphenylethylenediamine(DPEN) derivative" was developed as a chiral bifunctional organocatalyst and applied for asymmetric Michael additions of aromatic ketones to *trans*- β -nitroalkene compounds under neutral conditions. The isopropyl-substituted thiourea catalyst in neutral condition provides high chemical yield and enantioselectivities (ee) (up to 96% yield, 98% ee). The synthetic utility of the present catalytic asymmetric Michael addition was established by transformation to highly enantioselective products. Baclofen is used as a muscle relaxant, whereas Phenibut is a sleep inducer. These substances are derivatives of γ -aminobutyric acid, which is an inhibitory neurotransmission inhibitor acting on GABA receptors and receptors in our bodies. Therefore, further investigations on their synthesis are necessary because of their high applicability in medicine.

Keywords: Organocatalyst; enantioselectivity; yield; thiourea catalyst; asymmetric.

1. INTRODUCTION

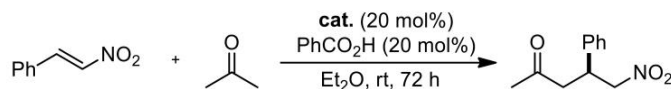
Metal catalysts have been used for asymmetric synthesis; however, recent research, excluding the metal catalysts, has attracted interest because of the high cost of metal catalysts and the instability of metal ions in moist air, which limits the reaction conditions [1]. In addition, metal catalysts can leave metal residues in the product. To identify alternatives to metal catalysts, asymmetric reactions using organocatalysts have been developed [2–12]. The Michael reaction is widely used as one of the most general methods for the formation of C–C bonds in organic synthesis. Michael Addition Reaction [13] is one of the most powerful methods in organic synthesis for C–C and C–X (X=O, N, S) bond formation [14]. Owing to the easy conversion of the electron-deficient nitro group to various functional groups, such as keto, amino, cyano, and carboxylic acid groups, research on asymmetric Michael reactions using the nitro group as the Michael acceptor has been conducted [15–23]. Jacobsen and Ma utilized catalysts with substituents on the thiourea of (*R, R*)-1,2-cyclohexyldiamine. In the Michael addition of aromatic ketones and *trans*- β -nitroalkenes, the stereoselectivity was high, but the yield was low [24,25]. The imidazole derivatives possess extensive spectrum of biological activities such as antibacterial, anticancer, antitubercular, antifungal, analgesic, and anti-HIV activities [26–28]. In 2009, Lao et al. reported the Michael reaction of acetone and *trans*- β -unsaturated nitroalkene using (*R, R*)-1,2-cyclohexyldiamine derivatives as the catalyst and compared the reactivity according to the acidity of amine in the catalyst. For catalysts with electron-withdrawing groups, the stereoselectivity was lower than for catalysts with electron-donating groups. Catalysts with electron-withdrawing groups show higher enantioselectivity than those with electron-donating groups in the N-aryl and N-(2-hydroxyethyl)-(S)-prolinamide derivatives- catalyzed aldol reaction of p-nitrobenzaldehyde and acetone [29,30]. In addition, the reactivity increased when the electrophile was activated via double

¹Department of Chemistry, Research Institute for Natural Sciences, Korea University, 145 Anam-ro Seongbuk-gu, Seoul 02841, Korea;

²Department of Chemistry Education and Research Institute of Natural Science, Gyeongsang National University, Jinju 52828, South Korea.

*Corresponding author: E-mail: bkim@gnu.ac.kr, dechha@korea.ac.kr;

hydrogen bonding of the catalyst. The effects of the N–H bond and hydrogen bond acidity on catalyst activity and the stereotactic properties of functional primary amino catalysts influenced the Michael C–C reaction (Scheme 1) [31–33].



entry	cat.	yield(%) ^a	ee(%) ^b	pK _a ^c
1		95	64	13.1
2		93	74	14.1
3		87	58	12.0
4		55	64	14.2

^aIsolated yield. ^bThe ee values were determined by chiral phase HPLC using AS-H column. ^cThe pK_a values were calculated with an ACD/Lab 11 program.

Scheme 1. Chiral primary amine organocatalysts

Shao and Kokotos [34,35] used (*R,R*)-1,2-diphenylethylenediamine thiourea derivatives as the catalyst and benzoic acid as the additive. During the reaction, aromatic ketones were activated by acid additives, leading to accelerated enamine formation of the catalyst. Asymmetric reactions of aromatic ketones and α , β -unsaturated nitroalkenes led to a high selectivity and high yield.

Nevertheless, it is necessary to develop catalysts for simple synthesis. Therefore, in this study, (*R,R*)-1,2-diphenylethylene-diamines were introduced into the basic framework of a chiral catalyst. We used ketones and *trans*- β -nitrostyrene, which has a powerful electro-withdrawing group, to conduct an enantioselective Michael reaction.

2. RESULTS AND DISCUSSION

2.1 Asymmetric Michael Addition of α , β -unsaturated Nitroolefins and Ketones

2.1.1 Catalyst screening

The Michael addition was performed using acetophenone and nitrostyrene to examine the catalytic effects of enantioselective Michael addition on ketones and α , β -unsaturated nitroalkenes. The catalysts used in the reaction are listed in (Fig. 1). First, *N*-mono-alkylated thiourea with 3-pentyl-substituted amine was used with benzoic acid as an additive.

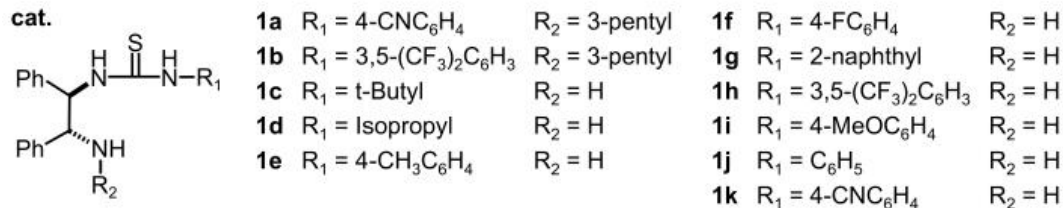


Fig. 1. DPEN-thiourea based catalysts

The reaction carried out in the toluene solvent at room temperature (Table 1, entries 1 and 2) did not proceed, likely because the steric hindrance of secondary amine thiourea with 3-pentyl-substituted amine hindered enamine formation, making the catalyst ineffective. Therefore, the reaction was carried out with *N*-mono-thiourea as the primary amine catalyst prior to amine alkylation. The amine was preserved from alkylation to promote enamine formation, which was activated through dehydration condensation between ketones and amines. The other amine was allowed to react with isothiocyanate to ensure that thiourea could create conditions suitable for double activation, thus, inducing hydrogen-bond formation at the nitro group. The reaction was carried out in toluene with benzoic acid as the additive at room temperature. The use of the isopropyl-substituted primary amine thiourea catalyst led to the highest product yields and enantioselectivities (Table 1, entry 4). This finding indicates that the enantioselectivity and yield of the reaction are improved by the appropriate steric hindrance imparted on the substituent rather than the hydrogen acidity of thiourea. Therefore, less steric hindrance leads to higher yields and enantioselectivity.

Table 1. Catalyst screening

Entry	Cat.	Yield [a]	ee [b]
1	1a	N.R. [c]	-
2	1b	N.R. [c]	-
3	1c	73	98
4	1d	85	98
5	1e	76	90
6	1f	58	92
7	1g	46	90
8	1h	78	94
9	1i	60	94
10	1j	51	92
11	1k	53	90

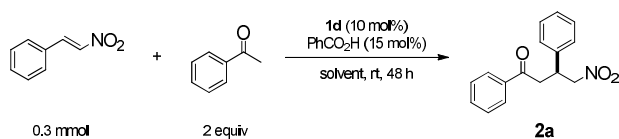
[a] Isolated yield. [b] The ee values were decided by chiral phase HPLC using an AD-H column. [c] N.R. = No Reaction

2.1.2 Solvent effects

The previous experiment reported in Section 2.1.1 confirms that the use of an isopropyl-substituted catalyst leads to the highest yield and enantioselectivity. Using this catalyst, reactivity and enantioselectivity in different solvents were investigated. The reaction proceeded smoothly in all solvents; high enantioselectivity was obtained regardless of the solvent polarity, although differences in the yield were observed. It is predicted that polar solvents would obstruct hydrogen bond formation between the reactant and the catalyst, thereby decelerating the reaction (Table 2, entry 1). In addition, when the reaction was performed without a solvent, the enantioselectivity decreased despite the high

yield (Table 2, entry 2). Among the non-polar solvents tested, toluene generated the highest enantioselectivity and yield (Table 2, entry 3); hence, it was selected as the reaction solvent for subsequent experiments.

Table 2. Solvent effects



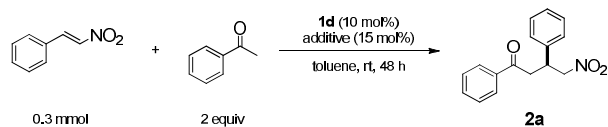
Entry	Solvent	Yield [a]	ee [b]
1	H ₂ O	63	88
2	neat	91	92
3	toluene	85	98
4	ether	80	98
5	CH ₂ Cl ₂	79	98
6	Tetrahydrofuran	74	94
7	methanol	60	94
8	CH ₃ CN	54	94

[a] Isolated yield [b] The ee values were decided by chiral phase HPLC using an AD-H column

2.1.3 Additive effect

The catalyst used in the previous experiment catalyst (**1d**) and toluene (solvent) were applied to the reaction to investigate the reactivity and stereoselectivity in the presence of different additives (Table 3). The reaction carried out without an additive did not proceed (Table 3, entry 1); therefore, an acid additive was employed to facilitate enamine formation. Nonetheless, certain acid additives prevented the progress of the reaction (Table 3, entries 2 and 3), presumably because binding between highly acidic additives and the catalyst degraded the catalytic activity. In addition, water as an additive was conducive to the reaction progress (Table 3, entries 8 and 9). These results confirm that the use of benzoic acid as additive leads to improved yields and enantioselectivities (Table 3, entry 6).

Table 3. Additive effects



Entry	Additive	Yield [a]	ee [b]
1	-	N.R. [c]	-
2	Trifluoroacetic acid	N.R. [c]	-
3	Oxalic acid	N.R. [c]	-
4	Salicylic acid	80	90
5	Terephthalic acid	73	86
6	Benzoic acid	85	98
7	Acetic acid	68	94
8	H ₂ O	74	98
9	H ₂ O (1 eq.)	70	98

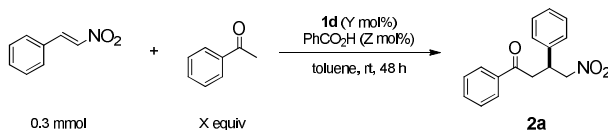
[a] Isolated yield. [b] The ee values were decided by chiral phase HPLC using an AD-H column. [c] N.R. = No Reaction

2.1.4 Equivalence effect

The acetophenone equivalent (eq.) did not cause any differences in the yield and enanti-oselectivity of the reaction (Table 4, entries 1 and 2). The use of 5 mol% of the catalyst resulted in a decreased

yield, and 20 mol% of the catalyst produced a yield and enantioselectivity similar to those obtained with 10 mol% of the catalyst (entries 1, 3, and 4). The results obtained with 5–15 mol% of benzoic acid were similar (Table 4, entries 1, 5, and 6). Thus, the use of 2 eq. acetophenone, 10 mol% catalyst, and 5 mol% benzoic acid additives produced the optimal results (Table 4, entry 5).

Table 4. Equivalence effect



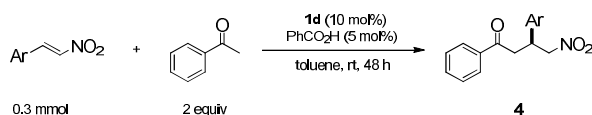
Entry	X (equiv)	Y (mol%)	Z (mol%)	Yield (%) [a]	ee (%) [b]
1	2	10	15	85	98
2	5	10	15	86	96
3	2	5	15	51	98
4	2	20	15	88	96
5	2	10	5	87	98
6	2	10	10	85	98

[a] Isolated yield. [b] The ee values were determined by chiral phase HPLC using an AD-H column

2.1.5 Temperature and time effects

The yield varied substantially when the reaction time ranged between 24 and 48 h (Table 5, entries 1 and 2). However, a slight difference in the yield and enantioselectivity was observed between the reaction times of 48 and 72 h (Table 5, entries 2 and 3). Thus, the optimal reaction time was determined as 48 h. Furthermore, when the temperature was increased, the rate constant increased with the reactivity, but the enantioselectivity decreased, indicating that the optimal result can be obtained when the reaction is carried out at room temperature (Table 5, entries 2, 4, and 5).

Table 5. Temperature and time effects



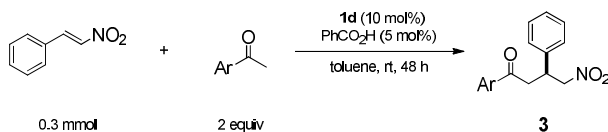
Entry	Temp (°C)	Time (h)	Yield (%) [a]	ee (%) [b]
1	r.t.	24	55	98
2	r.t.	48	87	98
3	r.t.	72	88	98
4	40	48	92	86
5	50	48	91	80

[a] Isolated yield. [b] The ee values were decided by chiral phase HPLC using an AD-H column

2.1.6 Reaction conditions according to the type of aromatic ketones

In the preceding experiments, the optimal conditions for the asymmetric Michael addition of acetophenone and various *trans*- β -nitrostyrenes were investigated. Under the optimal conditions, reactions between various aromatic ketones and *trans*-nitrostyrene were carried out (Table 6). There was difference in the enantioselectivity and yield according to the position of substitution in the aromatic ketones because of the steric hindrance (Table 6, entries 1 and 2). The enantioselectivity in the presence of an electron-donor substituent (Table 6, entries 4 and 5) was lower than that in the presence of an electron-acceptor substituted because of more nucleophilic (Table 6, entries 1, 2, and 3).

Table 6. Reaction conditions according to the type of aromatic ketones



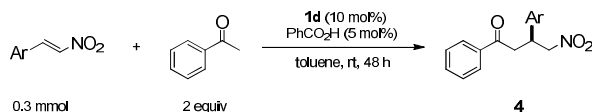
Entry	Ar	Product	Yield (%) [a]	ee (%) [b]
1	4-FC ₆ H ₄	3a	89	92
2	2-FC ₆ H ₄	3b	81	96
3	4-NO ₂ C ₆ H ₄	3c	85	94
4	4-MeOC ₆ H ₄	3d	91	86
5	2-naphthyl	3e	84	80

[a] Isolated yield. [b] The ee values were decided by chiral phase HPLC using an AD-H column

2.1.7 Reaction by unsaturated β -nitroalkenes

Under the optimal conditions established in the preceding experiments, reactions were carried out between acetophenone and various α , β -unsaturated nitroalkenes (Table 7). The resulting enantioselectivity were high when α , β -unsaturated nitroalkene was substituted with electron acceptors (Table 7, entry 2 and 3) as well as electron donors (Table 7, entry 4). And when α , β -unsaturated nitroalkene was substituted with 4-Me, it has a higher yield (Table 7, entry 1). When α , β -unsaturated nitroalkene was substituted with 2-MeO, the reactivity and enantioselectivity decreased compared to those observed when the substituent was 4-MeO because of the steric hindrance (Table 7, entries 4 and 5).

Table 7. Reaction by unsaturated nitroalkene type



Entry	Ar	Product	Yield (%) [a]	ee (%) [b]
1	4-MeC ₆ H ₄	4a	95	88
2	4-BrC ₆ H ₄	4b	89	92
3	4-ClC ₆ H ₄	4c	83	92
4	4-MeOC ₆ H ₄	4d	85	94
5	2-MeOC ₆ H ₄	4e	76	82

[a] Isolated yields [b] The ee values were determined by chiral phase HPLC using an AD-H column

2.1.8 Reaction of acetone with α , β -unsaturated nitroalkenes

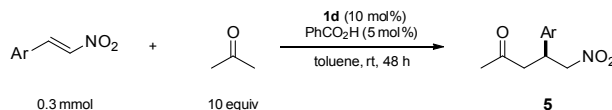
To investigate whether the addition proceeds with aliphatic ketones, reactions were carried out between acetone and various α , β -unsaturated nitroalkenes under the optimal conditions determined in previous experiments. The reactivity of acetone was lower than that of aromatic ketones; thus, 10 eq. acetone was used in the experiment (Table 8). The reaction between acetone and α , β -unsaturated nitroalkenes was found to proceed well, regardless of whether the substituent was an electron donor or electron acceptor. Contrary to the case of aromatic ketones, no general trend in enantioselectivity was observed for different substituent positions in α , β -unsaturated nitroalkenes.

2.1.9 Reaction mechanism to predicted transition state

The stereoselective Michael reaction was conducted using ketone and trans- β -nitrostyrene. The results suggest the catalytic mechanism in the reaction (Scheme 2). First, via the reaction of ketone with the acid catalyst, the reactivity of ketone would increase, leading to the formation of enamine by the reaction with the primary amine thiourea catalyst [36,37]. Double hydrogen bonding of hydrogen of

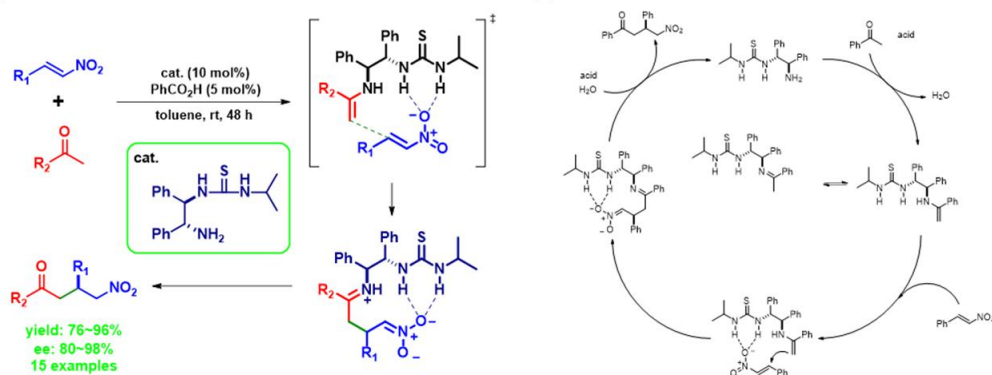
the thiourea catalyst and oxygen of α, β -unsaturated nitroalkene led to selective reactions. Enamine approached from the *si*-face of *trans*- β -nitrostyrene, leading to the *S*-selective product (Fig. 2).

Table 8. Reaction of acetone with α, β -unsaturated nitroalkenes



Entry	Ar	Product	Yield (%) [a]	ee (%) [b]
1	C ₆ H ₅	5a	88	94
2	4-MeC ₆ H ₄	5b	81	86
3	4-MeOC ₆ H ₄	5c	85	82
4	4-ClC ₆ H ₄	5d	76	86
5	2-MeOC ₆ H ₄	5e	83	94

[a] Isolated yields [b] The ee values were determined by chiral phase HPLC using an AD-H column



Scheme 2. Representative schematic of organocatalytic asymmetric Michael addition reaction

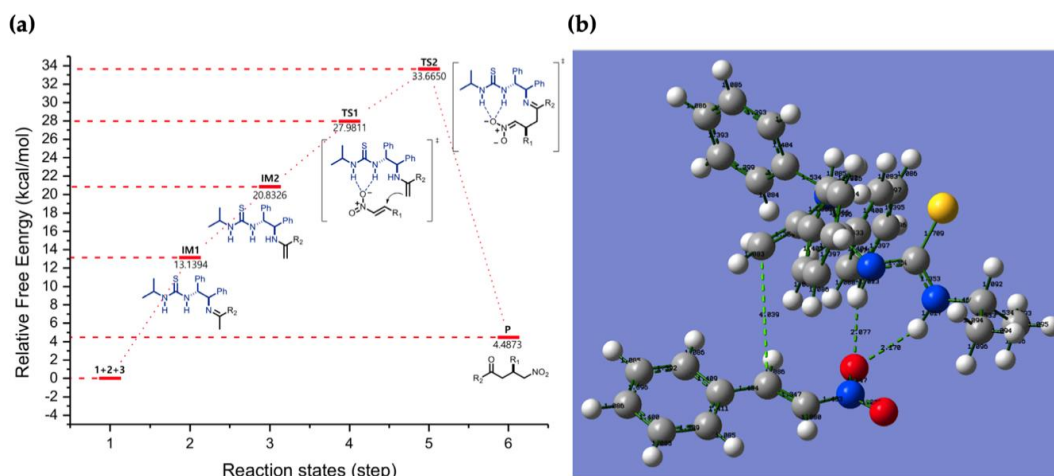


Fig. 2. (a) Proposed catalytic mechanism. B3LYP/6-31G(d,p) calculated free energy diagram of the (*R, R*)-1,2-diphenylethylenediamine(DPEN)-thiourea-catalyzed enantioselective Michael reaction. (b) B3LYP/6-31G(d,p)-calculated transition state of the DPEN-thiourea-catalyzed enantioselective Michael reaction. Transition state structures for the C-C bond formation, through which the main product (*S*) is possibly formed, are also shown

2.1.10 Synthesis of (S)-GABA derivatives and pyrrolidinone derivatives

We investigated the Michael reaction of the ketone compounds to various nitroolefins. Through oxidation and reduction of products 2a and 4c, respectively, phenibut and baclofen were formed [38]. The selective antagonist of the GABA_B receptor in phenibut inhibited the antidepressant and anti-adaptive effects. The optional GABA_B receptor agonist baclofen has previously reversed social deficits in mouse models and reduced repetitive behavior [39]. The GABA_B receptor blockage does not modify the inhibitor of ethanol ingestion induced by Hypericum perforation in rats [40,41].

3. MATERIALS AND METHODS

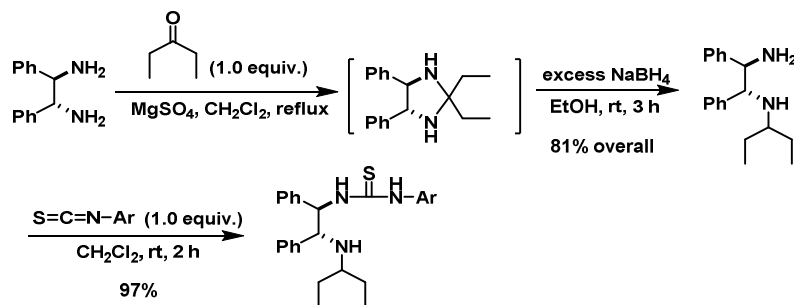
3.1 General Information

IR spectra were measured on a NICOLET 380 FT-IR spectrophotometer (Thermo Fisher Scientific Inc., Waltham, MA, USA). Optical rotations were performed with a Rudolph Automatic polarimeter (model name: A20766 APV/6w, Rudolph Research Analytical, Hackettstown, NJ, USA). ¹H, ¹³C NMR spectra were operated on a Bruker Avance 500 (500, 125 MHz, Bruker BioSpin GmbH, Silberstreifen 4, 76287 Rheinstetten, Billerica, MA, USA), Varian Mercury 400 (400, 100 MHz, Agilent, Santa Clara, CA, USA), or Varian Gemini 300 (300, 75 MHz, Agilent, Santa Clara, CA, USA) with TMS as an internal reference. Chiral HPLC analysis was measured on a Jasco LC-1500 Series HPLC system (JASCO, 4-21, Sennin-cho 2-chome, Hachioji, Tokyo 193-0835, Japan) with a UV detector. All experiments were performed in dried flasks under an argon filler. Toluene and THF were dried by chemical (CaH₂, Na, benzophenone) distillation before use. Commercial grade reagents were purchased from Aldrich (Louis, MO, USA), TCI (Tokyo, Japan) and were used without purification.

3.2 Synthesis of Catalysts (1a-n); General Procedure

3.2.1 Synthesis of monoalkylated thiourea catalysts

To a solution of (*R,R*)-1,2-diphenylethylenediamine (1.0 equiv.) in toluene (0.1 M) was added a solution of 3-pentanone (1.1 equiv.), MgSO₄ and the mixture was refluxed for 48 h. Then, MgSO₄ was removed and the mixture concentrated in vacuo. NaBH₄ (4.0 equiv.) and ethanol were added, and the mixture was stirred at ambient temperature for 1h, quenched with 1N NaOH solution and the mixture was extracted with 50 mL ethyl acetate (EA) (2 × 30 mL). The combined organic extracts were washed with brine, dried (Magnesium sulfate, anhydrous), and enriched in vacuo. The product was purified by chromatography on a silica-gel column (methanol/methylene chloride, 1:20). To monoalkylated DPEN (1.0 equiv.) in CH₂Cl₂ (0.1 M) thiourea (1.1 equiv.) was added, and the mixture was stirred at ambient temperature for 1 h and purified by flash column chromatography on silica gel with EA/hexane (hex) (1:5) to give the pure amide product (quantitative yield) as a white, foamy gel (Scheme 3).

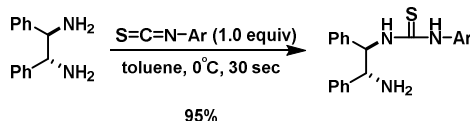


Scheme 3. Synthesis of monoalkylated thiourea catalysts

3.2.2 Synthesis of arylated thiourea catalysts

To a solution of (*R,R*)-1,2-diphenylethylenediamine (1.0 equiv.) in toluene (0.5 M) thiourea (1.0 equiv.) was added at 0°C and the mixture product was stirred for 30 s. The product was concentrated in

vacuo, the products filtered, and extracted with EA. The combined organic products were washed with brine, dried (Magnesium sulfate, anhydrous), and enriched in vacuo. They were purified by flash column chromatography on silica gel with mixed solvent (methanol/methylene chloride, 1:20) to give the pure amide product (quantitative yield) as a white foamy gel (Scheme 4).



Scheme 4. Synthesis of arylated thiourea catalysts

3.3 Synthesis of Product Compounds

3.3.1 General procedure of the asymmetric Michael addition

The *trans*- β -nitrostyrene (0.3 mmol), ketone (2.0 equiv.), and 10 mol% of cat. were added to toluene (0.1 M), 5 mol% of acid, and the reaction mixture was stirred at ambient temperature. The reaction conversion was monitored by TLC. After completion, ethyl acetate (0.2 mL) was added to the reaction product. This solution was washed twice with water (2×1.0 mL), dried over magnesium sulfate (anhydrous) and concentrated to yield the desired product. The product was purified by chromatography on a silica-gel column eluted with mixed solvent (hexanes/EA, 5:1).

3.3.2 Synthesis of (S)-Phenibut[®] and Baclofen[®]

A solution of the Michael adducts (2a or 4c) (0.10 mmol) in dry dichloromethane (1 mL) was added to a pressure vessel equipped with a stirring bar and cooled at 0°C. Then, *m*-CPBA (0.30 mmol) and TFA (0.10 mmol) were added, and the mixture product was heated at 70°C for 72 h. The crude product was washed with water and extracted with CH₂Cl₂ (2×10 mL). The organic phase was dried over anhydrous MgSO₄, enriched under reduced pressure, and purified by flash column chromatography using hexanes/ethyl acetate (8:2) to afford the desired product. Under an argon atmosphere, to the suspension of 6a or 6b (1.0 equiv.) and NiCl₂·6H₂O (1.0 equiv.) in MeOH (8.0 mL), NaBH₄ (10 equiv.) was added at 0°C. After the crude mixture was stirred for 7.5 h in ambient temperature, the crude mixture was quenched with NH₄Cl and diluted with CHCl₃. The organic layer was separated and dried over MgSO₄ (anhydrous), filtrated, and enriched in vacuo. The mixture product was purified by column chromatography on silica gel (MeOH/CHCl₃ = 1/20 as eluent) to afford the desired product (98%) as colorless powder. The powder (1.0 equiv.) in 6N HCl (2.7 mL) was refluxed at 100°C. After 12 h, the pure product was enriched in vacuo to afford (S)-(-)-Phenibut[®] (95%) and Baclofen[®] (92%) as white solids.

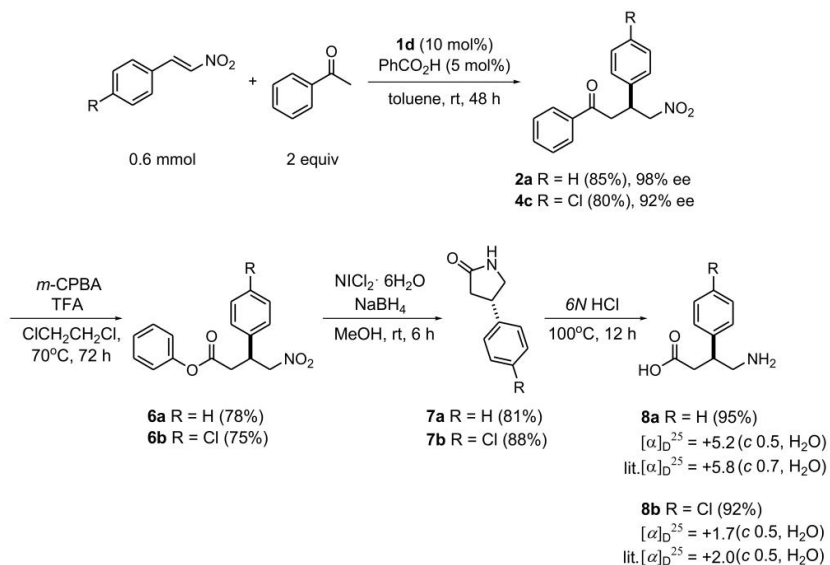
3.4 Results of DFT Calculations and Discussion

Density functional theory (DFT) calculations were performed with the Gaussian 16 and Gauss-View 6.0 programs. DFT computations were performed to show the mechanism of the substrates and catalysis. The solvation effects in toluene and the energy of the optimized geometries were accounted for by using the CPCM continuum solvation model parametrized at the B3LYP/6-31G(d,P) level. The geometries of the reactants, intermediates (IM), transition states (TS), and products were fully optimized, followed by vibrational frequency calculations at the same levels of theory to obtain the zero-point energies (ZPE) and to verify whether it is a minimum or a transition state on the potential energy surfaces (PES). The temperature-dependent enthalpy corrections and the entropy effects are computed at 298 K and 1 atm of pressure (Figure. S3).

4. CONCLUSIONS

We developed an efficient method for the organocatalytic asymmetric Michael reaction of aromatic ketones to *trans*- β -nitro compounds and obtained excellent enantioselectivity (up to 80%–90% ee).

Catalyst **1d** was found to be suitable for the simple synthesis of organocatalyst. The synthetic utility of the present catalytic asymmetric Michael addition was established by transformation to highly enantioselective products (Scheme 5). Baclofen is used as a muscle relaxant, whereas Phenibut is a sleep inducer. These substances are derivatives of γ -aminobutyric acid, which is an inhibitory neurotransmission inhibitor acting on GABA receptors and receptors in our bodies. Therefore, further investigations on their synthesis are necessary because of their high applicability in medicine.



Scheme 5. Synthesis of (S)-Baclofen, Phenibut

FUNDING

This work was supported by National Research Foundation of Korea (NRF) grant funded by the Korean government [NRF-2019R1814112], [NRF-2020R1C1C1013785].

ACKNOWLEDGEMENTS

We are grateful for the financial support provided by Dr. K. H. Kim. And thanks to Dr. Yeonsun Hong for your help.

COMPETING INTERESTS

There are no conflicts to declare. The funders had no role in the design of the study; in the collection, analyses, or interpretation of data; in the writing of the manuscript, or in the decision to publish the results.

REFERENCES

1. MacMillan DWC. The advent and development of organocatalysis. *Nature*. 2008;455:304–308.
2. Dalko PI, Moisan L. In the golden age of organocatalysis. *Angew. Chem. Int. Ed.* 2004;43:5138–5175.
3. Seayad J, List B. Asymmetric organocatalysis. *Org. Biomol. Chem.* 2005;3:719–724.
4. Berner OM, Tedeschi L, Enders D. Asymmetric Michael additions to nitroalkenes. *Eur. J. Org. Chem.* 2002;12:1877–1894.
5. Tsogoeva SB. Recent advances in asymmetric organocatalytic 1,4-conjugate additions. *Eur. J. Org. Chem.* 2007;1701–1716.
DOI: 10.1002/ejoc.200600653

6. Guo ZL, Xue JH, Fu LN, Zhang SE, Guo QX. The direct asymmetric alkylation of α -amino aldehydes with 3-indolylmethanols by enamine catalysis. *Org. Lett.* 2014;16:6472–6475.
7. Tan B, Hernández-Torres G, Barbas CF. Rationally designed amide donors for organocatalytic asymmetric Michael reactions. *Angew. Chem. Int. Ed.* 2012;51:5381–5385.
8. Curti C, Rassu G, Zambrano V, Pinna L, Pelosi G, Sartori A, Battistini L, Zanardi F, Casiraghi G. Bifunctional cinchona alkaloid/thiourea catalyzes direct and enantioselective vinylogous Michael addition of 3-alkylidene oxindoles to nitroolefins. *Angew. Chem. Int. Ed.* 2012;51:6200–6204.
9. Yan XY, Huang X, Gou S, Huang J, Wen Y, Feng X. Enantioselective cyanosilylation of ketones catalyzed by a nitrogen-containing bifunctional catalyst. *Adv. Synth. Catal.* 2006;348:538–544.
10. Kwiatkowski P, Dudzinski K, Łyżwa D. Effect of high pressure on the organocatalytic asymmetric Michael reaction: Highly enantioselective synthesis of γ -nitroketones with quaternary stereogenic centers. *Org. Lett.* 2011;13:3624–3627.
11. Gu Q, You SL. Desymmetrization of cyclohexadienones via cinchonine derived thiourea-catalyzed enantioselective aza-Michael reaction and total synthesis of (-)-Mesembrine. *Chem. Sci.* 2011;2:1519–1522.
12. Corey EJ, Zhang FY. Enantioselective Michael addition of nitromethane to α , β -Enones catalyzed by chiral quaternary ammonium salts. A Simple Synthesis of (R)-Baclofen. *Org. Lett.* 2000;2:4257–4259.
13. Perlmutter P. Conjugate addition reactions in organic synthesis; 1992.
14. Mohapatra S, Baral N, Mishra NP, Panda P, Nayak S. Michael addition of imidazole to α , β -unsaturated carbonyl/cyano compound. *Open Chemistry Journal.* 2018;5(1).
15. Sigman MS, Jacobsen EN. Schiff base catalysts for the asymmetric Strecker reaction identified and optimized from parallel synthetic libraries. *J. Am. Chem. Soc.* 1998;120:4901–4902.
16. Hiemstra H, Wynberg H. Addition of aromatic thiols to conjugated cycloalkenones, catalyzed by chiral. beta.-hydroxy amines. A mechanistic study of homogeneous catalytic asymmetric synthesis. *J. Am. Chem. Soc.* 1981;103:417–430.
17. Dolling UH, Davis P, Grabowski EJ. Efficient catalytic asymmetric alkylations. 1. Enantioselective synthesis of (+)-indacrinone via chiral phase-transfer catalysis. *J. Am. Chem. Soc.* 1984;106:446–447.
18. Oku JI, Inoue S. Asymmetric cyanohydrin synthesis catalysed by a synthetic cyclic dipeptide. *J. Chem. Soc. Chem. Commun.* 1981;229–230.
DOI: 10.1039/C39810000229
19. McGilvra JD, Unni AK, Modi K, Rawal VH. Highly diastereo- and enantioselective Mukaiyama aldol reactions catalyzed by hydrogen bonding. *Angew. Chem. Int. Ed.* 2006;45:6130–6133.
20. Huang Y, Unni AK, Thadani AN, Rawal VH. Single enantiomers from a chiral-alcohol catalyst. *Nature.* 2003;424:146.
21. Akiyama T, Itoh J, Yokota K, Fuchibe K. Enantioselective Mannich-type reaction catalyzed by a chiral Brønsted acid. *Angew. Chem. Int. Ed.* 2004;43:1566–1568.
22. Uraguchi D, Terada M. Chiral Brønsted acid-catalyzed direct Mannich reactions via electrophilic activation. *J. Am. Chem. Soc.* 2004;126:5356–5357.
23. Doyle AG, Jacobsen EN. Small-molecule H-bond donors in asymmetric catalysis. *Chem. Rev.* 2007;107:5713–5743.
24. Huang H, Jacobsen EN. Highly enantioselective direct conjugate addition of ketones to nitroalkenes promoted by a chiral primary amine–thiourea catalyst. *J. Am. Chem. Soc.* 2006;128:7170–7171.
25. Liu K, Cui HF, Nie J, Dong KY, Li XJ, Ma JA. Highly enantioselective Michael addition of aromatic ketones to nitroolefins promoted by chiral bifunctional primary amine-thiourea catalysts based on saccharides. *Org. Lett.* 2007;9:923–925.
26. Cardillo G, Tomasini C. Asymmetric synthesis of β -amino acids and α -substituted β -amino acids. *Chem Soc Rev.* 1996;25:117–28.
27. Seebach D, Matthews JL. β -Peptides: A surprise at every turn. *Chem Commun (Camb).* 1997;2015–22.
28. Li W, Li X, Wu W, Liang X, Ye J. Highly diastereo- and enantioselective one-pot Michael-Aldol reactions of α,β -unsaturated aldehydes with imidazole derivatives. *Chem Commun (Camb).* 2011;47(29):8325–7.

29. Tang Z, Jiang F, Cui X, Gong LZ, Mi AQ, Jiang YZ, Wu YD. *Proc. Natl. Acad. Sci. USA.* 2004;101:5755.
30. Du J, Li Z, Du DM, Xu J. Improving enantioselectivity via rationally tuning electronic effects of catalysts in the organocatalytic asymmetric aldol reaction. *ARKIVOC.* 2008;17:145-156.
31. Lao JH, Zhang XJ, Wang JJ, Li XM, Yan M, Luo HB. The effect of hydrogen bond donors in asymmetric organocatalytic conjugate additions. *Tetrahedron Asymmetry.* 2009;20:2818–2822.
32. Chen JR, Lu HH, Li XY, Cheng L, Wan J, Xiao W. Readily tunable and bifunctional l-prolinamide derivatives: Design and application in the direct enantioselective aldol reactions. *Org. Lett.* 2005;7:4543–4545.
33. Pansare SV, Kirby RL. Secondary–secondary diamine catalysts for the enantioselective Michael addition of cyclic ketones to nitroalkenes. *Tetrahedron.* 2009;65:4557–4561.
34. Sun ZW, Peng FZ, Li ZQ, Zou LW, Zhang SX, Li X, Shao ZH. Enantioselective conjugate addition of both aromatic ketones and acetone to nitroolefins catalyzed by chiral primary amines bearing multiple hydrogen-bonding donors. *J. Org. Chem.* 2012;77:4103–4110.
35. Tsakos M, Kokotos CG, Kokotos G. Primary amine-thioureas with improved catalytic properties for “difficult” Michael reactions: Efficient organocatalytic syntheses of (S)-Baclofen, (R)-Baclofen and (S)-Phenibut. *Adv. Synth. Catal.* 2012;354:740–746.
36. Yalalov DA, Tsogoeva SB, Schmatz S. Chiral thiourea-based bifunctional organocatalysts in the asymmetric nitro-Michael addition: A joint experimental-theoretical study. *Adv. Synth. Catal.* 2006;348:826–832.
37. Li BL, Wang YF, Luo SP, Zhong AG, Li ZB, Du XH, Xu DQ. Enantioselective Michael addition of aromatic ketones to nitroolefins catalyzed by bifunctional thioureas and mechanistic insight. *Eur. J. Org. Chem.* 2010;656–662.
38. Felluga F, Gombac V, Pitacco G, Valentin E. A short and convenient chemoenzymatic synthesis of both enantiomers of 3-phenylGABA and 3-(4-chlorophenyl) GABA (Baclofen). *Tetrahedron Asymmetry.* 2005;16:1341–1345.
39. Dambrova M, Zvejniece L, Liepinsh E, Cirule H, Zharkova O, Veinberg G, Kalvinsh I. Comparative pharmacological activity of optical isomers of phenibut. *Eur. J. Pharmacol.* 2008;583:128–134.
40. Perfumi M, Santoni M, Ciccocioppo R, Massi M. Blockade of γ -aminobutyric acid receptors does not modify the inhibition of ethanol intake induced by *Hypericum perforatum* in rats. *Alcohol.* 2002;37:540–546.
41. Bowery NG. GABAB receptor pharmacology. *Annu. Rev. Pharmacol. Toxicol.* 1993;33:109–147.

Biography of author(s)



Jae Ho Shim

Department of Chemistry, Research Institute for Natural Sciences, Korea University, 145 Anam-ro Seongbuk-gu, Seoul 02841, Korea;

Research and Academic Experience:

Organic, Catalysis, Drugs, DFT

Education

B.S. in Chemistry, Dae Jin University, Gyeonggi, Korea
(Mar. 2006. – Feb. 2010.) Chemistry Research Advisor: Prof. Man So Han
M.S. in Organic Chemistry, Dae Jin University, Gyeonggi, Korea
(Mar. 2010. – Feb. 2012.) Chemistry Research Advisor: Prof. Man So Han
M.S./Ph.D. in Organic Chemistry, Korea University, Seoul, Korea
(Aug. 2014. - Feb. 2020.) Chemistry Research Advisor: Prof. Deok-Chan Ha

Careers

Chemistry Research Engineer
(Display Research Center of LMS Corp. , Dec. 2011. – Jul. 2014.)
(Korea University Research Institute for Natural Sciences, Jul. 2017. – Feb. 2018.)
Instructor of Korea University
(Korea University Research Institute for Natural Sciences, Sep. 2019. – Current.)
CEO & Research director
(ABM Corp. , Dec. 2019. – Current.)

Research Area: Designing organic molecules for organocatalysis for reactions like asymmetric aldol, nitroso-aldol, Michael addition, cycloaddition, anhydride desymmetrization to provide chiral molecules and the use of the products to the synthesis of biologically important small natural products.

Number of Published papers: 3

Special Award (If any):

1. 2014 Graduate Students' Award for Excellence in Creative Studies and Project Support (Korea University)
2. Win the 2018 Business Idea Contest for University Students in Biotechnology (Korea Institute for Science and Technology Job Promotion)
3. Winner of 2019 the 4th Korea University Campestown Startup Competition (Seoul Metropolitan Government, Korea University)
4. 2019 BIO Start-up Idea Award Winner for Creative Design Competition (Korea Health Industry Development Institute)
5. 2019 Award-winning BIO field for excellence patent in Korea (Korea Institute of Patent Information, Korea Intellectual property strategy Agency)
6. 2020 Innovation Korean & POWER KOREA Grand Prize(Korea newspaper press)



Deok-Chan Ha

Department of Chemistry, Research Institute for Natural Sciences, Korea University, 145 Anam-ro Seongbuk-gu, Seoul 02841, Korea;

Research and Academic Experience:

Organic, Catalysis Education

- 1982 - 1986 : Ohio State University, Ph. D., Chemistry Research Advisor: Prof. David J. Hart
- 1980 - 1982 : Korea University, M. S., Organic Chemistry
- 1976 - 1980 : Korea University, B. S., Chemistry

Careers

- 1999.3 - present : Professor at Korea University
 - 1994.3 - 1999.2 : Associate Professor at Korea University
 - 1992.3 - 1994.2 : Assistant Professor at Korea University
 - 1989.3 - 1992.2 : Senior Research Scientist, Korea Research Institute of Chemical Technology
- 1987.1-1989.2 : Postdoctoral Research Associate at Harvard University, Chemistry Department (with Prof. Elias J. Corey)

Research Area: Designing organic molecules for organocatalysis for reactions like asymmetric aldol, nitroso-aldol, Michael addition, cycloaddition, anhydride desymmetrization to provide chiral molecules and the use of the products to the synthesis of biologically important small natural products.

Number of Published papers: 57

© Copyright (2020): Author(s). The licensee is the publisher (Book Publisher International).

DISCLAIMER

This chapter is an extended version of the article published by the same author(s) in the following journal. Catalysts, 10(618): 1-11, 2020.

SUPPLEMENTARY MATERIALS

The following are available online at www.mdpi.com/xxx/s1. Figure S1: Compound Characterization Data, Figure S2: Copy of HPLC Chromatograms, Figure S3: Computational Results of DFT Calculations for all Calculated Structures.

Available Here: http://sdiarticle4.com/prh/doc/Supplementary_File.pdf

High Photocatalytic Activity of the TiO₂/ZnO Mesoporous Composites Obtained by Solution Combustion Method

A. Luna-Flores^{1*}, I. Niño-Flores¹, M. A. Morales¹, A. D. Hernández-de la Luz², J. A. Luna-López², R. Portillo³, D. Cruz-González¹, R. Agustín-Serrano⁴ and M. P. Sampedro¹

DOI: 10.9734/bpi/cpcs/v2

ABSTRACT

In this work, the high photocatalytic activity of the TiO₂/ZnO mesoporous composites for the degradation of Methylene Blue and Rhodamine B dyes is reported. The composites were obtained by the solution combustion method at different ZnO/TiO₂ ratios in short synthesis times. X-Ray diffraction shows TiO₂ in the anatase phase and a hexagonal wurtzite structure for ZnO. According to these results, when the incorporation of ZnO into TiO₂ exceeds 32%, the zinc excess promotes the formation of zinc titanate. The UV-vis spectra for the composite show an absorption in the visible region associated with oxygen vacancies and carbon incorporated into the ZnO during the combustion process. The EDS analysis shows a carbon incorporation of up to 3.47%. When the photocatalytic process is carried out with UV-vis radiation, the photocatalytic activity improved by up to 20% compared to that obtained when used UV radiation only. The highest photocatalytic activity is presented by the semiconductor composite whose ZnO content is 32.1%. The improvement in photocatalytic activity is associated with a larger surface area and a better pore size distribution.

Keywords: Combustion solution method; composite; photocatalysis; mesoporosity.

1. INTRODUCTION

One of the best alternatives for the elimination of organic compounds in wastewater is heterogeneous photocatalysis, which uses oxidation-reduction reactions for the degradation of these compounds [1,2]. The materials most used as photocatalysts are semiconductor oxides, which, by irradiating them with electromagnetic energy, equal to or greater than their bandgap energy, generate electron-hole pairs. The photo-generated electron migrates and reaches the surface of the photocatalyst and it reacts with the adsorbed oxygen to produce highly reactive superoxide radicals (O₂^{•-}). Similarly, the photo-generated hole reacts at the surface of the photocatalyst with water adsorbed to produce hydroxyl radicals (•OH) [3]. These radicals are responsible for oxidation-reduction reactions that result in the complete degradation of the organic compounds [4].

TiO₂ and ZnO are the most used materials in the studies of photocatalytic degradation processes due to their high photosensitivity (in the UV range), very low toxicity, high chemical and mechanical

¹Facultad de Ingeniería Química, Benemérita Universidad Autónoma de Puebla, Av. San Claudio y 18 sur, Ciudad Universitaria, C.P. 72570, Puebla, Pue. México.

²Centro de Investigación en Dispositivos Semiconductores, Instituto de Ciencias (CIDS-ICUAP), Benemérita Universidad Autónoma de Puebla, Col. Jardines de San Manuel, Av. San Claudio y 14 Sur, Cd. Universitaria, Edificios IC-5 y IC-6. Puebla, Pue., 72570 México.

³Facultad de Ciencias Químicas, Benemérita Universidad Autónoma de Puebla, Av. San Claudio y 18 sur Ciudad Universitaria, C.P. 72570, Puebla, Pue. México.

⁴Facultad de Ciencias Físico Matemáticas, Benemérita Universidad Autónoma de Puebla, Av. San Claudio y 18 sur Ciudad Universitaria, C.P. 72570, Puebla, Pue. México.

*Corresponding author: E-mail: adan.luna@correo.buap.mx;

stability, high availability, and low cost. Because these materials have a bandgap energy of the order of 3.2-3.37 eV, their use with sunlight is limited since in the solar electromagnetic radiation only 4-5% is UV light, so the modification or adjustment of their bandgap energy becomes essential in order to the absorption range becomes wider which includes the visible region. In general, two methods are considered to modify the absorption range of the photocatalysts towards the visible region: impurification within the crystalline lattice (doping process) and surface sensitization [5,6]. In relation to the surface modification, the formation of composites by semiconductor materials can be considered. The formation of this composite can modify the transfer of charger-carriers of the materials due to the interfacial interactions, as a result, they are able to present a better performance in their photocatalytic activity because of an increase in the lifetime of charger carriers (due to a screening in the recombination process) [5,7]. For this reason, the synthesis of the composites is an interesting field to investigate the interrelationship between the charger-carriers transport at their interface and their photocatalytic activity [8].

Due to the position of the discontinuity of the energy edges of the valence and conduction bands of TiO₂ and ZnO when they are joined this semiconductor composite form a band diagram corresponding to a type II heterostructure [9,10]. Therefore, they provide an attractive possibility to achieve a more efficient charge carriers separation increasing their timelife and improving the efficiency of the charge transfer at the interface [11,12].

The TiO₂/ZnO is a TiO₂-based composite which has been synthesized by techniques such as hydrothermal [13-15], electrospinning [16], atomic layer deposition [17] and sol-gel [18-24], electrochemical and chemical bath [25]. In these works, different amounts of ZnO into TiO₂ were incorporated with synthesis times ranging from 3 to 24 h. The TiO₂/ZnO has shown a decrease in the process of recombination of electron-hole pairs due to the rapid transfer of electrons from the ZnO conduction band to the TiO₂ one and the transfer of holes from the TiO₂ valence band to the ZnO one [17,26]. This composite has shown properties such as degradation of organic compounds [13,18,27,28], antibacterial, gas sensor [29], cytocompatibility [30], H₂ production [26], biodiesel synthesis [31], and piezoelectricity [32].

In this work, we present the synthesis of the TiO₂/ZnO composite by the solution combustion method, which is a simple method with short synthesis times. The semiconductor composite has enhanced the photocatalytic activity in the degradation of dyes such as Methylene Blue and Rhodamine B, compared to the individual materials. In addition, the composite shows an improvement when it is irradiated with visible light.

2. MATERIALS AND METHODS

2.1 Synthesis of TiO₂/ZnO Composite

All reagents were used without any additional purification. The synthesis of the TiO₂/ZnO composite is carried out by the solution combustion method. In a typical procedure: 5 mL of deionized water and 500 mg of titanium dioxide (TiO₂, JT Baker) are added in a beaker. This mixture is dispersed by stirring and once the TiO₂ has been dispersed a corresponding amount of zinc nitrate hexahydrate (Zn(NO₃)₂·6H₂O, ALYT) is added to obtain the weight ratio Zn(NO₃)₂/TiO₂ of 0.5, 1, 1.5 and 2. Then 1.0 g of urea (CO(NH₂)₂, JT Baker) is added and placed under stirring for 5 min. Subsequently, the suspension is heated at 80°C to evaporate the maximum amount of water. Finally, the resulting paste is heat-treated in a preheated muffle at 600°C for 15 min, the material obtained is the photocatalyst. The material obtained is labeled as TZO-01, 02, 03 and 04, for the weight ratios 0.5, 1.0, 1.5 and 2.0, respectively. For comparison purposes, a sample of Urea-TiO₂ (UTiO₂) and a sample of Urea-Zn(NO₃)₂·6H₂O (UZnO) was synthesized.

2.2 Characterization and Analytical Techniques

X-Ray Diffraction (XRD) analysis was performed using a Bruker X-ray Diffraction D6-Discover equipment with Cu-K α radiation at a scan rate of 0.02° s⁻¹. The FTIR spectra were obtained using a Perkin Elmer Spectrum One spectrophotometer equipped with an ATR accessory. The SEM

micrographs were obtained with a JSM-6610LV JEOL electron microscope. The isotherms were used to calculate the Brunauer–Emmett–Teller (BET) specific surface area (S_{BET}) and the pore size distribution. The isotherm curve using an Autosorb 1C Quantachrome equipped with a Verlab VE-5600UV photometer and MetaSpec Pro analysis software. Diffuse Reflectance Spectroscopy (DRS) using a Varian Cary 400 spectrophotometer with a Harrick RD accessory was used for the optical characterization of the samples. The dye degradation was monitoring by GENESYS 10S UV-visible spectrophotometer (Thermo Scientific).

2.3 Degradation Tests

In this work, degradation tests of the dyes were carried out: Methylene Blue, and Rhodamine B. For each test, 60 mL of a 5 ppm solution of the dye with a 15 mg of photocatalyst is used. Once the photocatalyst is added to the dye, the solution is placed in an ultrasonic bath for better dispersion. The suspension is placed in the photo-reactor with a bubbling system using air and maintained in dark conditions for 15 min so that the adsorption-desorption equilibrium is established. Next, the suspension is subjected to radiation with ultraviolet light, using a commercial UV-lamp OSRAM (20 W), with a radiation wavelength in a range of 365-465 nm. For the case of UV-vis radiation, the UV lamp was combined with a LED lamp (OSRAM, 10W), which provides the visible radiation in a wavelength range of 450-850 nm. Degradation monitoring is carried out by UV-vis spectroscopy taking aliquots at regular intervals of time.

3. RESULTS AND DISCUSSION

3.1 FTIR Analysis

The FTIR spectra of the synthesized samples are shown in Fig. 1. The peaks around 600 and 850 cm^{-1} are associated with the symmetrical stretch vibration of the Ti-O-Ti and the vibration mode of the Zn-O-Ti groups, respectively [33]. It can be seen that as the concentration of ZnO increases in the samples, the intensity of the peak at 600 cm^{-1} increases and, on the contrary, the intensity of the peak at 850 cm^{-1} decreases because the Zn-O bonds predominate. The weaker peak located at 1033 cm^{-1} is attributed to the C–O–C symmetrical stretching vibrations [34]. The band around 3000 cm^{-1} is associated with stretching vibrations in the OH bonds, another around 2322 cm^{-1} is associated with atmospheric CO₂ [35].

3.2 XRD analysis

The x-ray diffractograms for the materials obtained are shown in Fig. 2. This figure shows the sample UTiO₂ in anatase phase (PDF 00-021-1272), with characteristic peaks located at $2\theta = 25^\circ, 38^\circ, 48.1^\circ, 54^\circ, 55^\circ, 62^\circ$ and 75° . The samples identified as UZO also show peaks located at $2\theta = 31.7^\circ, 34^\circ$ and 36° corresponding to the ZnO in hexagonal phase (PDF 04-020-0364), the intensity of the peaks increases in correspondence with the increase in the amount of Zn(NO₃)₂·6H₂O used in the synthesis of the composite. In the case of the diffractogram of the TZO-04 sample, it can be seen the appearance of peaks at $2\theta = 29.86^\circ, 36.79^\circ, 53.01^\circ$ and 62.03° corresponding to the zinc titanate (Zn₂TiO₄, PDF 00-025-1164). The percentage of ZnO in the composite is 10.3%, 18.6%, 32.1% and 27.1% for TZO-01, TZO-02, TZO-03, and TZO-04, respectively. It should also be considered that in the TZO-04 sample 18.7% corresponds to the zinc titanate in a cubic spinel structure (Zn₂TiO₄), its formation is in accordance with that reported by Chau et al. [36].

3.3 SEM Analysis

Fig. 3 shows the SEM images of the synthesized composites. The incorporation of ZnO into TiO₂ modifies the size and morphology of the particles. Thus, for example, in the sample TZO-01 (lowest concentration of ZnO) spheroidal particles of 0.1 μm can be seen, and for the sample TZO-04 the morphology shows clusters with average sizes of about 0.4 μm . Synthesized ZnO (UZnO), on the other hand, has the sheet shape with approximately 3 μm wide. According to EDS analysis (Table 1) for the samples as-synthesized, zinc content values are 8.95, 16.85, 24.57 and 27.09 %wt for TZO-01, TZO-02, TZO-03, and TZO-04, respectively.

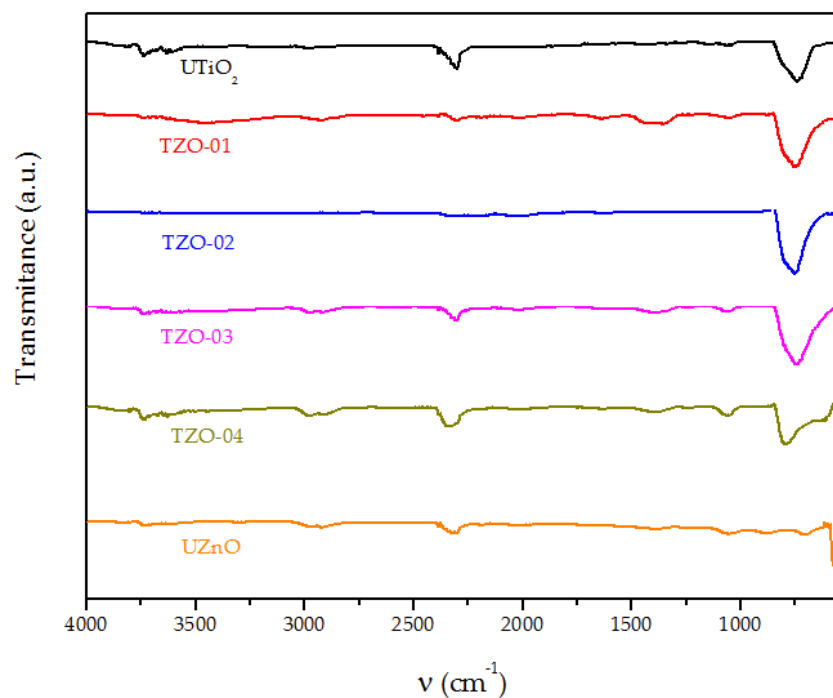


Fig. 1. FTIR spectra as-synthesized TZO- composites

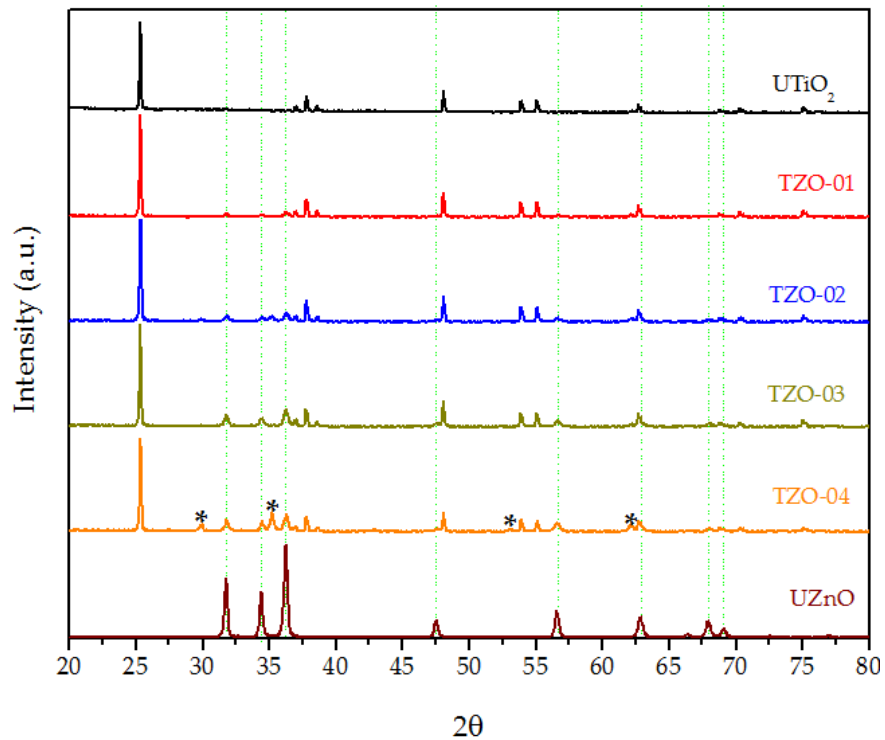


Fig. 2. DRX diffractograms of the as-synthesized composites showing the presence of TiO₂, ZnO and Zn₂TiO₄ (*)

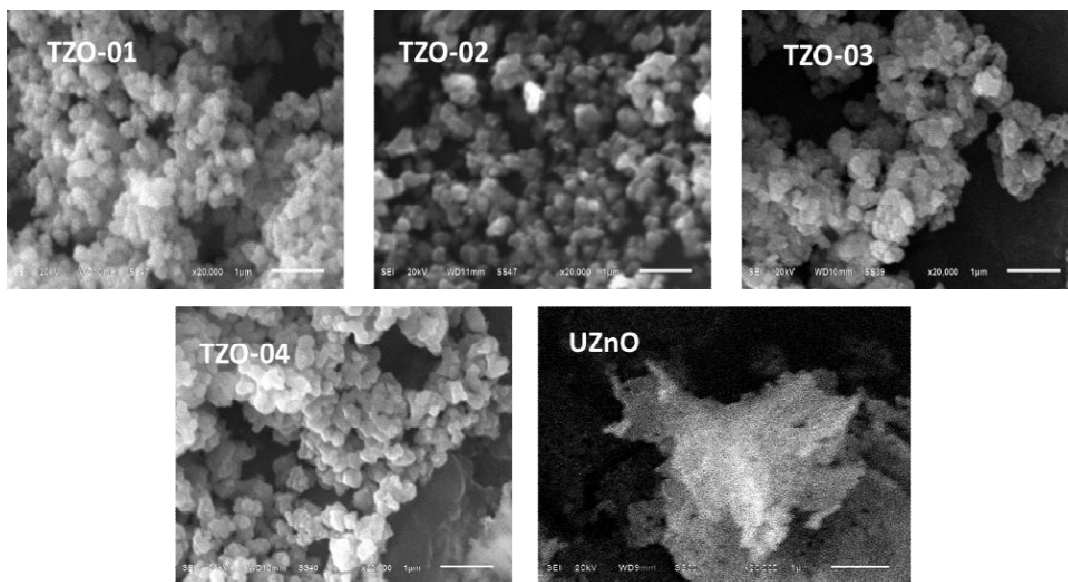


Fig. 3. SEM image of the TZO samples obtained at different amounts of Zn(NO₃)₂·6H₂O (scale-bar correspond to 1 μm)

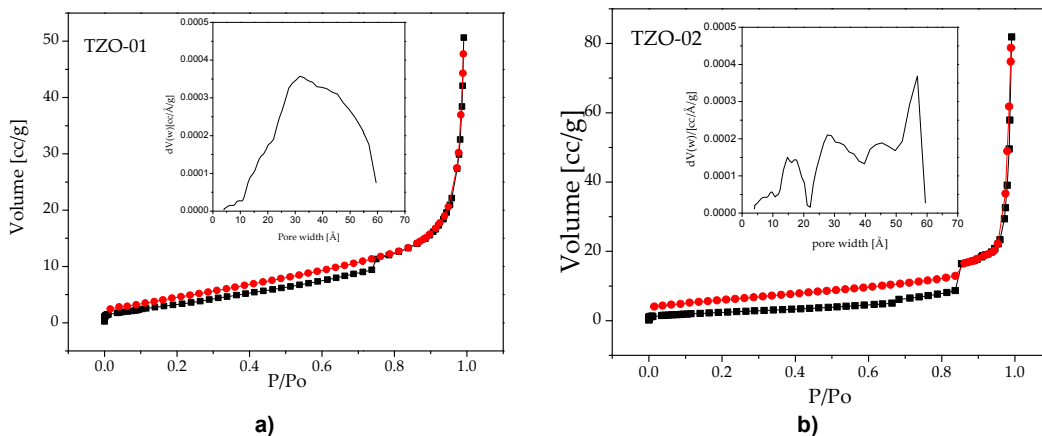
Table 1. EDS analysis for the as-synthesized composites (% wt)

Materials	Zn	Ti	O	C	I
TZO-01	8.95	47.86	41.82	1.22	0.15
TZO-02	16.85	41.07	38.61	3.47	0.0
TZO-03	24.57	37.86	36.14	1.13	0.3
TZO-04	27.09	35.09	34.42	3.40	0.0
UZnO	83.28	--	16.72	--	--

I: impurities

3.4 Surface Area Analysis

The nitrogen adsorption data on materials TZO-01, TZO-02, TZO-03 and TZO-04, provided important evidence that correlates scanning electron microscopy (SEM). The Type II adsorption isotherms (according to IUPAC) presented in Fig. 4 for the materials studied show three notable features related to the texture and morphology of the synthesized composites.



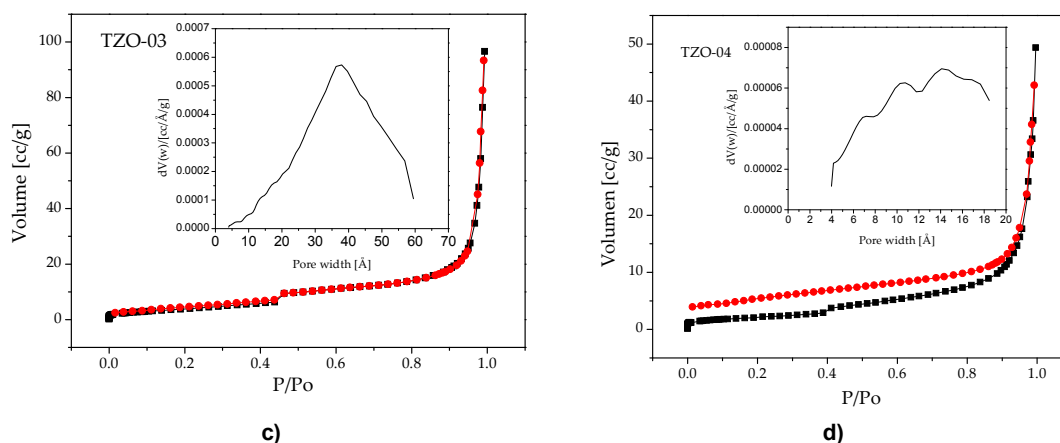


Fig. 4. Nitrogen adsorption isotherms of synthesized TZO composites: a) TZO-01, b) TZO-02, c) TZO-03, d) TZO-04. The inset figures correspond to the pore size distribution

The isotherms exhibit such a small knee in such a way that they strongly resemble to Type III isotherms. This suggests materials with specific surface and poorly developed porous systems, as well as a very weak interaction between their surfaces and N₂, since high pressure is required for significant adsorption to occur. The graphs of the DFT methodology show a small, but well-defined family of micropores (inset Figures). The BET specific surface of TZO-3 shows unusual increase compared with other composites. This increase is due to that, unlike the other composites, TZO-03 has more defined and better distribution of micropores, in addition to the fact that the total pore volume is much higher than the other photocatalyst (Table 2). Also, considering the results of the SEM analysis, it can be inferred that the porosity exhibited by the materials is not inherent in the structure of solid particles, but is determined by interconnected interstitial spaces formed among agglomerates (rather than aggregates) of primary spheroidal particles and, then among larger secondary particles, which can be reflected in reduced surface areas; SEM analysis confirms the presence of large particles and large and heterogeneous interstitial spaces. Table 2 shows the values of the textural properties of the studied composites, which were calculated using standard BET and BJH models.

Table 2. Textural properties of TZO composites

Materials	S _{BET} ^a (m ² /g)	V _T ^b (cc/g)	D _P ^c (Å)	D _{BJH} ^d (Å)
TiO ₂ ¹	50.46 ^{&}	-	-	-
TZO-01	13.5	0.07	192	32
TZO-02	9.3	0.09	384	141
TZO-3	13.6	0.12	348	36
TZO-4	7.8	0.05	267	36
ZnO ²	20.804 ^{&}	0.0546	-	-

^a BET surface; ^b Total pore volume; ^c Average pore diameter; ^d BJH Pore diameter. ¹[Ref 2]. ²[Ref 37]

The results in Table 2 confirm reduced surface areas, very small total pore volumes and large average pore size diameters but in the meso region. In general, as can be seen in the micrographs, the pore size distributions seem to depend on the degree of agglomeration of the primary particles and on the combustion temperature, rather than the semiconductor phase load ZnO (see inset of each isotherm of Fig. 4). This behavior as has been reported in an analogous case by Prasannalakshmi et al. [24]. From the Table 2, it is observed that an increase in ZnO content improves the pore size distributions of the TiO₂/ZnO composites, while the total pore volume decreases, to exception of sample TZO-03 that has the highest value as well as the largest surface area.

Another feature of the adsorption isotherms is that they appear to show two types of physisorption, evidenced by the appearance of a small step of adsorption that is not associated with capillary

nitrogen condensation. The first may be occurring on the main crystalline phase of TiO₂ and the second on a supported phase of nanocrystalline ZnO, as the pressure increases. The shape of the desorption isotherms confirms this idea, since the practically monotonous decrease in the amount of N₂ adsorbed with the pressure reduction does not show any rapid evacuation of condensate by evaporation from mesopores. Therefore, the non-reversibility of adsorption-desorption isotherms reveals a third trait that is not associated with the filling and emptying of mesoporosity. Except for the case of TZO-03 material, the amount of nitrogen retained by the rest of the materials, even at very low pressures, does not correspond to adsorbed nitrogen, but to nitrogen that most likely was incorporated into the structure of the phases or interfaces between aggregate primary particles.

Therefore, the TiO₂/ZnO composites synthesized by combustion method has an interstitial mesoporous composite. The spheroidal particles of the pseudo-sphere morphology composed of the agglomerates of ZnO nanocrystalline phase, which depends on the amount of ZnO formed during the synthesis as the precursor increases. The pore size distribution with spatial uniformity (TZO-01 and TZO-03) is the one that provides more favorable active sites in the process of adsorption and photocatalytic reaction, as can be seen in Table 3 and as will be shown in the next section.

3.5 UV-vis Analysis

Fig. 5 shows the UV-vis absorption spectra of the samples obtained. The UZnO photocatalyst show an absorption band in visible region, according to the EDS analysis, this material only contains Zn and O, so this absorption is associated to the oxygen vacancies according to the reported in the literature [38,39]. The absorption band around 500 nm exhibited by the composites may also be due to the incorporation of carbon from the fuel urea during the combustion process [40-42] as the EDS analysis shows in Table 1. The absorption in the visible range of TZO samples is associated with the incorporation of carbon into the crystalline ZnO lattice during its formation. Table 3 shows the values of the bandgap energy of each sample, where it is shown that as the amount of ZnO increases to the composite, the bandgap energy tends to the value of the synthesized ZnO.

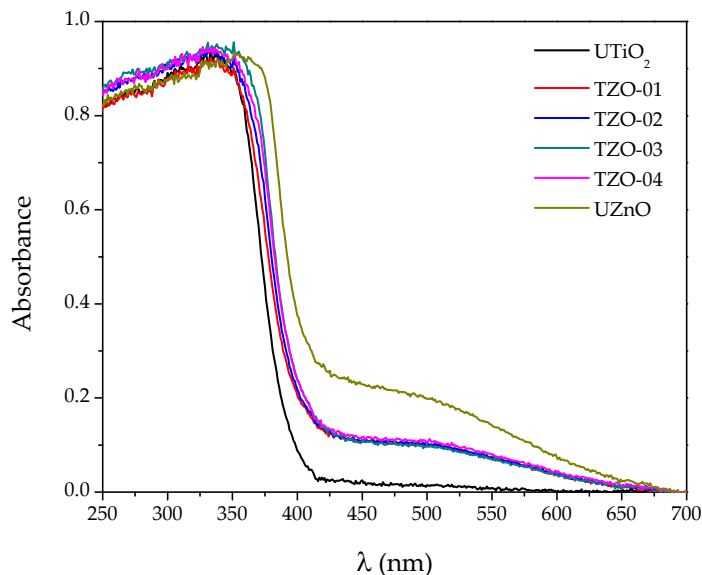


Fig. 5. UV-vis absorption spectra for the TZO composites synthesized

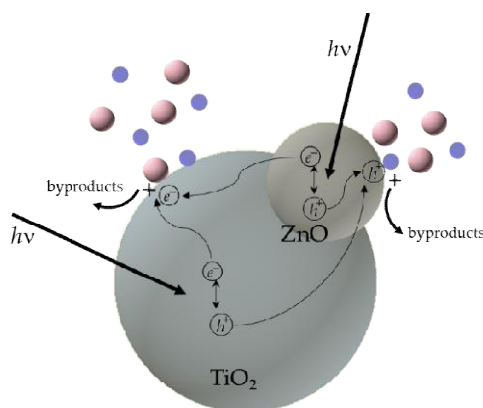
3.6 Photocatalytic Activity Analysis

The photocatalytic activity with UV irradiation for the TZO composites is analyzed from the adsorption-desorption process of the dye on the surface of the photocatalyst (Scheme 1). Once this equilibrium is reached, the photocatalytic process is carried out with UV irradiation for 90 min for the different dyes.

Table 3. Relevant characteristics of synthesized photocatalysts

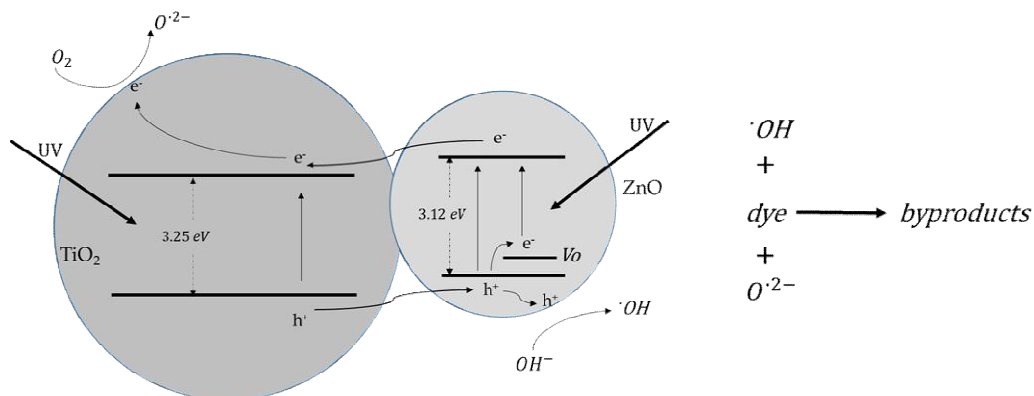
		UTiO ₂	TZO-01	TZO-02	TZO-03	TZO-04	UZnO
E _g (eV)		3.25	3.19	3.18	3.18	3.18	3.12
Methylene Blue	Ads ^e (%)	30.12	25.391	20.526	25.974	48.607	36.89
	Deg ^f (%)	72.80	87.8	92.9	89	72.1	78
	TR ^h (%)	81.00	91	94.3	91.9	85.7	86.1
	k ^g (mg/L min) ⁻¹	0.0517	0.12754	0.15559	0.11084	0.04691	0.05598
	R	0.88743	0.96725	0.96898	0.98635	0.96522	0.97236
Rodamina B	Ads (%)	22.80	14.7	11.7	11.9	20.1	13.3
	Deg (%)	85.50	88.7	68.2	85.5	84	53.5
	TR (%)	88.80	90.3	71.9	87.2	87.2	59.7
	k (min) ⁻¹	0.0222	0.02323	0.01118	0.0228	0.02081	0.00891
	R	0.99589	0.9947	0.95586	0.99681	0.99748	0.98783

^e Adsorption, ^f Degradation, ^g Kinetic constant, ^h Total Remotion. R: Correlation coefficient



Scheme 1. Photocatalytic degradation process of dyes on the surface of TZO semiconductor composites

The degradation mechanism is illustrated by Fa-tang Li et al. [43] where electrons in the conduction band are initially trapped by molecular oxygen to form O^{·2-} and the holes in the valence band are trapped by [·]OH of dissociation of water. These highly reactive radicals react with the dye to degrade it (Scheme 2).



Scheme 2. Possible mechanism of dye degradation under UV irradiation using the synthesized photocatalysts (Vo, oxygen vacancies)

Fig. 6 shows the UV-vis normalized absorption characteristic spectra of the monitoring of the degradation process. In Fig. 6a, b the degradation of methylene blue is compared by using UV and UV-vis radiation. As can be seen in these figures neither absorption spectrum undergoes a shift in the wavelength of the peak of maximum absorption (664 nm), which indicates that the degradation process is due only to the cleavage mechanism of the molecule [44].

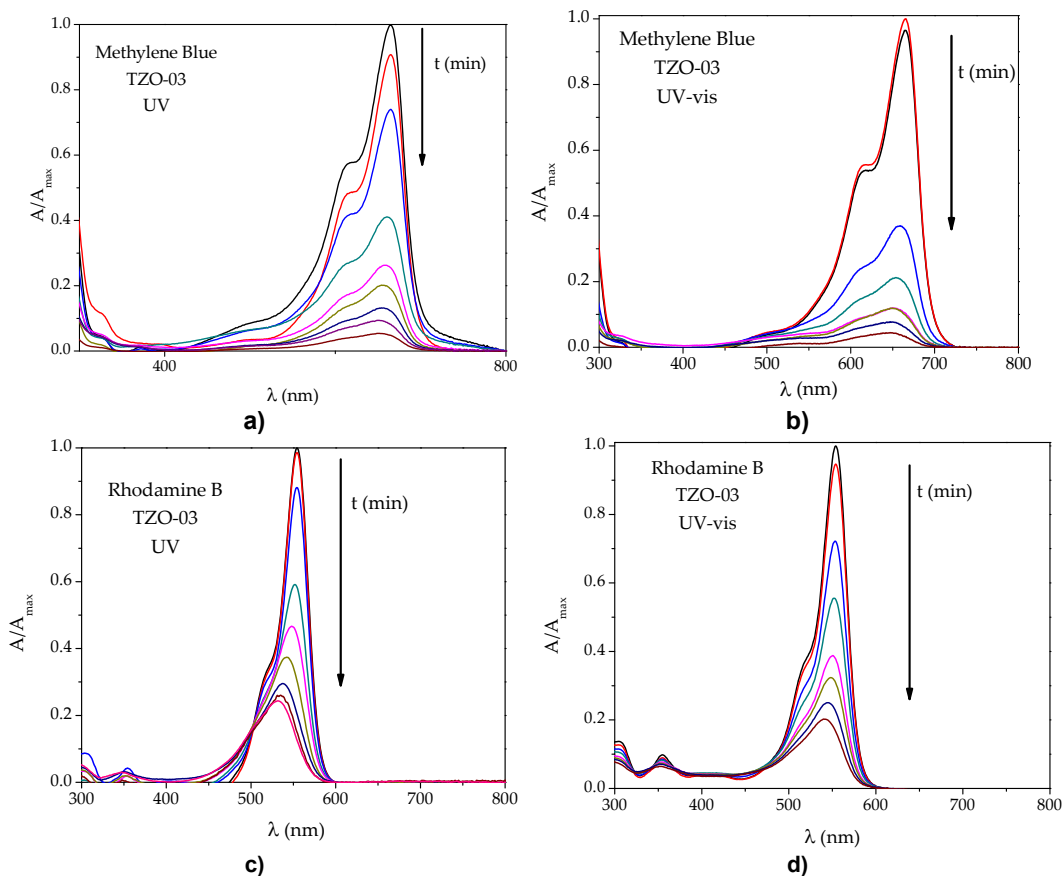


Fig. 6. Normalized absorption spectra during the degradation process for a) Methylene blue with UV irradiation, b) Methylene blue with UV-vis irradiation, c) Rhodamine B with UV irradiation, d) Rhodamine B with UV-vis irradiation

In Fig. 6c, d, the representative normalized absorption spectra for the degradation of Rhodamine B are compared when the photocatalyst is irradiated with UV and UV-vis light. These figures show a slight left-shift of the wavelength of the peak of maximum absorption (smaller wavelength) almost at the end of the degradation process. This means that at the beginning of the degradation process the main mechanism is the cleavage of the molecule and by decreasing the concentration of Rhodamine B the degradation mechanism changes slightly from cleavage to a de-ethylation process. In the case of Fig. 6c, the shift occurs from 554 nm (Rhodamine B) to approximately 530 nm, indicating the beginning of the formation of N, N'-ethyl Rhodamine (522 nm) and in the Fig. 6d, the shift goes from Rhodamine B to N, N, N'-triethyl Rhodamine (540 nm) [44].

Fig. 7a shows the variation profile of the normalized concentration of methylene blue for the different photocatalysts. This figure shows that the material with the highest photocatalytic activity, using UV radiation, for the degradation of methylene blue corresponds to the TZO-02 photocatalyst which as approximately 94.33%. The adsorption values of the dye and its degradation with each of the synthesized materials are shown in Table 3. In Table 3, the Adsorption row (Ads) refers only to the percentage of adsorption of the dye in dark conditions and the degradation row (Deg) refers to the

percentage of degradation of the dye (without taking adsorption into account). RT is the total elimination of the dye in the solution, considering its adsorption and the degradation.

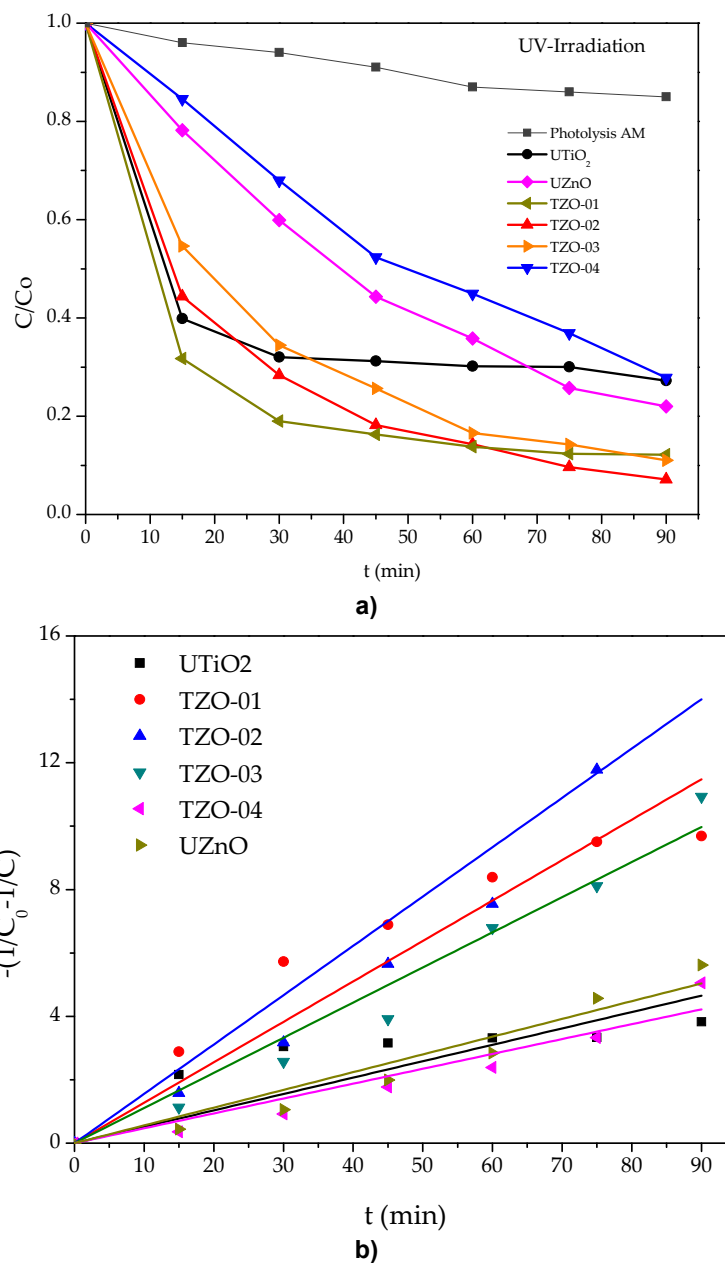


Fig. 7. a) Degradation of the methylene Blue dye, using different photocatalysts and UV irradiation. b) Kinetics constant of degradation of methylene blue, using UV irradiation

The apparent rate constant (*k*) were adjusted to a second-order kinetic equation of Langmuir-Hinshelwood [45], in accordance with

$$\frac{dc}{dt} = -kC^2 \tag{1}$$

for $t=0, C=C_0$ we obtain $C_1=-1/C_0$

Table 4. Publications about the performance of the TiO₂/ZnO composite in the degradation of Methylene Blue and Rhodamine B

Synthesis method	Synthesis time	Dye	Morphology of catalyst	Degradation time (min)	Degradation (%)	Irradiation	Reference
Solution combustion method	15 min	MB (5 ppm)	Spheroidal with nanocrystal aggregates (200 mg/L)	90	94.3 (97.5)	UV 20 W (UV-vis)	this work
		Rh B (5 ppm)		90	90.3	UV	this work
Sol-gel	19 h	MB (10 ppm)	Nanocomposites (5 mg/L)	75	90	100 W tungsten bulb	Upadhyay G. K. et. al. (2019) [21]
Electrochemical and chemical bath	5 h	Rh B (5 mg/L)	Nanotubes decorated of nanorices (Films)	240	94	UVA	Cirak B. B. et. al. 2019 [25]
Sol-gel spin coating	26 h	MB (240 mg/40 mL)	Thin films	240	94	UVC (6W)	Upadhyay D. et. al. 2019 [24]
Hydrothermal	10 h	Rh B (10 ⁻⁵ mol/L)	Microtubes-Nanosheets	80	90	Vis-lamp	Quin R. et. al. 2019 [48]
Waterbath reflux	55 h	Methylene Blue (10 mg/L)	Nanowires decorated of nanoparticles (10 mg)	70	98	Vis-lamp	Sun C. et. al. 2018 [49]
		Rh B (10 mg/L)		60	98		
Sol-gel	16 h	MB (1 mg/L)	Nanorods decorated of nanoparticles (1 mg)	25	98	Sunlight	Prasannalakshmi P. et. al. 2107 [22]
Hydrothermal growth	5 h	MB (68.4 μM)	Nanowires (1.5 mg)	210	95	UV-light	Ghobadi A. et. al. 2016 [14]
One-pot solvothermal	25 h	Rh B (20 μM/L)	Spheres decorated of clusters (1 mg)	45	80	UV-light	Pan L. et. al. 2015 [15]

Synthesis method	Synthesis time	Dye	Morphology of catalyst	Degradation time (min)	Degradation (%)	Irradiation	Reference
Hydrothermal	50 h	MB (20 ppm)	Nanorods decorated of nanoparticles	60	99	UV	Cheng et. al. 2014 [46]
Combustion sol-gel	4.35	Rhodamine 5 (10 mg/L)	Inhomogeneous (150 mg/L)	60	95	UV-lamp	Bachvarova et. al. 2013 [23]
				100	95	Vis-lamp	
Two-step anodization-pyrolysis	6 h	Rh B (5 mg/L)	Films	160	70	Xenon Lamp (300 W)	Xiao 2012 [47]

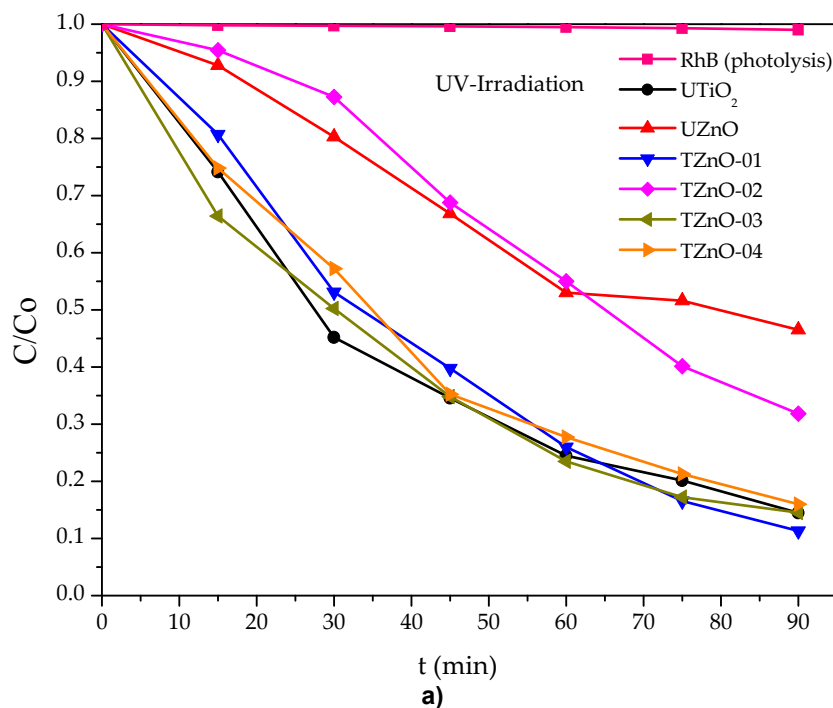
$$\frac{1}{c_0} - \frac{1}{c} = -kt \tag{2}$$

Thus, a graph of $-\left(\frac{1}{c_0} - \frac{1}{c}\right)$ vs t gives us a linear fit whose slope is k .

It is known that the reaction rate is directly proportional to the concentration of the reagents, therefore, due to the fact that the molecule of methylene blue is smaller than that of Rhodamine B, when these are adsorbed on the same surface area, a higher concentration of Methylene blue will be on the surface of the catalyst, so that, when reacting with photogenerated charge-carriers, the degradation rate of methylene blue is very high at the start, adjusting to an apparent second order reaction. For the different photocatalyst systems, the adjustment is shown in Fig. 7b.

Fig. 8a shows the degradation profiles of Rhodamine B. In this figure, we can see that with UV irradiation a greater photocatalytic activity is obtained with the TZO-01 photocatalyst with a degradation percentage of 88.7%. The degradation kinetics obtained is presented with the adjustment of the degradation data of the dye to a Langmuir-Hinshelwood pseudo-first order kinetics [45] showed in Fig. 8b.

According to the analysis of the photocatalytic activity of the synthesized materials when using UV irradiation, we can observe that the materials TZO-01 and TZO-03 are those that present the highest photocatalytic activity in the degradation of methylene blue with a degradation percentage of up to 91.85% and 90.92%, respectively. The two degradation mechanisms of the dye are cleavage and elimination of radicals. In the case of the simplest molecule (Methyl Blue), the dominant mechanism is that of cleavage. For a more complex molecule, such as Rhodamine B, the two aforementioned mechanisms are present, starting with the cleavage and ending with the elimination of radicals (de-ethylation), this sequence of mechanisms has already been reported in other works [14,15,21-23,25,46,47]. Table 4 shows different publications of the performance of the TiO₂/ZnO composite in its photocatalytic activity for the degradation of Methylene Blue and Rhodamine B obtained with different synthesis methods. Our method turns out to be easy to make and cheaper in time than others and with an acceptable efficient.



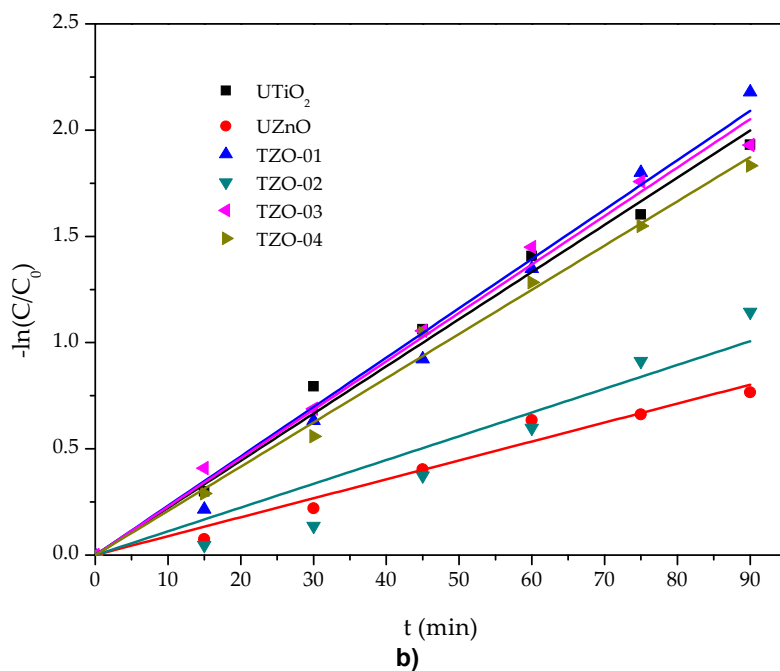
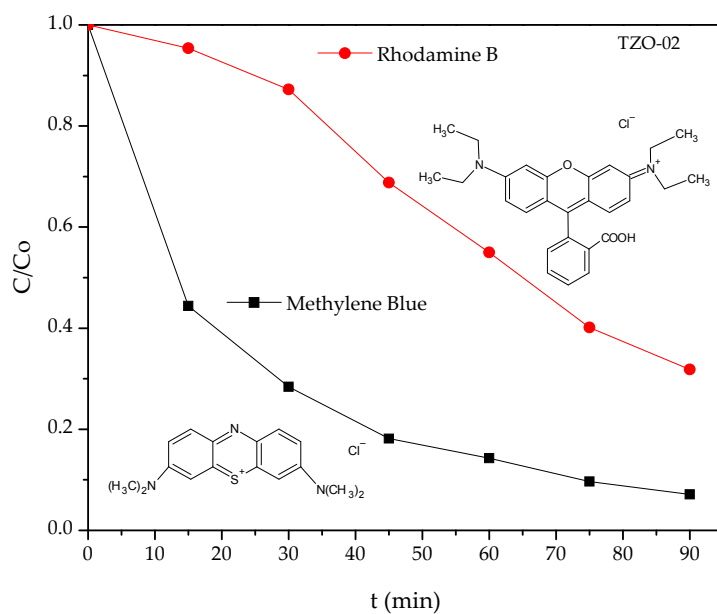


Fig. 8. a) Degradation of Rhodamine B dye, using different photocatalysts and UV irradiation, b) Kinetics constant of Rhodamine B degradation, using UV radiation

A comparison of the degradation of dyes according to their molecular structure for some materials synthesized in this work is presented in Fig. 9a, b. As can be seen in Fig. 9a, the photocatalytic activity of TZO-02 is diminished for more complex molecules, but not for the TZO-03 catalyst, where it practically presents the same degradation percentage for both Methylene Blue and Rhodamine B (see Fig. 9b), which is associated with its surface characteristics, as discussed above.



a)

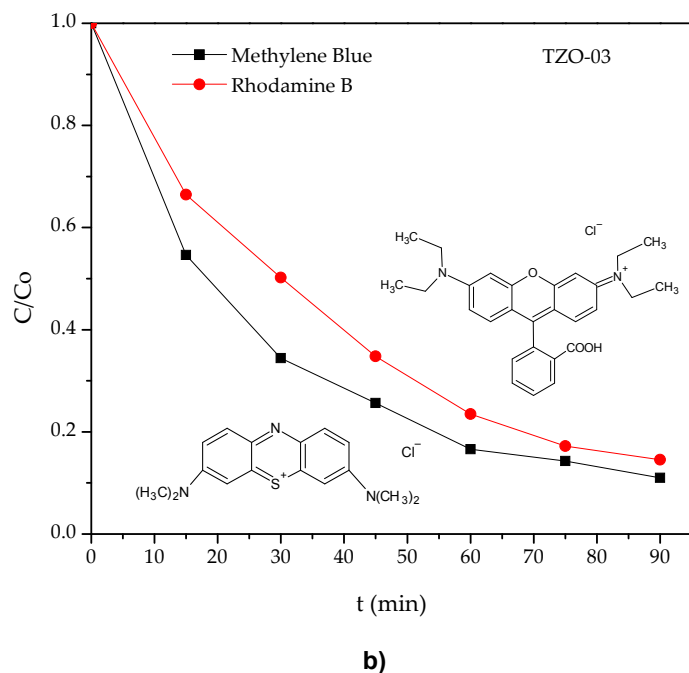
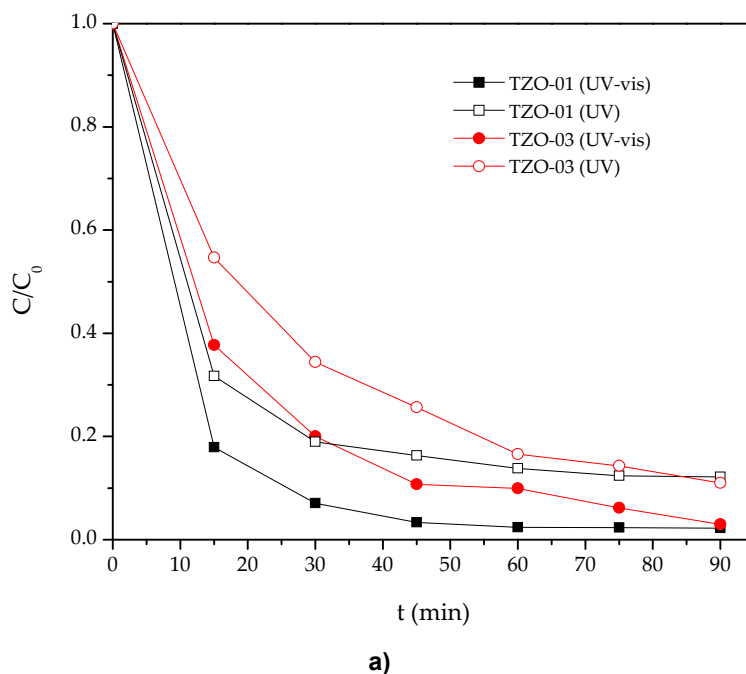


Fig. 9. a) Comparison in the degradation of dyes using the photocatalyst TZO-02,
 b) Comparison in the degradation of dyes using the photocatalyst TZO-03

According to the UV-vis absorption spectra of the photocatalysts (Fig. 4), they show absorption in the visible range. Fig. 10 shows the comparison in the degradation of Methylene Blue and Rhodamine B dyes using UV and UV-vis radiation. In the Fig. 10a an increase of 10% in the degradation of the Methylene Blue is registered and in the case of Rhodamine B (Fig. 10b) an increase until 20% can be appreciated. The degradation mechanism with visible irradiation has been previously explained [22].



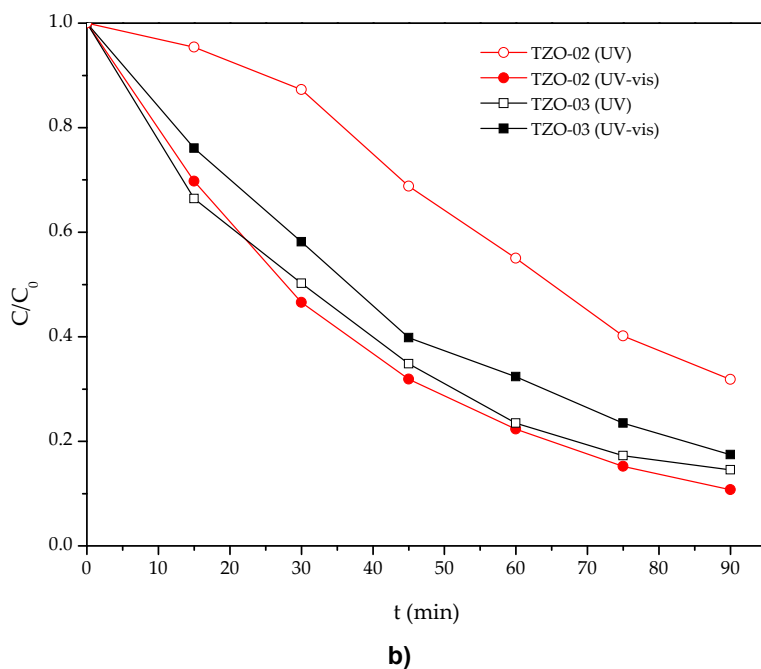


Fig. 10. a) Difference in the degradation of methylene blue when using UV and UV-vis radiation, b) Difference in the degradation of Rhodamine B when using UV and UV-vis radiation

Therefore, high photocatalytic activity is triggered by the photoelectric effect with origin in the active sites of the porosity distribution with greater spatial uniformity (TZO-01 and TZO-03 samples) due to their reduced surface areas, very small total pore volumes and large average pore-size diameters. An analogous case has been reported in elsewhere [50] with ZnO/Burkeite composite where a very low surface area, has an improvement photocatalytic activity compared with ZnO nanoparticles

4. CONCLUSIONS

The synthesis of the TiO₂/ZnO semiconductor composite is presented by a simple method, the solution combustion method which, in addition, uses very short synthesis times. The semiconductor composite has favored and improved the photocatalytic activity due to a good attachment at the interface of the two materials that enriches the transfer of the charge carriers and, also, due to the oxygen vacancies and incorporation of carbon into to the structure of ZnO. The compound enhanced its photocatalytic activity by the use of irradiation including the visible range, in the degradation of the dyes.

The TiO₂/ZnO composites synthesized by combustion method have an interstitial mesoporous composite. The particles of spheroidal morphology composed of the agglomerates of nanocrystalline phase ZnO depend on the amount of ZnO formed during the synthesis as the precursor increases. This gives rise to a pore size distribution (TZO-02 and TZO-03) that provides more favorable active sites in the photocatalytic reaction, which is due to photoexcitation of charge carriers (photoelectric effect, where the low surface area is offset by an increase in transfer rate of charge carriers to carry out redox reactions) from the interface localized in the mesoporosity of the TiO₂/ZnO composites.

COMPETING INTERESTS

Authors have declared that no competing interests exist.

REFERENCES

1. Banerjee S, Pillai SC, Falaras P, O'Shea KE, Byrne JA, Dionysiou DD. New insights into the mechanism of visible light photocatalysis. *J. Phys. Chem. Lett.* 2014;5:2543–2554.
DOI: 10.1021/jz501030x
2. Sakthivel S, Neppolian B, Shankar MV, Arabindoo B, Palanichamy M, Murugesan V. Solar photocatalytic degradation of azo dye: Comparison of photocatalytic efficiency of ZnO and TiO₂. *Sol. Energy Mater. Sol. Cells.* 2003;77:65-82.
DOI: 10.1016/S0927-0248(02)00255-6
3. Tariq Qamar M, Aslam M, Iqbal M, Ismail I, Numan Salah, Hameed A. Synthesis, characterization and sunlight mediated photocatalytic activity of CuO coated ZnO for the removal of nitrophenols. *ACS Appl. Mater. Interfaces.* 2015;7:8757–8769.
DOI: 10.1021/acsami.5b01273
4. Pelaez M, Nolan NT, Pillai SC, Seery MK, Falaras P, Kontos AG, Dunlop PSM, Hamilton JWJ, Byrne JA, O'Shea K, Entezari MH, Dionysiou DD. A review on the visible light active titanium dioxide photocatalysts for environmental applications. *Appl. Catal. B: Environ.* 2012;125:331–349.
DOI: 10.1016/j.apcatb.2012.05.036
5. Kumar SG, Devi LG. Review on modified TiO₂ photocatalysis under UV/Visible light: Selected results and related mechanisms on interfacial charge carrier transfer dynamics. *J. Phys. Chem. A.* 2011;115:13211–13241.
DOI: 10.1021/jp204364a
6. Schneider J, Matsuoka M, Takeuchi M, Zhang J, Horiuchi Y, Anpo M, Bahnemann DW. Understanding TiO₂ photocatalysis: Mechanisms and materials. *Chem. Rev.* 2014;114:9919–9986.
DOI: 10.1021/cr5001892
7. Fang-Xing X. Construction of highly ordered ZnO–TiO₂ nanotube arrays (ZnO/TNTs) heterostructure for photocatalytic application. *ACS Appl. Mater. Interfaces.* 2012;4:7055–7063.
DOI: 10.1021/am302462d
8. Jiang J, Zhang X, Sun P, Zhang L. ZnO/BiOI heterostructures: Photoinduced charge-transfer property and enhanced visible-light photocatalytic activity. *J. Phys. Chem. C.* 2011;115:20555–20564.
DOI: 10.1021/jp205925z
9. Ivanov SA, Piryatinski A, Nanda J, Tretiak S, Zavadil KR, Wallace WO, Werder D, Klimov VI. Type-II core/shell CdS/ZnSe nanocrystals: Synthesis, electronic structures and spectroscopic properties. *J. Am. Chem. Soc.* 2007;129:11708-11719.
DOI: 10.1021/ja068351m
10. Chen S, Wang LW. Thermodynamic oxidation and reduction potentials of photocatalytic semiconductors in aqueous solution. *Chem. Mater.* 2012;24:3659–3666.
DOI: 10.1021/cm302533s
11. Zha R, Nadimicherla R, Guo X. Ultraviolet photocatalytic degradation of methyl orange by nanostructured TiO₂/ZnO heterojunctions. *J. Mater. Chem. A.* 2015;3:6565–6574.
DOI: 10.1039/c5ta00764j
12. Zhang J, Ma X, Zhang L, Lu Z, Zhang E, Wang H, Kong Z, Xi J, Ji Z. Constructing a novel n–p–n dual heterojunction between anatase TiO₂ nanosheets with coexposed {101}, {001} facets and porous ZnS for enhancing photocatalytic activity. *J. Phys. Chem. C.* 2017;121:6133–6140.
DOI: 10.1021/acs.jpcc.7b00049
13. Xu X, Wang J, Tian J, Wang X, Dai J, Liu X. Hydrothermal and post-heat treatments of TiO₂/ZnO composite powder and its photodegradation behavior on methyl orange. *Ceram. Int.* 2011;37:2201–2206.
DOI: 10.1016/j.ceramint.2011.03.067
14. Ghobadi TG, Ulusoy R, Garifullin MO, Guler AK, Okyay. A heterojunction design of single layer hole tunneling ZnO passivation wrapping around TiO₂ nanowires for superior photocatalytic performance. *Sci. Rep.* 2016;6:30587.
DOI: 10.1038/srep30587

15. Pan L, Shen GQ, Zhang JW, Wei XC, Wang L, Zou JJ, Zhang X. TiO₂-ZnO composite sphere decorated with ZnO clusters for effective charge isolation in photocatalysis. *Ind. Eng. Chem. Res.* 2015;54(29):7226-7232.
DOI: 10.1021/acs.iecr.5b01471
16. Wang HY, Yang Y, Li X, Li LJ, Wang C. Preparation and characterization of porous TiO₂/ZnO composite nanofibers via electrospinning. *Chin. Chem. Lett.* 2010;21:1119-1123.
DOI: 10.1016/j.cclet.2010.03.009
17. Kayaci F, Vempati S, Ozgit-Akgun C, Donmez I, Biyikli N, Uyar T. Selective isolation of the electron or hole in photocatalysis: ZnO-TiO₂ and TiO₂-ZnO core-shell structured heterojunction nanofibers via electrospinning and atomic layer deposition. *Nanoscale.* 2014;6:5735-5745.
DOI: 10.1039/c3nr06665g
18. El Mragui I, Daou O, Zegaoui. Influence of the preparation method and ZnO/(ZnO + TiO₂) weight ratio on the physicochemical and photocatalytic properties of ZnO-TiO₂ nanomaterials. *Catal. Today.* 2019;321-322:41-51.
DOI: 10.1016/j.cattod.2018.01.016
19. Wang L, Fu X, Han Y, Chang E, Wu H, Wang H, Li K, Qi X. Preparation, characterization and photocatalytic activity of TiO₂/ZnO nanocomposites. *J. Nanomater.* 2013;6. ID: 321459.
DOI: 10.1155/2013/321459
20. Liao DL, Badour CA, Liao BQ. Preparation of nanosized TiO₂/ZnO composite catalyst and its photocatalytic activity for degradation of methyl orange. *J. Photochem. Photobiol. A: Chem.* 2008;194:11-19.
DOI: 10.1016/j.jphotochem.2007.07.008
21. Upadhyay GK, Rajput JK, Pathak TK, Kumar V, Purohit LP. Synthesis of ZnO:TiO₂ nanocomposites for photocatalyst application in visible light. *Vacuum.* 2019;160:154-163.
DOI: 10.1016/j.vacuum-2018.11.026
22. Prasannalakshmi P, Shanmugam N. Fabrication of TiO₂/ZnO nanocomposites for solar energy driven photocatalysis. *Mater. Sci. Semicond. Process.* 2017;61:114-124.
DOI: 10.1016/j.mssp.2017.01.008
23. Bachvarova-Nedelcheva R, Iordanova A, Stoyanova R, Gegova Y, Dimitriev A, Loukanov. Photocatalytic properties of ZnO/TiO₂ powders obtained via combustion gel method. *Cent. Eur. J. Chem.* 2013;11(3):364-370.
DOI: 10.2478/s11532-012-0167-2
24. Upadhaya D, Kumar P, Purkayastha DD. Superhydrophobic ZnO/TiO₂ heterostructure with significantly enhanced photocatalytic activity. *J. Mater. Sci. Mater. Electron.* 2019;30:10399.
DOI: 10.1007/s10854-019-01381-2
25. Çırak BB, Caglar B, Kılınc T, Karadeniz SM, Erdoğan Y, Kılıç S, Kahveci E, Ekinci AE, Çırak Ç. Synthesis and characterization of ZnO nanorice decorated TiO₂ nanotubes for enhanced photocatalytic activity. *Mater. Res. Bull.* 2019;109:160-167.
DOI: 10.1016/j.materresbull.2018.09.039
26. Chen Q, Tong R, Chen X, Xue Y, Xie Z, Kuang Q, Zheng L. Ultrafine ZnO quantum dots modified TiO₂ composite photocatalysts: The role of quantum size effect in heterojunction-enhanced photocatalytic hydrogen evolution. *Catal. Sci. Technol.* 2018;8:1296-1303.
DOI: 10.1039/c7cy02310c
27. Kansal SK, Singh M, Sud D. Studies on TiO₂/ZnO photocatalysed degradation of lignin. *J. Hazard. Mater.* 2008;153:412-417.
DOI: 10.1016/j.jhazmat.2007.08.091
28. Marci G, Augugliaro V, López-Muñoz MJ, Martín C, Palmisano L, Rives V, Schiavello M, Tilley RJD, Venezia AM. Preparation characterization and photocatalytic activity of polycrystalline ZnO/TiO₂ systems. 2. Surface, bulk characterization, and 4-Nitrophenol photodegradation in liquid-solid regime. *J. Phys. Chem. B.* 2001;105:1033-1040.
DOI: 10.1021/jp003173j
29. Wang Y, Jia W, Strout T, Schempf A, Zhang H, Li B, Cui J, Lei Y. Ammonia gas sensor using polypyrrole-coated TiO₂/ZnO nanofibers. *Electroanalysis.* 2009;21(12):1432-1438.
DOI: 10.1002/elan.200904584

30. Pang S, He Y, Zhong R, Guo Z, He P, Zhou C, Xue B, Wen X, Li H. Multifunctional ZnO/TiO₂ nanoarray composite coating with antibacterial activity, cytocompatibility and piezoelectricity. *Ceram. Int.* 2019;45:12663–12671.
DOI: 10.1016/j.ceramint.2019.03.076
31. Madhuvilakku R, Piraman S. Biodiesel synthesis by TiO₂–ZnO mixed oxide nanocatalyst catalyzed palm oil transesterification process. *Bioresour. Technol.* 2013;150:55–59.
DOI: 10.1016/j.biortech.2013.09.087
32. Wang L, Liu S, Wang Z, Zhou Y, Qin Y, Wang ZL. Piezotronic effect enhanced photocatalysis in strained anisotropic ZnO/TiO₂ nanoplatelets via thermal stress. *ACS Nano.* 2016;10(2):2636–2643.
DOI: 10.1021/acs.nano.5b07678
33. Ajmal I, Majeed RN, Malik H, Idriss MA, Nadeem. Principles and mechanisms of photocatalytic dye degradation on TiO₂ based photocatalysts: A comparative overview. *RSC Adv.* 2014;4:37003–37026.
DOI: 10.1039/c4ra06658h
34. Chen H, Ding L, Sun W, Jiang Q, Hu J, Li J. Synthesis and characterization of Ni doped SnO₂ microspheres with enhanced visible-light photocatalytic activity. *RSC Adv.* 2015;5:56401-56409.
DOI: 10.1039/c5ra10268e
35. Mohammadzadeh S, Olya ME, Arabi AM, Shariati A, Khosravi Nikou MR. Synthesis, characterization and application of ZnO-Ag as a nanophotocatalyst for organic compounds degradation, mechanism and economic study. *J. Environ. Sci.* 2015;35:194-207.
DOI: 10.1016/j.jes.2015.03.030
36. Sahu R, Chaurashiya K, Hiremath A, Dixit. Nanostructured zinc titanate wide band gap semiconductor as a photoelectrode material for quantum dot sensitized solar cells. *Sol. Energy.* 2018;163:338–346.
DOI: 10.1016/j.solener.2018.01.092
37. Schelonka D, Tolasz J, Štengl V. Doping of zinc oxide with selected first row transition metals for photocatalytic applications. *Photochem. Photobiol.* 2015;91:1071-1077.
DOI: 10.1111/php.12469
38. Wang J, Wang Z, Huang B, Ma Y, Liu Y, Qin X, Zhang X, Dai Y. Oxygen vacancy induced band-gap narrowing and enhanced visible light photocatalytic activity of ZnO. *ACS Appl. Mater. Interfaces.* 2012;4:4024–4030.
DOI: 10.1021/am300835p
39. Kavitha MK, Jinesh KB, Philip R, Gopinath P, John H. Defect engineering in ZnO nanocones for visible photoconductivity and nonlinear absorption. *Phys. Chem. Chem. Phys.* 2014;16:25093-25100.
DOI: 10.1039/c4cp03847a
40. Ramachandran S, Sivasamy A. Synthesis and characterization of nanocrystalline N-doped semiconductor metal oxide and its visible photocatalytic activity in the degradation of an organic dye. *J. Environ. Chem. Eng.* 2018;6:3770–3779.
DOI: 10.1016/j.jece.2016.11.045
41. Payra S, Ganeshan SK, Challagulla S, Roy S. A correlation story of syntheses of ZnO and their influence on photocatalysis. *Adv. Powder Technol.* 2020;31:510-520.
DOI: 10.1016/j.apt.2019.11.006
42. Qi Q, Liu S, Li X, Kong C, Guo Z, Chen L. *In situ* fabrication of ZnO@N-doped nanoporous carbon core-shell heterostructures with high photocatalytic and adsorption capacity by a calcination of ZnO@MOF strategy. *J. Solid State Chem.* 2017;255:108–114.
DOI: 10.1016/j.jssc.2017.08.004
43. Li FT, Zhao Y, Hao YJ, Wang XJ, Liu RH, Zhao DS, Chen DM. N-doped P25 TiO₂–amorphous Al₂O₃ composites: One-step solution combustion preparation and enhanced visible-light photocatalytic activity. *J. Hazard. Mater.* 2012;239–240:118–127.
DOI: 10.1016/j.jhazmat.2012.08.016
44. Pica M, Calzuola S, Donnadio A, Gentili PL, Nocchetti M, Casciola M. De-Ethylation and cleavage of rhodamine b by a zirconium phosphate/silver bromide composite photocatalyst. *Catalysts.* 2019;9:3.
DOI: 10.3390/catal9010003

45. Liu Y, Shen L. From Langmuir kinetics to First- and Second-Order rate equations for adsorption. *Langmuir*. 2008;24:11625-11630.
DOI: 10.1021/la801839b
46. Cheng C, Amini A, Zhu C, Xu Z, Song H, Wang N. Enhanced photocatalytic performance of TiO₂-ZnO hybrid nanostructures. *Sci. Rep.* 2014;4:4181.
DOI: 10.1038/srep04181
47. Xiao FX. Construction of highly ordered ZnO-TiO₂ nanotube arrays (ZnO/TNTs) heterostructure for photocatalytic application. *ACS Appl. Mater. Interfaces*. 2012;4(12):7055-7063.
DOI: 10.1021/am302462d
48. Qin R, Meng F, Khan MW, Yu B, Li H, Fan Z, Gong J. Fabrication and enhanced photocatalytic property of TiO₂-ZnO composite photocatalysts. *Mater. Lett.* 2019;240:84-87.
DOI: 10.1016/j.matlet.2018.12.139
49. Sun C, Xu Q, Xie Y, Ling Y, Hou Y. Designed synthesis of anatase-TiO₂ (B) biphasic nanowire/ZnO nanoparticle heterojunction for enhanced photocatalysis. *J. Mater. Chem. A*. 2018;6(18):8289-8298.
DOI: 10.1039/c7ta10274g
50. Luna-Flores A, Morales MA, Agustín-Serrano R, Portillo R, Luna-López JA, Pérez-Sánchez GF, Hernández-de la Luz AD, Tepale N. Improvement of the photocatalytic activity of ZnO/Burkeite heterostructure prepared by combustion method. *Catalysts*. 2019;9(10):817.
DOI: 10.3390/catal9100817

Biography of author(s)



A. Luna-Flores

Facultad de Ingeniería Química, Benemérita Universidad Autónoma de Puebla, Av. San Claudio y 18 sur, Ciudad Universitaria, C.P. 72570, Puebla, Pue. México.

Research and Academic Experience: He studied chemical engineering at Benemérita Universidad Autónoma de Puebla (BUAP), where he obtained his MSc working on the conceptual design of reactive distillation column in 2008. He obtained his PhD in 2017 from Instituto de Ciencias from BUAP, where he focused on photocatalytic materials synthesis. He is currently a researcher and professor in the Chemical Engineering Faculty from BUAP. He has been working on the conceptual design in reactive distillation columns to the green solvents production. Recently his research interest focuses on the designs of the photocatalytic materials to the wastewater treatment and the chemical process photocatalytic design.

Research Area: Photocatalytic chemical process

Number of Published papers: 10



I. Niño-Flores

Facultad de Ingeniería Química, Benemérita Universidad Autónoma de Puebla, Av. San Claudio y 18 sur, Ciudad Universitaria, C.P. 72570, Puebla, Pue. México.

She studied environmental engineering at Benemérita Universidad Autónoma de Puebla (BUAP). She has interested in the chemistry of materials and its various applications. Her interest in the chemistry of materials is because when she started

working with it she found that the synthesis route modifies superficial characteristics of elements and this gives her the opportunity to think about different branches to develop researches related to that topic. She decided to do research about photocatalysis because this gives a lot of opportunities to develop new applications of different materials, such as TiO₂/ZnO. When she started working with those elements, she discovered that their mesoporous components make possible the delete of pollution in the water that textile factories contaminate. With this project, she discovered the positive impact that those materials have, and all the time she kept in mind that she would obtain something to help the environment. Now she researches interest focus on new projects in wastewater treatment to reuse water from the textile industry.



M. A. Morales

Facultad de Ingeniería Química, Benemérita Universidad Autónoma de Puebla, Av. San Claudio y 18 sur, Ciudad Universitaria, C.P. 72570, Puebla, Pue. México.

He received a bachelor's degree in Physics from the Faculty of Physical Mathematical Sciences (FCFM) of the Benemérita Universidad Autónoma de Puebla (BUAP), a Master's degree in Sciences (Physics) at the Institute of Physics of the UNAM and a PhD in Applied Physics by the FCFM of BUAP. He is currently Professor-Researcher at the BUAP Faculty of Chemical Engineering. He is the author and co-author of more than 15 indexed articles in the areas of Mathematical Modeling, Materials Science and Physics of Soft and Condensed Matter, Computational Physics, and Nonlinear Physics, as well as the author and co-author of 4 request of patent and a patent grant.



A. D. Hernández-de la Luz

Centro de Investigación en Dispositivos Semiconductores, Instituto de Ciencias (CIDS- ICUAP), Benemérita Universidad Autónoma de Puebla, Col. Jardines de San Manuel, Av. San Claudio y 14 Sur, Cd. Universitaria, Edificios IC-5 y IC-6. Puebla, Pue., 72570 México.

Research and Academic Experience: He received the Ph.D. (Physics) from the Institute of Physics at the Benemérita Universidad Autónoma de Puebla (BUAP), México. He is currently a researcher and professor in the Instituto de Ciencias (Centro de Investigaciones en Dispositivos Semiconductores, CIDS-ICUAP) from BUAP. He has been working on the optical properties of semiconductors in the framework of the local and nonlocal theory. Recently his research interest is focused on the electrical, luminescent, morphological and compositional properties of nanotubes, Graphene, metallic oxides and silicon rich oxides, also in the electrical properties of the field effect transistor with channel of carbon nanotubes.

Research Area: Optical and electrical properties of semiconductor nanostructures

Number of Published papers: 35



J. A. Luna-López

Centro de Investigación en Dispositivos Semiconductores, Instituto de Ciencias (CIDS- ICUAP), Benemérita Universidad Autónoma de Puebla, Col. Jardines de San Manuel, Av. San Claudio y 14 Sur, Cd. Universitaria, Edificios IC-5 y IC-6. Puebla, Pue., 72570 México.

Research and Academic Experience: He obtained a Ph.D. on Electronics at National Institute of Astrophysics, Optics and Electronics (INAOE), Mexico in 2007. He has two postdoctoral stays, in Center Nanoscience's and Nanotechnology of Mexico National Autonomous University of Mexico (CNN-UNAM) and in Benemérita Universidad Autónoma de Puebla (BUAP). He is currently a researcher and professor in the Institute of Science (Instituto de Ciencias-Centro de Investigaciones en Dispositivos Semiconductores, IC-CIDS) from BUAP, Puebla, México. He has been working on structural, electrical, and optical characterization of nanostructure materials (SRO, PSi, Phthalocyanines, CNTs, TCO, etc.) and different structures as MOS, M-S, TFT, Shottky barrers, etc. His research interest is the physics and technology of material nanostructures with nanocrystals (organic and inorganic) and optoelectronics devices. Additionally, his research interests are nanotechnology, material characterization, and photonics devices such as sensor, LEDs, and solar cells.

Research Area: Nanostructural materials, characterization, nanotechnology, and devices photonics.

Number of Published papers: Most of 90 articles

Most of 90 articles: 5 Books chapters, 20 graduate students (PhD and Master)



R. Portillo

Facultad de Ciencias Químicas, Benemérita Universidad Autónoma de Puebla, Av. San Claudio y 18 sur Ciudad Universitaria, C.P. 72570, Puebla, Pue. México.

He is a professor-researcher at the Department of Physicochemistry of the Faculty of Chemical Sciences of the Autonomous University of Puebla. He has 45 years of experience in teaching and research in physical chemistry. His lines of work are related to the synthesis, characterization and application of solid oxides as adsorbents or catalysts of interest for organic synthesis reactions and industrial wastewater remediation processes. He is author and co-author of 37 articles published in international specialized journals. He took First Place at the Postgraduate Level in the Second National Convention on Applied Research and Technological Development (2007). He worked in "Strategies to optimize the catalytic section of sulfur recovery plants", Sectorial Fund CONACYT-SENER HIDROCARBUROS (2012-2014).



D. Cruz-González

Facultad de Ingeniería Química, Benemérita Universidad Autónoma de Puebla, Av. San Claudio y 18 sur, Ciudad Universitaria, C.P. 72570, Puebla, Pue. México.

He has a doctorate in nuclear sciences from the Autonomous University of the State of Mexico, a master's degree in nuclear science from the Autonomous University of the State of Mexico and is a chemical engineer from the Meritorious Autonomous University of Puebla. He is a professor-researcher at the Faculty of Chemical Engineering of the Meritorious Autonomous University of Puebla since 2006, where he has directed and collaborated in various research projects, as well as directed theses at the undergraduate and graduate level. He has been Coordinator of the Academy of the College of Materials and Coordinator of Continuing Education and Bonding; He currently works as Administrative Secretary where he is responsible for preparing and managing PROFEXCE resources. He is a member of the Inter-Institutional Network of Sustainability Specialists. He is a member of the National System of Researchers Level 1, he has been a member of the CONACYT Registry of Accredited Evaluators (RCEA), in Area 1. Physics, Mathematics and Earth Sciences "registration number RCEA-01-20541-2010", member of the Program for Teacher Professional Development (PRODEP), member of the Register of Researchers of the Meritorious Autonomous University of Puebla, member of the academic body "Development of Chemical Materials and Processes", has participated as an advisor in the Science Program in your Hands, Young Researchers and Summer of Scientific and Technological Research of the Pacific. Finally, he has published several refereed and indexed research articles at the national and international level in the areas of nuclear sciences, materials and environmental remediation.



R. Agustín-Serrano

Facultad de Ciencias Físico Matemáticas, Benemérita Universidad Autónoma de Puebla, Av. San Claudio y 18 sur Ciudad Universitaria, C.P. 72570, Puebla, Pue. México.

He received a bachelor's degree in Physics from the Faculty of Physical-Mathematical Sciences (FCFM) of the Benemérita Universidad Autónoma de Puebla (BUAP), the degree of Master of Science in Optoelectronics and a Doctor of Applied Physics from BUAP. He is currently a teacher and researcher at the FCFM-BUAP. He is the author and co-author of more than 16 indexed articles in the area of Materials Science and Engineering as well as the author and co-author of 3 patent application.



Dr. M. P. Sampedro

Facultad de Ingeniería Química, Benemérita Universidad Autónoma de Puebla, Av. San Claudio y 18 sur, Ciudad Universitaria, C.P. 72570, Puebla, Pue. México.

She has been a researcher and professor at the Faculty of Chemical Engineering of the Benemérita Universidad Autónoma de Puebla (BUAP), Mexico since 2009 and belongs to the Mexican National System of Researchers (level 1) since 2007. She is an evaluator in the Engineering Knowledge Area of the projects and the entrance to the Researcher's Register of the Vice Rector of Graduate Studies of the BUAP. She Received a bachelor's degree in Electronics at the Faculty of electronic Sciences of the (BUAP), the degree of Master of Science in Semiconductor Devices at the Science Institute of the BUAP and PhD in Science in Optoelectronics from the Faculty of Mathematical Physics of the BUAP, with postdoctoral appointment at Physical Institute and Faculty of Chemical Engineering BUAP. Her research specialty is / nanomaterials/ photonics crystals/ She continues to be an active researcher with 16 papers, 2 co-author of patent applications and 1 edited book. She advised 8 undergraduate theses and 1 master's thesis. She has attended international congresses in Mexico, Sevastopol Russian Federation and Dublin Ireland.

A Study on Thermal Degradation of Hydrazinated Transition Metal Acetamido Benzoates

E. Helen Pricilla Bai¹ and S. Vairam^{2*}

DOI: 10.9734/bpi/cpcs/v2

ABSTRACT

A study on the preparation of hydrazinated metal complexes of isomeric acetamido benzoic acids with Co, Ni, Zn and Cd metals and characterization using analytical, FT IR, UV reflectance, micro elemental analysis, simultaneous TG-DTA, powder XRD, magnetic susceptibility measurements and SEM-EDX studies have been made and reported here. The complexes have the formulae, $[\text{Ni}(2\text{-acamb})_2(\text{Hz})] \cdot 2\text{H}_2\text{O}$; $[\text{M}(2\text{-acamb})_2(\text{Hz})] \cdot \text{H}_2\text{O}$, where M = Co, Cd and Zn; $[\text{M}(3\text{-acamb})_2(\text{Hz})] \cdot \text{H}_2\text{O}$, where M = Ni and Co and $[\text{M}(3\text{-acamb})_2(\text{Hz})] \cdot 2\text{H}_2\text{O}$ where M = Cd and Zn; $[\text{Co}(4\text{-acamb})_2(\text{Hz})] \cdot \text{H}_2\text{O}$ and $[\text{M}(4\text{-acamb})_2(\text{Hz})] \cdot 2\text{H}_2\text{O}$ where M = Ni, Cd and Zn, 2-acambH = 2-acetamido benzoic acid, 3-acambH = 3-acetamido benzoic acid, 4-acambH = 4-acetamido benzoic acid and Hz = N_2H_4 . Among them Ni, Co and Cd complexes of 2-acambH and 4-acambH were obtained at pH 5 and 6 respectively, whereas Zn complexes of both acids were formed at pH 3. 3-acambH complexes were prepared at pH 5. The IR spectra of the compounds show the N-N stretching frequency absorptions in the range of 984-926 cm^{-1} , implying the bridging bidentate coordination of hydrazine. The compounds show $\nu(\text{C}=\text{O})$ (asym) values in the range 1611-1582 cm^{-1} and the $\nu(\text{C}=\text{O})$ (sym) values at 1555-1422 cm^{-1} . The difference of $\nu(\text{C}=\text{O})$ (asym) and $\nu(\text{C}=\text{O})$ (sym), which is found to be 48-162 cm^{-1} , indicates that the carboxylate anion is coordinated to the metal ion in the bidentate fashion. These complexes eliminate water molecules in the range of 140-177°C first and then undergo oxidative decomposition showing exotherms in the range of 200-278°C and in the range of 400-682°C to their metal oxides. Cadmium and zinc complexes indicate their intermediates as carbonates. The electronic spectra and the magnetic susceptibility values suggest that the coordination number of the complexes is 6 with distorted octahedral geometry. XRD patterns show isomorphism among the complexes with similar molecular formulae. The SEM-EDX studies reveal the presence of respective metal oxides.

Keywords: IR; simultaneous TG-DT88A; acetamido benzoate; electronic spectra.

1. INTRODUCTION

Hydrazine due to its basic nature, forms variety of compounds with more number of carboxylic acids, such as simple aliphatic mono and di carboxylic acids [1,2] aromatic mono and di carboxylic acids [3,4] tri and tetra carboxylic acids [5,6], which have been reported in the literature. Hydrazine is thermodynamically unstable, but the thermodynamic properties of hydrazine [7,8,9] per se are not useful in predicting the nature of the organic products obtained when hydrazine is used as a reducing agent [10]. Many bis-hydrazine and hydrazinium metal carboxylates are used as precursors for metal oxides and mixed metal oxides [11,12,13,14,15,16,17,18,19]. Though studies have been done on 4-acetamido benzoate, synthesis of lanthanide coordination polymers using 4-acetamido benzoic acid and various modes of coordination of 4-acetamido benzoate (monodentate, chelating, multidentate bridging nature and crystal structure of Zinc complex) [20,21,22,23], triboluminescent and crystal structure of Copper complex of 2-acetamido benzoate [24,25], catalytic synthesis and thermodynamic properties in relation with crystal structure of isomers of acetamido benzoic acid [26,27,28], a detailed study of transition metal complexes of isomeric acetamido benzoic acids in the presence of hydrazine

¹Department of Chemistry, Park College of Engineering and Technology, Kaniyur, Coimbatore-641 659, India.

²Department of Chemistry, KPR Institute of Engineering and Technology, Arasur, Coimbatore - 641407, Tamil Nadu, India.

*Corresponding author: E-mail: vamshen@yahoo.com;

has not been attempted so far. In this paper, we report the synthesis, spectral and thermal studies of some transition metal complexes of 2-acetamido, 3-acetamido and 4-acetamido benzoates with hydrazine. The structures of the isomeric forms acetamido benzoic acids are given in the Figs. 1-3.

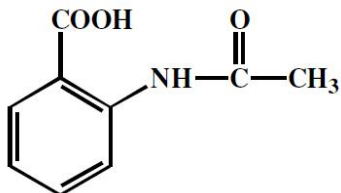


Fig. 1. 2-Acetamido benzoic acid (2-acambH)

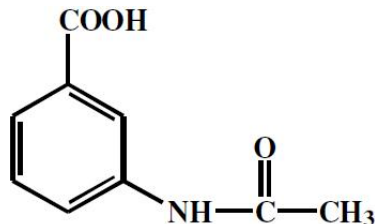


Fig. 2. 3-Acetamido benzoic acid (3-acambH)

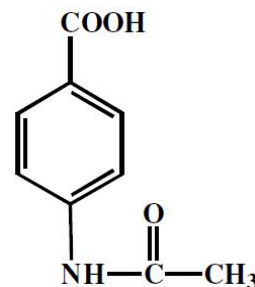


Fig. 3. 4-Acetamido benzoic acid (4-acambH)

2. EXPERIMENTAL

The chemicals and solvents used were of AR grade received from Fluka chemicals. The double distilled water was used for the preparation and chemical analyses. Hydrazine hydrate 99.99% pure was used as such.

Preparation of $[M\{(2-),(3-)\text{ and } (4-)\text{ acamb}\}]_2(\text{Hz}) \cdot x\text{H}_2\text{O}$, where $\text{Hz} = \text{N}_2\text{H}_4$, 2-acambH = 2-acetamido benzoic acid, $M = \text{Ni}$ and $x = 2$ and $M = \text{Co}$, Cd and $x = 1$; where 3-acambH = 3-acetamido benzoic acid, $M = \text{Ni}$, Co and $x = 1$ and $M = \text{Cd}$ and $x = 2$; where 4-acambH = 4-acetamido benzoic acid $M = \text{Ni}$, Cd and $x = 2$ and $M = \text{Co}$ and $x = 1$.

The complexes were prepared by adding metal nitrate [e.g., $\text{Ni}(\text{NO}_3)_2 \cdot 6\text{H}_2\text{O}$, 0.291 g, 1 mmol in 20 mL of H_2O] solution, to a solution obtained by mixing hydrazine hydrate (99.99% pure, 0.1 g, 2 mmol) with a slurry of acetamido benzoic acid (0.1792 g, 1 mmol in 60 mL of hot water). Crystalline products of complexes were formed when the solution mixture was heated over a hot water bath at 80°C .

2-Acetamido benzoic acid complexes were formed at pH 5 immediately whereas 3-acetamido and 4-acetamido benzoic acid complexes formed at pH 5 when the reaction mixture is heated for 90 min and at pH 6 when heated for 2h 30 min respectively.

The complexes formed were filtered through filter paper, washed with distilled water, ethanol then with ether and dried in a desiccator.

Preparation of $[\text{Zn}(\text{acamb})_2(\text{Hz})] \cdot x\text{H}_2\text{O}$, where $\text{Hz} = \text{N}_2\text{H}_4$, 2-acambH = 2-acetamidobenzoic acid and $x = 1$ and 3-acambH = 3-acetamido benzoic acid, 4-acambH = 4-acetamidobenzoic acid and $x = 2$.

These complexes were also prepared by the same procedure in absolute alcohol medium. As mentioned above, complexes of **2** isomer were formed immediately at pH 3 and those of **3** and **4** isomers were formed at pH 5 and 3 in 90 min and 2 h 30 min respectively.

The complexes were filtered, washed and dried as mentioned above.

Physico-chemical techniques: The composition was established by chemical analysis. Hydrazine content was determined by titrating against standard KIO_3 solution (0.025 mol L^{-1}) under Andrew's conditions [29]. The metal content was determined by EDTA (0.01 mol L^{-1}) complexometric titration [29] after decomposing a known weight of the sample with 1:1 HNO_3 . Magnetic measurements were carried out by using Guoy balance and Gauss meter DGM102 (Besto) keeping $\text{Hg}[\text{Co}(\text{NCS})_4]$ as calibrant. The electronic spectra for solid state complexes were obtained using a Varian, Cary 5000

recording spectrophotometer. Infrared spectra were recorded using KBR disc ($4000\text{-}400\text{ cm}^{-1}$) on a Shimadzu FTIR-8201 (PC)S spectrophotometer. The simultaneous TG-DTA studies were done on a Perkin Elmer, Diamond TG/DTA analyzer and the curves were obtained using 5-10 mg of the samples at the heating rate of 10°C per min in air atmosphere. Platinum cups were employed as sample holders and alumina as reference and the temperature range was ambient to 700°C . The XRD patterns were recorded on a Bruker AXS D₈ advance diffractometer with an X-ray source Cu, wavelength 1.5406 \AA using a Si (Li) PSD detector. The elemental analysis was carried out using an Elementar Vario ELIII CHNS elemental analyzer. The SEM with EDS analysis was obtained using JEOL model JSM-6390 LV and JEOL model JED-2300 instrument.

3. RESULTS AND DISCUSSION

Electronic spectra and magnetic susceptibility: The absorption maximum and assignments are summarized in Table 1. Since the complexes were insoluble in water and organic solvents, the electronic reflectance spectra were recorded in solid-state. Based on the absorptions term states assigned are ${}^4T_{1g}(P) \rightarrow {}^4T_{2g}$ and ${}^4A_{2g}$ for cobalt and ${}^3T_{2g} \rightarrow {}^3T_{1g}$ and 1E_g for nickel complexes. These assignments evidence the distorted octahedral geometry of the complexes [30]. The magnetic moment values obtained for the cobalt and nickel complexes were 5.20 and 3.31 BM respectively, which supports the geometry of cobalt and nickel compounds.

Table 1. Electronic spectra values of the complexes

Complex	Absorption maximum (cm^{-1})	Assignment
[Ni(2-acamb ₂ (Hz)).2H ₂ O]	20534, 16807 and 15408 8313, 7257 and 6725	${}^3T_{1g}$ ${}^3T_{2g}$
[Ni(3-acamb ₂ (Hz)).H ₂ O]	20000, 16447, 13459 and 12136 8224 and 7257	${}^3T_{1g}$ ${}^3T_{2g}$
[Ni(4-acamb ₂ (Hz)).2.H ₂ O]	20000 and 13459 11933 7955 and 6064	${}^3T_{1g}$ ${}^1E_{1g}$ ${}^3T_{2g}$
[Co(2-acamb ₂ (Hz)).H ₂ O]	21186, 11806 8467, 7348 and 6667	${}^4T_{1g}(P)$ ${}^4A_{2g}$ ${}^4T_{2g}$
[Co(3-acamb ₂ (Hz)).H ₂ O]	23148 11561 8313, 7117, 6489 and 5780	${}^4T_{1g}(P)$ ${}^4A_{2g}$ ${}^4T_{2g}$
[Co(4-acamb ₂ (Hz)).H ₂ O]	12755 8224, 7184, 6667 and 6017	${}^4A_{2g}$ ${}^4T_{2g}$

IR spectra of complexes: The IR spectral data of the complexes are summarized in Table 2. The pka values of 2-acambH, 3-acambH and 4-acambH were found to be 3.63, 4.07 and 4.28 respectively. These indicate that 4-isomer is least acidic and the lowest value of $\nu(\text{C}=\text{O})$ 1672 cm^{-1} of the same may be due to its highest pka value.

The IR spectra of pure acids show absorption at 1707 , 1694 and 1672 cm^{-1} corresponding to $\nu(\text{C}=\text{O})$ (acid). But the spectra of complexes show $\nu(\text{C}=\text{O})$ asym (acid) at $1582\text{-}1611\text{ cm}^{-1}$ and $\nu(\text{C}=\text{O})$ sym (acid) in the range $1555\text{-}1422\text{ cm}^{-1}$ with the difference of $48\text{-}162\text{ cm}^{-1}$ between $\nu(\text{C}=\text{O})$ (asym) and $\nu(\text{C}=\text{O})$ (sym), which supports the bidental coordination of carboxylate ions to metal. The absorption at $984\text{-}926\text{ cm}^{-1}$ observed in IR spectra of complexes is assigned to $\nu(\text{N-N})$ stretching of hydrazine present in the complexes, which reveals that N_2H_4 is coordinated to metal ion in bridged bidentate fashion. The O-H stretch of water molecules are noticed at $3543\text{-}3304\text{ cm}^{-1}$ in all complexes. An additional band observed at $594\text{-}518\text{ cm}^{-1}$ also supports the presence of lattice water molecules [31]. The C=O frequency of amide group of the compounds is observed at $1709\text{-}1635\text{ cm}^{-1}$. The N-H stretching frequencies of amide and that of hydrazine are found to be a merged broad band at $3281\text{-}3173\text{ cm}^{-1}$.

Thermal data of all the complexes are given in Table 3.

Table 2. Analytical and IR data of complexes

Molecular formula of the Complexes	Analytical data					IR data (cm ⁻¹) b= broad; s = sharp ; m = medium							
	C Fd (calc.)	H Fd (calc.)	N Fd (calc.)	N ₂ H ₄ (Hz) Fd (calc.)	M Fd (calc.)	$\nu(\text{C=O})$ (asym)	$\nu(\text{C=O})$ (sym)	$\nu(\text{N-N})$	$\nu(\text{OH})$	$\nu(\text{N-H})$	$\nu(\text{C=O})$ (amido gp)	ρ_r H ₂ O	$\nu(\text{M-O})$
2-acambH complexes													
[Ni(2-acamb) ₂ (Hz)].2H ₂ O	45.6(44.7)	4.4(5.0)	12.0(11.6)	6.4(6.6)	12.9(12.2)	1595 b	1433 b	964 s	3464 b	3233 b	1684 m	527 s	422 m
[Co(2-acamb) ₂ (Hz)].H ₂ O	46.0(46.4)	4.3(4.8)	12.1(12.0)	6.4(6.9)	12.4(12.7)	1589 s	1439 s	966 s	3304 m	3175 m	1661 s	594 s	438 s
[Cd(2-acamb) ₂ (Hz)].H ₂ O	41.8(41.6)	4.3(4.3)	10.7(10.8)	6.3(6.2)	21.3(21.7)	1584 b	1422 b	959 s	3543 s	3235 b	1676 m	594 s	509 s
[Zn(2-acamb) ₂ (Hz)].H ₂ O	45.3(45.8)	4.5(4.7)	11.8(11.9)	6.8(6.8)	13.7(13.9)	1599 s	1447 s	970 s	3320 s	3219 b	1661 s	567 s	463 s
3-acambH complexes													
[Ni(3-acamb) ₂ (Hz)]. H ₂ O	46.5(46.4)	4.5(4.8)	12.0(12.0)	6.7(6.9)	12.4(12.6)	1582 s	1460 s	984 s	3392 b	3277 b	1709 b	525 s	476 m
[Co(3-acamb) ₂ (Hz)].H ₂ O	46.4(46.4)	4.7(4.8)	12.1(12.0)	6.9 (6.9)	12.6(12.7)	1611 m	1487 s	980 s	3339 s	3271 b	1635 b	552 s	459 s
[Cd(3-acamb) ₂ (Hz)]. 2H ₂ O	41.3(40.2)	4.2(4.5)	10.9(10.4)	6.5(6.0)	20.1(20.9)	1611 s	1462 s	926 m	3376 b	3281 s	1659 s	559 s	459 s
[Zn(3-acamb) ₂ (Hz)]. 2H ₂ O	43.9(44.1)	4.7(4.9)	11.6(11.4)	7.0(6.5)	14.3(13.4)	1607 s	1487 s	974 s	3305 s	3215 b	1607 b	559 s	430 s
4-acambH complexes													
[Ni(4-acamb) ₂ (Hz)].2H ₂ O	44.4(44.7)	4.5(5.0)	11.8(11.6)	7.4(6.6)	13.2(13.1)	1582 b	1530 b	964 s	3360 m	3183 b	1672 m	544 s	500 s
[Co(4-acamb) ₂ (Hz)].H ₂ O	46.2(46.4)	4.7(4.8)	12.0(12.0)	6.7 (6.9)	12.8(12.7)	1601 b	1528 b	968 s	3335 b	3173 b	1680 b	546 s	500 s
[Cd(4-acamb) ₂ (Hz)].2H ₂ O	41.2(40.2)	3.8(4.5)	11.3(10.4)	6.2(6.0)	21.3(20.9)	1603 b	1555 b	964 s	3377 b	3260 b	1668 b	581 s	500 s
[Zn(4-acamb) ₂ (Hz)].2H ₂ O	44.7(44.1)	4.1(4.9)	12.4(11.4)	7.0(6.5)	14.4(13.4)	1597 b	1521 s	972 s	3315 s	3270 b	1672 m	518 s	503 s

Table 3. Thermal data of complexes

Complex	DTA Temp	Thermogravimetry			Nature of the Reaction
		Weight Loss %			
		Obsd.	Calc		
[Ni(2-acamb) ₂ (Hz)].2H ₂ O	150(+)	60-200	7.1	7.1	Dehydration
	278(-) 420(-)	200-700	7.2	7.2	Formation of metal oxide
[Co(2-acamb) ₂ (Hz)].H ₂ O	177(+)	60-190	4.0	4.0	Dehydration
	214(-)	190-300	3.9	3.9	Dehydrazination
	400(-)	300-700	82.6	82.8	Formation of cobalt oxide (Co ₃ O ₄)
[Cd(2-acamb) ₂ (Hz)].H ₂ O	160(+)	40-180	3.6	3.5	Dehydration
	275(-)	180-300	9.8	9.6	Dehydrazination
	400(-)	300-480	57.1	57.1	Formation of cadmium carbonate
	490(-)	480-700	75.0	75.2	Formation of cadmium oxide
	556(-)				
[Zn(2-acamb) ₂ (Hz)].H ₂ O	140(+)	100-180	3.9	3.8	Dehydration
	274(-)	180-700	83.0	82.7	Formation of Zinc oxide
	500(-)				
[Ni(3-acamb) ₂ (Hz)].H ₂ O	140(+)	100-200	3.6	3.9	Dehydration
	260(-)	200-400	10.7	10.8	Dehydrazination
	500(-)	400-700	84.7	84.9	Formation of nickel oxide
	590(-)				
[Co(3-acamb) ₂ (Hz)].H ₂ O	160(+)	120-200	3.8	3.9	Dehydration
		200-340	10.5	10.7	Dehydrazination
		340-700	83.8	83.9	Formation of cobalt oxide
[Cd(3-acamb) ₂ (Hz)].2H ₂ O	122(+)	80-200	6.6	6.7	Dehydration
	210(-)	200-400	55.2	55.0	Formation of cadmium carbonate
	317(-)	400-700	76.1	76.0	Formation of cadmium oxide
	494(-)				
[Zn(3-acamb) ₂ (Hz)].2H ₂ O	145(+)	100-200	7.2	7.5	Dehydration
	240(-)	200-700	83.4	83.3	Formation of Zinc oxide
	468(-)				
	553(-)				
[Ni(4-acamb) ₂ (Hz)].2H ₂ O	175(+)	50-190	7.4	7.5	Dehydration
	251(-)	190-390	14.0	14.1	Dehydrazination
	401(-)	390-700	85.3	85.5	Formation of nickel oxide
	486(-)				
	[Co(4-acamb) ₂ (Hz)].H ₂ O	120(+)	60-180	4.0	3.9
239(-)		180-280	10.6	10.7	Dehydrazination
324(-)		280-700	82.6	82.8	Formation of cobalt oxide (Co ₃ O ₄)
390(-)					
450(-)					
[Cd(4-acamb) ₂ (Hz)].2H ₂ O	150(+)	50-180	6.8	6.7	Dehydration
	240(-)	180-320	12.9	12.7	Dehydrazination
	401(-)	320-460	55.0	55.2	Formation of cadmium carbonate
	625(-)	460-800	75.8	76.0	Formation of cadmium oxide
	682(-)				
[Zn(4-acamb) ₂ (Hz)].2H ₂ O	145(+)	75-160	7.2	7.4	Dehydration
	236(-)	160-400	63.8	64.0	Formation of zinc carbonate
	350(-)				
	533(+)		400-600	84.0	

Thermal data of [M(2-acamb)₂(Hz)₂].xH₂O complexes, where M = Ni and x = 2, where M = Co, Cd and Zn and x = 1

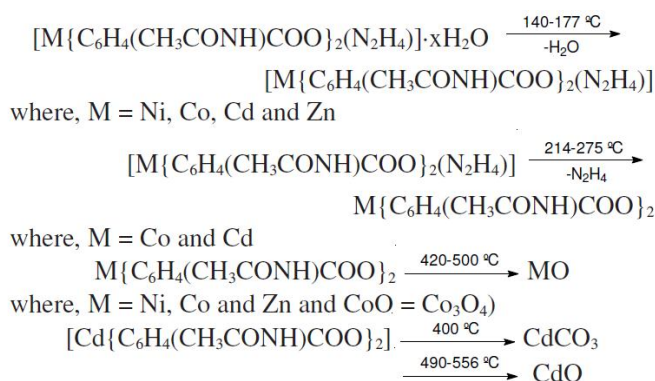
The 2-acambH complexes show endothermic dehydration in the range 140-177°C. The high temperature dehydration reveals that these lattice water molecules are held up strongly [31]. Co and Cd complexes show exothermic dehydrazination at 214-275°C, whereas the dehydrazination was not clearly visible in Ni and Zn compounds.

The cadmium complex shows a broad exotherm at 400°C indicating the formation of metal carbonate intermediate [32] and the corresponding weight loss is observed between 300-470°C in its thermogravimetric curve. It is also inferred that the complex undergoes oxidative decomposition to form the metal oxide residue, which is accompanied by an exothermic doublet at 490 and 556°C indicating the weight loss temperature of 470-700°C.

The TG-DTA curves of Ni, Co and Zn complexes show that the dehydrazinated metal carboxylates decompose to give the metal oxide as their final residue. As the intermediates are highly unstable and they could not be isolated. They show exotherms in the range 420-500°C attributing the formation of metal oxide residue with the mass loss temperature in the range of 200-700°C is observed in their TG.

Reaction Scheme-I

The reaction scheme of the 2-acambH complexes is given below:

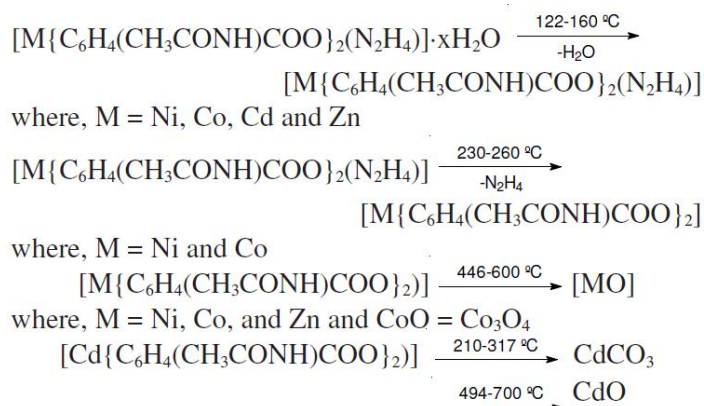


Thermal data of $[M(3\text{-acamb})_2(Hz)_2] \cdot xH_2O$; where $M = Ni, Co$ and $x = 1$; $M = Cd, Zn$ and $x = 2$

Similar to 2-acambH complexes, 3-acambH complexes show an endothermic dehydration at 122-160°C. Ni and Co complexes show exothermic dehydrazination in the range of 230-260°C, while Cd and Zn complexes do not. The inter-mediate of Ni, Co and Zn compounds were unstable and could not be identified. They further decompose to their respective metal oxides at 500-600°C. In case of cadmium oxidative decomposition occurs *via* its carbonate intermediate. Its decomposition temperature, 494°C was comparable to that of the reported [6], with the corresponding weight loss between 400-700°C.

Reaction Scheme-II

The reaction scheme of 3-acetamidobenzoate complexes is given as follows:



Thermal data of $[M(4\text{-acamb})_2(\text{Hz})_2] \cdot x\text{H}_2\text{O}$; where $M = \text{Ni, Cd, Zn}$ and $x = 2$; $M = \text{Co}$ and $x = 1$

4-acambH complexes show endothermic dehydration at 120-175°C. Exothermic dehydrazination is observed between 239-251°C for Ni, Co and Cd complexes and no distinct step was observed in case of Zn complex.

Ni and Co complexes undergo oxidative decomposition to their metal oxide as final residue accompanied by the exotherms in the range 324-486°C with a corresponding weight loss between 230-700°C.

In the final step, cadmium and zinc show exothermic decomposition at 350 and 401°C *via* the carbonate intermediate [32], which decompose further to their metal oxides showing broad exotherms in the range of 533-682°C showing the mass loss between 400-800°C, to 75.8% for cadmium and 83.9% for zinc.

The TG-DTA of $[\text{Ni}(2\text{-acamb})_2(\text{Hz})] \cdot 2\text{H}_2\text{O}$, $[\text{Cd}(3\text{-acamb})_2(\text{Hz})] \cdot 2\text{H}_2\text{O}$ and $[\text{Zn}(4\text{-acamb})_2(\text{Hz})] \cdot 2\text{H}_2\text{O}$ complexes are shown as representative examples in Figs. 4-6.

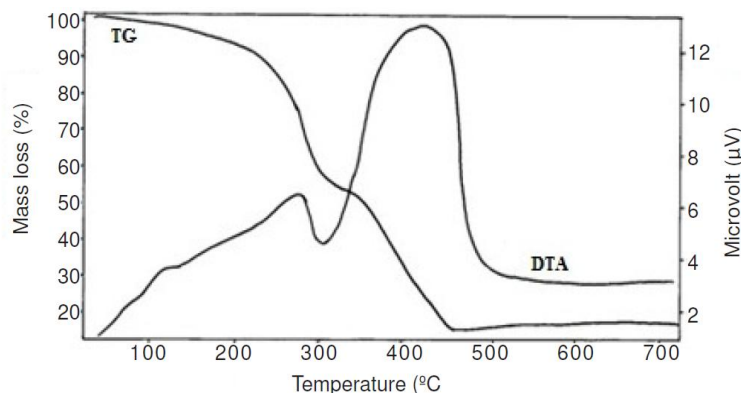


Fig. 4. TG-DTA of $[\text{Ni}(2\text{-acamb})_2(\text{Hz})] \cdot 2\text{H}_2\text{O}$

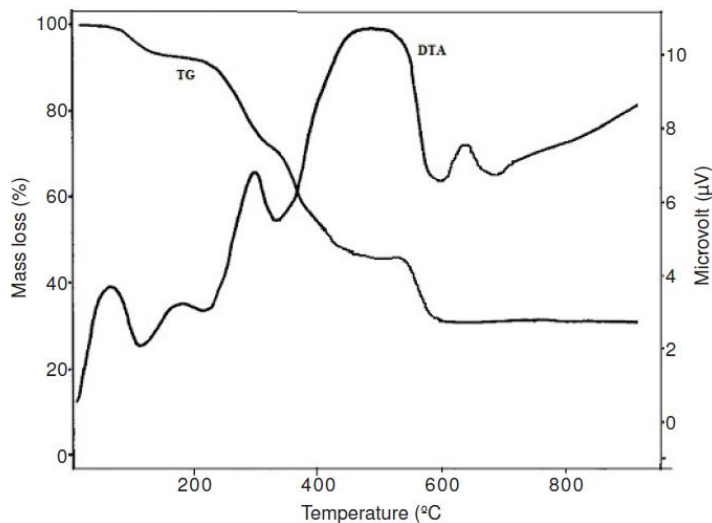


Fig. 5. TG-DTA of $[\text{Cd}(2\text{-acamb})_2(\text{Hz})] \cdot 2\text{H}_2\text{O}$

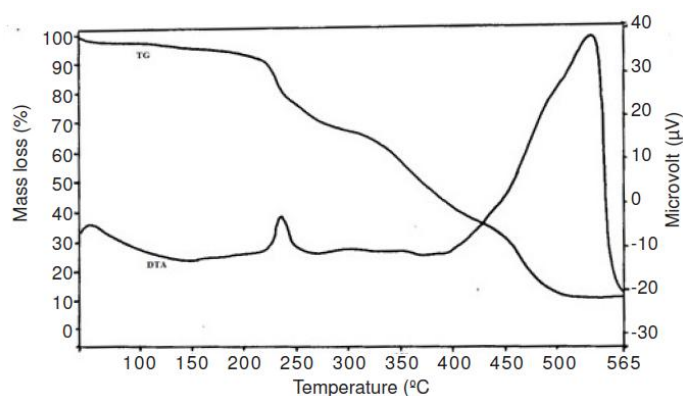
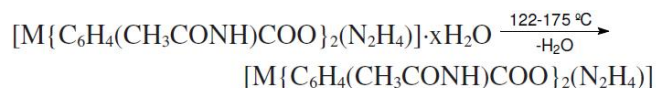


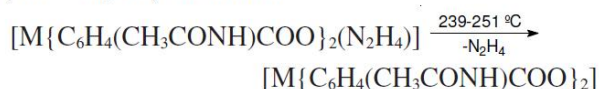
Fig. 6. TG-DTA of $[\text{Zn}(4\text{-acamb})_2(\text{Hz})]\cdot 2\text{H}_2\text{O}$

Reaction Scheme-III

The reaction scheme of 4-acetamidobenzoate complexes are given as follows:



where, M = Ni, Co, Cd and Zn



where, M = Ni and Co



where, M = Ni and Co and $\text{CoO} = \text{Co}_3\text{O}_4$

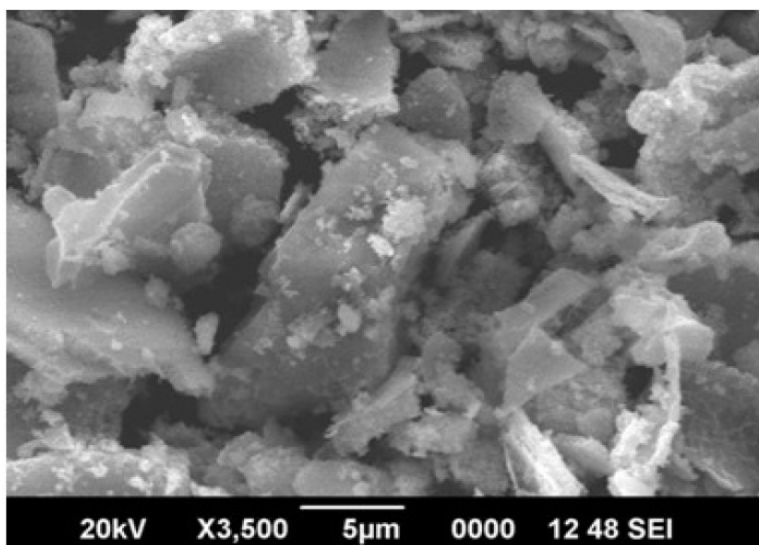
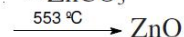
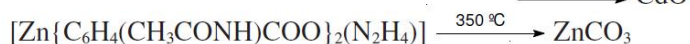
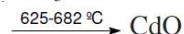
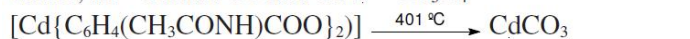


Fig. 7. SEM image of CoO obtained from $[\text{Co}(2\text{-acamb})_2(\text{Hz})]\cdot \text{H}_2\text{O}$

XRD-data of complexes: The powder XRD patterns with their d-spacings are given in Table 4. They imply that each set of complexes with similar composition possesses isomorphism among them.

All the complexes were found to be crystalline even though compounds of 2-acambH show more crystallinity.

SEM-EDX studies: The SEM-EDX images of metal oxides of the complexes $[\text{Co}(2\text{-acamb})_2(\text{Hz})]\cdot\text{H}_2\text{O}$, $[\text{Cd}(3\text{-acamb})_2(\text{Hz})]\cdot 2\text{H}_2\text{O}$ and $[\text{Zn}(4\text{-acamb})_2(\text{Hz})]\cdot 2\text{H}_2\text{O}$ are given as representative examples in Figs. 7-12. These metal oxides are obtained by incinerating the corresponding complexes at their decomposition temperature followed by sintering them for 0.5 h. They have yielded probably nanosized metal oxides.

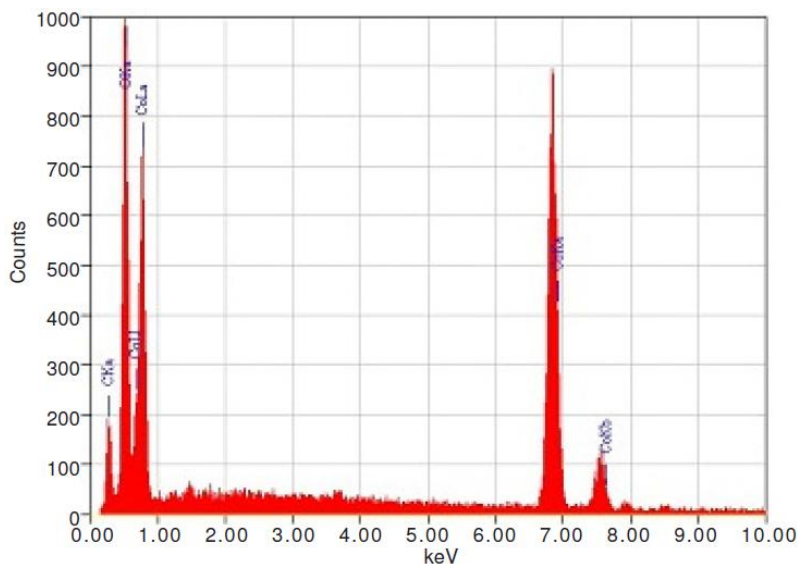


Fig. 8. SEM-EDX picture of CoO

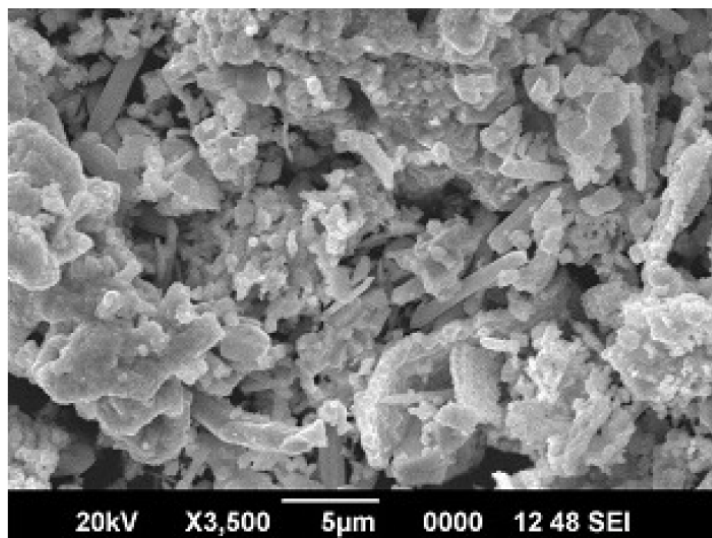


Fig. 9. SEM image of CdO obtained from $[\text{Cd}(3\text{-acamb})_2(\text{Hz})]\cdot 2\text{H}_2\text{O}$

Table 4. XRD data of complexes (d-spacing in Å units and intensity in parentheses)

[M (2-acamb) ₂ (Hz)].xH ₂ O (where M = Ni & x = 2 and M=Co,Cd, Zn & x = 1) Hz = N ₂ H ₄ 2-acambH = 2-acetamido benzoic acid				[M(3-acamb) ₂ (Hz)].xH ₂ O (where M=Ni, Co & x = 1 and M = Cd, Zn & x = 2) Hz = N ₂ H ₄ 3-acambH = 3-acetamido benzoic acid				[M (4-acamb) ₂ (Hz)].xH ₂ O where M =Co & x =1 & M = Ni, Cd, Zn & x = 2) Hz = N ₂ H ₄ 4-acambH = 4-acetamido benzoic acid			
Ni	Co	Cd	Zn	Ni	Co	Cd	Zn	Ni	Co	Cd	Zn
	15.30 (22.20)	22.34 (3.23)						20.17 (41.67)	20.57 (65.00)		21.92 (100.00)
13.79 (29.10)	13.30 (40.00)	11.37 (100.00)	11.35 (5.56)				9.43 (33.00)	11.11 (19.00)	10.45 (32.00)	11.30 (34.00)	12.44 (42.00)
10.51 (100.00)	10.12 (100.00)	10.25 (12.90)	9.46 (100.00)								
8.95 (38.20)	8.95 (15.56)	9.19 (6.45)	9.05 (29.63)				8.00 (10.00)		8.57 (68.00)		
8.30 (45.50)	7.47 (35.56)	7.12 (4.84)	7.48 (94.44)				7.30 (8.33)	7.44 (100.00)		7.57 (50.00)	7.54 (13.00)
6.40 (54.50)	6.76 (4.44)	6.47 (6.45)	6.05 (85.19)			6.49 (98.3)	6.70 (20.00)	6.44 (19.00)	6.36 (47.00)	6.18 (12.00)	6.91 (9.00)
5.55 (32.70)	6.19 (40.00)	5.73 (29.00)	5.77 (18.52)	5.48 (71.19)		5.64 (71.67)	5.65 (30.00)	5.99 (10.00)	5.83 (100.00)	6.48 (22.00)	6.45 (36.00)
5.32 (38.20)	5.41 (37.78)	5.53 (22.58)				5.34 (30.00)	5.37 (100.00)		5.29 (63.00)		5.35 (15.00)
4.44 (5.50)	5.11 (35.56)	5.07 (16.67)	4.96 (29.63)		3.32 (87.50)	4.71 (15.00)	4.73 (48.33)	4.44 (31.00)	4.44 (58.00)	4.56 (38.00)	4.83 (58.20)
	4.86 (17.78)	4.58 (3.23)	4.75 (29.63)	4.04 (100.00)	2.50 (100.00)	4.25 (51.66)	4.17 (28.33)				4.42 (9.00)
3.98 (27.30)	4.47 (2.20)	3.95 (3.23)	4.63 (33.33)			3.96 (40.00)	3.93 (18.30)		3.78 (42.00)	3.71 (12.00)	4.11 (16.00)
3.42 (25.50)	4.13 (4.44)	3.83 (4.84)	4.39 (3.50)			3.73 (50.00)	3.69 (76.66)	3.65 (13.00)	3.31 (53.00)	3.32 (20.00)	3.95 (11.00)
	3.96 (13.33)	3.72 (3.23)	4.13 (22.22)			3.40 (46.00)	3.42 (36.00)			3.10 (16.00)	3.66 (100.00)
	3.59 (8.89)	3.56 (6.45)	4.05 (16.67)			3.17 (26.66)	3.17 (70.00)			2.84 (14.00)	3.40 (60.00)
2.81 (16.40)	3.41 (6.67)	3.39 (4.84)	3.94 (57.41)			2.92 (41.67)	3.07 (33.00)				3.11 (16.00)
2.63 (9.10)	3.11 (4.44)	3.21 (3.23)	3.87 (2.60)			2.89 (100.00)	2.91 (6.60)				2.99 (11.00)

2.50 (7.30)	3.06 (3.23)	3.76 (2.60)	2.81 (18.30)	2.83 (10.00)	2.66 (47.00)	2.84 (27.27)
	2.89 (3.23)	3.67 (9.26)	2.72 (23.33)	2.59 (15.00)	2.60 (63.00)	2.75 (7.00)
		3.39 (57.41)	2.60 (13.33)	2.48 (18.30)	2.54 (63.00)	2.58 (7.00)
		3.35 (29.63)	2.44 (20.00)	2.24 (10.00)	2.30 (47.00)	2.40 (15.00)
		3.25 (33.33)	2.24 (13.33)	2.19 (10.00)	2.14 (37.00)	2.28 (6.00)
		3.17 (7.40)	2.17 (20.00)	2.04 (15.00)	2.05 (42.00)	1.90 (14.00)
		2.90 (11.11)	2.09 (15.00)	1.85 (5.00)	1.97 (47.00)	2.17 (7.00)
		2.84 (9.26)	2.03 (16.66)	1.80 (5.00)	1.91 (74.00)	2.05 (7.00)
		2.49 (7.40)	1.96 (20.00)	1.61 (5.00)	1.84 (58.00)	1.89 (7.00)
		2.36 (11.11)	1.87 (23.33)		1.73 (37.00)	1.82 (4.00)
		2.22 (12.96)	1.79 (6.66)			1.77 (6.00)
		2.18 (7.40)	1.67 (8.33)			1.65 (4.00)
		1.98 (7.40)	1.61 (8.33)			1.55 (4.00)

[M (2-acamb)₂(Hz)].xH₂O
(where M = Ni & x = 2 and M=Co, Cd, Zn & x = 1) Hz = N₂H₄
2-acambH = 2-acetamido benzoic acid

[M(3-acamb)₂(Hz)].xH₂O
(where M=Ni, Co & x = 1 and
M = Cd, Zn & x = 2) Hz = N₂H₄
3-acambH = 3-acetamido benzoic acid

[M (4-acamb)₂(Hz)].xH₂O
where M =Co & x =1 & M = Ni, Cd, Zn & x = 2) Hz = N₂H₄
4-acambH = 4-acetamido benzoic acid

Ni	Co	Cd	Zn	Ni	Co	Cd	Zn	Ni	Co	Cd	Zn
						1.56 (5.00)			1.55 (47.00)		1.45 (4.00)
						1.52 (5.00)			1.46 (53.00)		
						1.45 (6.66)			1.42 (53.00)		
						1.42 (5.00)			1.38 (42.00)		

	1.37
	(32.00)
	1.34
	(42.00)
	1.32
	(32.00)
	1.29
	(47.00)
	1.27
	(53.00)
	1.25
	(53.00)
	1.22
	(47.00)

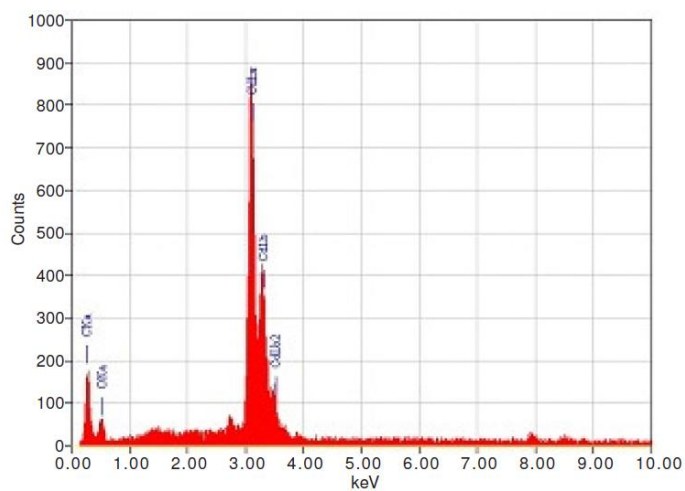


Fig. 10. SEM-EDX picture of CdO

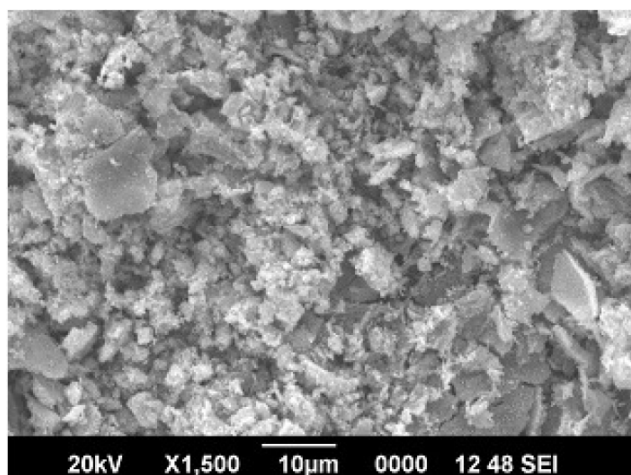


Fig. 11. SEM image of ZnO obtained from $[\text{Zn}(4\text{-acamb})_2(\text{Hz})_2\text{H}_2\text{O}]$

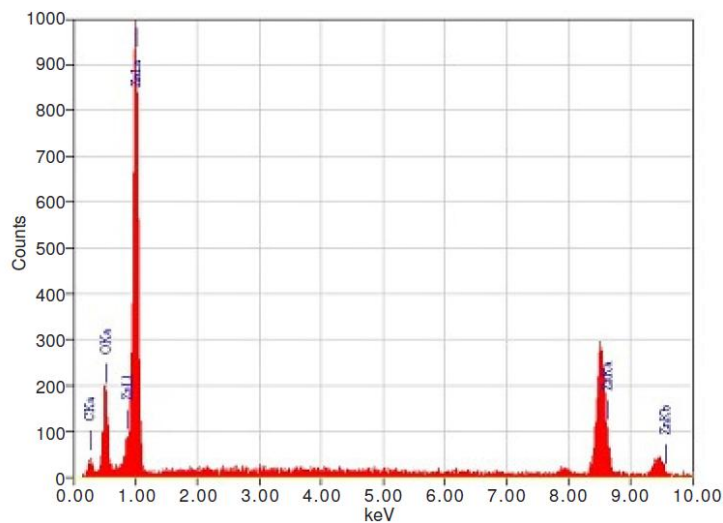


Fig. 12. SEM-EDX picture of ZnO

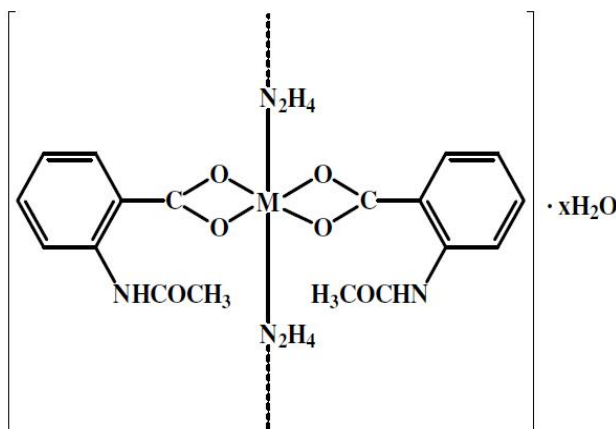


Fig. 13. Proposed structures of transition metal complexes of 2-acetamido benzoate with formula $[M(2\text{-acamb})_2(\text{Hz})] \cdot x\text{H}_2\text{O}$, where $M = \text{Ni}$ and $x = 2$; $M = \text{Co, Cd, Zn}$ and $x = 1$

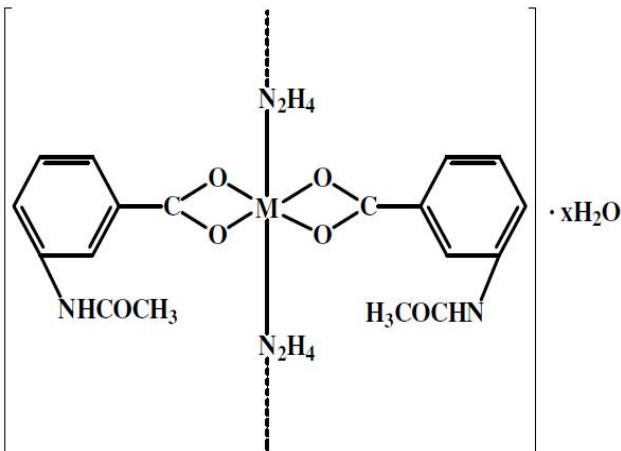


Fig. 14. Proposed structures of transition metal complexes of 3-acetamido benzoate with formula $[M(3\text{-acamb})_2(\text{Hz})] \cdot x\text{H}_2\text{O}$, where $M = \text{Ni, Co}$ and $x = 1$; $M = \text{Co, Cd, Zn}$ and $x = 2$

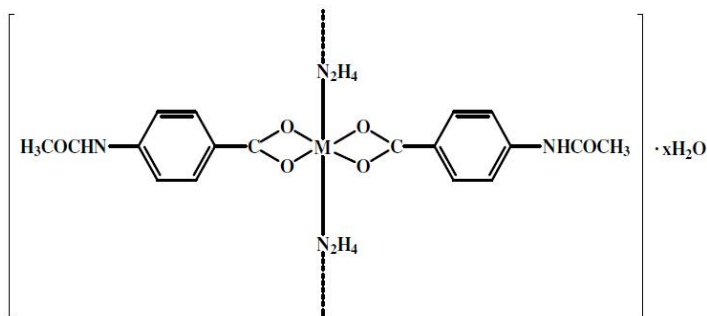


Fig. 15. Proposed structures of transition metal complexes of 4-acetamido benzoate with formula $[M(4\text{-acamb})_2(\text{Hz})] \cdot x\text{H}_2\text{O}$, where $M = \text{Ni, Cd, Zn}$ and $x = 2$; $M = \text{Co}$ and $x = 1$

4. CONCLUSION

All the three isomeric acetamido benzoic acids have formed two categories of hydrated neutral hydrazine complexes with the formulae $[M\{(2-), (3-) \text{ and } (4-) \text{ acamb}\}_2(\text{Hz})] \cdot x\text{H}_2\text{O}$ where 2-acambH =

2-acetamido benzoic acid, M = Ni and x = 2; M = Co, Cd and Zn and x = 1, 3-acambH = 3-acetamido benzoic acid, M = Ni, Co and x = 1; M = Cd and Zn and x = 2 and 4-acambH = 4-acetamido benzoic acid, M = Co and x = 1; M = Ni, Cd and Zn and x = 2. The NHCOCH₃ group is both larger and less strongly electron donating than the NH₂ group and hence has not involved in complexation.

The IR frequencies reveal the coordination of the hydrazine with metal and the coordination mode of the carboxylate ion to metal. XRD patterns show isomorphism among the 88 complexes with similar molecular formulae. The SEM-EDX studies confirm the formation of respective metal oxides. The thermal data reveals that various steps of decomposition of the compounds to form their metal oxide. The electronic spectra and the magnetic susceptibility values reveal the coordination and geometry. They suggest that Ni, Co, Cd and Zn complexes possess distorted octahedral geometry with coordination number [30]. The proposed structures of these complexes are represented in the Figs. 13-15. However, they may be confirmed by single crystal XRD only.

ACKNOWLEDGEMENTS

The authors acknowledged to All India Council for Technical education (AICTE) for granting the financial support for this work (grant in aid No./8023/BOR/RID/RPS- 2, 2008-2009).

COMPETING INTERESTS

Authors have declared that no competing interests exist.

REFERENCES

1. Sivasankar BN, Govindarajan S. Acetate and Malonate complexes of cobalt (II), nickel (II) and zinc (II) with hydrazinium cation - Preparation, spectral and thermal studies. *J. Therm. Anal. Calorim.* 1997;48:1401-1413.
2. Yasodhai S, Govindarajan S. Coordination compounds of some divalent metals with hydrazine and dicarboxylate bridges. *Synth. React. Inorg. Met.-Org. Chem.* 2000;30:745-760.
3. Kuppusamy K, Govindarajan S. Benzoate complexes of dipositive first row transition metal ions with hydrazine. *Synth. React. Inorg. Met.-Org. Chem.* 1996;26:225-243.
4. Kuppusamy K, Govindarajan S. Hydrazinium cation as a ligand: Preparation and spectral, thermal and XRD studies on hydrazinium metal phthalates. *Eur. J. Solid State Inorg. Chem.* 1995;32:997-1012.
5. Vairam S, Premkumar T, Govindarajan S. Trimellitate complexes of transition metals with hydrazinium cation. *J. Therm. Anal. Calorim.* 2010;100:955-960.
6. Vairam S, Premkumar T, Govindarajan S. Preparation and thermal behavior of divalent transition metal complexes of pyromellitic acid with hydrazine. *J. Therm. Anal. Calorim.* 2010;101:979-985.
7. Audrieth LF, Ogg BA. *Chemistry of hydrazine.* John Wiley and Sons, Inc., New York; 1951.
8. Clark CC. *Hydrazine.* Mathieson Chemical Corp., Baltimore, Md.; 1953.
9. Latimer WM. *The oxidation states of the elements and their potentials in aqueous solution.* 2nd Ed., Prentice-Hall, Inc., New York; 1952.
10. Furst A, Berlo RC, Hooton S. Hydrazine as a reducing agent for organic compounds (catalytic hydrazine reductions). *Chemical Reviews.* 1965;65(1):51-68.
11. Gajapathy D, Govindarajan S, Patil KC, Manohar H. Synthesis, characterization and thermal properties of hydrazinium metal oxalate hydrates – crystal and molecular structure of hydrazinium copper oxalate monohydrate. *Polyhedron.* 1983;2:865.
12. Govindarajan S, Patil KC, Poojary MD, Manohar H. Synthesis, characterization and X-ray structure of hexahydrazinium diuranil pentaoxalate dihydrate, (N₂H₅)₆(UO₂)₂(C₂O₄)₅·2H₂O. *Inorg. Chim. Acta.* 1986;120:103-107.
13. Premkumar T, Govindarajan S. Preparation and thermal behaviour of transition metal complexes of 4,5-imidazoledicarboxylic acid. *J. Therm. Anal. Calorim.* 2003;74:325-333.
14. Premkumar T, Govindarajan S. Transition metal complexes of pyrazinecarboxylic acids with neutral hydrazine as a ligand. *J. Therm. Anal. Calorim.* 2005;79:115-121.

15. Arunadevi N, Vairam S. 3-Hydroxy-2-naphthoate complexes of transition metals with hydrazine - preparation, spectroscopic and thermal studies. *E.-J. Chem.* 2009;6(S1):S413-421.
16. Premkumar T, Govindarajan S. The chemistry of hydrazine derivatives—thermal behavior and characterisation of hydrazinium salts and metal hydrazine complexes of 4,5-imidazolecarboxylic acid. *Thermochim Acta.* 2002;386:35-42.
17. Premkumar T, Govindarajan S. Divalent transition metal complexes of 3,5-pyrazoledicarboxylate. *J. Therm. Anal. Calorim.* 2006;84:395-399.
18. Vikram L, Sivasankar BN. Hydrazinium metal(II) and metal(III) ethylenediamine tetraacetate hydrates. *J. Therm. Anal. Calorim.* 2008;91:963-970.
19. Raju B, Sivasankar BN. Spectral, thermal and X-ray studies on some new *Bis*-hydrazine lanthanide(III) glyoxylates. *J. Therm. Anal. Calorim.* 2008;94:289-296.
20. Yin X, Fan J, Wang Z, Zhang WG. Synthesis, crystal structures and photoluminescence of lanthanide coordination polymers with 4-acetamidobenzoate. *Z. Anorg. Allg. Chem.* 2011;637:773-777.
21. Wang ZH, Fan J, Zhang WG. Studies of Radii-dependent lanthanides coordination behaviour with 4-Acetamido benzoate and 1,10-Phenanthroline. *Z. Anorg. Allg. Chem.* 2009;635:2333-2339.
22. Li W, Li CH, Yang YQ, Kuang YF. Hydrothermal synthesis, crystal structure and thermal stability of the complex $[Zn(p-ABA)_2(phen) \cdot (H_2O)] \cdot H_2O$. *Chin J Inorg Chem.* 2007;23:2023-27.
23. Wang YB, Zheng XJ, Zhuang WJ, Jin LP. First examples of ternary lanthanides 2,2'-diphenyl dicarboxylate complexes: Hydrothermal synthesis, structure of lanthanide coordination polymers of 2,2'-diphenyl dicarboxylic acid and 1, 10 phenanthroline. *Eur. J. Inorg. Chem.* 2003;3572-82.
24. Mascarenhas YP, de Almeida VN, Lechat JR, Barelli N. *N*-Acetylanthranilic acid (*o*-acetamidobenzoic acid), a strongly triboluminescent material. *Acta Cryst.* 1980;B36:502-504. DOI: <https://doi.org/10.1107/S0567740880003688>
25. Li W, Li CH, Yang YQ, Kuang YF. Hydrothermal synthesis, crystal structure and Electrochemical properties of the complex $[Cu(o-ABA)_2(2,2'-bipy)] \cdot (H_2O)$. 2007;23:2027-2030.
26. Junior DV, Tilley JW, Lemahieu RA. Practical, catalytic synthesis of anthranilic acids. *J. Org. Chem.* 1981;46:4614-4617.
27. Manin AN, Voronin AP, Perlovich GL. Acetamidobenzoic acid isomers: Studying sublimation and fusion processes and their relation with crystal structures. *Thermochimica Acta.* 2014;583:72-77.
28. Almeida Ana RRP, Sousa Carlos AD, Santos Luís MNBF, Monte Manuel JS. Thermodynamic properties of sublimation of the ortho and meta isomers of acetoxy and acetamido benzoic acids. *Journal of Chemical Thermodynamics.* 2015;86:6-12. ISSN: 0021-9614.
29. Vogel IA. *A text book of quantitative inorganic analysis.* Longmans, London. 1975;380,433.
30. Lever ABP. *Inorganic electronic spectroscopy.* Elsevier, Amsterdam; 1984.
31. Nakamoto K. *A text book of infrared and Raman spectra of inorganic and coordination compounds.* John Wiley and Sons, USA. 1986;228-229.
32. Weast RC, *CRC hand book of chemistry and physics.* CRC Press: Cleveland, Ohio; 1976/1977.

Biography of author(s)



Dr. E. Helen Pricilla Bai

Department of Chemistry, Park College of Engineering and Technology, Kaniyur, Coimbatore-641 659, India.

She is currently working as a Professor of Chemistry in Park College of Engineering and Technology, Kaniyur-641659, Coimbatore District, India. She has acquired 15 years of Professional experience in teaching at University level and rich experience in Research as well. She had successfully completed an AICTE - RPS Project Worth 5.25 lakhs. She along with Dr. S. Venkatachalapathy were jointly sanctioned with partial financial assistance for the conduction of a national level seminar entitled "Heuristic approach on nano based batteries and Green Chemistry" from Tamil Nadu State Council for Science and Technology during 2019. She carried out a collaborative M.E Project (Aeronautical) of PCET with NAL Bangalore in a CSIR sponsored project titled 'Satellite Micro thrusters' using CEA program of NASA. She had acted as joint supervisor for various B.E final year projects. She was appointed as the session chair for many International conferences. Four of her papers were published in reputed journals, 4 publications in national and international conferences and authored 2 Engineering Chemistry books as well. Her expertise was utilized in one of the leading Journal "Advances in Applied Research" and valued as a recognized reviewer. She had attended a short term training Program entitled "Recent trends in Atmospheric sciences" at IIT-Madras. Furthermore she had participated in a national level workshop at Chandigarh organized by SASE-DRDO in association with CRREL, US Army Corps of Engineers, Hanover, USA to discuss "Issues and Advancements of De-icing and Anti-icing Systems". She continues to be the source of inspiration by offering guest lectures at various Engineering and Science (PG) Research Institutions.



Dr. S. Vairam

Department of Chemistry, KPR institute of Engineering and Technology, Arasur, Coimbatore - 641407, Tamil Nadu, India.

He worked as a Professor of Chemistry for 33 years at Government College of Technology, Coimbatore-13, and India. He is currently serving as Professor of Chemistry and Controller of Examinations at KPR Institute of Engineering and Technology, Arasur, Coimbatore-407, India, after his retirement from government service. His area of research is Solid state Inorganic chemistry and he is at present pursuing his research on polymeric metal complexes and carbon- nano metal oxide composites. He has published around 52 research papers in reputed International and National journals, and authored 4 books in Engineering Chemistry and Environmental Science, among which one is being published by Wiley India. He has been awarded certificates as recognized reviewer by many Elsevier and RSC journals, and as outstanding reviewer by the journal, Environmental Chemical Engineering. He has successfully guided 12 PG students for their dissertations and 11 PhD Scholars. He has 34 years of experience in teaching profession at the University level. He has also operated one AICTE Research project and completed two TEQIP projects in collaboration with Department of Civil Engineering and Electrical Engineering in the Centre of Excellence. He has conducted several national conferences and Faculty Development Programs in Government College of Technology, Coimbatore. He has completed many assignments of Anna University, Chennai-25, as an executive member in Boards of studies of many Engineering Colleges of Tamilnadu, and Inspection committee member for the award of Anna University recognition of Research Laboratory and University Affiliation Committee member.

© Copyright (2020): Author(s). The licensee is the publisher (Book Publisher International).

DISCLAIMER

This chapter is an extended version of the article published by the same author(s) in the following journal.
Asian Journal of Chemistry, 25(1): 209-216, 2013.

Studies on the Formulation of Sustained Release Zolpidem Tartrate Matrix Tablets through Optimization and Their Evaluation

Masheer Ahmed Khan^{1*} and S. C. Chaturvedi¹

DOI: 10.9734/bpi/cpcs/v2

ABSTRACT

The objective of the present study was to develop a sustained release system of the hypnotic agent zolpidem useful for the treatment of insomnia. Matrix tablet is the least complicated device to sustain the release of drug candidates. Two polymers HPMCK4M and HPMCK15M were selected to sustain the release up to 12 h. Optimization techniques using factorial design for two factors at three levels (3^2) was selected to optimize varied response variables viz., release rate exponent (n), t_{50} %, k, amount of drug released in 12 h and mean dissolution time. Software Zorel was used to calculate the release kinetics. The design expert software was used to generate ANOVA for selected five responses Furthermore, the *in vitro* and *in vivo* studies were performed with newly formulated sustained- release zolpidem tablets and were compared with conventional marketed tablet (zoldem). *In vivo* investigation in rabbits showed sustained- release pharmacokinetic profile of zolpidem from the matrix tablets formulated using combination of HPMCK4M and HPMCK15M. In conclusion, the results suggest that the developed sustained-release matrix tablets could provide quite regulated release of zolpidem tartrate up to nearly 12 h. Conclusively, the current study attained the successful design, development and optimization of formulation of zolpidem tartrate matrix tablets.

Keywords: Zolpidem tartrate; matrix tablets; sustained release; HPMC; polymer; factorial design.

1. INTRODUCTION

A computer optimization technique, based on response-surface methodology has proven to be a useful approach for selecting pharmaceutical formulations. Factorial designs are the most popular response surface designs [1-3]. A factorial design for two factors at three levels (3^2) which is equivalent to a central composite design (CCD) for two factors was selected to optimize varied response variables viz., release rate exponent (n), t_{50} %, k, amount of drug released in 12 h and mean dissolution time (MDT) [4,5]. Extended-release drug delivery system releases the drug over a longer period of time or the drug is penetrated or absorbed over an extended period of time [6,7].

In particular zolpidem (ZP), N,N,6-trimethyl-2-p-tolylimidazol[1,2-a]pyridine- 3-acetamide-L-(+)-tartrate (2:1), exhibits strong hypnotic and sedative action with negligible anxiolytic, muscle relaxant or anticonvulsant properties and is widely prescribed for the treatment of the insomnia and sleep disorders. It binds in the central nervous system to GABA a receptors. The pharmacokinetic profile of zolpidem is characterized by rapid absorption from gastro intestinal tract and a short elimination half-life (2.5 h). Due to the short elimination half-life, the plasma drug concentration cannot be achieved during late hours of sleep. It could be useful to develop formulations enabling sustained release of this drug for elucidating the potential of zolpidem in the treatment of different insomnia categories. Zolpidem is used in decreasing the time to sleep, onset and increasing total sleep time; but, its effect on sleep maintenance has not been systematically explained [8,9].

¹School of Pharmacy, Devi Ahilya Vishwavidyalaya, Takshshila Campus, Khandwa Road, Indore, M.P., India.

*Corresponding author: E-mail: masheerak@yahoo.com;

Zolpidem is marketed in US, India and elsewhere in immediate release tablets. More recently, controlled release tablets have been introduced into the US market, which are two layer tablets and require use of specialized equipment. Therefore, the object of the present study is to develop matrix tablets to provide sustained release of the drug content up to 12 h [10-15].

Matrix tablet is the least complicated approach in devising a sustained release dosage form. This involves the direct compression of blend of drug, retardant material and additives to form a tablet in which the drug is embedded in a matrix core of the retardant. Hydrophilic matrices are well mixed composite of one or more drugs with a hydrophilic polymer. Hydrophilic matrices possesses major advantages over other alternatives in developing oral controlled release drug delivery as they have a capacity to incorporate large doses of drugs, these can't be disintegrated throughout the GI tract so the dose dumping is not there [16-19].

In the current study different grades of HPMC like methocel K4M, K15M and K100M were selected during preliminary studies for regulating the release of zolpidem tartrate. Two polymers HPMCK4M and HPMCK15M were further selected for optimization studies [20,21].

2. EXPERIMENTAL

Zolpidem tartrate was obtained as a gift sample from Ranbaxy Labs. Ltd., Dewas, (M.P.), methocel (K4M, K15M, K100M) were provided by Colorcon India Ltd., Goa, dicalcium phosphate, microcrystalline cellulose (Avicel), talc, magnesium stearate and all other reagent used were of analytical grade.

2.1 Pre-Optimization Studies

Nine formulations employed for pre-optimization investigations containing different ratios of HPMC of different grades, keeping the total tablet weight constant at 120 mg. The tablets were prepared by direct compression. The values of response variables viz. n , released in 12 h, mean dissolution time, t_{50} , t_{70} and t_{80} % were studied to help in choosing the best possible combination for further optimization studies.

2.2 Factorial Design

The 3^2 factorial design was selected using two factors (polymers) at three levels and the factor levels were suitably coded. Nine formulations were prepared as per the design and coded F1, F2, F3, ..., F9. The two polymers HPMCK4M and HPMCK15M were selected and their limits were chosen for subsequent detail studies using the factorial design. The amount of drug, magnesium stearate and talc were kept constant while dicalcium phosphate was taken in sufficient quantity to maintain a constant tablet weight of 120 mg. The translation of the coded factor level as amount of ingredients is listed in Table 1.

Table. 1. Translation of experimental conditions into physical units

Coded factor	Level	Factor(X1)	Factor (X2)	Units
		HPMC K ₄ M	HPMC K ₁₅ M	
-1	Low	15	10	mg
0	Intermediate	20	15	mg
1	High	25	20	mg

2.3 Preparation of Tablets and Physical Evaluation

Tablet batches consisting of 100 tablets were prepared by direct compression method. All the product and process variables (other than the concentration of two polymers) like mixing time, compaction force, etc., were kept constant. Ten tablets from each batch were weighed individually and subjected to physical evaluation.

2.4 Dissolution Studies

Dissolution studies were carried out for all the nine formulations in triplicate, employing dissolution apparatus, using distilled water pH 6.3 as the dissolution medium at 50 rpm and $37 \pm 0.5^\circ\text{C}$. An aliquot of sample was periodically withdrawn at suitable time intervals and volume replaced with equivalent amounts of plain dissolution medium. The samples were analyzed at 245 nm.

2.5 Data Analysis

The raw data obtained from *in vitro* dissolution was analyzed using the ZOREL software. The software has in built provisions for calculating the values of amount of drug release, percentage of drug release, log fraction released at various time interval, log time, mid-point of time intervals and rate of drug release [22-24].

The software also calculates the kinetic constant (K), the diffusional release exponent (n) using logarithmic transformation, based on phenomenological analysis, the type of release, whether Fickian, non-Fickian (anomalous) or zero-order, was predicted. The software also calculates coefficient of determination (R^2), standard error of estimation (SEOE), significance test 't' values and 'p' values. The response variables, which were considered for optimization included, n, mean dissolution time (MDT), release at 12 h, t_{50} %.

The design expert software generates the second order polynomial equation with added interaction terms to correlate the studied responses with the examined variables. The polynomial regression results were demonstrated using 3-D plots and contour plots. Finally, the prognosis of optimum formulation was conducted in two stages. First, a feasible space was located and second, an exhaustive grid search was conducted to predict the possible solutions. Six optimum formulations were selected by the critical evaluation of the tabulated grid search values.

2.6 Validation of the Predicted Formulation

The tablet formulations were compressed using the chosen optimal composition and evaluated for physical test, tablet assay and dissolution performance. The observed and predicted responses were critically compared.

2.7 In vivo Evaluation

In vivo evaluation was carried out in rabbits for selected optimized formulation of zolpidem tartrate tablet in comparison with one marketed conventional formulation. Evaluation was carried by established HPLC method to check the bioavailability of the formulation [25,26]. Analyses were performed on a Shimadzu (Japan) liquid chromatographic system composed of SPD-M 10 AVP variable wavelength detector, LC-10 ATVP pump and analytical column C₁₈.

Rabbits of either sex weighing (2.2-2.6 kg) were divided into two groups each consisting of three animals. First group received marketed tablets and second group received the formulated optimized tablets. Food was withdrawn from the rabbit 12 h before drug administration. All rabbits had free access to water throughout the study. The institutional animal ethical committee approved the protocol for this study.

2.8 HPLC Assay

The quantitative determination of drug in plasma was performed by HPLC assay using the mobile phase acetonitrile and disodium hydrogen phosphate in the ratio 40:60. Before analysis, the mobile phase was filtered and degassed. The flow rate was adjusted at 1.2 mL/min. All determination was performed at 245 nm wavelengths at room temperature.

2.9 Bioavailability Studies

Blood samples were collected in tubes from marginal ear vein at defined time intervals. Collected blood was centrifuged at 5000 rpm for 5 min (Remi equipment, Mumbai, India). Plasma was

separated then acetonitrile was added for protein precipitation. The tubes were centrifuged for 5 min at 5000 rpm. The supernatant layer was filtered through 0.45 μm filter and the sample was reconstituted with 500 μL of mobile phase and again agitated for 30 s. The drug concentration in the sample was then determined by assay.

2.10 *In vitro-in vivo* Correlations

Model independent pharmacokinetic parameters were computed from blood level data. Subsequently by plotting per cent of drug release *versus* per cent of drug absorbed the *in vitro-in vivo* correlation performed.

3. RESULTS AND DISCUSSION

3.1 Pre-Optimization Studies Results

The data obtained during the pre-optimization studies reveals that as the molecular weight or the viscosity of the polymer increases, release rate of the drug from the formulation decreases. These studies help in the selection of the appropriate range of polymer for the further optimization studies.

Fig. 1a and 1b shows the swelling behavior of zolpidem matrix tablet formulations at different time intervals, the top view and side view, respectively. The top view shows the radial swelling increase and the side view indicates the axial swelling increase with the increase in dissolution time (coded in Fig. 1 as A-G from 1-12 h time intervals).

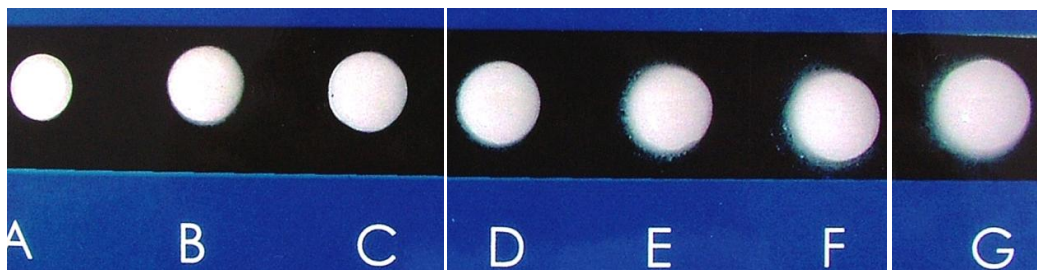


Fig. 1(a). Top view (swelling behavior of Zolpidem, matrix tablet formulations at different time intervals)

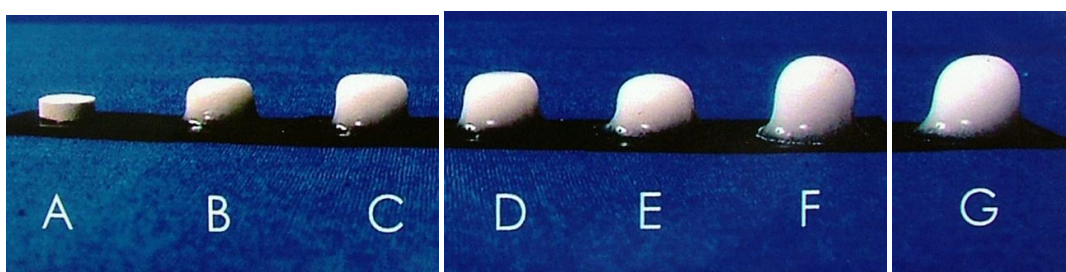


Fig. 1(b). Side view, (swelling behavior of Zolpidem, matrix tablet formulations at different time intervals)

3.2 Physical Evaluation and Assay of Tablet

The tablet weights of all the nine batches vary between 120 and 125 mg, diameter between 6.8-6.81 mm, thickness between 2.8-2.81 mm and tablet hardness between 5.5-5.9 Kg.

The assay values varied between 95.83-98.75%. The tablet friability ranged between 0.5-0.8%. The physical parameters of the manually compressed tablets were found within control.

3.3 Release Profile Studies

The dissolution parameters of nine formulations as per design containing HPMCK4M and HPMCK15M polymer combination with different ratios, obtained are shown in the Table 2. Fig. 2 shows the release pattern between per cent drug releases *versus* time.

Table 2. Dissolution parameters of (K4-K15) polymer combinations with different ratios during Optimization studies using 32 factorial design

Formulation code	n	k	MDT	Rel 12 hr	Rel 24 hrt	50% t	60% t	80% t	90% t	da/dt
F1	0.5565	0.2983	3.148	103.35	—	2.529	3.509	5.885	7.272	1.457
F2	0.5299	0.2799	3.8268	93.71	—	2.987	4.214	7.251	9.056	1.244
F3	0.5144	0.2433	5.302	89.9	—	4.057	5.782	10.116	12.719	1.013
F4	0.5011	0.2522	5.2197	91.25	—	3.918	5.639	10.019	12.677	1.167
F5	0.4768	0.25	5.9073	88.08	—	4.268	6.261	11.464	14.686	1.009
F6	0.4711	0.2467	6.2476	84.47	102.62	4.479	6.597	12.149	15.6	0.955
F7	0.4698	0.2509	6.0634	86.23	103.34	4.338	6.395	11.797	15.158	0.977
F8	0.4548	0.2295	7.9448	75.26	86.18	5.536	8.266	15.559	—	0.834
F9	0.428	0.2506	7.5954	74.39	94.5	5.018	7.683	15.045	19.811	0.862

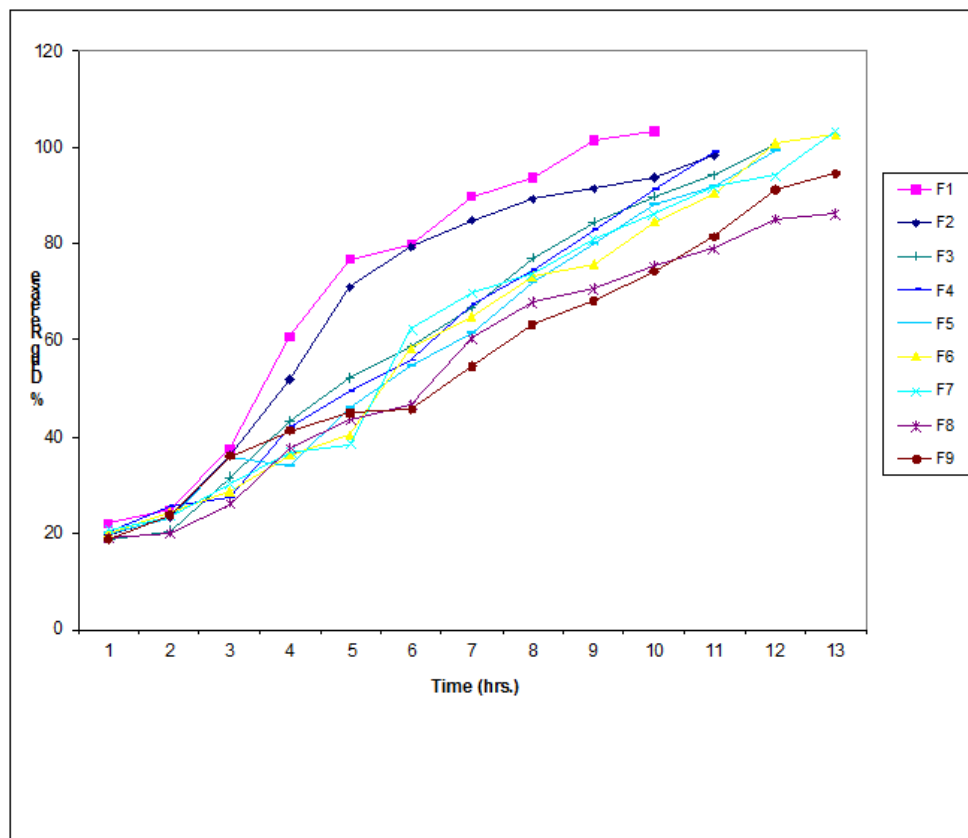


Fig. 2. Plot between percent drug release and time for combinations as per factorial design

3.4 Response Surface Analysis-Calculation of Coefficient

The coefficients of the polynomial equations for five responses n, k, released in 12 h, mean dissolution time and t_{50} % are listed Table 3 along with their values of R^2 . Five coefficients (B_1 - B_4) were calculated with B_0 as the intercept. Since the values of R^2 are quite high for released in 12 h, t_{50} %, n and mean dissolution time, so for these responses, the polynomial equations form excellent fits to all the experimental data and statistically valid. Further the model diagnostic plots are plotted to investigate the goodness of fit of the proposed model. Actual *versus* predicted, graph was plotted between the actual and the predicted response values. Residual *versus* predicted, graph was also plotted. Residual (or error) is the magnitudinal difference between the observed and the predicted response(s). These plots were obtained by use of software and shown in Fig. 3 for various responses.

3.5 Search for Optimum Formulations

The criterion for selection of suitable feasible region (shown with highlighted cells) was primarily based on highest possible values of n, released in 12 h, mean dissolution time and t_{50} %. Two regions were selected on the basis of following criteria.

Region 1

rel 12 hr >95%; n > 0.50; MDT > 3.1; t_{50} % > 2.5 hr.

Region 2

rel 12 hr >96.9; n > 0.52; MDT > 4.1; t_{50} % > 3.5 hr

The response surface plot and contour plots known to facilitate an understanding of the contribution of the variables and their interactions are shown in Fig. 4.

3.6 Validation of Optimum Formulation

The results of the physical evaluation and tablet assay of the optimized formulation were within limits. Dissolution parameters like n, k, mean dissolution time, released in 12 h and k were tabulated for six optimized matrix tablets formulation coded A-F and shown in Table 4.

Table 3. Values of the coefficient for the polynomial equations and R^2 for various response variables of the formulations

Coefficient	n	MDT	Rel 12th Hr.	t_{50}	k
B0	0.490	5.700	87.400	4.130	0.260
B1	-0.038	1.510	-8.780	0.840	-0.012
B2	-6.156	0.097	0.530	0.096	-6.078
B3	-0.018	0.690	-4.480	0.390	-8.844
B4	-1.989	0.200	-1.720	0.140	-2.578
Rsquare	0.989700	0.943800	0.966600	0.891000	0.637500

Actual *versus* predicted and residual *versus* observed, graph was also plotted between the actual and the predicted responses of optimized formulations Fig. 5a-5d. Comparisons of the observed responses with that of the anticipated responses along with percentage error were done (Table 5). As per cent error in prognosis was minimum, hence the prognostic ability of matrix tablet formulations of zolpidem tartrate using RSM optimization validated.

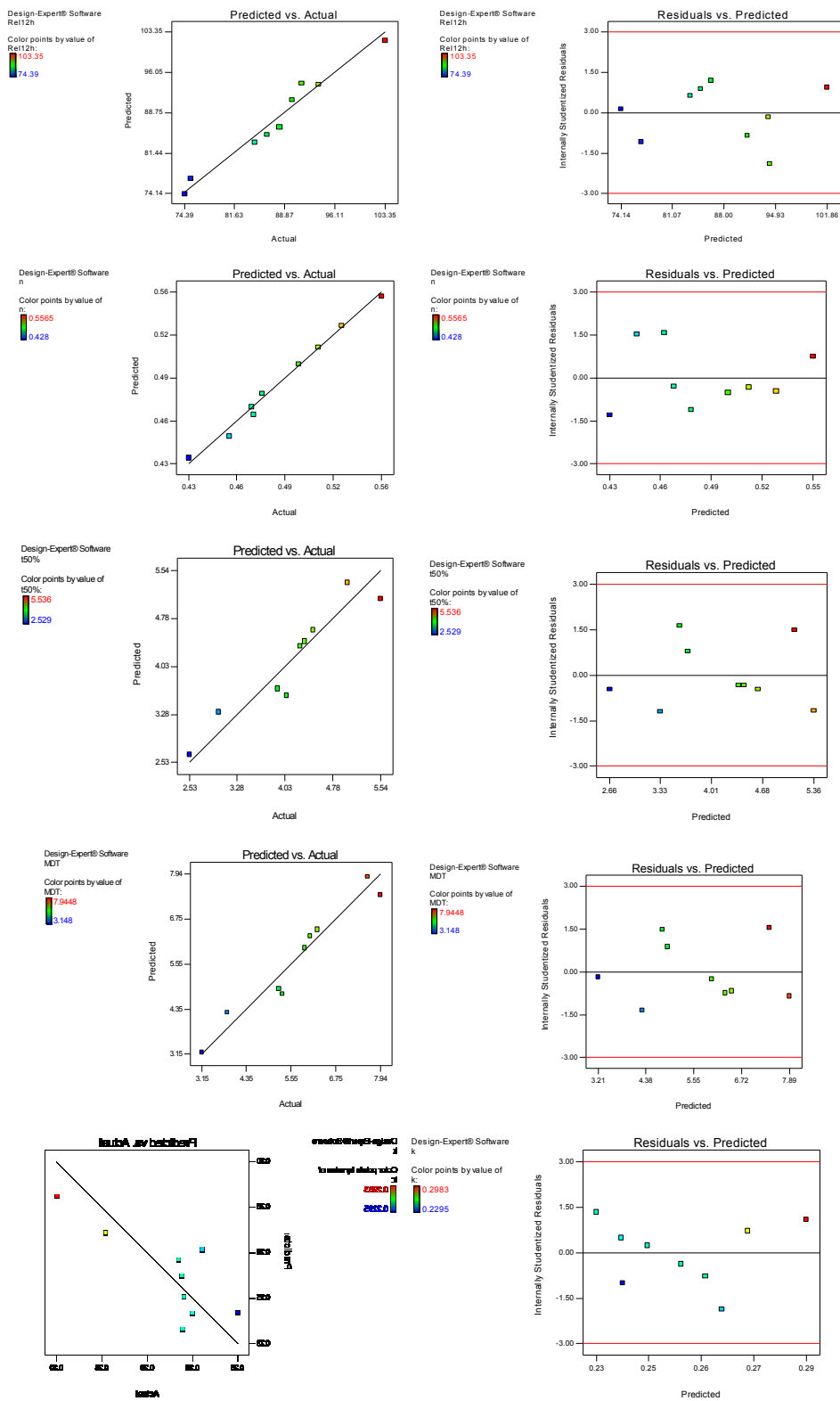
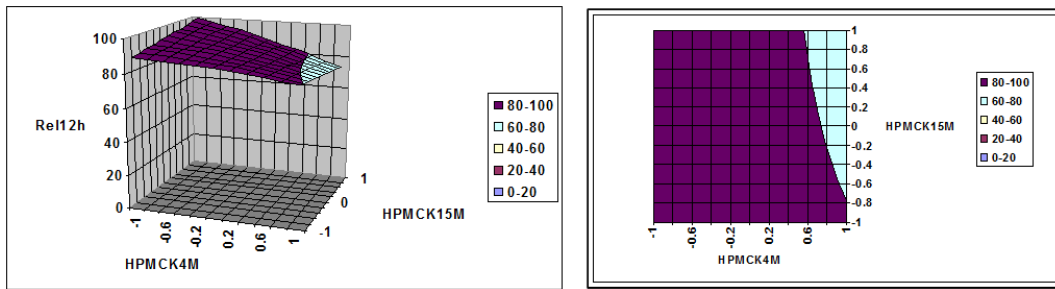
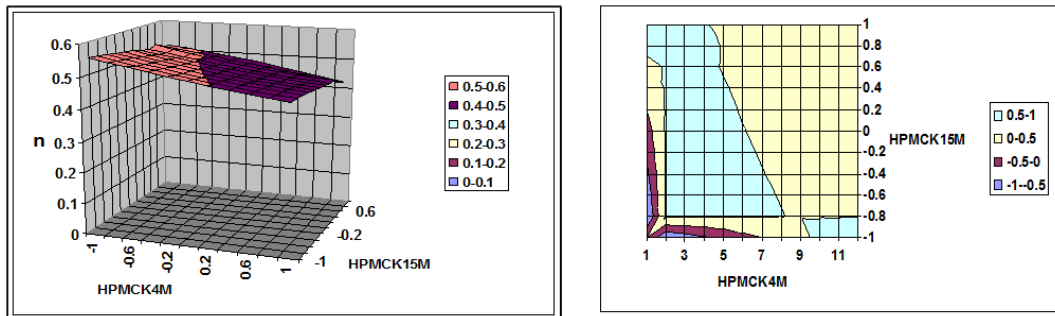


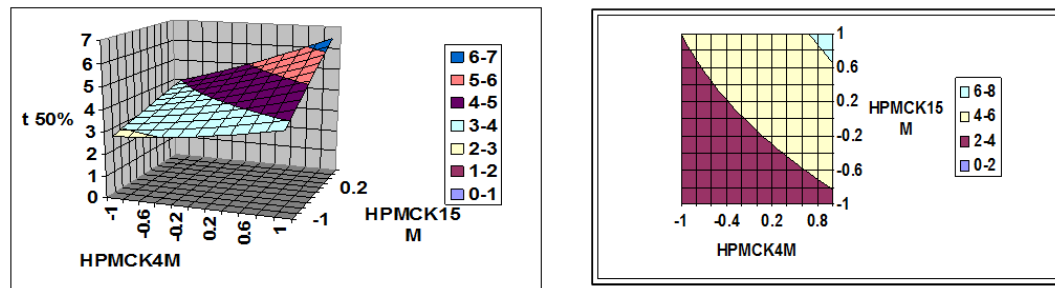
Fig. 3. Plots between actual and predicted responses



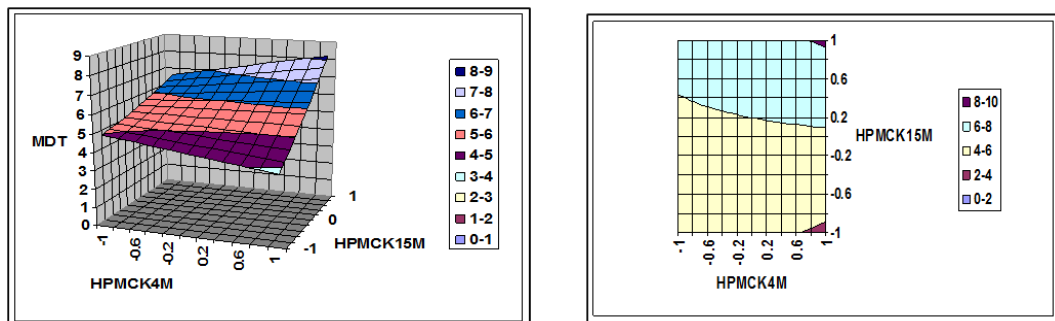
Response surface and contour plots for values of Rel 12 h



Response surface and contour plots for values of n



Response surface and contour plots for values of t 50%



Response surface and contour plots for values of MDT

Fig. 4. Response surface and contour plots for various responses

Table 4. Values of release parameters of six optimized matrix tablet formulations of Zolpidem tartrate using different amounts of HPMCK4M and HPMCK15M

Formulation composition			n	k	MDT	Rel 12h	t50%
HPMC K4	HPMC K15	Code					
14.4	12	A	0.5219	0.260	4.090	97.80	3.859
14.4	11.2	B	0.5210	0.2490	4.1179	96.94	3.777
15	4	C	0.5330	0.2417	4.2706	94.65	3.557
15	4.8	D	0.5310	0.237	4.2460	95.45	3.589
13.8	12	E	0.538	0.2466	4.149	96.79	3.675
13.8	11.2	F	0.519	0.2530	4.175	96.60	3.80

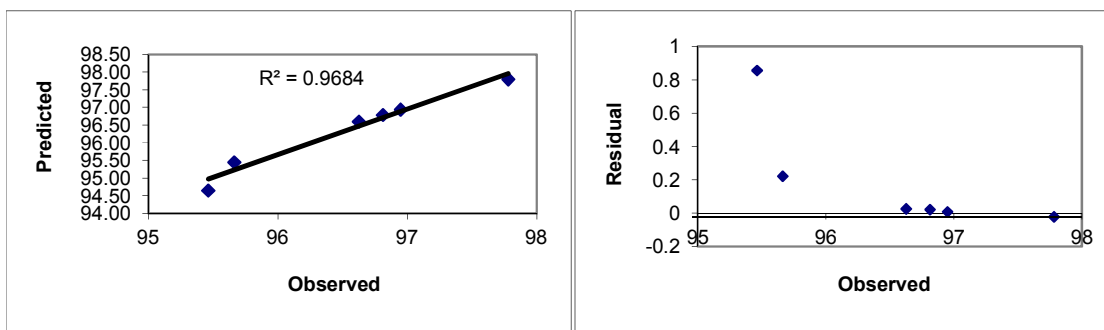


Fig. 5(a). Linear and residual plots between observed and predicted values of Rel12

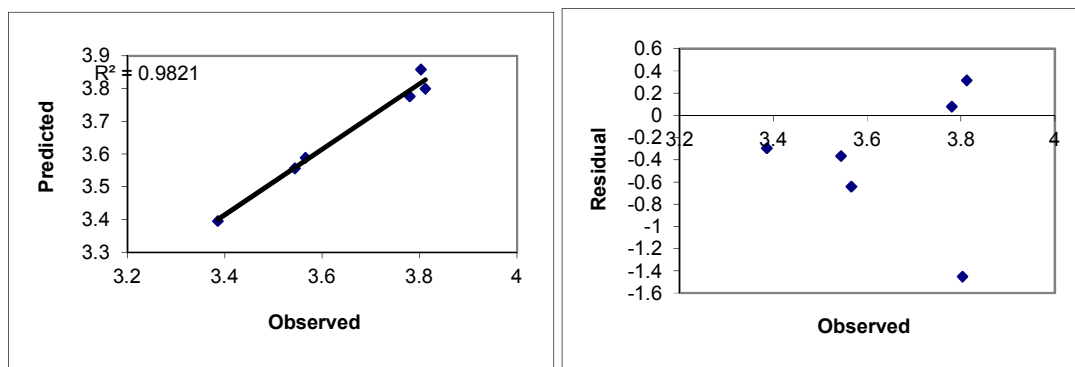


Fig. 5(b). Linear and residual plots between observed and predicted values of t50%

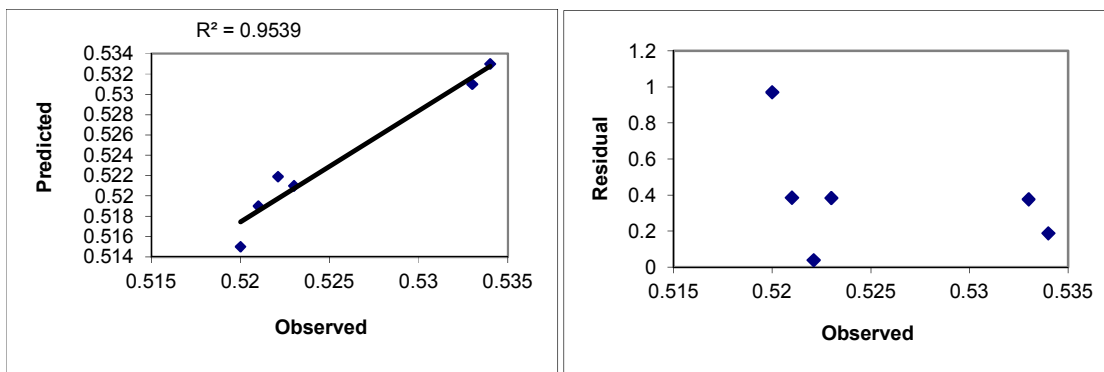


Fig. 5(c). Linear and residual plots between observed and predicted values of n

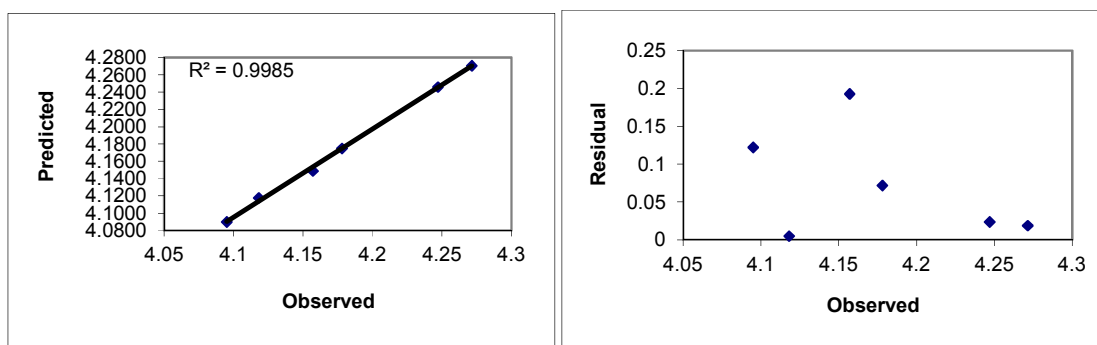


Fig. 5(d). Linear and residual plots between observed and predicted values of mdt

3.7 In-vivo Evaluation

Plasma concentration and pharmacokinetic parameters after oral administration of one optimized matrix tablets and conventional tablets were summarized (Table 6). Chromatogram and peak reports of plasma concentration were obtained by HPLC at different intervals [Fig. (6a-6e)]. The following parameters were calculated using non compartmental model: area under the plasma concentration-time curve from zero to last measurable zolpidem concentration sample time, maximum plasma drug concentration (C_{max}) and time to reach C_{max} (T_{max}). The values of C_{max} and T_{max} were obtained directly from the concentration curve and AUC was calculated (Fig. 7).

3.8 In-vitro-in-vivo Correlation

A good correlation between the dissolution profile and bioavailability was observed. *In vitro-in vivo* correlation was determined by plotting a graph showing the fraction of drug absorbed *versus* the fraction of drug released *in vitro* (Fig. 8).

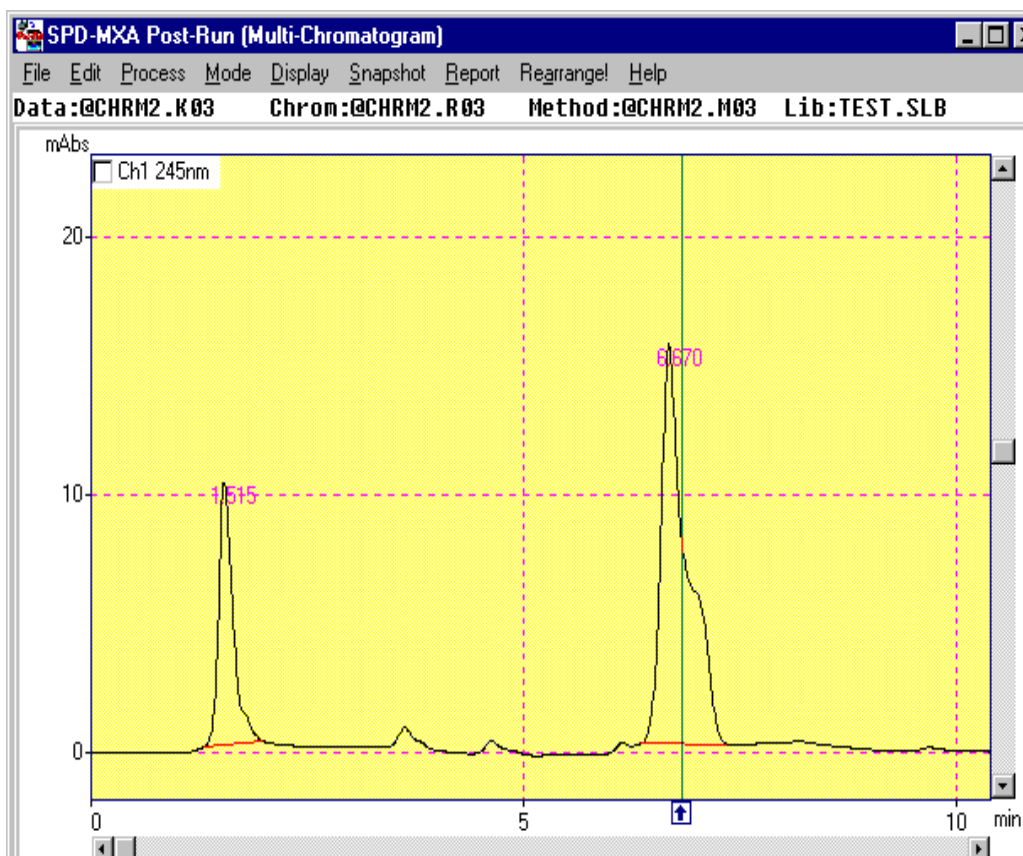
The dissolution data indicates that as the content of HPMCK4M and HPMCK15 increased, the value of n was found to decrease, except when HPMCK4M content increased from intermediate to high level. In general the release pattern tends to approach Fickian release with increase in polymer content.

The values of k showed however no distinct trend with increase in concentration of polymers. The value remained practically invariant ranging from 0.2295-0.2983. This is in accordance with the characteristic nature of the kinetic constant, which is a function of the proportion of the matrix polymer *viz.*, solubility, molecular weight, viscosity, *etc.* It depicts insignificant change in overall polymer characters.

Table 5. Comparison of experimental results with predicted responses for Zolpidem tablets

Composition	Response	Predicted value	Experimental value	Percentage error
HMPCK4/HPMCK15M				
14.4/12	Rel 12h	97.78	97.800	-0.020
	t50%	3.803	3.8590	-1.451
	n	0.5221	0.5219	0.038
	MDT	4.095	4.0900	0.122
14.4/11.2	Rel 12h	96.949	96.940	0.009
	t50%	3.780	3.7770	0.079
	n	0.523	0.5210	0.384
	MDT	4.1181	4.1179	0.005
15/4	Rel 12h	95.462	94.650	0.858
	t50%	3.544	3.5570	-0.365
	n	0.534	0.5330	0.188
	MDT	4.2714	4.2706	0.019

Composition		Response	Predicted value	Experimental value	Percentage error
HMPCK4/HPMCK15M					
15/4.8	Rel 12h		95.663	95.450	0.223
	t50%		3.566	3.5890	-0.641
	n		0.533	0.5310	0.377
	MDT		4.247	4.2460	0.024
13.8/12	Rel 12h		96.812	96.790	0.023
	t50%		3.386	3.3960	-0.294
	n		0.520	0.5150	0.971
	MDT		4.157	4.1490	0.193
13.8/11.2	Rel 12h		96.626	96.600	0.027
	t50%		3.812	3.8000	0.316
	n		0.521	0.5290	-1.512
	MDT		4.178	4.1750	0.071



Peak Report - @CHRM2.K03								
PKNO	ChNO	TIME	AREA	HEIGHT	MK	PURITY_UP	PURITY_DOWN	IDNO
1	1	1.515	119504	10212				
2	1	6.670	323349	15537				
TOTAL			442852	25749				

Fig. 6(a).

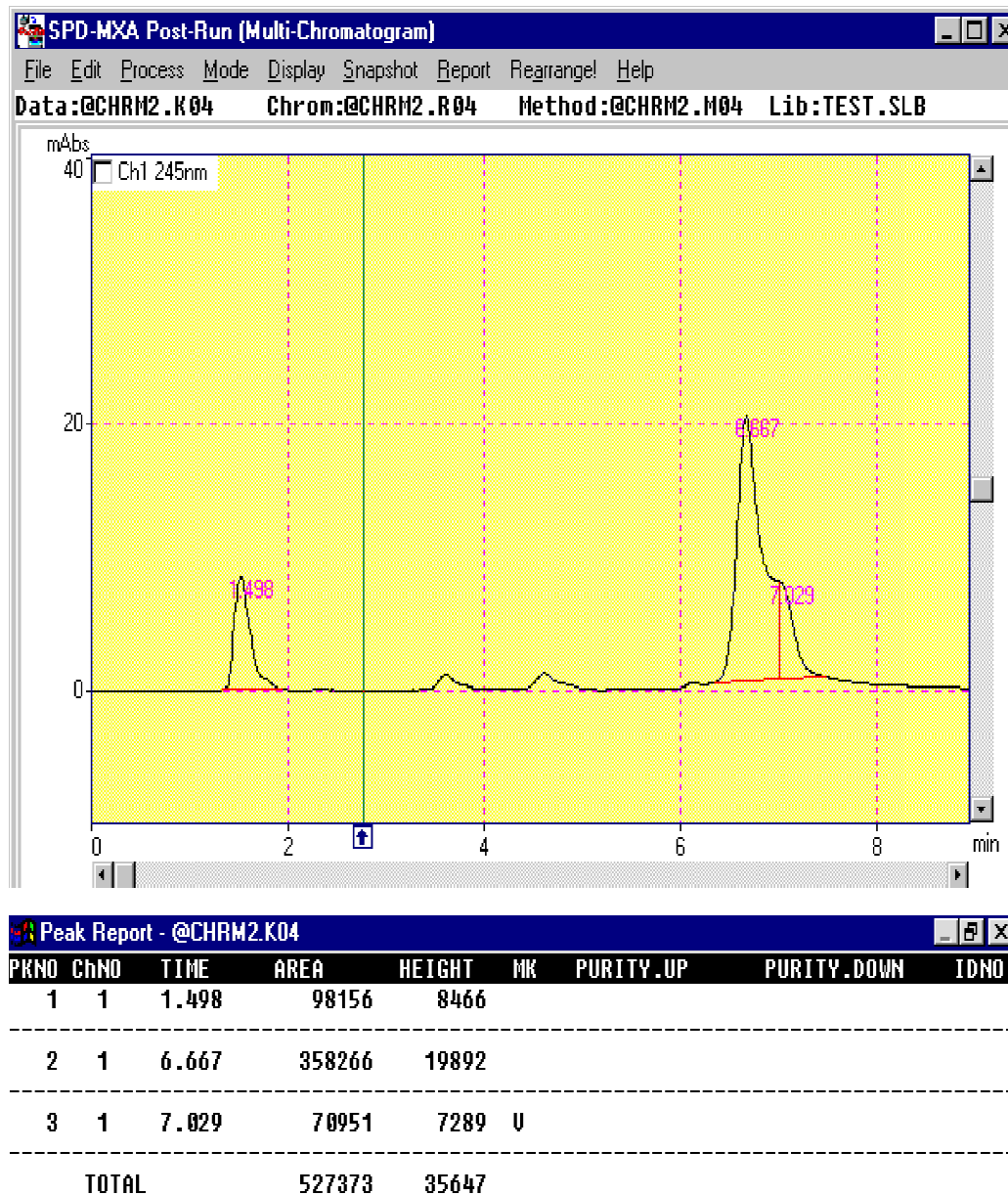


Fig. 6(b).

The values of drug released in 12 h showed that with an increasing total polymer content resulted in the decrease in the drug release. The inverse relationship is there between the total polymer content and drug release.

The value of overall rate of release decreases with increasing concentration of HPMCK4M and HPMCK15M from low to intermediate levels. Increasing the concentration to high level of HPMCK4M and HPMCK15 did not have any significant effect or release rate, in accordance with the previous reports, wherein a saturation effect occurred at high concentration. The general pattern was a decrease in release rate with an increase in amount of total polymer content. This is in clear accordance with earlier findings.

The values of mean dissolution time showed that with increasing total polymer content resulted in the increase of mean dissolution time. Mean dissolution time is used to characterize drug release rate from a dosage form and indicates the drug release retarding efficiency of polymer. The 3D response surface plots and contour plots demonstrated the graphical representation of results.

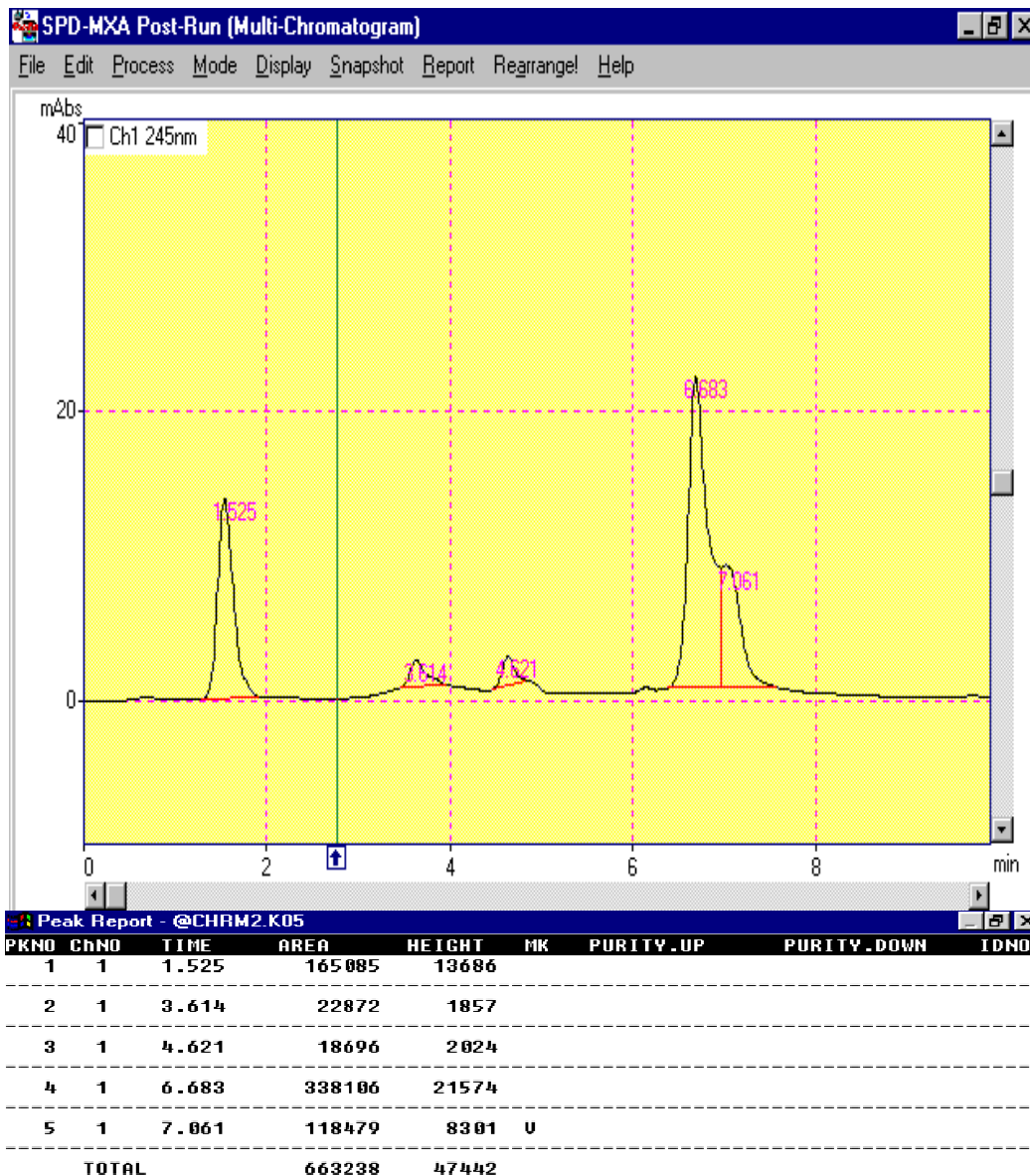


Fig. 6(c).

Comparisons of the observed responses with that of the anticipated responses along with percentage error for dissolution parameters like n , k , mean dissolution time, drug released in 12 h and k of six optimized matrix tablets formulation shows the prognostic ability of matrix tablet formulations of zolpidem tartrate using RSM optimization method and is validated.

Bioavailability studies shows that no sustained blood level of zolpidem was evident after oral administration of the conventional formulation. Although, plasma concentration time was

characterized significantly by higher plasma concentration after 2 h of administration followed by decline in plasma concentration.

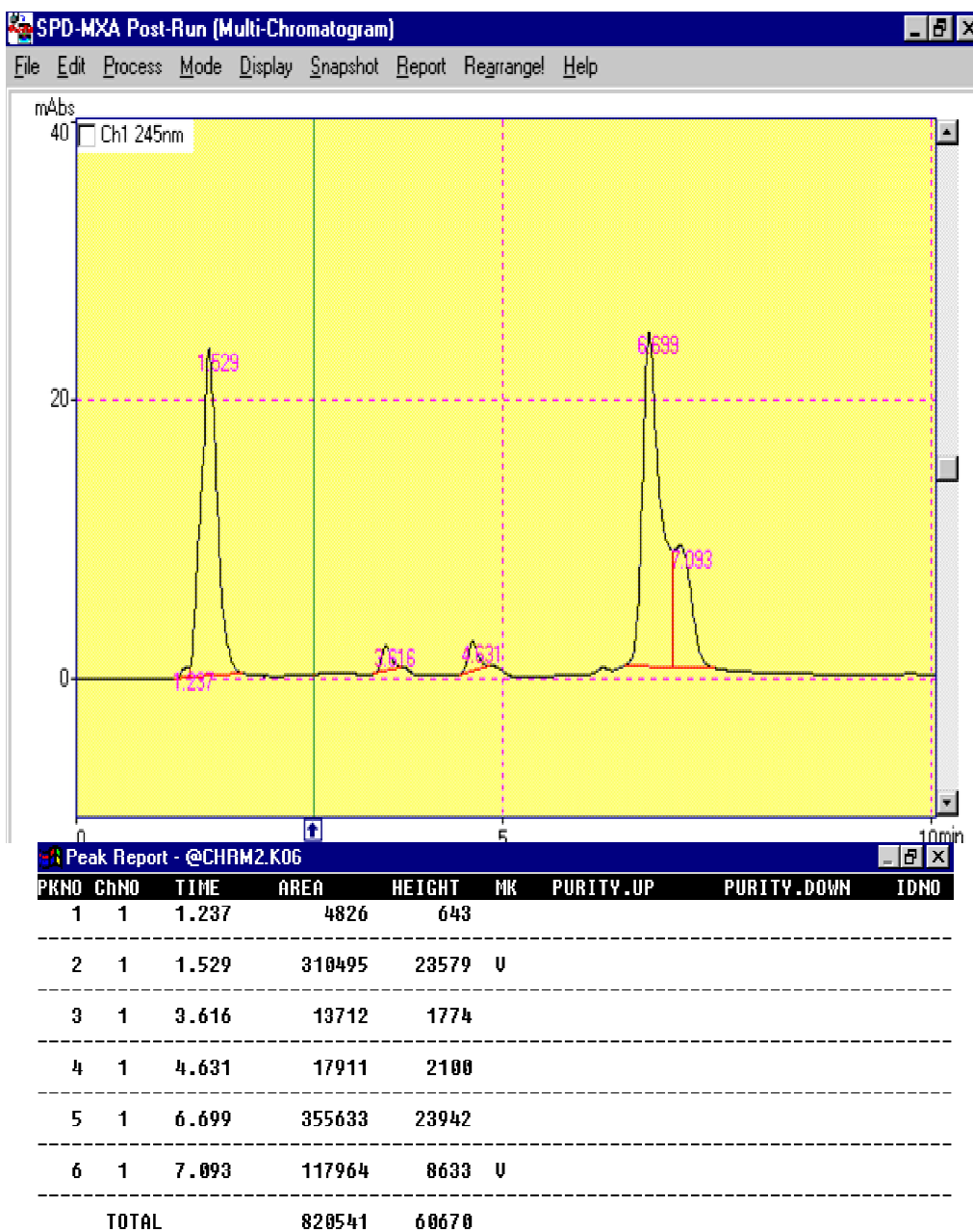


Fig. 6(d).

The formulated matrix tablets showed significantly lower C_{max} then conventional tablet and required significantly more time to reach C_{max} (T_{max} 2.5 h) as compared with conventional tablets (T_{max} 1.8 h). However the tablets maintained extended constant plasma concentration up to 12 h.

A high value of correlation R^2 (0.9037) suggested good correlation between *in vitro-in vivo* data.

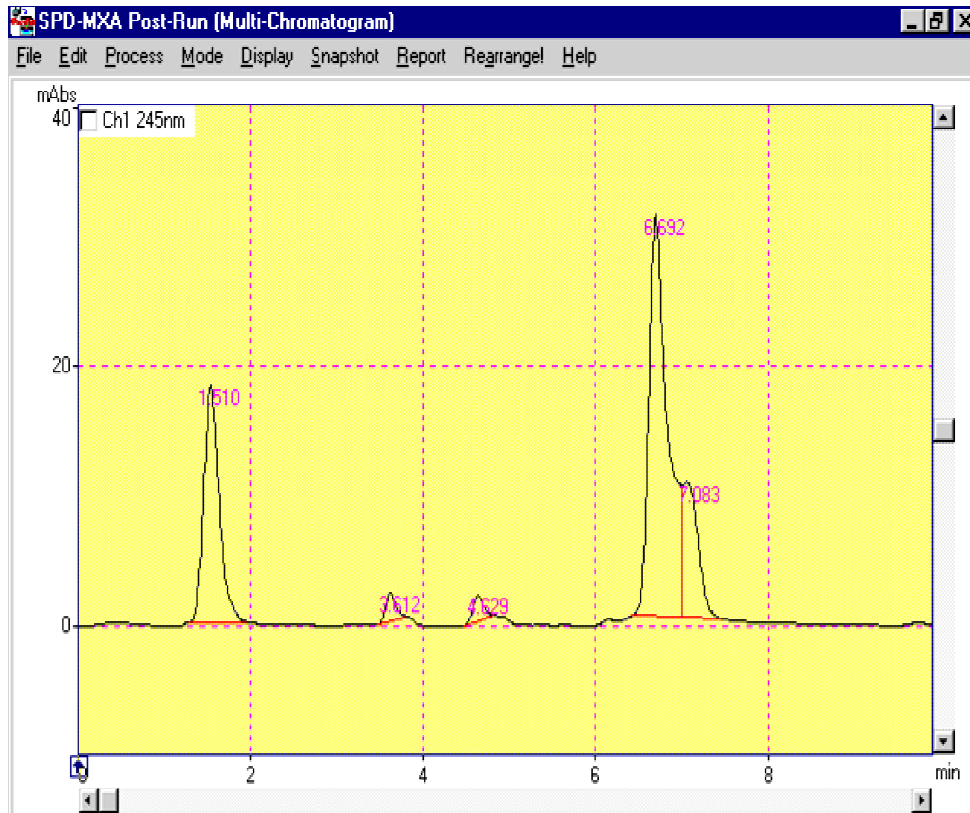


Fig. 6(e).

Table 6. Pharmacokinetic parameters

	AUC	Cmax	Tmax
Conventional tablet	0.154 ± .01	0.305 ± 0.3	1.8 ± 0.2
Optimized tablet	0.179 ± 0.2	0.296 ± 0.1	2.5 ± 0.3

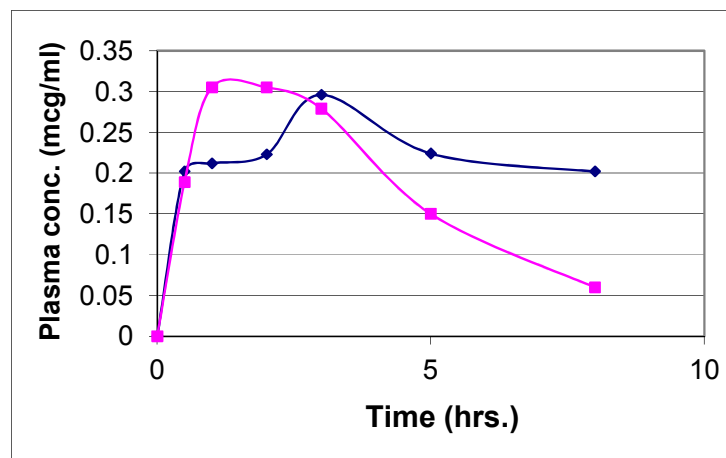


Fig. 7. Plasma concentration time profile of optimized batch of matrix tablet and conventional tablet after oral administration

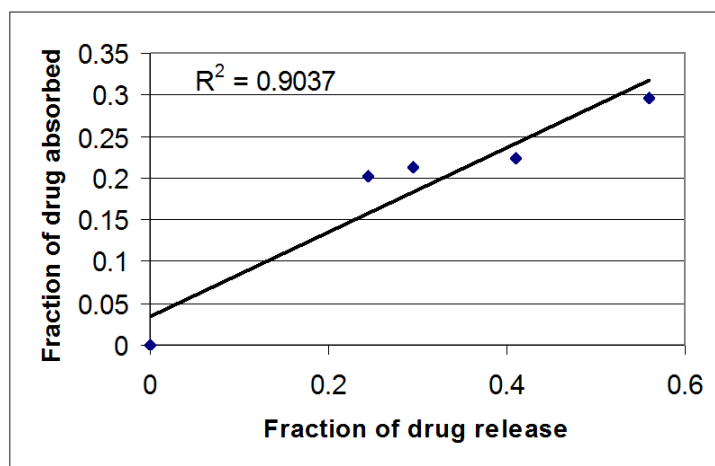


Fig. 8. Fraction of drug absorbed versus fraction of drug release (*In vitro- In vivo*) co-relation for optimized batch of matrix tablets

4. CONCLUSION

Zolpidem tartrate matrix tablets containing combination of polymers HPMCK4M and HPMCK15M, confirms excellent promises for drug release prolongation. Results of the dissolution studies for optimized formulation fulfilled maximum requisites because of better regulation of release rate. Rational use of optimization methodology helped to predict the best possible formulations and confirms the prognostic ability of RSM optimization method and validated. Results of bioavailability studies confirm lower C_{max} and significant more T_{max} (2.5 h) of formulated matrix tablets in comparison to conventional tablets. A high value of R^2 0.9037 confirms the *in-vivo-in-vitro* correlation at level A between fraction of drug absorbed and fraction of drug release.

Conclusively, the current study attained the successful design, development and optimization of formulation of zolpidem tartrate matrix tablets.

COMPETING INTERESTS

Authors have declared that no competing interests exist.

REFERENCES

1. Swarbric J, Boylan JC. Encyclopedia of pharmaceutical technology. Marcel Dekker, New York; 1995.
2. Bolton S. Pharmaceutical statistics: Practical and clinical applications. Marcel Dekker Inc, New York, Edn. 2; 1990.
3. Banker G, Rhodes C. Modern pharmaceuticals. Marcel Dekker, New York; 1996.
4. Lewis GA, Mathieu D, Phan-Tan-Luu R. Pharmaceutical experiment design (drugs and pharmaceutical sciences). Marcel Dekker, Inc., New York; 1999.
5. Box G, Connor C, Cousins W, Davies O, Himsforth F, Sillito G. The design and analysis of industrial experiments. In Eds.: O.L. Davies, Oliver and Boy, London, Edn. 2; 1960.
6. Pradhan R, Budhathoki U, Thapa P. Formulation of once a day controlled release tablet indomethacin based on HPMC mannitol. Eng Tech. 2008;1:55-67.
7. Dhanalakshmi S, Baratam SR. Design and evaluation of zolpidem tartrate matrix tablets for extended release using natural gums and HPMC K100M. Journal of Applied Pharmaceutical Science. 2018;8(07):072-077.
8. Scharf MB, Roth T, Vogel GW, et al. A multicenter, placebocontrolled study evaluating zolpidem in the treatment of chronic insomnia. J Clin Psychiatry. 1994;55:192-9.

9. Roth T, Roehrs T, Vogel G. Zolpidem in the treatment of transient insomnia: A double-blind, randomized comparison with placebo. *Sleep*. 1995;18:246–51.
10. Trapani G, Lopedota A, Boghetich G, Latrofa A, Franco M, Sanna E, Liso G. *Int. J. Pharm.* 2003;268(47).
11. Trapani G, Franco M, Latrofa A, Pantaleo MR, Provenzano MR, Sanna E, Maciocco E, Liso G. *Int. J. Pharm.* 1999;184(121).
12. Greenblatt DJ, Legangneux E, Harmatz JS, Weinling E, Freeman J, Rice K, Zammit GK. *J. Clin. Pharmacol.* 2006;46:1469.
13. Weinling E, McDougall S, Andre F, Bianchetti G, Dubruc C, *Fundam. Clin. Pharmacol.* 2006;20(397).
14. Barkin RL. *Am. J. Ther.* 14:299.
15. Zammit G. *Exp. Opin. Drug Toxicol.* 2008;4(325).
16. Liberman H, Lachman L, Schwartz J. *Pharmaceutical dosage forms: Tablets. Revised and Expanded*, Dekker, New York. 2005;1(2).
17. Liberman H, Lachman L, Schwartz J. *Pharmaceutical dosage forms: Tablets. Revised and Expanded*, Dekker, New York. 2005;3(2).
18. Remington. *The Science and Practice of Pharmacy*, Lippincott Williams & Wilkins. 2000;1.
19. Kuksal A, Tiwary AK, Jain NK, Jain S. *AAPS Pharm. Sci. Tech.* 2006;7(1).
20. Rao KVR, Devi KP. *Int. J. Pharm.* 1988;48(1).
21. Efentakis M, Vlachou M, Choulis NH. *Drug Dev. Ind. Pharm.* 1997;23:107.
22. Singh B, Singh S. *Ind J. Pharm. Sci.* 1998;60(358).
23. Singh B, Ahuja N. *Drug Dev. Ind. Pharm.* 2002;28(431).
24. Singh B, Gupta RK. FACTOP: A software aid to optimize pharmaceutical dosage forms through factorial design in 48th Indian Pharmaceutical Congress, Chennai. 1996;AP63.
25. El Zeany BA, Moustafa AA, Farid NF. *J. Pharma. Biomed. Anal.* 2003;33:393.
26. Laviana L, Mangas C, Fernandez-Mari F, Bayod M, Blanco D. *J. Pharma. Biomed. Anal.* 2004;36:925.

Biography of author(s)



Dr. Masheer Ahmed Khan

School of Pharmacy, Devi Ahilya Vishwavidyalaya, Takshshila Campus, Khandwa Road, Indore, M.P., India.

He is an Assistant Professor at Devi Ahilya University, Indore, MP, India with an extensive teaching experience of more than 17 years. Formerly into the field of Pharma Marketing, he always had a passion for research and teaching. Industrial Pharmacy is his specialization and the thrust area of research which is formulation and optimization of various dosage forms. With a sound research background he has published around 37 research articles in various reputed national and international journals. He worked as a principal Investigator on Major research projects, obtained from University Grants Commission (UGC), New Delhi, and Madhya Pradesh Council of Science and Technology (MPCOST), Bhopal, MP. He is a Supervisor and guide to students pursuing Ph.D. He attended many pharmaceutical conferences, seminars and workshops, refresher courses and orientation programs. He is the Life member of various professional bodies like IPA, APTI etc. He has active participation in the corporate life with different capacities as chairman, convener, judge, co-chairman etc. He has OSD for central valuation center of the university. He also held the position of Program Officer of NSS. Now he is working sincerely on to publish various books of pharmaceutical sciences in future.



Prof. S. C. Chaturvedi

School of Pharmacy, Devi Ahilya Vishwavidyalaya, Takshshila Campus, Khandwa Road, Indore, M.P., India.

He is an eminent personality among pharmacy profession with a very vast teaching experience of more than 45 years in India as well as abroad (Nigeria). At present holding a position of Director at Sri Aurobindo Institute of Pharmacy, Indore, M.P., India. Along with teaching, he has a very strong administrative background while holding various eminent positions like Officiating Vice-Chancellor of RGPV, Bhopal, and many times as an Acting Vice-Chancellor of Devi Ahilya Vishwavidyalaya, Indore. He is Pioneer to start the Pharmacy education in Indore region of state Madhya Pradesh. He held the position of Professor and Head, for more than a decade at S.G.S.I.T.S, Indore and also held the position of Head, School of Pharmacy, at DAVV, Indore and Dean, Faculty of Pharmacy for many years. He has a nomination as a Governing Body Members in various academic bodies and associations. He has a very sound research background with more than 170 International and National Research publications in various high impact factor journals. He has received "Prof. M.L.Khurana Memorial best paper award, 2000" and IDMA best research paper award, 2005". He also received "Certificate of Appreciation" by American Chemical Society Publication in 2013. He has been awarded by various research projects from funding agencies like AICTE and UGC. He has participated in International conferences held at various countries. He is an author of many book chapters in various book publications and many more research publications are in pipeline.

© Copyright (2020): Author(s). The licensee is the publisher (Book Publisher International).

DISCLAIMER

This chapter is an extended version of the article published by the same author(s) in the following journal.
Asian Journal of Chemistry, 22(6): 4749-4762, 2010.

Solution Behavior and Optical Properties of Platinum Complexes Featuring “Pt(pq)(C≡C^tBu)” Units Connected by N-donor Ligands

Elena Lalinde^{1*}, M. Teresa Moreno^{1*}, Santiago Ruiz¹ and Sergio Sánchez¹

DOI: 10.9734/bpi/cpcs/v2

ABSTRACT

The synthesis, spectroscopic (including X-ray for **2a** and **4a**) and optical properties of a series of binuclear complexes $[\{Pt(pq)(C\equiv C^tBu)\}_2\{\mu-(N-N)\}]$ (**1a–5a**), having ditopic dinitrogen linker ligands (N–N) and of a trinuclear $[\{Pt(pq)(C\equiv C^tBu)\}_3(\mu-L)]$ (**6a**) featuring a 1,3,5-tris(pyridine-4-ylethynyl)benzene as a central core are presented. In this chapter particular attention is devoted to the unusual behavior of the binuclear complexes illustrated with complex $[\{Pt(pq)(C\equiv C^tBu)\}_2\{\mu-4,4'-bpy\}]$ (**2a**). Thus, upon solution, complexes **1a–5a** establish a fast dynamic equilibrium with the alkynyl bridging starting material $[Pt(pq)(\mu-C\equiv C^tBu)]_2$ (**Pt-1**), the corresponding mononuclear complex with a terminal N-donor ligand $[Pt(pq)(C\equiv C^tBu)(N-N)]$ (**1b–5b**) and the free ligand (N–N). Additionally, the effects of concentration, temperature and solvent properties on the equilibrium, and their optical properties (absorption and emission), supported also by theoretical calculations on **2a**, are commented.

Keywords: Alkynyl; cyclometalated; luminescence; platinum; N-donor ligand.

1. INTRODUCTION

Alkynyl platinum(II) complexes have attracted much interest in the last decades due to their rich structural diversity [1–4], interesting chemical reactivity [1] and more recently from their increasing potential in material science [5–17]. In this field, phosphorescent alkynyl cycloplatinated platinum complexes have been extensively explored owing to their promising use as components in electroluminescent devices, chemosensors and photovoltaic cells [8,18–21]. In these complexes, the efficient singlet to triplet intersystem crossing, facilitated by the heavy Pt atom, generally induces phosphorescent emissions with high radiative yield. The presence of carbon donor atoms (C≡CR, C[^]N) destabilizes σ -antibonding ligand and metal center states, thus preventing access to nonradiative deactivation pathways through molecular distortion. The lowest excited states of these complexes are typically admixtures $^3LC / ^3MLCT / ^3L'LCT$ (L'LCT= interligand charge transfer), that are tunable by varying the cyclometalated group and the alkynyl ligand (L'). Furthermore, some of these complexes are particularly prone to show solid-state polymorphism and interesting photophysical properties related to non-covalent Pt^{II}–Pt interactions and π – π stacking, which induce new low-lying emissions ascribed to metal-to-metal charge transfer (MMLCT) or excimers [22,23]. This behavior has demonstrated potential application in white organic light emitting diodes (WOLEDs) and as sensor or labels systems [24].

By using the triple bond of the Pt–C≡CR units, we and others have reported the synthesis and properties of di- and triplatinum complexes in which the Pt^{II} centers are connected by one C≡CR or a double alkynyl bridging systems, exhibiting planar or bent $Pt(\mu-C\equiv CR)_2Pt$ conformations [25–36], with the alkynyl acting as $\mu-\kappa C^\alpha:\eta^2-C\equiv CR$ ligands. Although the reactivity of these systems has been scarcely explored, it has been demonstrated that diplatinum complexes such as $[trans-Pt(\mu-$

¹Departamento de Química-Centro de Síntesis Química de La Rioja (CISQ), Universidad de La Rioja, 26006, Logroño, Spain.

*Corresponding author: E-mail: elena.lalinde@unirioja.es, teresa.moreno@unirioja.es;

$C\equiv CR)(C_6F_5)(PPh_3)_2)_2$ and $[Pt(C^{\wedge}P)(\mu-C\equiv CR)]_2$ undergo bridge-splitting with classical donor ligands to give mononuclear σ -alkynyl Pt^{II} complexes [25,30,31,34].

On the other hand, since the rationale design of the molecular square $[\{Pd(en)(\mu-4,4'-bpy)\}_4](NO_3)_8$ by self-assembly of $[Pd(en)(ONO_2)_2]$ (en = ethylenediamine) with the linear linker 4,4'-bipyridine (4,4'-bpy) [37], numerous and fascinating molecular and metallocsupramolecular structures with different levels of complexity have been prepared by using linear, angular, triangular or flexible linkers with bidentate or tridentate binding nitrogen units. Several reviews have thoroughly covered this amazing field in the last years [38–46]. In this field, the research on the construction of luminescent metallacycles and metallasupramolecular structures featuring luminescent Pt^{II} units in the corners and luminophore *N*-groups as linkers has attracted considerable attention because of their extensive applications mainly in host – guest chemistry and biomedicine [47]. Comparatively, diplatinum complexes with dinitrogen donor ligands bridging the metal centers are less represented [48–55] and particularly those with cycloplatinated fragments are rather scarce [48–52].

We recently reported the synthesis and a detailed study of luminescent properties of the series $[Pt(pq)(\mu-C\equiv CR)]_2$ (Hpq = phenylquinoline; R = ^tBu, Tol, C₆H₄OMe-3, C₆H₄CF₃-4) [56], which represent the first examples of cycloplatinated complexes stabilized by double alkynyl bridging complexes. In these bimetallic complexes the metal centers are relatively close to one another, and their photophysical properties were found to be influenced by the substituents on the alkynyl ligands in response to the variation of the Pt···Pt distance. Thus, the *ter*-butyl derivative $[Pt(pq)(\mu-C\equiv C^tBu)]_2$ exhibits a relatively short Pt···Pt distance of 3.0936(3) Å and, in accordance, displays an emission originated from a mixed metal-metal-alkynyl to $pq^3[(MM + L')LCT]$ excited state. By contrast, the aryl derivatives have longer Pt···Pt distances, as found in complex $[Pt(pq)(\mu-C\equiv CTol)]_2$ [3.2109(3) Å], and therefore their emission mainly arises from a ³L'LCT excited state with negligible ³MMLCT contribution. Following this work, we summarize here the properties of a different kind of bi- and trinuclear complexes in which the platinum units "Pt(pq)(C≡C^tBu)" are connected by ditopic *N-N*-donors (pyrazine (pyz) **L**₁, 4,4'-bipyridine (bpy) **L**₂, 1,2-bis(bipyridyl)ethane (bpa) **L**₃, *trans*-1,2-bis(4-pyridyl)ethylene (bpe) **L**₄ and 1,2-bis(4-pyridyl)acetylene (bpac) **L**₅ [57]), and the rigid and branched pyridyl alkynyl ligand (1,3,5-tris(pyridine-4-ylethynyl)benzene (**L**₆) [58]). This study allowed us to examine the influence of the linker in the properties of the final complexes.

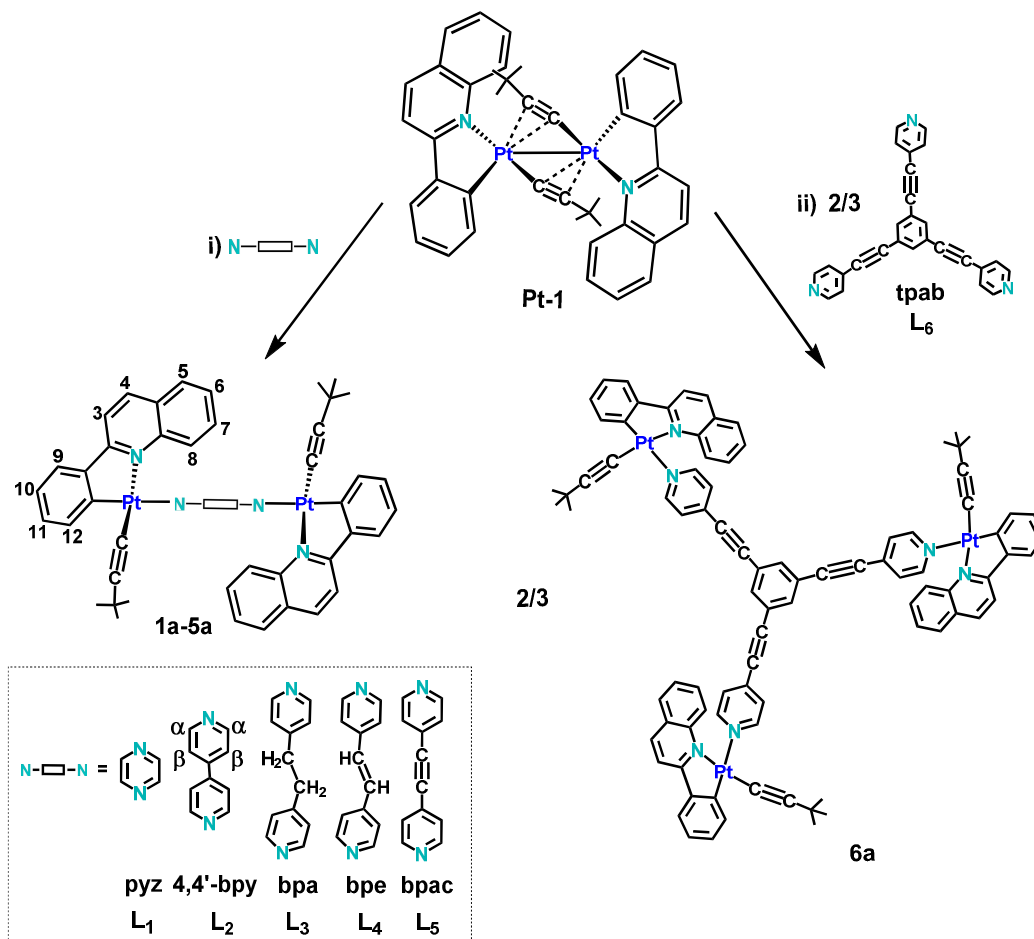
2. RESULTS AND DISCUSSION

2.1 Synthesis and Characterization

The synthesis of the new diplatinum derivatives $[\{Pt(pq)(C\equiv C^tBu)\}_2(\mu-L)]$ (L = pyz **1a**, bpy **2a**, bpa **3a**, bpe **4a**, bpac **5a**) and the trinuclear complex **6a** is outlined in Scheme 1. The complexes are formed by treatment of the binuclear derivative $[Pt(pq)(\mu-C\equiv C^tBu)]_2$ (**Pt-1**) with the corresponding dinitrogen donor ligand, which causes the rupture of the alkynyl bridging system. In the case of complexes **2a**, **3a** and **5a**, their formation takes place by treatment of the starting material with only one equivalent of the ligand, while for the isolation of **1a** and **4a** as pure solids in the solid state, two equivalents of the ligand are required. The branched trinuclear platinum complex $[\{Pt(pq)(C\equiv C^tBu)\}_3(\mu-tpab)]$ (**6a**) was obtained using the same strategy but with a **Pt-1**:ligand molar ratio of 3:2 (For experimental details see reference [59]). It worth to note that a particularly reliable indicator of the obtaining of the complexes is the lack of bridging $\nu(C\equiv C)$ band in the IR spectra of the final solids.

A combination of crystallography, NMR, IR, elemental analyses (C, N, H) and mass spectrometry provides a complete picture of the behavior of these complexes. In the solid state, these complexes are isolated as the species **1a-6a** formulated in the Scheme 1. Notably, their IR spectra show one $\nu(C\equiv C)$ intense absorption (2114–2118 cm⁻¹) in the typical range for terminal σ -coordinated alkynyl ligands, thus confirming the cleavage of the alkynyl bridging ($\mu-C\equiv C^tBu$)₂ system. Furthermore, complexes **5a** and **6a** show one additional band at higher frequency (2223 **5a**, 2212 cm⁻¹ **6a**), assigned to the $\nu(C\equiv C)$ stretch of the inner ethynyl entity of the 4-pyridylacetylene groups in the bpac and the tpab ligands, respectively. The X-ray crystallographic studies on complex **2a** and **4a** [59] confirm the stereochemistry shown, with the C≡C^tBu ligand occupying the *cis* position to the metallated carbon atom, in agreement with the lower *trans* influence of the N-pyridine donor atom

compared to the $C\equiv C^tBu$ ligand. It is worth to note that in **4a** the asymmetric unit is formed by one independent molecule and two half ones, which are completed by application of symmetry elements. The conformation and metrical details of the three molecules are, however, similar. As shown in Fig. 1, the molecular structures confirm the expected formation of binuclear entities with a 4,4'-bpy (**2a**) or bpe (**4a**) group bridging the Pt^{II} centers. The Pt atoms complete a distorted square planar environment with a bidentate pq ligand and one terminal alkynyl group. In both complexes, the *N*-pyridine bridging group is *trans* to the cyclometalated carbon, thus confirming that the reactions take place with retention of the geometry in the precursor, and the Pt units adopt an *anti*-configuration. The Pt-N (bpy or bpe) distances [2.113(4), 2.125(4) Å **2a**, 2.114(7)–2.145(7) Å **4a**] are in the range found in other cycloplatinated complexes for Pt-N distances *trans* to metalated carbon atom [48,49].



In the bridging ligand, the two pyridyl rings form a small dihedral angle (**2a**, 16.45°; **4a**, 24.0° in the complete molecule and coplanar in the other two molecules). However, the dihedral angles with its corresponding Pt coordination plane are, as expected, higher [67.47°, 82.18° (**2a**) and 60.36–80.41° (**4a**)] reducing the electronic communication between the Pt units. These values can be compared to those reported in related binuclear complexes featuring the tridentate cyclometalating 1,3-bis(piperidylmethyl)benzene ligand (pip_2NCN^-) [$\{Pt(pip_2NCN)\}_2(\mu-NN)\}^{2+}$ [NN = bpy 86°, bpe 85.2°]] [48,49]. In both complexes the phenylquinolyl (pq) ligand is fluttered (dihedral angles of ~ 13–14° **2a**; 20° and 10.04° **4a**), as observed in related Pt(pq) complexes [56]. Crystal packing reveals a pairwise stacking only in complex **2a** forming dimers through moderate intermolecular $\pi\cdots\pi$ (pq \cdots pq) interactions (3.271, 3.336 Å), which interacts through secondary interactions with the crystallization

solvents (CHCl₃, *n*-hexane) and with other dimers (Hpy⋯πC≡C/Cpq). However, the supramolecular structure of **4a** does not show π⋯π interactions.

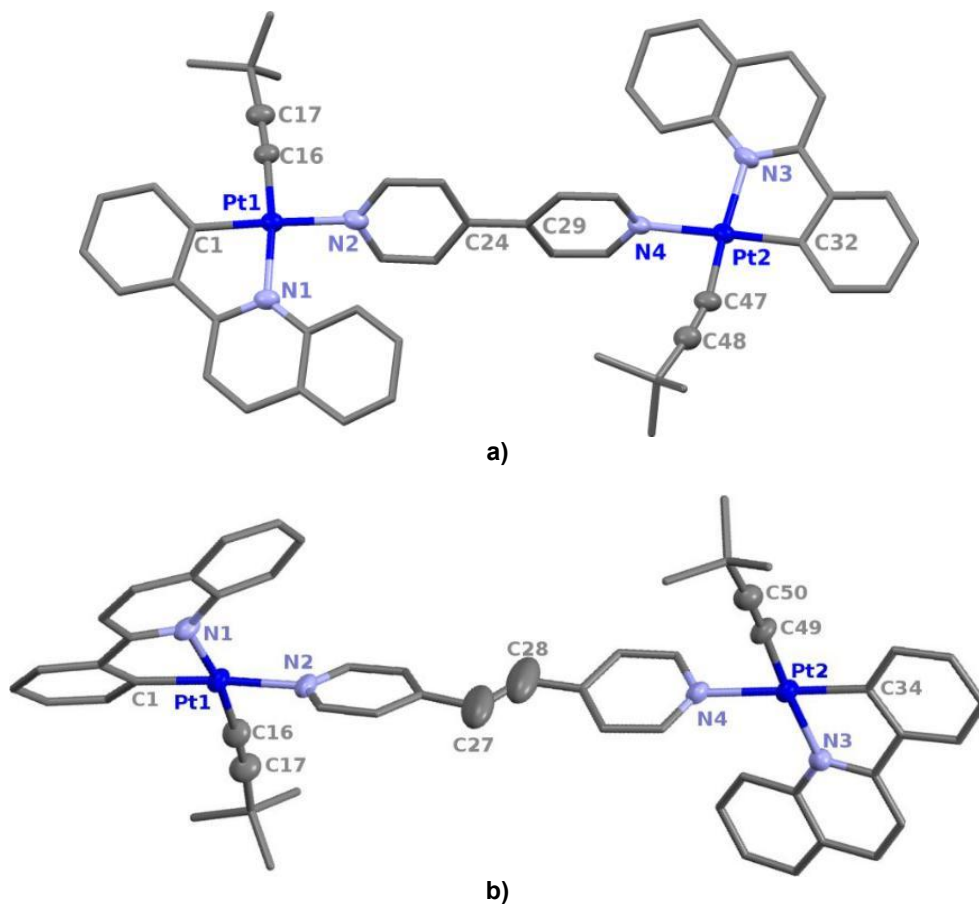


Fig. 1. a) View of the molecular structure of the complex $[\{\text{Pt}(\text{pq})(\text{C}\equiv\text{C}^t\text{Bu})\}_2(\mu\text{-}4,4'\text{-bpy})]\cdot 2\text{CHCl}_3\cdot\text{C}_6\text{H}_{14}$ ($2\text{a}\cdot 2\text{CHCl}_3\cdot\text{C}_6\text{H}_{14}$), b) View of the independent molecule in the asymmetric unit in the molecular structure of the complex $[\{\text{Pt}(\text{pq})(\text{C}\equiv\text{C}^t\text{Bu})\}_2(\mu\text{-bpe})]\cdot 4\text{CHCl}_3$ ($4\text{a}\cdot 4\text{CHCl}_3$)

The behavior in solution is different. Firstly, the analysis of the mass spectra of complexes in CH₂Cl₂ solution [ESI (+)] reveals the presence of the corresponding molecular peak [M]⁺ for each complex and the fragmentation peak [Pt(pq)(C≡C^tBu)L]⁺ (species **b**) (or {Pt₂(pq)₂(C≡C^tBu)₂L}⁺ in the trinuclear derivative **6a**), generated by loss of the fragment [Pt(pq)(C≡C^tBu)] (Fig. 2). Interestingly, in all cases there are also intense peaks ([Pt(pq)(C≡C^tBu)]⁺, *m/z* 961; [Pt₂(pq)₂(C≡C^tBu)]⁺, *m/z* 879 and [Pt(pq)(C≡C^tBu)]⁺, *m/z* 481), which are associated with the starting material **Pt-1** in solution. These mass spectra are in good qualitative agreement with the observations in the NMR spectra in solution.

So, surprisingly, the room temperature ¹H NMR spectra of the corresponding solid complexes **1a–6a** in CDCl₃ are consistent with the presence of four different molecules in solution, which are collected in Scheme 2. The resonances are associated with the presence of the new diplatinum complex (species **a**), the starting material [Pt(pq)(μ-C≡C^tBu)]₂ (**Pt-1**), the free ligand (L₁–L₅) and, also the corresponding mononuclear complex with the dinucleating ligand acting as monodentate terminal group [Pt(pq)(C≡C^tBu)(L-κN)], (hereafter denoted as species **1b–5b**) [59].

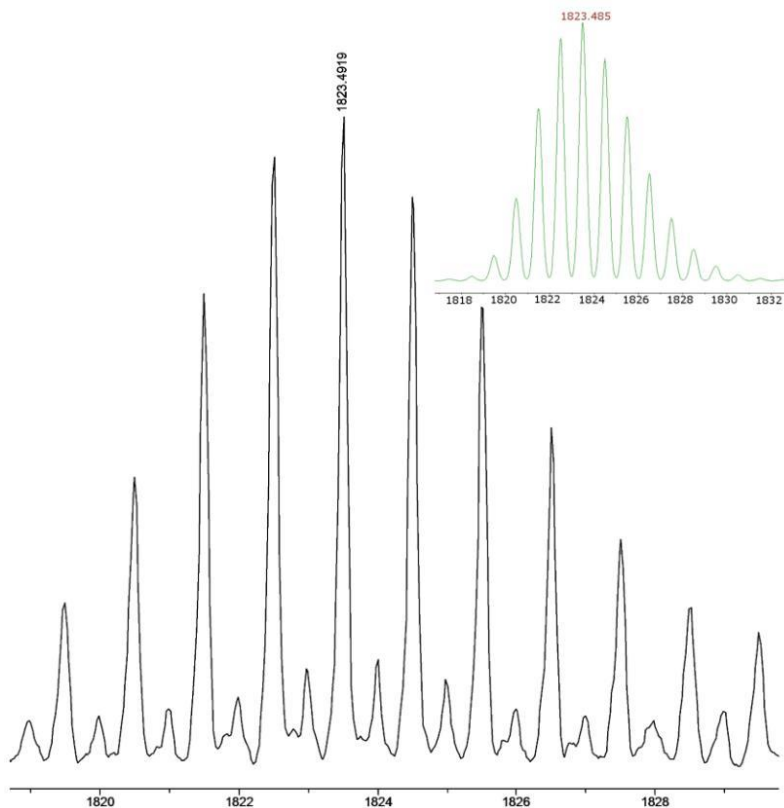
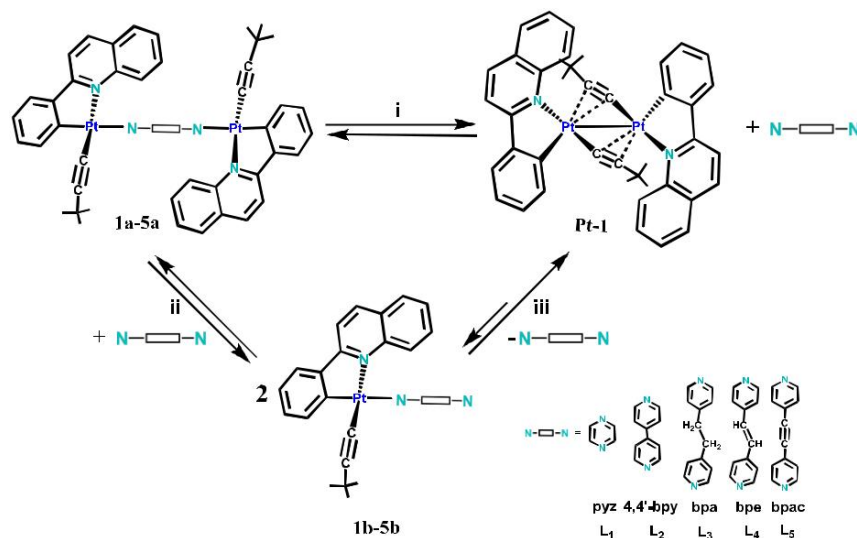


Fig. 2. Experimental isotope pattern and predicted isotopic distribution (green) in the electrospray mass spectrum of 6a, showing the peak $[Pt_3(pq)_3(C\equiv C^tBu)_3(tpab)]^+$

As illustration, we only discuss the behavior of the 4,4'-bpy complex $[Pt(pq)(C\equiv C^tBu)_2(\mu-bpy)]$ (**2a**). The 1H NMR spectra of the microcrystalline **2a** complex (**B**), the starting material **Pt-1** (**C**) and a mixture **Pt-1**:4,4'-bpy in 1:4 molar ratio (**A**) are presented in Fig. 3. It should be noted that the coordination of the pyridine N atoms to the Pt center is supported by the well-known coordination-induced shifts of the α -Hpy protons to downfield in relation to the free 4,4'-bpy (δ 8.75), which has been ascribed to the loss of electron density upon pyridine ring coordination. As seen in Fig. 3B, only one signal appears at δ 9.00 (d, green), which is assigned to the bridging species $[Pt(pq)(C\equiv C^tBu)_2(\mu-bpy)]$ **2a**, whereas the two expected different resonances located at 8.96 (d), 8.79 (d) (blue) correspond to α -Hpy protons of the coordinated and uncoordinated pyridine units of the monomer $[Pt(pq)(C\equiv C^tBu)(4,4'-bpy)]$ **2b**. It should be noted that this later signal (δ 8.79) lies close to that of the free bpy (δ 8.75) also present in solution. A particularly reliable indicator of the presence of starting material (**Pt-1**) is the signal H^8 of the pq ligand, very deshielded (δ 9.75) in relation to the others. Fortunately, in all systems under study, the pyridine protons (pyrazine for **1a**) and the H^8 pq signal of the precursor **Pt-1** are sufficiently separated from the other signals, allowing us to establish the approximate ratios of the species from their integrations. However, due to remarkable overlapping (or even coincidence for pq signals) an accurate assignment for the rest of signals to the corresponding individual complexes was not possible.

As noted above, the presence of these species in solution is consistent with a fast evolution of the bimetallic species **1a-5a** in solution through a series of reasonable equilibria (slow on the NMR scale), that are shown in Scheme 2. This evolution seems to be initiated through a partial dissociation of the N-bridging ligand at room temperature in $CDCl_3$ (Scheme 2, i), which could be driven by the *trans* labilizing effect of the C-cyclometalate atom on the N-donor ligand and the remarkable stability of the σ/π - $C\equiv C^tBu$ bridging system in the precursor **Pt-1**. By a subsequent interaction of the free ditopic 4,4'-bpy with **2a**, the corresponding mononuclear species **2b** can be generated in solution.



Scheme 2. Equilibrium proposed between the species a, b, Pt-1 and the free ligand in systems 1–5

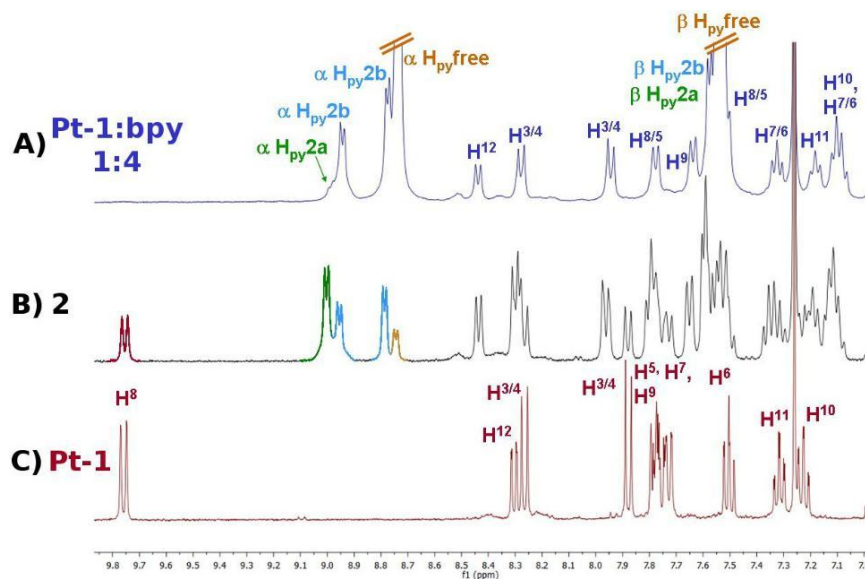


Fig. 3. ^1H NMR spectra (CDCl_3 , 400 MHz, 298 K, aromatic region) of: (A) Aliquot of a reaction mixture Pt-1/4,4'-bpy in a 1:4 molar ratio; (B) Microcrystalline sample of $[\{\text{Pt}(\text{pq})(\text{C}\equiv\text{C}^t\text{Bu})\}_2(\mu\text{-4,4}'\text{-bpy})]$ (2a); (C) $[\text{Pt}(\text{pq})(\mu\text{-C}\equiv\text{C}^t\text{Bu})]_2$ (Pt-1)

A comparison of the analysis of the ^1H NMR spectra of these five bimetallic assemblies by using similar sample concentration, allow us to conclude that the extend of the evolution of the bimetallic species **1a-5a** depend on the *N*-donor ligand [59]. Thus, the higher proportion and, therefore, the higher stability of the bimetallic species (**a**) in solution was found with the more flexible and better donor ligands (bpa, bpe), whereas the lowest was with the short and rigid pyrazine ligand, being the order: bpa \approx bpe > bpac \approx bpy \gg pyz. It should be noted that for the trinuclear complex **6**, signals due to coordinated and free α -H pyridine protons are also observed together with that of the H^8_{pq} proton of **Pt-1**. However, in this system the possible occurrence of stepwise decoordination of more than one cyclometalating Pt unit cannot be excluded.

Equilibria were found to be significantly influenced by concentration, temperature or solvent as is illustrated for **2a** in Figs. 4-6. As shown in Fig. 4, dilution of a solution from 6×10^{-3} to 1×10^{-3} M causes a progressive shift of the equilibria (i) and (ii) to the right, increasing the presence of **Pt-1**, **2b** and free 4,4'-bpy with concomitant decreasing of **2a**. By contrast, upon lowering the temperature to 218 K (Fig. 5) the concentration of **2a** increases, whereas those of **Pt-1**, **2b** and free 4,4'-bpy decrease (**2a**:**Pt-1**:**2b**:**N-N** ratio, 298 K \approx 1:0.8:1.3:0.2; to 218 K 1:0.4:0.8:0.1 for a solution 3×10^{-3} M in CDCl_3). These results clearly confirm that the three complexes and the free ligand are involved in a dynamic equilibrium. By using CD_3COCD_3 as solvent for **2a** the final ratio found was **a**:**Pt-1**:**b**:**N-N** \approx 1:2.2:2.4:1.2 (Fig. 6). Therefore, in this solvent not only the equilibria (i and ii) are shifted to the right in more extension to that observed in CDCl_3 , but also the formation of **Pt-1** and bpy (equilibrium i) was favored in relation to **2b** (ii).

As was expected, the final ratio between the bimetallic and mononuclear complexes **a/b** in solution was influenced by the concentration of the dinucleating *N-N* ligand. Thus, the ^1H NMR spectra recorded for solutions formed by a mixing of **Pt-1/L (L2-L5)** 1:4 in CDCl_3 (established by UV-vis, see below) show mainly the signals associated to the mononuclear species (**b**), together with the free ligand in excess and small amount of the bimetallic species (**a**). As shown in Fig. 3A, for the **Pt-1/4,4'-bpy** system, the final ratio found was (\approx 1: 0: 8: 14 for **2a**: **Pt-1**: **2b**: **4,4'-bpy**). In this system, no signals associated with the starting material (**Pt-1**) were observed, indicating that the equilibria drawn in Scheme 2 are essentially shifted in counterclockwise in the presence of excess ligand. However, in the case of the pyrazine system, a large excess of ligand was required to eliminate completely the presence of the precursor (**Pt-1**:pyz \approx 1:20). This fact is in good agreement with the greater amount of starting material observed when the solid **1a** is dissolved.

It is worth noting that all attempts to obtain the mononuclear complexes **1b-5b**, as pure solids from reaction mixtures having excess of ligands were fruitless. From these systems, only the binuclear complexes **1a-5a** and mixtures **1a-5a** /**1b-5b** could be isolated. However, the proton spectra obtained in presence of excess of ligands have allowed us to carry out a reasonable assignment of the signals of the mononuclear complexes **1b-5b** ($2\text{D } ^1\text{H}-^1\text{H}$ spectra). Taking into account the characterization of **1b-5b** and known the resonances of the starting material and of the free ligands, it was possible to identify and to assign with some certainty some characteristic signals observed for the bimetallic solid samples (**1a-5a**) in CDCl_3 solution [59].

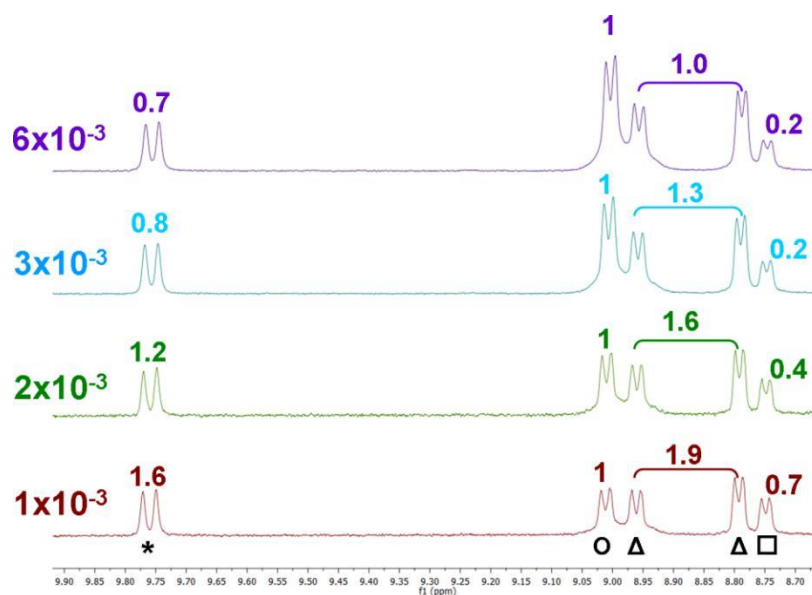


Fig. 4. ^1H NMR spectra at 298 K of **2a** at different concentrations (mol/L). Selected resonances: **Pt-1** (*), **2a** (O), **2b** (Δ), free **bpy** (\square)

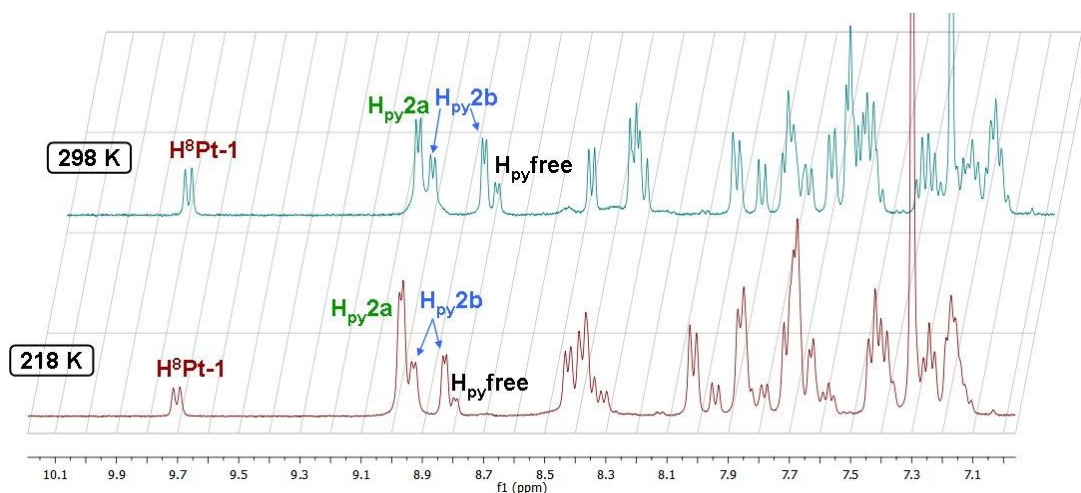


Fig. 5. ^1H NMR spectra at 298 K and at 218 K of a sample of recently dissolved solid **2a** in CDCl_3 (3×10^{-3} M)

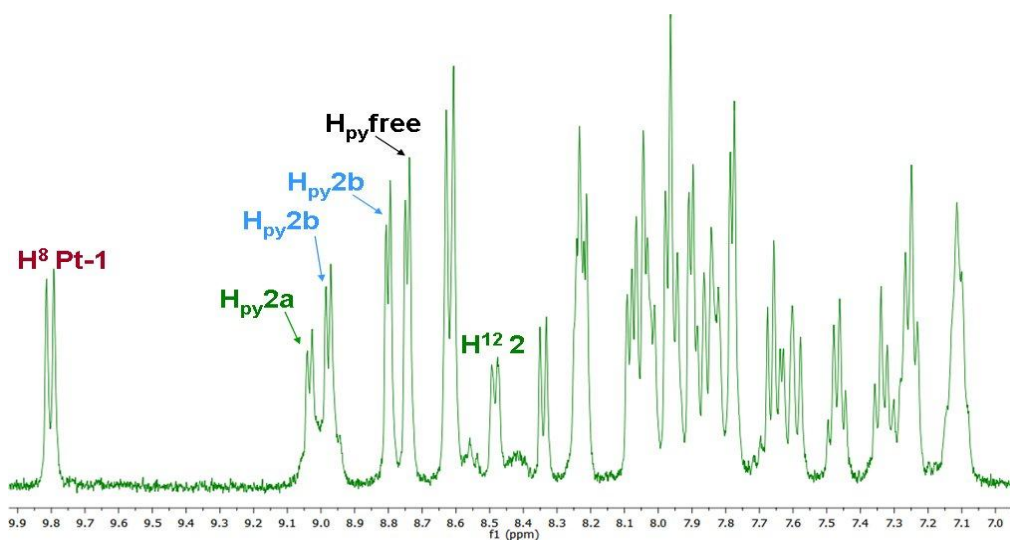


Fig. 6. ^1H NMR spectra at 298 K in CD_3COCD_3 (3×10^{-3} M) of a sample of recently dissolved solid **2a**

2.2 Photophysical Properties and Calculations

2.2.1 Electronic absorption spectroscopy

Relevant data of the room-temperature absorption spectra of the binuclear complexes **1a-6a** in the solid state (Diffuse Reflectance) and of mononuclear species **1b-5b**, generated from mixtures **Pt-1**:L (1:4) (**L2-L6**) and 1:14 (**L1**) in CH_2Cl_2 solution, were summarized in Table 1 and illustrative spectra are provided in Fig. 7.

In the solid state, the binuclear complexes **1a-5a** are characterized by a distinctive low energy feature in the range 500–540 nm, tentatively ascribed, on the basis of TD-DFT calculations for **2a**, to charge transfer from the $\text{Pt}(\text{pq})(\text{C}\equiv\text{C}^t\text{Bu})$ units to the central N-N linker $^1[(\text{M} + \text{L} + \text{L}')\text{L}''\text{CT}]$.

In CH_2Cl_2 solution, the absorption spectra of solids **1a–6a**, provide a further support of the occurrence of the fast dynamic equilibrium between the bimetallic complexes (**a**), the starting material (**Pt-1**), the monometallic species (**b**) and the free ligand shown in Scheme 2. The spectra of freshly prepared CH_2Cl_2 solutions of solid **1a–6a** display intense bands in the 240–330 nm region due to spin allowed ligand centered transitions ^1LC (pq, $\text{C}\equiv\text{CR}$ and *N-N*-donor ligand). As illustration the spectra of **2a**, **Pt-1** and 4,4'-bpy are presented in Fig. 7A. The moderately vibronic band resolved at ca. 355 nm coincides with that observed in the starting material **Pt-1** and is attributed to ^1LC located on the phenylquinolinyl pq ligand. The low-energy absorption (408–413 nm) is suggested to be originated mainly from the $[\text{d}(\text{Pt})/\text{C}\equiv\text{C}\rightarrow\pi^*(\text{pq})] \ ^1[(\text{M} + \text{L}')\text{LCT}]$ mixed state. This band appears remarkably blue-shifted in relation to the lowest manifold in the precursor (436 nm), supporting cleavage of the double-alkynyl bridging system. Although the influence of the ancillary *N-N* ditopic ligand in the low energy manifold is minimal (Fig. 7C), the slight blue shift observed for the less electron donating pyrazine ligand (408 nm) and the slightly red shift seen for the most electron donating 1,2-bis(4-pyridyl)ethane (bpa, 413 nm) is also coherent with this assignment. Increasing the σ donor capability of the auxiliary ligand increases the gap between the ^1LC and $^1\text{MLCT} / ^1\text{LLCT}$ states, causing a slight shift to longer wavelengths. However, due to the low lying nature of some of the π^* diimine ligands, contribution from platinum-alkynyl to *N*-donor ligand charge transfer $^1[\text{Pt}(\text{C}\equiv\text{C})\rightarrow\pi^*(\text{N-donor})]$ could be also plausible. This contribution is apparent in the bpac system (**5**), which displays enhanced absorption in the low energy tail (line violet).

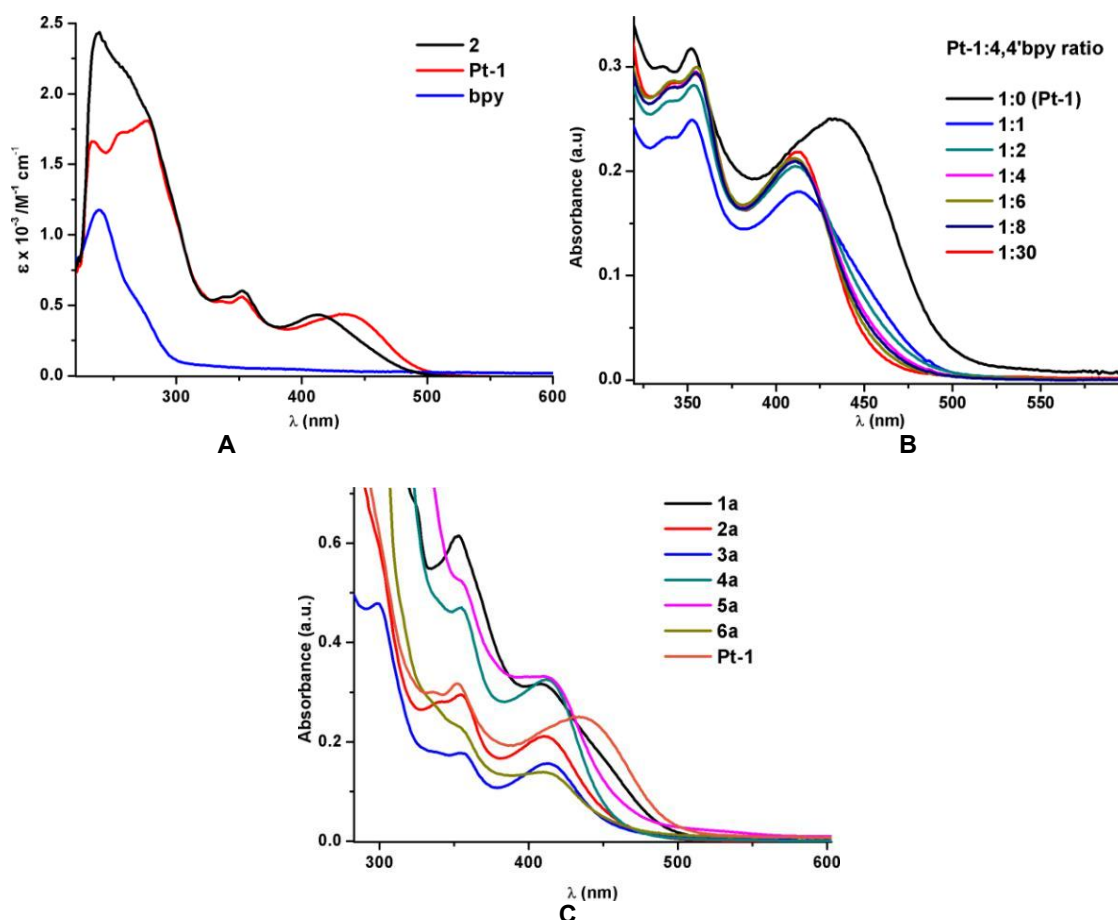


Fig. 7. A) Absorption spectra of **2a**, $[\text{Pt}(\text{pq})(\mu\text{-C}\equiv\text{C}^t\text{Bu})_2]$ (**Pt-1**) and free 4,4'-bpy in CH_2Cl_2 ; **B)** Normalized absorption spectra in CH_2Cl_2 of $[\text{Pt}(\text{pq})(\mu\text{-C}\equiv\text{C}^t\text{Bu})_2]$ (**Pt-1**) and successive additions of 1, 2, 4, 6, 8 and 30 equiv. of 4,4'-bpy; **C)** Low energy region of the absorption spectra of solids **1a–6a** and **Pt-1** in CH_2Cl_2

In accordance with the dynamic equilibrium and the NMR spectra commented before, the progressive addition of the corresponding *N-N*-donor ligand essentially causes the disappearance of **Pt-1** in solution. By way of illustration, Fig. 7B shows the spectra of the precursor (**Pt-1**), together with the changes observed upon successive addition of 4,4'-bpy. As it is observed, the maximum of the band is shifted from 436 nm in **Pt-1** to 410 nm with only 1 equiv. of ligand, but the band shows a long tail in the region where **Pt-1** still absorbs, thus confirming its presence. Upon addition of ca. 4 equiv. of ligand, the red-side of band decreases considerably, in accordance with the essentially disappearance of **Pt-1**. Upon addition of more ligand (6–30 equiv.) the changes in the maximum of band are minimal except for a small decrease in the tail. At this point, we attributed this minimal to a complete disappearance of the bimetallic species (**a**) in solution, leaving mononuclear **b** complexes as the predominant metallic components. The fact that the stepwise addition of ligand takes place keeping the low energy maximum at 410 nm (with minor changes in the tail) indicates that the absorption profiles and electronic structures of bimetallic (species **a**) and mononuclear complexes (species **b**) are likely rather similar. This behavior is not unexpected and has been previously observed in related systems [48]. In the case of the pyz-system **1** (**Pt-1/L₁**), a relation of ca. 1:14 was required for the disappearance of the precursor **Pt-1**, what is also in agreement with a greater dissociation of the *N*-ligand in the assembly.

2.2.2 Emission spectroscopy

Notably, these series of complexes **1-6** (**a** and **b**) are intensely luminescent in all media with efficiencies higher than those observed for the precursor. Table 1 summarizes emission data and Fig. 8 illustrates the emission profiles of **1a-6a** in the solid state at room and at 77 K. Upon photoexcitation (range 350–540 nm), the bimetallic complexes **1a-6a** give rise, at room temperature, unstructured bands in the range 590–615 nm, whereas at low temperature the profiles become structured and slightly blue shifted (572–598 nm). The lifetimes were adequately modeled by a single exponential function in the range of microseconds (τ 0.3–11.4 μ s 298 K; 7.6–39.2 μ s 77 K), confirming triplet parentage. As observed in Fig. 8, the emission profile of the bpe-bridged binuclear compound **4a**, is highly structured at 77 K, with peak maxima (588, 648 and 702 nm) which are close to those observed for the free ligand. This observation and the long lifetime (39.2 μ s) are consistent with a predominantly bpe-centered 3LC $^3(\pi\pi)^*$ excited state. The emission profiles of **1a** (pyz) and **2a** (bpy) are rather similar [$\lambda_{max}(nm)/T$: 590/298 K; 572 **1a**, 574 **2a** /77 K] and compare to those seen for other phenylquinoyl platinum complexes [60,61], being attributable to a mixed 3MLCT / $^3L'LCT$ (Pt(d) \rightarrow pq/C≡C^tBu \rightarrow pq) excited state. The low temperature profiles of complexes **3a**, **5a** and **6a** are similar to those of **1a** and **2a**, with the maxima slightly red shifted [$\lambda_{max}(nm)$ 598 **6a**(tpac) < 596 **5a**(bpac) < 588 **3a**(bpa)], suggesting similar 3MLCT / $^3L'LCT$ excited state with some contribution of the central *N-N* linker ligand.

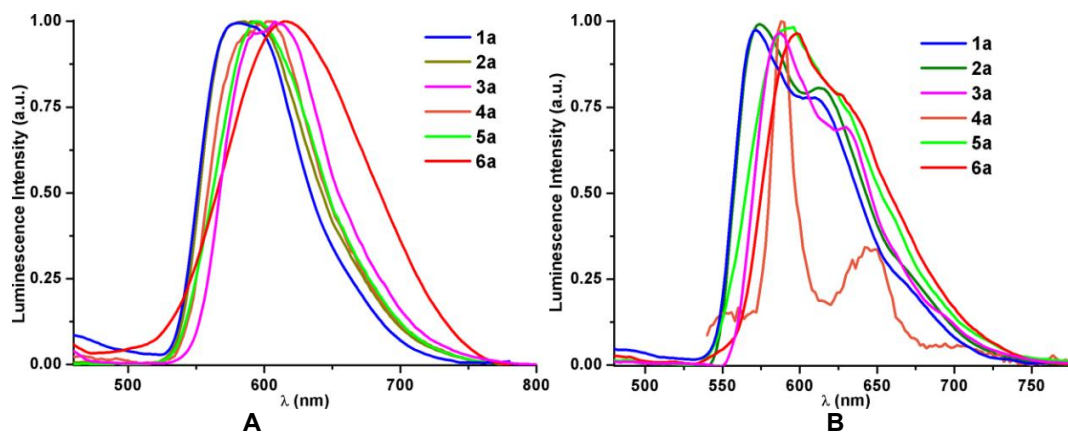


Fig. 8. Normalized emission spectra of **1a-6a** in solid state, **A**) at 298 K; **B**) at 77 K (λ_{exc} 400 nm)

Table 1. Relevant data of absorption and emission for complexes in solid state (1a–6a) and in solution [mixtures Pt-1:L (1:4) (L₂–L₆) and 1:14 (L₁) in CH₂Cl₂, 5 × 10⁻⁵ M; predominant species: 2b-5b, mixtures of 1a/1b or 6a/6b]

Compound	Medium	(T ^a /K)	λ _{abs} /nm ^a (10 ³ ε M ⁻¹ cm ⁻¹)	λ _{em} /nm ^b	τ/μs	Φ(%)
1	Solid	298	530	590	8.0	13.8
		77		572	14.0	
2	Solution	298	408 (20.6)	595		13.1
		77		570		
		298	410 (13.3)	590	9.9	
3	Solution	77		570	12.2	9.4
		298	525	610	9.9	
		77		588	7.7	
4	Solution	298	413 (17.7)	595		4.9
		77		570		
		298	535	605	10.4	
5	Solution	77 ^c	412 (20.7) ^d	578	39.2	6.8
		77		578	13.8	
		298	540	596	11.4	
6	Solution	77		596	15.2	1.1
		298	410 (20.8)	595	9.2	
		77		576	14.4	
6	Solution	298	545 ^e	615	0.3	1.1
		77		598	7.6	
		298	410 (6.0)	595		
		77		570		

^a Lowest-energy absorption peak; ^b Highest-energy emission peak; ^c Non emissive at 298 K; ^d 298 K; ^e Tail to 630 nm

Taken into account the occurrence of the dissociation process for the bimetallic complexes **1a–6a** commented above, the study of the emissions in solution was carried out using CH₂Cl₂ solutions with a **Pt-1**:L proportion of 1:4 (data are listed in Table 1). Under these conditions, the predominant species in solution are the mononuclear complexes for **2b** to **5b**. However, mixtures with the corresponding binuclear complexes are expected in the systems with pyrazine and the trinucleating 1,3,5-tris(pyridyl)acetylene ligand (**1** and **6**).

The bpe complex (**4b**) is not emissive in fluid. This behavior is not unexpected and might be attributed to a relatively fast nonradiative relaxation by forming a twisted triplet state (³p) [48,62–64]. As shown in Fig. 9A, the remaining complexes display a rather similar intense broad emission located at around 595 nm, thus suggesting a negligible influence of the N-donor auxiliary ligand in the emissive state. The emission shifts remarkably to higher energies at 77 K, developing structured profiles (Fig. 9B) with minimal variations in λ_{max} (range 570–576 nm). At 77 K, the bpe complex **4b** is also emissive (line orange) exhibiting similar structured profile with a peak maximum at 578 nm, pointing to a similar emissive state. In fact, lifetime measurements for two representative complexes with ligands bpe (**4b**) and bpac (**5b**) in glass state are also similar (13.8 **4b**; 14.4 μs **5b**). The emission is mainly attributed to typical mixed excited state ³MLCT/³L'LCT of the mononuclear species [Pt(pq)(C≡C^tBu)(N-N)] (**1b–5b**) generated in solution.

It is worth to note that identical emission profiles but with reduced intensity were obtained from solution of the binuclear **1a–3a** and **5a** solids (or by using **Pt-1**/L 1:1 molar ratio). This fact might be attributed to similar luminescence response of the species **a** and **b** (both present in solution), which are clearly more emissive than the starting material. Interestingly, in contrast to the nonemissive behavior of the mononuclear complex **4b**, a diluted solution (5 × 10⁻⁵ M) of the solid bpe binuclear

complex **4a** displays an unstructured band located at 600 nm upon excitation at 420 nm, which could be related to the presence of the more rigid **4a** in solution.

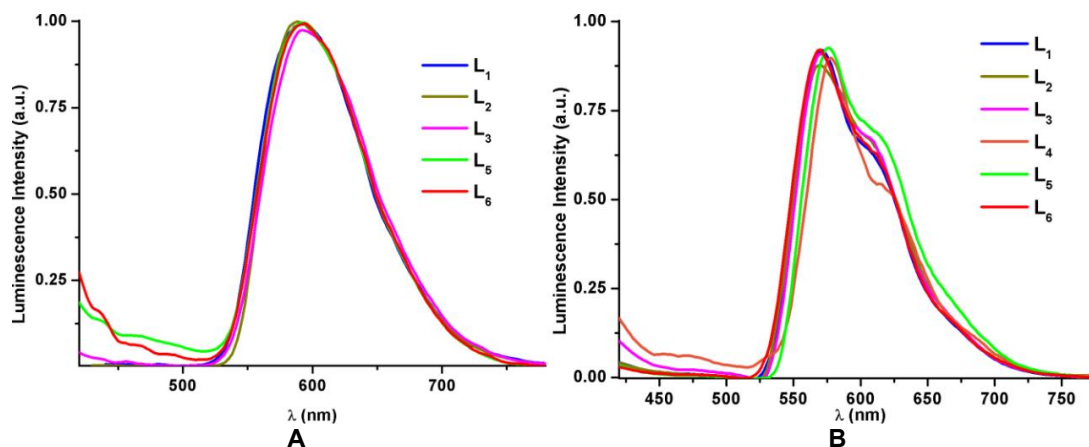


Fig. 9. Emission spectra of species **b** from mixtures (see text) of Pt-1:L (1:4 ratio) in CH_2Cl_2 (5×10^{-5} M) at A) 298 K and B) 77 K

2.2.3 Theoretical calculations

TD-DFT and DFT calculations were conducted for the species **2a**, as a representative example, to unveil the electronic transition behavior of the binuclear complexes. Calculations were performed with the B3LYP functional associated with the LanL2DZ/6-31G(d,p) basis sets [59].

Fig. 10 shows some selected orbitals in its optimized ground state (S_0) in gas phase. The HOMO and HOMO-1 are degenerated and are contributed from the alkynyl donor ($\sim 60\%$) and the Pt atom, whereas the electron density of the HOMO-2 and HOMO-3, of similar energy, mainly resides on one Pt(pq)(C≡CtBu) unit and the HOMO-4 is located on the other unit. In these orbitals, the computed contribution of the alkynyl unit decreases and increases the participation of the cyclometalated pq [*i.e.* H-4 Pt (30%), pq (55%) and C≡CtBu (13%)]. The LUMO is mainly centered on the bipyridine ligand with a computed contribution of 94%, but the two following and nearly degenerated low lying virtual orbitals LUMO+1 and LUMO+2 are, however, localized on the cyclometalated pq groups. The lowest electronic transition ($S_0 \rightarrow S_1$) is dominated by the electronic transition from HOMO-4 to LUMO and can be described to charge transfer from one Pt(pq)(C≡CtBu) unit to the central N-N linker, having $^1[(M + L + L')L''CT]$ character. The calculated value (494 nm) compares to that seen in the solid reflectance spectrum at 530 nm. The computational results for the following excitations ($S_{2,3} \sim 482$ nm), which could be correlated with the experimental feature located at 500 nm, reveal significant charge transfer from HOMO and HOMO-1 to LUMO+1 and LUMO+2, being ascribed to platinum-alkynyl to pq charge transfer $^1[(M + L')LCT]$ associated to both metal fragments.

By taking into consideration the solvent (CH_2Cl_2), a blue shift is calculated in the lowest singlet excitations in agreement with its charge transfer nature. The lowest energy excitations $S_{1,3}$, close in energy (435, 431 and 428 nm), involve electronic transitions from HOMO-3 – HOMO to LUMO – LUMO+2 and can be related with the broad experimental absorption band located at 410 nm in CH_2Cl_2 solution. As a consequence, this band could be ascribed as an admixture of platinum-alkynyl-pq to pq charge transfer $^1[(M + L' + L)LCT]$ with contribution to the central bpy linker $^1[(M + L' + L)L''CT]$ ($L = \text{pq}$, $L' = \text{C}\equiv\text{CtBu}$, $L'' = \text{bpy}$).

The calculated emission in phase gas (584 nm) is in accordance with the experimental value in the solid state (590 nm). This emission is dominated by the SOMO-1 \leftarrow SOMO electronic transition (Fig. 11) and is mainly attributed to a mixed excited state having platinum-alkynyl to phenylquinolynyl charge transfer $^3[(M + L')LCT]$ with some intraligand character 3LC . This result reinforces the experimental data indicating a negligible influence of the N-donor linker.

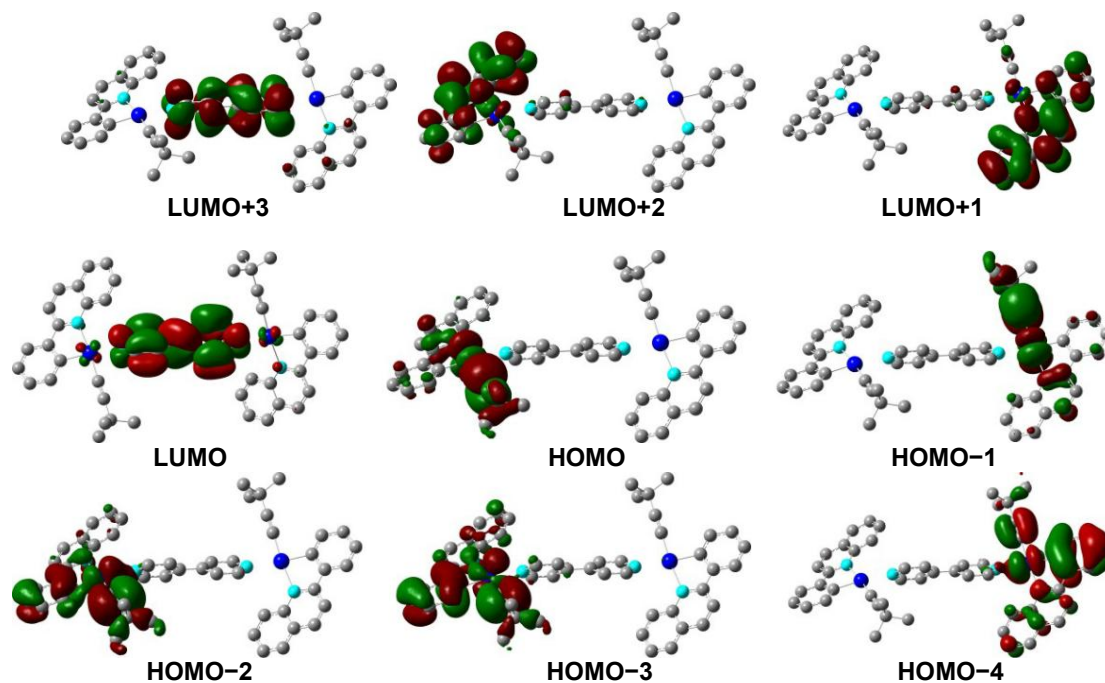


Fig. 10. Molecular orbital plots for the computed S_0 state in gas phase of **2a** [Pt(2) left; Pt(1) right]

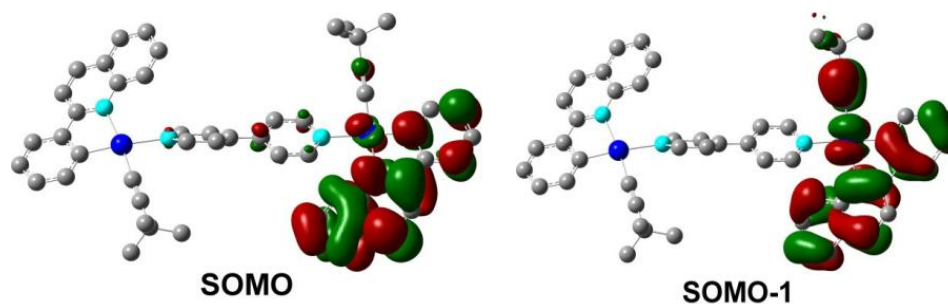


Fig. 11. Molecular orbital plots for the computed T_1 state of complex **2a**

3. CONCLUSIONS

The synthesis and properties of a series of binuclear $[\{\text{Pt}(\text{pq})(\text{C}\equiv\text{C}^t\text{Bu})\}_2(\mu\text{-L})]$ (**1a–5a**) and a trinuclear $[\{\text{Pt}(\text{pq})(\text{C}\equiv\text{C}^t\text{Bu})\}_3(\mu\text{-L})]$ (**6a**) complexes having bidentate *N,N*-donor ligands of different lengths and flexibility and one *N,N,N*-tridentate ligand is reported. These polymetallic complexes rearrange in solution giving rise to a fast dynamic equilibrium between the diplatinum complexes (**1a–5a**), the mononuclear species $[\text{Pt}(\text{pq})(\text{C}\equiv\text{C}^t\text{Bu})(\text{L-}\kappa\text{N})]$ (**1b–5b**), the bimetallic precursor $[\text{Pt}(\text{pq})(\mu\text{-C}\equiv\text{C}^t\text{Bu})_2]$ (**Pt-1**) and the free ligand (L), as confirmed by ^1H NMR experiments and UV-Vis spectroscopy. This equilibrium, attributed to the *trans* labilizing effect of the C-metalated atom in the species **a** and the high stability of the bimetallic $[\text{Pt}(\text{pq})(\mu\text{-C}\equiv\text{C}^t\text{Bu})_2]$ **Pt-1**, is affected by the concentration, temperature, solvent polarity and the nature of the linker. The higher proportion of the bimetallic species (**a**) in solution appears with the more flexible and donor linkers (bpa, bpe) at high solution concentration, low temperatures and in lesser polar solvents.

On the basis of calculations on **2a**, the low-energy absorption band in the solid (500–540 nm) is ascribed to charge transfer from the $\text{Pt}(\text{pq})(\text{C}\equiv\text{C}^t\text{Bu})$ to 4,4'-bpy. However, in solution, the blue shifted

low energy band (408–413 nm) is due to admixture of platinum/alkynyl/pq to cyclometalate (pq) charge transfer $^1[d(\text{Pt})/\text{C}\equiv\text{C}/\text{pq}\rightarrow\pi^*(\text{pq})]$ $^1[(\text{M} + \text{L}' + \text{L})\text{LCT}]$ with minor contribution to the *N,N*-donor ligand $^1[d(\text{Pt})/\text{C}\equiv\text{C}/\text{pq}\rightarrow\pi^*(\text{N-donor})]$.

All these assemblies exhibit more intense emissions than the starting material (**Pt-1**) both, in solid and solution. For the bpe-dimer **4a**, its emissive properties are typical of a bpe-centered $^3\text{LC } ^3(\pi\pi^*)$ excited state, whereas the emission of **1a-3a** and **5a** is ascribed to a mixed $^3[(\text{M} + \text{L}')\text{LCT}]$ state with minor contribution of the central *N,N* linker in **3a** and **5a**. This assignment is in accord to the calculations for **2a**, which reveals that, upon excitation, the energy of the π^* diimine-based orbitals increases above the cyclometalated-based orbitals causing a remarkable change in the nature of SOMO–SOMO-1 vs HOMO–LUMO. In fluid solution, the binuclear species (**a**) and the mononuclear species (**b**) (mixtures **Pt-1**:L 1:4) display similar emission, suggesting a similar excited state for both types of species.

ACKNOWLEDGEMENTS

The authors are grateful to the Spanish Projects (CTQ2008-06669-C02-02/BQU, CTQ2013-45518-P and PID2019-109742GB-I00) for its financial support.

COMPETING INTERESTS

Authors have declared that no competing interests exist.

REFERENCES

1. Berenguer JR, Lalinde E, Moreno MT. An overview of the chemistry of homo and heteropolynuclear platinum complexes containing bridging acetylide ($\mu\text{-C}\equiv\text{CR}$) ligands. *Coordination Chemistry Reviews*. 2010;254:832–857.
2. Lang H, George DSA, Rheinwald G. Bis(alkynyl) transition metal complexes, $\text{R}^1\text{C}\equiv\text{C}-[\text{M}]-\text{C}\equiv\text{CR}^2$, as organometallic chelating ligands; formation of $\mu,\eta^{1(2)}$ -alkynyl-bridged binuclear and oligonuclear complexes. *Coordination Chemistry Reviews*. 2000;206:101–197.
3. Lang H, Köhler K, Blau S. η^2 -Alkyne copper(I) and silver(I) compounds; From polymeric $[\text{M}^{\text{I}}\text{R}]_n$ to monomeric $[\text{M}^{\text{I}}\text{R}]$ units (M = Cu, Ag). *Coordination Chemistry Reviews*. 1995;143:113–168.
4. Forniés J, Lalinde E. Synthesis, structure and reactivity of homo- and hetero-polynuclear complexes of platinum bearing $\text{C}\equiv\text{CR}$ groups as unique bridging ligands. *Journal of the Chemical Society, Dalton Transactions*. 1996;2587–2599.
5. Wong KMC, Yam VWW. Self-assembly of luminescent Alkynylplatinum(II) Terpyridyl complexes: Modulation of photophysical properties through aggregation behavior. *Accounts of Chemical Research*. 2011;44:424–434.
6. Yam VWW. Molecular design of transition metal alkynyl complexes as building blocks for luminescent metal-based materials: Structural and photophysical aspects. *Accounts of Chemical Research*. 2002;35:555–563.
7. Hissler M, McGarrah JE, Connick WB, Geiger DK, Cummings SD, Eisenberg R. Platinum diimine complexes: Towards a molecular photochemical device. *Coordination Chemistry Reviews*. 2000;208:115–137.
8. Rossi E, Colombo A, Dragonetti C, Roberto D, Ugo R, Valore A, Falciola L, Brulatti P, Cocchi M, Williams JAG. Novel $\text{N}^{\wedge}\text{C}^{\wedge}\text{N}$ -cyclometallated platinum complexes with acetylide co-ligands as efficient phosphors for OLEDs. *Journal of Materials Chemistry*. 2012;22:10650–10655.
9. Yam VWW. Luminescent metal alkynyls—From simple molecules to molecular rods and materials. *Journal of Organometallic Chemistry*. 2004;689:1393–1401.
10. Wong WY. Luminescent organometallic poly(aryleneethynylene)s: Functional properties towards implications in molecular optoelectronics. *Dalton Transactions*. 2007;4495–4510.
11. Chen ZN, Zhao N, Fan Y, Ni J. Luminescent groups 10 and 11 heteropolynuclear complexes based on thiolate or alkynyl ligands. *Coordination Chemistry Reviews*. 2009;253:1–20.

12. Castellano FN, Pomestchenko IE, Shikhova E, Hua F, Muro ML, Rajapakse N. Photophysics in bipyridyl and terpyridyl Platinum(II) acetylides. *Coordination Chemistry Reviews*. 2006;250:1819–1828.
13. Wong KMC, Yam VWW. Luminescence Platinum(II) terpyridyl complexes—From fundamental studies to sensory functions. *Coordination Chemistry Reviews*. 2007;251:2477–2488.
14. Yang W, Zhao J. Photophysical properties of visible-light-harvesting Pt^{II} Bis(acetylide) complexes. *European Journal of Inorganic Chemistry*. 2016;5283-5299.
15. Zhou GJ, Wong WY. Organometallic acetylides of Pt^{II}, Au^I and Hg^{II} as new generation optical power limiting materials. *Chemical Society Reviews*. 2011;40:2541-2566.
16. Liao C, Shelton AH, Kim KY, Schanze KS. Organoplatinum chromophores for application in high-performance nonlinear absorption materials. *ACS Applied Materials & Interfaces*. 2011;3:3225-3238.
17. Green KA, Cifuentes MP, Samoc M, Humphrey MG. Metal alkynyl complexes as switchable NLO systems. *Coordination Chemistry Reviews*. 2011;255:2530–2541.
18. Williams JAG, Develay S, Rochester DL, Murphy L. Optimising the luminescence of platinum(II) complexes and their application in organic light emitting devices (OLEDs). *Coordination Chemistry Reviews*. 2008;252:2596-2611.
19. Rossi E, Colombo A, Dragonetti C, Roberto D, Ugo R, Valore A, Falciola L, Brulatti P, Cocchi M, Williams JAG. Novel N^CN-cyclometallated platinum complexes with acetylide co-ligands as efficient phosphors for OLEDs. *Journal of Materials Chemistry*. 2012;22:10650-10655.
20. Lu W, Mi BX, Chan MCW, Hui Z, Che CM, Zhu N, Lee ST. Light-emitting tridentate cyclometalated platinum(II) complexes containing σ -alkynyl auxiliaries: Tuning of Photo- and electrophosphorescence. *Journal of the American Chemical Society*. 2004;126:4958-4971.
21. Qiu D, Li M, Zhao Q, Wang H, Yang C. Cyclometalated Platinum(II) terpyridylacetylide with a Bis(arylamine) donor as a proton-triggered luminescence chemosensor for Zn²⁺. *Inorganic Chemistry*. 2015;54:7774-7782.
22. Yam VWW, Au VKM, Leung SYL. Light-emitting self-assembled materials based on d⁸ and d¹⁰ transition metal complexes. *Chemical Reviews*. 2015;115:7589-7728.
23. Aliprandi A, Genovese D, Mauro M, Cola LD. Recent advances in phosphorescent Pt(II) complexes featuring metallophilic interactions: Properties and applications. *Chemistry Letters*. 2015;44:1152-1169.
24. Fan C, Yang C. Yellow/orange emissive heavy-metal complexes as phosphors in monochromatic and white organic light-emitting devices. *Chemical Society Reviews*. 2014;43:6439-6469.
25. Berenguer JR, Forniés J, Lalinde E, Martín A, Serrano B. Preparation and characterisation of neutral double- and mono-alkynyl bridged diplatinum complexes. *Journal of Chemical Society, Dalton Transactions*. 2001;2926-2936.
26. Ara I, Falvello LR, Fernández S, Forniés J, Lalinde E, Martín A, Moreno MT. Synthesis and reactivity of σ -Alkynyl/*P*-Bonded phosphinoalkyne platinum complexes toward *cis*-[M(C₆F₅)₂(thf)₂] (M = Pt, Pd). *Organometallics*. 1997;16:5923–5937.
27. García A, Lalinde E, Moreno MT. Ethynyltolan platinum complexes with (Arylalkynyl)phosphane ligands. *European Journal of Inorganic Chemistry*. 2007;3553–3560.
28. Forniés J, Gómez-Saso MA, Lalinde E, Martínez F, Moreno MT. Preparation of doubly acetylide-bridged binuclear platinum-platinum and platinum-palladium complexes. Structures of [(dppe)Pt(C≡CPh)₂]Pt(C₆F₅)₂] and (PMePh₃)₂(C₆F₅)₂Pt(μ -C≡CPh)₂Pt(C₆F₅)₂]. *Organometallics*. 1992;11:2873–2883.
29. Falvello LR, Forniés J, Gómez J, Lalinde E, Martín A, Martínez F, Moreno MT. Some Platinum(II) complexes containing bis(diphenylphosphino)acetylene PPh₂C≡CPh₂: Synthesis, characterisation and crystal structures. *Journal of Chemical Society, Dalton Transactions*. 2001;2132-2140.
30. Berenguer JR, Forniés J, Martínez F, Cubero JC, Lalinde E, Moreno MT, Welch AJ. Synthesis and reactivity of bimetallic acetylide-bridged Pt-Pt complexes. Crystal and molecular structure of [(PPh₃)(C₆F₅)Pt(μ -C≡CPh)₂Pt(C₆F₅)(PPh₃)]. *Polyhedron*. 1993;12:1797–1804.
31. Falvello LR, Forniés J, Martín A, Gómez J, Lalinde E, Moreno MT, Sacristán J. Synthesis of heterobridged (μ -C≡CR)(μ -X) (X = PPh₂, PPh₂O) platinum–rhodium or platinum–iridium dimers. *Inorganic Chemistry*. 1999;38:3116–3125.

32. Aullón G, Álvarez S. Molecular structure and isomerization in square-planar edge-sharing dinuclear complexes with alkynyl bridges. *Organometallics*. 2002;21:2627–2634.
33. Hoogervorst WJ, Elsevier CJ, Lutz M, Spek AL. New *cis*- and *trans*-arylplatinum(II) acetylide compounds containing a bis(imino)aryl [NCN] ligand. *Organometallics*. 2001;20:4437–4440.
34. Casas JM, Forniés J, Fuertes S, Martín A, Sicilia V. New mono- and polynuclear alkynyl complexes containing phenylacetylide as terminal or bridging ligand. x-ray structures of the compounds $\text{NBu}_4[\text{Pt}(\text{CH}_2\text{C}_6\text{H}_4\text{P}(\text{o-tolyl})_2\text{-}\kappa\text{C,P})(\text{C}\equiv\text{CPh})_2]$, $[\text{Pt}(\text{CH}_2\text{C}_6\text{H}_4\text{P}(\text{o-tolyl})_2\text{-}\kappa\text{C,P})(\text{C}\equiv\text{CPh})(\text{CO})]$, $[\{\text{Pt}(\text{CH}_2\text{C}_6\text{H}_4\text{P}(\text{o-tolyl})_2\text{-}\kappa\text{C,P})(\text{C}\equiv\text{CPh})\}_2]$ and $[\{\text{Pt}(\text{CH}_2\text{C}_6\text{H}_4\text{P}(\text{o-tolyl})_2\text{-}\kappa\text{C,P})(\text{C}\equiv\text{CPh})_2\text{Cu}\}_2]$. *Organometallics*. 2007;26:1674–1685.
35. Forniés J, Lalinde E, Martín A, Moreno MT. Di- and tri-nuclear platinum complexes with double acetylide bridges. Molecular structure of $[\text{NBu}_4]_2[\text{Pt}_3(\text{C}_6\text{F}_5)_4(\mu\text{-C}\equiv\text{CPh})_4] \cdot 4\text{thf}$ (thf = tetrahydrofuran). *Dalton Transactions*. 1994;135-141.
36. Berenguer JR, Forniés J, Lalinde E, Martínez F. Unusual stabilization of cationic $\text{M}(\eta^3\text{-allyl})^n$ (M = Pt, Pd) units by a dianionic $\text{cis-}\{\text{Pt}(\text{C}_6\text{F}_5)_2(\text{C}\equiv\text{CSiMe}_3)_2\}^{2-}$ fragment. *Journal of Organometallic Chemistry*. 1994;470:C15–C18.
37. Fujita M, Yazaki J, Ogura K. Preparation of a macrocyclic polynuclear complex, $[(\text{en})\text{Pd}(4,4'\text{-bpy})_4(\text{NO}_3)_8]$ (en = ethylenediamine, bpy = bipyridine), which recognizes an organic molecule in aqueous media. *Journal of the American Chemical Society*. 1990;112:5645–5647.
38. Harris K, Sun QF, Fujita M. Coordination self-assembly: Structure and function updated. In *Comprehensive Inorganic Chemistry II (Second Edition)*, Reedijk J, Poeppelemeier K., Eds. Elsevier: Amsterdam. 2013;31-57.
39. Huang SL, Andy Hor TS, Jin GX. Metallacyclic assembly of interlocked superstructures. *Coordination Chemistry Reviews*. 2017;333:1-26.
40. Zangrando E, Casanova M, Alessio E. Trinuclear metallacycles: Metallatriangles and much more. *Chemical Reviews*. 2008;108:4979–5013.
41. Xu L, Wang YX, Yang HB. Recent advances in the construction of fluorescent metalocycles and metalocages via coordination-driven self-assembly. *Dalton Transactions*. 2015;44:867-890.
42. Sun Y, Chen C, Stang PJ. Soft materials with diverse suprastructures via the self-assembly of metal-organic complexes. *Accounts of Chemical Research*. 2019;52:802-817.
43. Saha ML, Yan X, Stang PJ. Photophysical properties of organoplatinum(II) compounds and derived self-assembled metallacycles and metalocages: Fluorescence and its applications. *Accounts of Chemical Research*. 2016;49:2527-2539.
44. Cook TR, Stang PJ. Recent developments in the preparation and chemistry of metallacycles and metalocages via coordination. *Chemical Reviews*. 2015;115:7001-7045.
45. Schmidt A, Casini A, Kühn FE. Self-assembled M_2L_4 coordination cages: Synthesis and potential applications. *Coordination Chemistry Reviews*. 2014;275:19–36.
46. Amouri H, Desmarests C, Moussa J. Confined nanospaces in metalocages: Guest molecules, weakly encapsulated anions and catalyst sequestration. *Chemical Reviews*. 2012;112:2015–2041.
47. Allendorf MD, Bauer CA, Bhakta RK, Houk RJT. Luminescent metal-organic frameworks. *Chemical Society Reviews*. 2009;38:1330–1352.
48. Jude H, Krause BJA, Connick WB. Luminescent Platinum(II) dimers with a cyclometalating aryldiamine ligand. *Inorganic Chemistry*. 2005;44:1211–1220.
49. Jude H, Krause BJA, Connick WB. Tuning the electronic structures of platinum(II) complexes with a cyclometalating aryldiamine ligand. *Inorganic Chemistry*. 2004;43:725–733.
50. Shi LL, Liao Y, Yang GC, Su ZM, Zhao SS. Effect of π -conjugated length of bridging ligand on the optoelectronic properties of Platinum(II) dimers. *Inorganic Chemistry*. 2008;47:2347–2355.
51. Jude H, Krause BJA, Connick WB. Synthesis, structures and emissive properties of Platinum(II) complexes with a cyclometalating aryldiamine ligand. *Inorganic Chemistry*. 2002;41:2275–2281.
52. Fuertes S, Woodall CH, Raithby PR, Sicilia V. Heteropolynuclear Pt(II)–M(I) clusters with a C^NC Biscyclometalated ligand. *Organometallics*. 2012;31:4228–4240.
53. Zhao F, Xu X, Khoo SB, Hor TSA. Structure-dependent electrochemical behavior of Thienylplatinum(II) complexes of *N,N*-Heterocycles. *European Journal of Inorganic Chemistry*. 2004;1:69–77.

54. Rao YL, Wang S. Impact of Constitutional isomers of (BMes₂)phenylpyridine on structure, stability, phosphorescence and lewis acidity of mononuclear and dinuclear Pt(II) complexes. *Inorganic Chemistry*. 2009;48:7698–7713.
55. Meijer MD, de Wolf E, Lutz M, Spek AL, van Klink GPM, van Koten G. C,N-2-[(Dimethylamino)methyl]phenylplatinum complexes functionalized with C₆₀ as macromolecular building blocks. *Organometallics*. 2001;20:4198–4206.
56. Lalinde E, Moreno MT, Ruiz S, Sánchez S. Synthesis, structural and photophysical studies of phenylquinoline and phenylquinolinyl alkynyl based Pt(II) complexes. *Organometallics*. 2014;33:3078–3090.
57. Coe BJ, Harries JL, Harris JA, Brunschwig BS, Coles SJ, Light ME, Hursthouse MB. Syntheses, spectroscopic and molecular quadratic nonlinear optical properties of dipolar ruthenium(II) complexes of the ligand 1,2-phenylenebis(dimethylarsine). *Dalton Transactions*. 2004;2935-2942.
58. Amoroso AJ, Cargill TAMW, Maher JP, McCleverty JA, Ward MD. Di-, Tri- and Tetranucleating Pyridyl ligands which facilitate multicenter magnetic exchange between paramagnetic molybdenum centers. *Inorganic Chemistry*. 1995;34:4828–4835.
59. Lalinde E, Moreno MT, Ruiz S, Sánchez S. Attachment of luminescent neutral "Pt(pq)(C≡C^tBu)" units to Di and Tri N-Donor connecting ligands: Solution behavior and photophysical properties. *Inorganics*. 2014;2:565-590. (Special Issue "Organoplatinum Complexes").
60. Berenguer JR, Díez A, Lalinde E, Moreno MT, Ruiz S, Sánchez S. Luminescent cycloplatinated complexes containing Poly(pyrazolyl)-borate and -methane ligands. *Organometallics*. 2011;30:5776–5792.
61. Martínez-Junquera M, Lara R, Lalinde E, Moreno MT. Isomerism, aggregation-induced emission and mechanochromism of isocyanide cycloplatinated(II) complexes. *Journal of Materials Chemistry C*. 2020;8:7221-7233.
62. Dattelbaum DM, Itokazu MK, Murakami INY, Meyer TJ. Mechanism of metal-to-ligand charge transfer sensitization of olefin *trans*-to-*cis* isomerization in the *fac*-[Re^I(phen)(CO)₃(1,2-bpe)]⁺ cation. *Journal of Physical Chemistry A*. 2003;107:4092–4095.
63. Schanze KS, Lucia LA, Cooper M, Walters KA, Ji HF, Sabina O. Intramolecular energy transfer to *trans*-Stilbene. *Journal of Physical Chemistry A*. 1998;102:5577–5584.
64. Saltiel J, Marchand GR, Kirkor-Kaminska E, Smothers WK, Mueller WB, Charlton JL. Nonvertical triplet excitation transfer to *cis*- and *trans*-stilbene. *Journal of the American Chemical Society*. 1984;106:3144–3151.

Biography of author(s)



Elena Lalinde

Departamento de Química-Centro de Síntesis Química de La Rioja (CISQ), Universidad de La Rioja, 26006, Logroño, Spain.

She studied Chemistry at the University of Zaragoza where she received her PhD in 1983. She moved to the University College in Logroño (La Rioja) associated to Zaragoza University and she spent postdoctoral periods at the University of Sheffield working with Prof. Peter Maitlis. She was promoted to Professor Titular of Inorganic Chemistry in 1989 and finally to Full professor of La Rioja University in 2007. Her research has been focused on the chemistry of alkynyl and alkynylphosphine and cyclometalated ligands of homo and heteropolynuclear metal complexes mainly of d⁶ (Ir, Rh; Pt), d⁸ (Pt), d¹⁰ (Cu, Ag, Cd) and ns²d¹⁰ (Tl, Pb) metal centers, including reactivity and luminescence studies and their potential applications (biological and OLEDs). More recently her interest also focuses on the preparation of mesoporous functional solids (silice) and the study of their structure-property correlations.



M. Teresa Moreno

Departamento de Química-Centro de Síntesis Química de La Rioja (CISQ), Universidad de La Rioja, 26006, Logroño, Spain.

She received her degree in Chemistry from the Autonomous University of Madrid (UAM) and she obtained her Ph.D. from the University of Zaragoza in 1991. She made a postdoctoral stay at the University of Bristol (1996) working with Prof. Neil Connely, where she became acquainted with electrochemical techniques. She was promoted to Professor Titular of Inorganic Chemistry in 1999 and later to Full Professor of La Rioja University in 2018. Her current research interests focus on the design of photoluminescent transition metal coordination and organometallic compounds (mainly with metals of groups 8-11) with potential applications in light-emitting diodes, bioimaging, sensors or biological activity.



Santiago Ruiz

Departamento de Química-Centro de Síntesis Química de La Rioja (CISQ), Universidad de La Rioja, 26006, Logroño, Spain.

He completed his studies in Chemistry in 2008 at the La Rioja University, where he obtained his PhD in Chemistry in 2014. Meanwhile, he spent a three-month stay in the group of Prof. Véronique Guerschais at the University of Rennes 1-CNRS, working in photochromic platinum complexes as switches for nonlinear optics. At present, he is a teacher in a Secondary School. His main research interest is centered in luminescent cycloplatinated compounds.



Sergio Sánchez

Departamento de Química-Centro de Síntesis Química de La Rioja (CISQ), Universidad de La Rioja, 26006, Logroño, Spain.

He received his degree in Chemistry from the La Rioja University, where he obtained his PhD in 2012. He made two postdoctoral stays, at the Manchester University (2013-2016) with Prof. Benjamin Coe and at the Calgary University (2016-2017) with Prof. Thomas Baumgartner. Currently, he is a research chemist in the enterprise FREDsense Technologies in Calgary, Canada. His earlier academic endeavors cover the study of electronic communication in organometallic systems, theoretical calculations, luminescence, non-linear optical properties and photocatalysis. His current researches are focused on subjects involving biological-based electrochemical detection of analytes in ground and surface water and the design and testing of sensors.

© Copyright (2020): Author(s). The licensee is the publisher (Book Publisher International).

DISCLAIMER

This chapter is an extended version of the article published by the same author(s) in the following journal. *Inorganics*, 2(4): 565-590, 2014.

Investigation of the Anatomical Variability of the Trunk and Root Tissues of *Rhizophora racemosa* (G. Mey) and *Avicennia germinans* (Linné): A Bioaccumulation of Heavy Metals and Pollution Effects on Mangrove Trees Study

S. B. Mabicka Iwangou^{1,2}, P. Soulounganga^{1,3}, A. Besserer²,
R. Safou Tchiamia^{1,4*}, C. Ndoutoume¹, T. Andzi Barhé^{1,5} and P. Gerardin²

DOI: 10.9734/bpi/cpcs/v2

ABSTRACT

Aim: To evaluate the anatomical variability between the wood tissues of *R. racemosa* and *A. germinans* and to control the impact of metal trace elements (MTE) pollution in the chemical composition and the natural durability of these Gabon mangrove trees.

Study Design: Laboratory-experiment design was used for this study.

Place and Duration of Study: Fresh roots and trunks of *R. racemosa* and *A. germinans* were collected at the non-polluted sites of Oveng and Ayémé Maritime mangroves of Libreville. The wood samples from MTE polluted were obtained at Alénakiri public discharge mangrove of Libreville. The study was carried out from March 2015 to July 2020 at the LaReVa Bois in Gabon, and the LERMAB at the University of Lorraine in France.

Methodology: The vessel and sclerous cells diameter (μm) and their corresponding number/ mm^2 were calculated after microtome cutting and optic microscopy analysis. The extractives content was obtained after accelerated solvent extraction (ASE), MTE was identified by scanning electronic microscopy (SEM) coupled to EDS and X-ray microanalysis. The chemical structure of organic compounds was determined by Gas chromatography coupled mass spectroscopy (GC-M). The natural durability of the wood was controlled based on the mass loss of samples exposed to the white rot-fungus (*T. versicolor*) and the brown rot-fungus (*P. placenta*).

Results: It was found that *A. germinans* roots were less abundant in cells number/ mm^2 than its trunk which exhibited the largest cells diameter. *R. racemosa* roots and trunk didn't exhibit significant difference between their cells number. Nevertheless, the trunk of that mangrove tree displayed the largest cells diameter and somewhat traumatic channels. Any interspecies variability was found between their trunk vessel diameters. However, significant difference was found on their vessels number/ mm^2 ; *A. germinans* trunk was richer in vessels compared to *R. racemosa*. The roots of the latter were more abundant in vessels and displayed the largest cell diameters. Broad parenchyma bands and sclerous cells lacked within *R. racemosa* while they were richer in *A. germinans* roots and trunk. The occurrence of those anatomical structures which storage substances was thought to act in the highest heavy metals bio-remediation of Avicenniaceae than Rhizophoraceae. The wood of *A. germinans* exposed to metallic trace element (MTE) pollution have not shown substantial chemical changes on fatty acid of low molecular weight and polar molecules content. The strong concentration

¹Laboratoire de Recherche et de Valorisation du Matériau Bois (LaReVa Bois), Ecole Normale Supérieure d'Enseignement Technique (ENSET), BP. 3989, Libreville, Gabon.

²Université de Lorraine, Inra, Laboratoire d'Etudes et de Recherche sur le Matériau Bois (LERMAB), Faculté des Sciences et Technologies Boulevard des Aiguillettes BP 70239. 54506 Vandœuvre lès Nancy Cedex-France.

³Laboratoire Pluridisciplinaire des Sciences, Ecole Normale Supérieure, BP 17009, Libreville, Gabon.

⁴Laboratoire de Chimie des Substances Naturelles et de Synthèses Organométalliques, Unité de Recherche en Chimie (URChi), Université des Sciences et Techniques de Masuku, BP. 941, Franceville, Gabon.

⁵Laboratoire de Recherche en Chimie Appliquée (LARCA), Ecole Normale Supérieure (ENS), Université Marien Nguabi, Brazzaville, Congo.

of Cl, K and Ca on *A. germinans* sapwood from polluted area suggested physiological perturbations on these mineral accumulation in contaminated area. Cr and Cu were mostly accumulated in *A. germinans* sapwood than heartwood. The wood durability of *A. germinans* towards *Poria placenta* was slightly decreased by MTE pollution. A high resilience of *A. germinans* to MTE was claimed.

Conclusion: This study has pointed out anatomical differences between the trunk and the roots of *R. racemosa* and *A. germinans* from the mangrove trees of Gabon. *R. racemosa* trunk exhibited few traumatic channels located along its growth rings while the roots and the trunk of *A. germinans* displayed sclerous cells located along the broad parenchyma band limits. The mineral pollution would provoke physiological perturbation on Cl, K and Ca production from the xylem of the polluted site where Cu, Ni, Ir, Cr and Sr were the majors MTE accumulated in *A. germinans*. The heartwood was more degraded by *P. placenta* while the sapwood gained in durability. Further investigations are necessary to better understand the reasons which govern the change of durability of *A. germinans* xylem from polluted site and on the bioremediating capability of *R. racemosa* and *A. germinans* towards heavy metals accumulation.

Keywords: Mangrove; parenchyma bands; sclerous cells; bioremediation; heavy metals.

1. INTRODUCTION

The wastewater treatment is one of the major environmental issues. Wastewater can be produced by more than 80% of the total consumed water in urbanized areas [1,2]. Its amount increases with increasing population and industrial activities [3] near rivers or waterways; which provokes significant environment pollution [4], insalubrity and medical risks. The measurements of urban sewage are depended on water quality modeling of chemical, physical, and biological properties [5]. The wastewaters from these uncontrolled activities are discharged in the sea, releasing like this toxic organic products and serious mineral pollutants including heavy metals.

National strategies for efficient depollution of seas or waterways are a challenge for underdeveloped countries where mangrove is growing interest because it should give response to sea level or climate changes [6]. On the other hand, mangrove is a natural stock of active molecules; stem bark from mangrove plants like *Xylocarpus granatus* which contain tannins displaying antiradical and antioxidant activity [7] and the roots of marine mangrove such as *Ceriops tagal* within chemotherapeutic drugs have been identified [8] were found in that ecosystem indeed. In addition, mangrove ecosystem was described as potential for carbon stock [9,10]. However, financial stakes and pollutions risks connected to human and goods transport in the mangrove ecosystem [11,12] as well as the decrease of socio-economic profits for rural communities as consequence of mangrove degradation by drought and hydraulic dam has been pointed out [13]. The mangrove sediments have high metal binding capacity because sediments have anaerobic nature with richness of sulphide content, which can easily catch the metals and increase the concentration of metals in the mangrove sediments, therefore this availability of metal concentration leads to bioaccumulation in the plant tissues [14,15]. Nevertheless, the ability of mangrove for metals accumulation was previously discussed [14,16,17], and about 400 species including mangrove trees were identified as potential factories for toxic heavy metals storage from wastewaters [18]. *R. racemosa* and *A. germinans* belonging to the family of Rhizophoraceae and Avicenniaceae respectively, have roots system with high capability for filtering wastewater nutrients and decrease hazardous metals in the costal seas or mangrove soils [19]. Previous studies have found that *Avicennia* wood concentrated more metals than *Rhizophora* one [20]. Furthermore, *Avicennia marina* roots concentrated more heavy metals compared to its air parts [21]. On the other hand, the high capacity of trunk woody tissues to allocate metals was described to be an alternative for the recovery of excess metallic elements from degraded soils [22].

The trend of Rhizophoraceae and Avicenniaceae to concentrate heavy metals was also described [23,24]. But, the anatomical variability between the trunk wood and the roots of *R. racemosa* and *A. germinans* regarding parenchyma as storages for substances [25] or other characteristics like sclerous cells, vessels number or diameter has received little attention.

Recent trends on mangrove deterioration by human deforestation, mineral and organic based-compounds pollution have been observed in some West African countries like Gabon. The side

effects of these increasing incivilities are land inundations and perturbation of various aquatic species breeding areas. Although the empiric and distressing spectacle of deteriorated wood or other mangrove species, a direct correlation between the mineral pollution of that fragile ecosystem and the anatomical structure, chemical composition or natural durability of the wood xylem from mangrove species have not been reported.

The aim of this study was to investigate the anatomical variability between the trunk and the roots of *R. racemosa* and *A. germinans* concerning the vessels diameter and number as well as the sclerous cells width and number in the cross section of the wood, in order to understand the differences observed in the storage of heavy metals within those mangrove wood tissues. The changes occurring in the wood tissues of mangrove trees exposed to mineral pollution are discussed based on *R. racemosa* and *A. germinans*.

2. MATERIALS AND METHODS

2.1 Chemicals

Blue of methylene, ethanol (90%) and concentrated xylene (98.5%) were purchased from Aldrich and used without any purification. Javel La Croix (8° chl eq.2.4% c.a.) and distilled water were obtained from MEDILAB.

2.2 Area of Study

The samples from clean sites were collected in the mangrove of Ayéme Maritime, located approximately at 40 km from Libreville in the province of Estuaire. This zone is characterized by a low tide in the morning; high tide in afternoon and the mangrove is consequently invaded by water. Additional clean sites were Mamboumba and Oveng while the contaminated wood samples were collected at the discharge of Alénakiri, these are located at Libreville.

2.3 Wood Sampling

2.3.1 Collection of the wood samples

Four trees of each mangrove wood were randomly harvest on the morning in Ayémé Maritime in the month of March 2015 at high tide. The trees were randomly chosen following their vigorous aspect, good conformity of stem and superior or equal to the minimum 16-18 cm of diameter. *R. racemosa* was in the mud, at the edge of the river; that mangrove tree was sampled between 940' 31.22 " for longitude and 017' 17.41 " for Northern latitude. *Avicennia germinans* was on the same area but in the opposed side, in a totally dry medium located between 940' 26.57 " for longitude and 017' 07.15 " for Northern latitude. The samples collected at Mamboumba were such as the Northern latitude was 00°70.499' with a longitude of 05 °48.450'. Those from Oveng were of Northern longitude 00°28.8516' and 009°30.9994' for latitude; that site is located in a protected area. Alenakiri is in an opened landfill and located at 00°18.7014' for the Northern longitude and 009°31.3013' of latitude.

For each tree tank, the geographic data were taken with a Garmin map 60 csx GPS mark. Then, small wood discs of 10 cm of thickness were collected at 1.30 m of height from each tree with a chainsaw STILL 066 trade mark.

Samples were placed on shelves and air dried to avoid any deterioration by the light or biological agents. Then, wood discs were polished and three types of sticks were sawn in the radial direction and in North exposition: the first according to the East-West direction, the second following the Nord-South direction and the third in the oblique direction at more or less +45°C of the first setting stick.

2.3.2 Samples cutting for analysis

The polished wood discs were cut into 128 test-tubes of 10 cm x 10 cm x10 cm in the radial, tangential and longitudinal (R x T x L) direction according to Normand procedure [26].

2.4 Anatomical Structure Analysis by Optical Microscopy

The anatomical structure of *R. racemosa* and *A. germinans* was performed by an adaptation of a published procedure [27] as follows: The test-tubes were softened in hot distilled water for 24 and 18 hours, respectively. The heating was stopped when the sticks fell down to the vessel bottom. Then, the softened wood sticks were cut with a semi-automatic microtome "TBS 2500" in the transversal direction to obtain samples for which thickness was between 20-30 μm . The slant between the microtome knife and the section surface was about $+8^\circ$.

The thin wood test-tubes were soaked in water and scalded in a Javel: Water (10:90) mixture until fading the samples. The faded wood stickers were soaked once in distilled water to eliminate any traces of Javel. The rinsed wood stickers were then coloured in blue of methylene and successively dehydrated by soaking in ethanol solution and concentrated xylene. The colorful cuts were then deposited on a blade carrying an object, and a cover-object was carefully set down above the cuts to avoid bubbles of air between the blade and the gill. The blades were dried to eliminate any traces of chemicals used for dehydration.

The anatomical analysis was performed with an optic microscope "Motic 2.0" to a magnification of forty x. The observation was facilitated by a Ken-A-Vision camera connected to a computer. The software Vision 4 allowed to take pictures and to measure the constituent of the woody plan. The following anatomical characters were measured: the number of vessels or sclerous cells by mm^2 and the lumen vessels diameter in transverse section.

2.5 Extractives Content of the Mangrove Trees

5 g of milled wood sawdust ($\varnothing < 0.5 \text{ mm}$) was passed thorough serial extraction using different solvents with different polarities including dichloromethane, hexane, acetone, toluene/ethanol (1:1, v:v) and water for 3x6 min at 80°C with a Dionex 350 Thermo Scientific accelerated solvent extractor (ASE). Each extraction was performed in triplicate and the overall procedure was repeated twice. Extracts were evaporated and yields were calculated by weighting and reported to wood dry mass.

2.6 Quantitative Measurement of Mineral Compounds

The semi-quantitative determination of mineral elements was carried out on wood samples collected on the experimental sites of interest (Oveng and Alenakiri). 10 g of the wood randomly harvested on wood washers coming from three different trees were ground in powder ($\varnothing < 0.5 \text{ mm}$). Pellets of 1cm diameter have been made and subjected to scanning electronic microscopy (SEM) coupled to EDS and X-ray microanalysis. Nine spectra were collected on each pellet. Three pellets were analyzed for each type of sample.

2.7 Gas Chromatography Mass Spectroscopy (GC-MS) Analysis

GC-MS analysis was carried out with dichloromethane extracts obtained from ASE (80°C with 3 runs of 6 min). The final volume extracts was 100 ml. Then, 0.9 ml of extracts + 0.1 ml of 0.806 mg/ml anthraquinone (AQ) solution were injected. The Rtx 200 (60 m x 0.25 mm, 0.25 μm) column was used for separation in positive scanning mode. Peak identification was performed by comparing mass fragmentation with NIST 2002 spectra database. Semi-quantitative data were calculated from GC chromatograms using the equation (1):

$$M_x = \frac{A_x \times C_{EI}}{A_{EI} \times 0.9 \times 5} \times 100 \quad (1)$$

With M_x , mass of a given compound (x) content (mg anthraquinone equivalent per g of dry wood). A_x , was the peak area of a given compound (x). C_{EI} , was the anthraquinone concentration in the analyzed extracts (0.806 mg/ml). A_{EI} , was the peak area of anthraquinone.

2.8 Decay Resistance Measurement

The natural durability of the mangrove trees was assessed by an adaptation of the NF EN 113 of December 1986 for classification and previously published procedure [28].

2.9 Data Analysis

All the data were analysis using the one-way analysis test of variance (ANOVA) followed by the Fischer's LSD (last significant difference) test at $\alpha=0.05$ level of significance with Rr643.0.2 software.

3. RESULTS

3.1 Variability within *R. racemosa* in Transverse Section

The anatomical structure of *R. racemosa* trunk is depicted in Fig. 1 and 2a, the roots can be observed in Fig. 2b. Some parts of the trunk exhibited larges and hallow pellets looking like traumatic channels located along the broad and dark bands having the appearance of growth ring limits. However, these traumatic channels were not noticeable in the root tissues of *R. racemosa* (Fig. 2b).

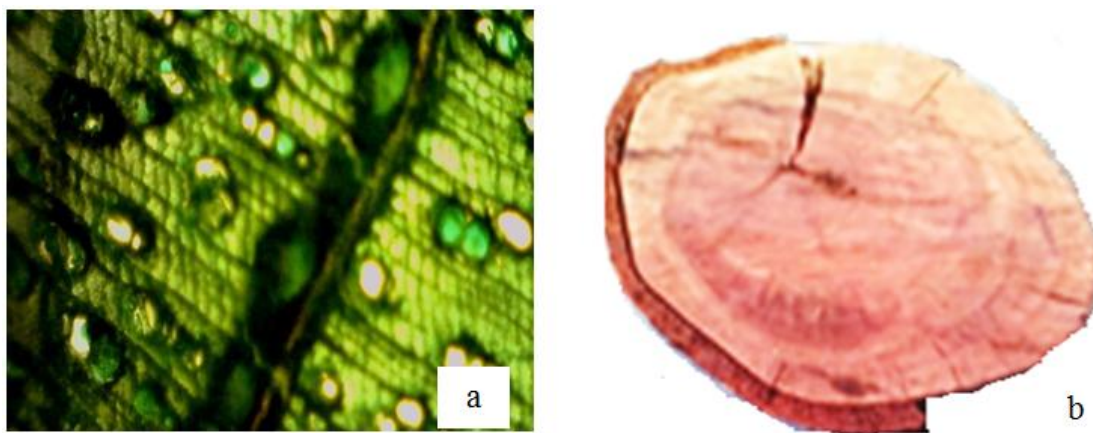


Fig. 1. Trunk of the red mangrove tree *R. racemosa* in transverse section with traumatic channels along the growth rings, there was no evidence of parenchyma bands (GX40) (a); Fresh trunk from Ayémé clean site (b)

The mean vessels number/mm² of the trunk and the roots didn't exhibit significant difference ($p>0.05$), while significantly difference ($p=0.01$) was found between their mean vessels diameter (Table 1). No evidence of sclerous cells was found within the trunk and the root tissues from *R. racemosa* mangrove tree (Table 1).

3.2 Intra and Inter Species Variability in Transverse Section

Fig. 3 shows clearly that *A. germinans* trunk and roots contained sclerous cells along their large parenchyma band limits. Furthermore, that mangrove tree has pointed out a within species variability concerning the anatomical parameters as corroborated by the strong significant difference ($p<0.0001$) obtained from Table 1. The trunk was not only richer in vessels number/mm² than the roots, it exhibited the largest vessels diameter also. Nevertheless, the trunk of *A. germinans* was less abundant in sclerous cells number/mm² compared to the roots, even if that aerial part of *A. germinans* wood displayed the highest sclerous cells diameter with regard to its roots.

Table 1. Vessels and sclerous cells number/mm², vessels and sclerous cells diameter mean in the transverse section of the trunk and the roots of *R. racemosa* and *A. germinans*

Biological tissues	Vessels number/mm ²		Vessels diameter (µm)		Sclerous cells number/ mm ²		Sclerous cells diameter (µm)	
	<i>R. racemosa</i>	<i>A. germinans</i>	<i>R. racemosa</i>	<i>A. germinans</i>	<i>R. racemosa</i>	<i>A. germinans</i>	<i>R. racemosa</i>	<i>A. germinans</i>
Trunk	10.89±5.56 ^a	17.22±6.54 ^b	62.12±7.78 ^d	63.72±8.28 ^d	0	1.19±0.38 ^g	-	225.05±51.46 ⁱ
Roots	12.09±4.8 ^a	5.24± 3.05 ^c	57.21±7.73 ^e	47.67±11.09 ^f	0	2.11±0.63 ^h	-	153.89±37.98 ^j

Means with the same letters are not statistically different at α=0.05 level of significant

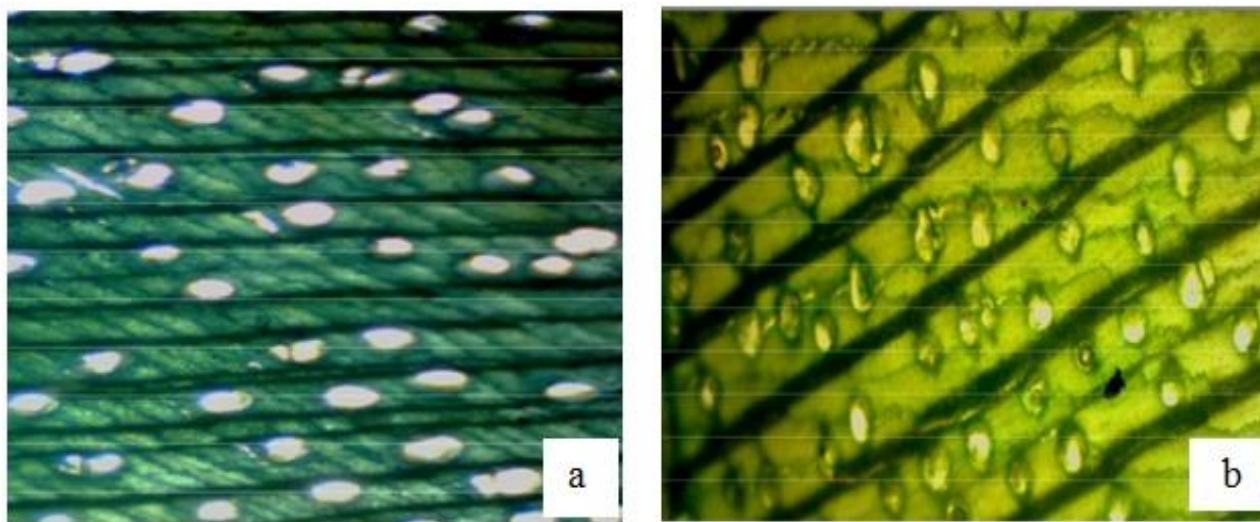


Fig. 2. Trunk (a) and roots (b) of *R. racemosa* without traumatic channels, sclerous cells in transverse section or broad parenchyma bands. Evidence of scalariform vessels (G 40x)

The data collected in Table 1 pointed out that the trunk of *A. germinans* was the most abundant in vessels number/mm² with a high level of significant ($p < 0.0001$) regarding *R. racemosa* one. Nevertheless, *R. racemosa* roots were the richest in vessels number/mm² ($p < 0.0001$) than *A. germinans*. However, no significant difference ($p = 0.43$) was found between the mean vessels diameter of the trunks from the two mangrove trees, while the vessels diameter of *R. racemosa* roots were higher ($p < 0.0001$) with regard to those from *A. germinans*. Furthermore, the trunk and the roots of *R. racemosa* did not exhibit any sclerous cells compared to *A. germinans* trunk and roots within they were in a higher extend (Table 1).

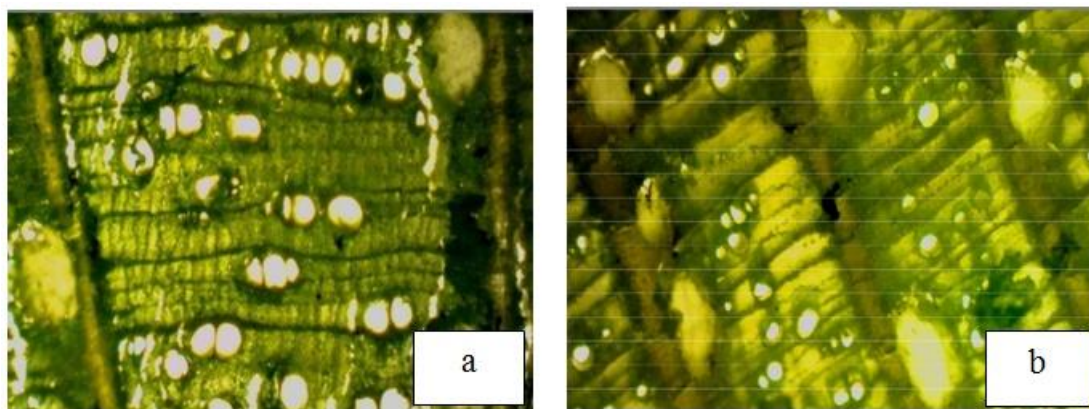


Fig. 3. Trunk (a) and roots (b) of *A. germinans* in transverse section with evidence of sclerous cells. Parenchyma broad bands and simple perforations in the trunk and high content of parenchyma broad bands and vessels with small diameter in the roots. (GX40)

3.3 Variability Regarding the Chemical Composition

3.3.1 Mineral composition and total extracts content

Quantitative analysis of mineral content of the wood by XRMF (X ray microanalysis) is depicted in Fig. 4. It could be observed that the sapwood which is the conductive part of the wood was accordingly more abundant in mineral elements. Furthermore, Cr, Ni, Cu and Ir accounted for heavy metals accumulated in *A. germinans* sapwood from Alénakiri when compared to unpolluted wood (Oveng). Interestingly, physiological markers (S, Cl, K, Mn and Ca) were found to follow the same trend. This suggested a boost of the leaf evapotranspiration and overall sap transfer in *A. germinans* in response to MTE stress. Heavy metals were not accumulated in the heartwood of trees growing in polluted site (Alenakiri) with the exception of Ca which increased strongly (Fig. 4a).

Since Ca is involved in chelation mechanism, it was attempted that *Avicennia* used calcium chelation and sap dilution to drive MTE contaminant to leaf were they will be excreted. Therefore, using this tolerance mechanism would poorly affect the wood differentiation.

Table 2. Extractives content of *A. germinans* heartwood from Oveng and Alénakiri submitted to various solvent expressed as percentage of dried material

Experimental sites	Hexane (%)	Toluene/Ethanol (%)	Acetone (%)	H ₂ O (%)
Alénakiri	12±1.41 ^a	3.5±1.41 ^b	8.5±1.41 ^c	2±0.71 ^d
Oveng	9.75±1.60 ^a	3±0.00 ^b	10.95±1.48 ^c	2.68±1.45 ^d

n=3 experiences. In a column, means with the same letters are not statistically different at $\alpha=0.05$ level of significant

The interesting marker that might be used for wood quality and wood development is the extractives content. *A. germinans* is described to be rich in extractives. Thus, the effect of MTE pollution on the wood extracts content was investigated by three solvents of gradient polarity (hexane, acetone-

ethanol, acetone and water). It was obvious that no significant difference was found ($p>0.05$) between the extracts content of Alénakiri and Oveng heartwoods extracted by the solvents used (Table 2); thus supporting that the extracts synthesis by parenchyma cells was poorly affected by MTE pollution.

3.3.2 Pollution indicators

GC-MS analysis of dichloromethane extracts of *A. germinans* heartwood from the Oveng clean site and Alénakiri polluted site (Table 3) showed that lapachol and its derivatives decreased in Alénakiri's wood tissues exposed to mineral contaminants. The content of lapachol which is one of the most abundant extracts in *A. germinans* heartwood [29] decreased from 11 to 4 mg/gDM (64%) in the wood blocks from polluted.

Table 3. GC-MS relative abundances of lapachol and corresponding derivatives identified in the wood tissues of *A. germinans* heartwood from unpolluted site (Oveng) and mineral contaminated site (Alénakiri) expressed in mg Equivalent Anthraquinone (EAQ)/g of dried material (DM)

Compounds	Rt (min)	Relative abundance (mgEAQ/g DM)	
		Alénakiri	Oveng
Lapachol	28.3	4.2	11
3-chlorodeoxylapachol	30.2	2.1	2.7
Dehydro- α -lapachone	31.5	2.2	4.4
α -lapachone	33.0	0.0	0.3

Rt: Retention time

3.4 Natural Durability Control of Mangrove Trees Exposed to Fungal Activities

Lapachol and its derivatives are naphthoquinones belonging to the phytoalexins family that are characterized by antimicrobial activity [30]. To test whether MTE could affect the natural durability of *A. germinans*, sapwood and heartwood from MTE polluted site were compared to those collected at clean sites. Table 4 showed that the resistance to fungal attack depended not only on the wood sample, but also on the type of rot fungus.

Studies related to mangrove *Avicennia* from Oveng or other clean sites of Libreville (personal data) didn't display significant differences ($p>0.05$) on their natural durability against the brow rot *P. placenta* and the white rot *C. versicolor*.

For a given rot fungus, the sapwood was indeed more susceptible to fungal attack than the heartwood. Hence, the weight loss of Oveng heartwood attacked by *P. placenta* was least ($3.5\pm 1.6\%$) than that the sapwood ($15.5\pm 9.7\%$). But both could be classified very durable according to EN 113. The better natural durability of *A. germinans* heartwood ($8.7\pm 4.3\%$) was once again observed for *C. versicolor* for the sapwood mass loss was $43.7\pm 12.2\%$. It could be claimed that *A. germinans* heartwood was very durable to *C. versicolor* while the sapwood was moderately durable against the studied white rot fungus.

Table 4. Mass loss of *A. germinans* sapwood and heartwood from Alénakiri MTE polluted site and one clean sites of Libreville submitted to *C. versicolor* and *P. placenta* fungal activities

Experimental sites	Mass loss (%)	
	<i>P. placenta</i> (%)	<i>C. versicolor</i> (%)
Alénakiri-SW	5.6 ± 1.9^a	52.4 ± 19.5^e
Alénakiri-HW	2.2 ± 1.0^b	13.9 ± 9.1^f
Oveng-SW	15.8 ± 9.7^c	43.7 ± 12.2^e
Oveng -HW	3.5 ± 1.6^d	8.7 ± 4.3^f

$n=12$ replicates. In a column, and for the same part of the wood, means with the same letters are not statistically different at $\alpha=0.05$ level of significant. With Alénakiri-SW: Alénakiri sapwood; Alénakiri-HW: Alénakiri heartwood; Oveng-SW: Oveng sapwood; Oveng -HW: Oveng heartwood

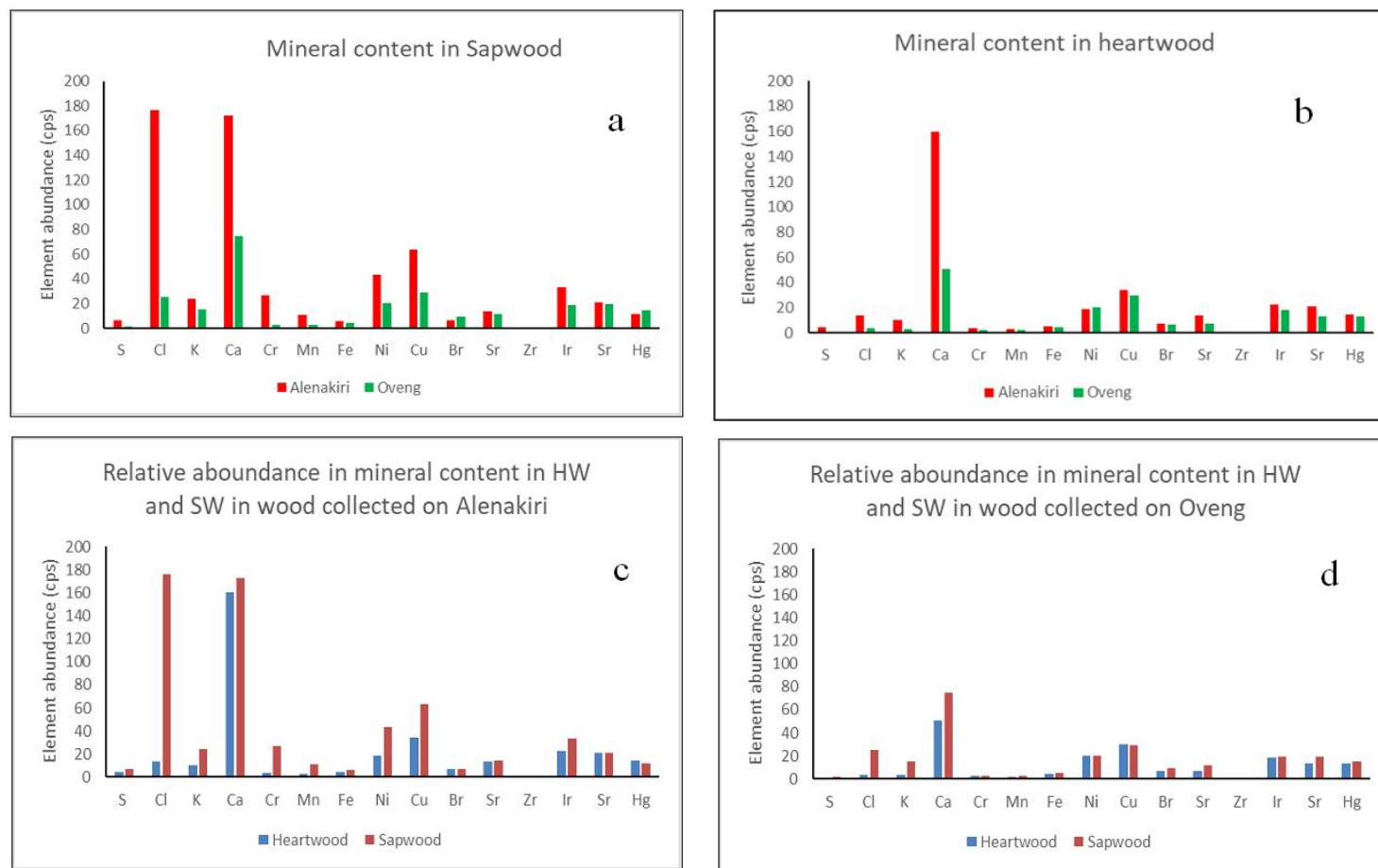


Fig. 4. Mineral content of *A. germinans* from polluted site (Alénakiri) and unpolluted site (Oveng) determined by X-ray microanalysis. MTE content in the sapwood (a) and the heartwood (b) from different sites of harvest. MTE of the wood at Alénakiri polluted site (c) and Oveng unpolluted (d) site

However, no significant difference ($p > 0.05$) was found between the natural durability of the mangrove *Avicennia* trees from Oveng and Alénakiri MTE polluted site attacked by *C. versicolor* (Table 4). Nevertheless, major changes were observed for *A. germinans* collected from MTE polluted site where the sapwood became very durable with a mass loss of $5.6 \pm 1.9\%$ while the heartwood remained weakly attacked by the brow rot fungus *P. placenta*.

4. DISCUSSION

The roots of *R. racemosa* didn't point out traumatic channels neither growth ring limits. But both of those anatomical structures were found within the trunk tissues of that mangrove tree. Their occurrence was in agreement with that previously found by Beeckman et al. [31] who showed that within mangrove trees such as *Rhizophora mucronata*, clear wood bands were formed during the dry season while a dark wood shape was noticeable in the rainy season. So, assuming that species belonging to the same family possess common properties [26], the alternated bands observed within *R. racemosa* trunk should be assigned to growth rings (Fig. 1). Nevertheless, the closed channels located along the growth rings remained controversial and were discussed for a long time. According to Boureau [32], species attacked by pathologies should produce traumatic channels in order to face the medium pressures; and those traumatic channels should be distinct from the normal channels by their position at the end of growth rings in cross and tangential section. Therefore, these channels of big size and missing constancy in all the trunk of *R. racemosa* should result from pathological origin. Thought that the specific environmental conditions inside with the mangrove tree grow include decay processes which should affect the organic matter [20,33] of that specific ecosystem. Regarding the vessels numbers/mm², any within specie variability was found for *R. racemosa* (Table 1). The statistical analysis didn't exhibit significant difference ($p > 0.05$) between the trunk and the roots of *R. racemosa* indeed; whereas a significant difference was obtained for their vessels diameter ($p = 0.01$). The trunk of *R. racemosa* displayed the highest vessels diameter than the roots ones (Table 1) and that should explain the better water conduction of the scalariform perforating slabs of *Rhizophora sp.* planting woods, as observed by Balde [34].

However, a strong significant difference ($p < 0.0001$) was found between the vessels number/mm² and the same trend was observed concerning the vessels diameter means of the trunk and the roots of *A. germinans* which exhibited a very significant difference ($p < 0.0001$) too. It was noteworthy that the trunk displayed not only the highest vessels number content, but also the largest vessels diameter than the roots (Table 1). That intra-species variability within the wood of *A. germinans* was in agreement with that published for a species like *Picea mariana* (Mill.) where these anatomical characters varied from the bottom towards the high parts of the wood [35]. Furthermore, the data of Table 1 corroborated the intra-specie variability between the trunk and the roots of *A. germinans*. The sclerous cells number/mm² displayed a significant difference ($p < 0.0001$) between the two parts of *A. germinans* wood; and the root tissues were richer in sclerous cells number than the trunk ones. On the other hand, the sclerous cells diameter of the trunk and the roots displayed a strong significant difference ($p < 0.0001$), and the sclerous cells diameter were the highest inside the trunk tissues. The occurrence of those sclerous cells located at the limits of the broad parenchyma bands were previously described for *Avicennia marina* [26], which suggests that sclerous cells and parenchyma bands are typical of Avicenniaceae. Those sclerous cells contain sclerenchyma composed of dead cells, and the sclerous cell walls are thickened with lignin conferring hardness and rigidity to *A. germinans* which can easily face to environmental constraints like tide movements [36].

The data depicted in Table 1 pointed out an inter-species variability for the vessels number/mm² as well as the sclerous cells number/mm² and diameter which varied very significantly ($p < 0.0001$) between the trunks and the roots of *R. racemosa* and *A. germinans* (Table 1). A strong inter-species variability was found also between the vessels diameter ($p < 0.0001$) of the roots of the two mangrove woods. However, no significant difference was found ($p > 0.05$) between the vessels diameter of the trunk tissues from *R. racemosa* and *A. germinans*.

Although the accumulation and the distribution of heavy metals in plants depends on factors such as plant species, element species, chemical and bioavailability, redox, pH, cation exchange capacity, dissolved oxygen, temperature and secretion of roots [37]; the general tendency of the roots for

concentrating more heavy metals than the other parts of Rhizophoraceae and Avicenniaceae mangrove trees was fully discussed [38,39,40,41]. The strong ability of *Rhizophora apiculata* roots to concentrate more Cu and Pb than the leaves and the bark was found by Kamaruzzaman et al. [23]. Despite the significant ($p < 0.05$) low vessels diameter of the roots ($57.21 \pm 7.73 \mu\text{m}$) than the trunk ($62.12 \pm 7.78 \mu\text{m}$) tissues we found in our study, the trend of *R. racemosa* roots for having a high level of bio-accumulation of heavy metals such as Fe ($402.43 \pm 0.31 \text{ mg/kg}$), Ni ($40.08 \pm 0.09 \text{ mg/kg}$), Cd ($24.39 \pm 0.22 \text{ mg/kg}$) than the stem wood was described by Erakhrumen [40]. In addition, the results obtained by Zheng et al. [42] displayed the strongest bio-remediating capability of the roots of *Rhizophora stylosa* to retain more heavy metals such as Ni ($208.4 \mu\text{g m}^{-2} \text{ yr}^{-1}$), Cd ($56 \mu\text{g m}^{-2} \text{ yr}^{-1}$), Pb ($229.8 \mu\text{g m}^{-2} \text{ yr}^{-1}$) compared to the trunk wood which exhibited concentrations as follows: Ni ($96.9 \mu\text{g m}^{-2} \text{ yr}^{-1}$), Cd ($2.6 \mu\text{g m}^{-2} \text{ yr}^{-1}$), Pb ($51.6 \mu\text{g m}^{-2} \text{ yr}^{-1}$). Those results suggest that the vessels diameter should not be a major factor for metal concentration within *Rhizophora*.

On the other hand, the highest bio-concentration of heavy metals in Avicenniaceae through the roots or even via their stems and leaves for their accumulation in the plant tissues which take up elements selectively was investigated [16,17,23,43,44]. It was noticeable that despite the highest vessels number/mm² and vessels diameter of the trunk tissues we obtained for *A. germinans*; previous works have found that the roots of that mangrove tree concentrated more heavy metals than the trunk [14]. That was in close agreement with the result displayed above by *R. racemosa*. Thus, the vessels number and the vessels diameter didn't look like major factors for metal concentration within the trunk and the roots of *A. germinans* also.

Furthermore, the microscopic analysis of tissues from the studied mangrove trees showed a high content of the broad parenchyma bands within the roots than the trunk tissues of *A. germinans* (Fig. 3). Thought that parenchymas are storages for substances [25], their high content within the roots of Avicenniaceae should lead them to concentrate more organic wastes and heavy metals than the trunk. That should support in some extent, the high heavy metals concentration previous authors have found inside the roots of *A. germinans* [14,17,23].

The abundance of sclerous cells and broad parenchyma bands within the wood of *A. germinans* (Table 1) should explain the results obtained by Marchand [14] who found the following metals concentration for the wood of *Avicennia*: Zn ($12.5 \mu\text{g/dry wt}$), Cu ($13.2 \mu\text{g/dry wt}$) and Cr ($26.5 \mu\text{g/dry wt}$) while the heavy metals content inside *Rhizophora* which was lacking sclerous cells and broad parenchyma bands was as follows: Zn ($00.00 \mu\text{g/dry wt}$), Cu ($00.00 \mu\text{g/dry wt}$) and Cr ($11.40 \mu\text{g/dry wt}$).

The minerals concentration in mangrove trees of Libreville (Fig. 4) showed clearly that this area of Gabon has been yet contaminated by human activities so that Cu, Ni, Ir and Cr were the major metallic trace elements (MTE). The high content of these minerals in the trunk of *A. germinans* agreed with that reported by Marchand [20] who found that Cu and Cr were more concentrated in that mangrove tree xylem than *R. racemosa* one.

In addition, the strong increase of Ca on the polluted site xylem and the deregulation of Cl and K highlighted strong physiological perturbations in the wood of polluted sites (Fig. 4a and 4b). However, the dilution of Cl and K as well as the chelation of Ca mechanisms should have been performed by *Avicennia* to face the MTE pollution. The chelation of Ca by MTE supported the presence of crystals in *A. germinans* parenchyma as revealed by the SEM of wood blocks (Fig. 5).

Moreover, the strong concentration of inorganic elements for Alenakiri mangrove could justify a qualification of "MTE polluted" site. As underline above, the chemical perturbation of mangrove trees subject to MTE pollution appeared more evident for possible changes in some wood properties like the natural durability.

The lack of significant difference on extracts content whatever the solvent used ($p > 0.05$) showed that the highest concentration of heavy metals on *A. germinans* heartwood from the MTE polluted site did not trigger global change for extractive biosynthesis. The lack of changes for acetone extracts would support that the biosynthesis of polyphenols (tannins, coumarins, proanthocyanes...) usually found in

that solvent extractives was not affected by the high concentration of heavy metals (Cr, Cu, Ni) inside *A. germinans* heartwood from the MTE polluted site.

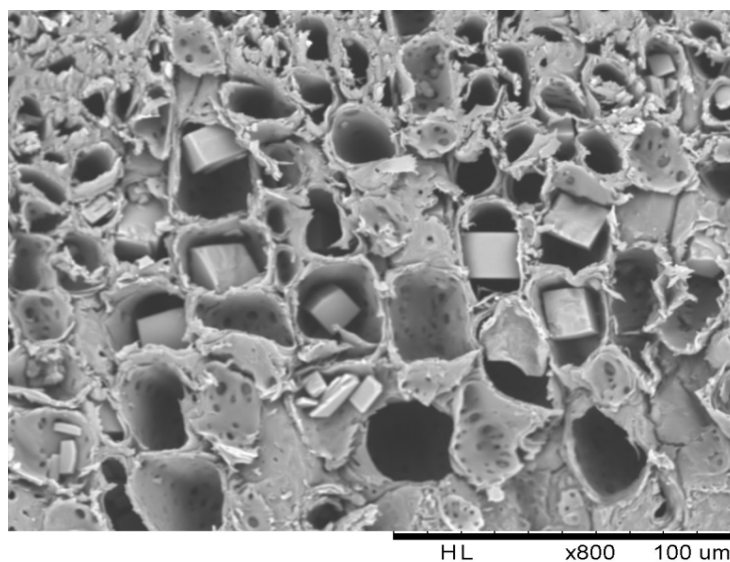


Fig. 5. Typical scanning electronic microscopy of *A. germinans* sapwood from mangrove MTE polluted sites of Libreville. Presence of Ca^{2+} crystals in the parenchyma

The results of this study emphasize for the lack of perturbation on the biosynthesis of apolar and polar compounds of *A. germinans* heartwood by the MTE identified at Alénakiri discharge (Fig. 6a). However, the darkening of the wood (Fig. 6d) suggested that some discoloration which need further investigations occurred.

The only changes on organic compounds content in the wood exposed to MTE pollution was observed for pollution indicator like lapachol (Table 3). The decrease of lapachol type compounds in *A. germinans* heartwood from Alénakiri site agreed with that found by Jones and coworkers [10] indeed.

Although the lack of changes on extractives content (Table 2), that result corroborated in some extent a pollution in that mangrove inside which the relative diminution of lapachol series suggested differences on their response to harmful substances. So, with the exception of lapachol which decreased for 64%, ketones like α -lapachone disappeared completely in the contaminated heartwood while dehydro- α -lapachone dropped to 45%. 3-chlorodeoxyolapachol decreased for 22%. Other all, that finding contrasted with that obtained from hydrocarbons + MTE polluted sites where lapachol and its derivatives disappeared completely in the heartwood (personal data).

Therefore, the extractives conservation plus residual lapachol like compounds contained in *A. germinans* heartwood could explain the lack of discoloration and differentiation between the heartwood and the sapwood of that mangrove tree and other wood species like *R. racemosa* from that MTE contaminated site (Fig. 6d).

Data of Table 4 showed that *A. germinans* heartwood from Oveng clean site was very durable to *P. placenta* and *C. versicolor*, that result agreed with the claimed high natural durability of the mangrove tree *A. germinans*. Moreover, the heartwood of that hardwood species should contain extractives resistant to the enzymatic hydrolysis of polysaccharides by *P. placenta* during the Fenton reaction.

These extractive molecules would also protect the heartwood from lignin alkyl chain oxidation, phenyl groups demethoxylation and $\text{C}_\alpha\text{-C}_\beta$ cleavages provoked by *C. versicolor*'s laccases [45,46].



Fig. 6. Burnt wastes of Alénakiri's public discharge (a). Died mangrove trees in flooded sol of Alénakiri's discharge (b). Delimitation of the sapwood and heartwood in *A. germinans* (c) and *R. racemosa* (d) trunks collected from a Alénakiri. The xylem of *R. racemosa* from the MTE polluted site was darker (d)

Exposing *A. germinans* heartwood in the MTE polluted site increased slightly the Cr, Sr and Ir content (Fig. 4) without any negative effect on the extractives content (Table 2) which protect the wood against fungal attack [47]. That should explain the strong natural durability of Alénakiri's heartwood and its lack of significant difference ($p > 0.05$) with the clean site (Table 4). In addition, the similar mass loss of the two sapwoods submitted to *C. versicolor* degradation (Table 4) supported that no changes occurred also in the sapwood from MTE polluted site where the Cu, Ni, Sr and Cr content increased strongly (Fig. 4). Therefore, increasing chromium or the concentration of metal listed above in the wood tissues of *A. germinans* mangrove tree should not limit the enzymatic degradation of lignin by *C. versicolor* in particular.

Nevertheless, the mass loss of wood blocks attacked by *P. placenta* revealed a negative effect of the pollution on the natural durability of *A. germinans* heartwood. Although the presence of Cu which is used in CCA complex where Cr should inhibit *P. placenta*'s activity [48], the contaminated inner wood increased however the virulence of *P. placenta* against the inner wood's polysaccharides (Table 4). On the other hand, the mass loss of the darkened sapwood (Fig. 6d) from the MTE polluted site turned into weak ($5.6 \pm 2.1\%$), thus changing the sapwood from durable (clean site, Fig. 1b) to very durable according to EN 113. It was thought that the high concentration of Cr in the sapwood from contaminated site (Fig. 4) could be highly toxic to fungi [48] like the brow rot fungus *P. placenta* so that the strong degradation of polysaccharides have reduced dramatically the wood mass (Table 4).

5. CONCLUSION

This study has pointed out anatomical differences between the trunk and the roots of *R. racemosa* and *A. germinans* from the mangrove trees of Gabon. It was demonstrated that the trunk vessels number/mm² was the highest for *A. germinans*. However, the roots of *R. racemosa* were the richest in vessels number. But no significant difference was found between the trunk vessels diameter of the two mangrove woods, whereas the root vessels diameter was larger for *R. racemosa* than *A. germinans*. On the other hand, *R. racemosa* trunk exhibited few traumatic channels located along its growth rings; but they did not appear in all the trunk and they were lacking in its roots. Those traumatic channels cannot assume to be characteristic of Rhizophoraceae tissues. It was observed that the roots and the trunk of *A. germinans* displayed sclerous cells located along the broad parenchyma band limits. These anatomical structures which seemed to be characteristics of Avicenniaceae were not found within the trunk and the roots tissues of *R. racemosa* while they were strongly abundant in the trunk wood of *A. germinans* for which the root tissues exhibited the highest content of those anatomical structures.

However, the lack of studies on the anatomical variability between the trunk and the root tissues of those mangrove trees and the very limited information regarding the correlation between the type of heavy metals and the storage cells render difficult further comparison and discussion. Nevertheless, *A. germinans* from mangrove MTE polluted did not show changes regarding the chemical composition on fatty acid of low molecular weight and polar compounds soluble in water, whereas the acetone extracts increases slightly. That mineral pollution was thought to provoke physiological perturbation on Cl, K and Ca production from the xylem of the polluted site. Cu, Ni, Ir, Cr and Sr were the majors MTE accumulated in *A. germinans* sapwood and heartwood from polluted site. The heartwood contaminated by Cu, Sr and Ir was more degraded by *P. placenta* while the sapwood which was the richest in all metals with a strong accumulation of Cr and Ni gained in durability.

Although the reasons which govern the lost on lapachol compounds or the change of durability of *A. germinans* xylem from polluted site against *P. placenta* need susceptibility, the general trend for heavy metal concentration within the roots tissues of the studied mangrove species as well as the better capability of *A. germinans* tissues which were found to be richer in sclerous cells and broad parenchyma bands than *R. racemosa* will be further investigated in order to discriminate between the environmental conditions and the anatomical structure control on the bioremediating capability of *Rhizophora racemosa* and *Avicennia germinans* towards heavy metals accumulation.

ACKNOWLEDGEMENTS

This research was possible as a result of the RIFFEAC (Réseau des Institutions de Formation Forestière et Environnementale en Afrique Centrale) Master of Science degree in wood sciences scholarship program. We would like to thank ENEF Gabon (Ecole Nationale des Eaux et Forêts) for his funding and all supports he brought to this research. The study was also supported by a fellowship granted by the ANBG (Agence Nationale des Bourses du Gabon). Dr. Eric Masson of the Ecole Nationale Supérieure des Technologies et Industries du Bois (ENSTIB) of Epinal (France) is thanked for his helpful contribution for ASE and GC-MS analyses. Authors thank also the Sylvatech imaging technical platform of INRAe for mineral analysis. The high scientific and material contribution of the LERMAB is recognized for the fulfillment of this PhD thesis program.

COMPETING INTERESTS

Authors have declared that no competing interests exist.

REFERENCES

1. Metcalf E. Wastewater engineering, treatment and reuse. McGraw-Hill, New York; 2003.
2. Baharvand S, Daneshvar MRM. Impact assessment of treating wastewater on the physicochemical variables of environment: A case of Kermanshah wastewater treatment plant in Iran. *Environmental Systems Research*. 2019;8(1):18.
3. Herteman M. Evaluation des capacités bioremédiatrices d'une mangrove impactée par des eaux usées domestiques. Application au site-pilote de Malamani, Mayotte. Thèse de Doctorat, Université de Toulouse, Toulouse. 2010;13.
4. Kamal M, Ghaly AE, Mahmoud N, Côté R. Phytoaccumulation of heavy metals by aquatic plants. *Env. Int.* 2004;29(8):29-39.
DOI: [http://dx.doi.org/10.1016/S0160-4120\(03\)00091-6](http://dx.doi.org/10.1016/S0160-4120(03)00091-6)
5. Zhang R, Qian X, Yuan X, Ye R, Xia B, Wang Y. Simulation of water environmental capacity and pollution load reduction using QUAL2K for water environmental management. *Int. J. Environ. Res. Public Health*. 2012;9:4504–4521.
6. Blasco F, Saenger P, Janodet E. Mangroves as indicators of coastal change. *Catena*. 1996;27(3-4):167-178.
DOI: [http://dx.doi.org/10.1016/0341-8162\(96\)00013-6](http://dx.doi.org/10.1016/0341-8162(96)00013-6)
7. Chacha M. Flavanol derivatives with antioxidant activity from the stem bark of *Xylocarpus granatum*. *Int. J. Biol. Chem. Sci.* 2010;4(2):371-376.
DOI: <http://dx.doi.org/10.4314/ijbcs.v4i2.58127>
8. Chacha M. Terpenoids from the roots of *Ceriops tagal* induces apoptosis through activation of caspase-3 enzyme. *Int. J. Biol. Chem. Sci.* 2011;5(2):402-409.
DOI: <http://dx.doi.org/10.4314/ijbcs.v5i2.72057>
9. Donato DC, Kauffman JB, Murdiyarto D, Kurnianto D, Stidham M, Kanninen M. Mangroves among the carbon-rich forests in the tropics. *Nature Geo.* 2011;293-297.
DOI: 10.1038/NGEO1123
10. Jones T, Rastsimb H, Ravaorinoroahoarana G, Cripps G, Bey A. Ecological variability and carbon stock estimates of mangrove of mangrove ecosystems in Noverthen Madagascar. *Forests*. 2014;5:177-205.
DOI: 10.3390/f5010177
11. Ajonina GN, Dibong SD, Ebonji Seth R, Gah-Muti Y, Elougou Ndinga N, Nkomba A. *Int. J. Biol. Chem. Sci.* 2015;9(4):1851-1862.
DOI: <http://dx.doi.org/10.4314/ijbcs.v9i4.11>
12. Ajonina G, Kemajou J, Bitchick AC, Nguekambe. Rapport technique sur l'évaluation chiffrée de la dégradation d'une partie de la mangrove du littoral: OPED. 2013;103.
13. Tendeng M, Ndour N, Sambou B, Diatta M, Aouta A. Dynamique de la mangrove du marigot de Bignona autour du barrage d'Affiniam (Casamance, Sénégal). *Int. J. Biol. Chem. Sci.* 2016;10(2):666-680.
DOI : <http://dx.doi.org/10.4314/ijbcs.v10i2.18>

14. MacFarlane GR, Pulkownik A, Burchett MD. Accumulation and distribution of heavy metals in the grey mangrove, *Avicennia marina* (Forsk.) Vierh.: Biological indication potential. *Environmental Pollution*. 2003;123(1):139–51.
DOI: [http://dx.doi.org/10.1016/S0269-7491\(02\)00342-1](http://dx.doi.org/10.1016/S0269-7491(02)00342-1)
15. Kannan N, Thirunavukkarasu N, Suresh A, Rajagopal K. Analysis of heavy metals accumulation in mangroves and associated mangroves species of Ennore mangrove ecosystem, East Coast India. *Indian J. Sci and Technol*. 2016;9(46):1-12.
16. Ramos e Silva SC, Da Silva AP, De Oliveira SR. Concentration, stock and transport rate of heavy metals in a tropical red mangrove, Natal, Brazil. *Marine Chem*. 2006;99:2-11.
DOI: <http://dx.doi.org/10.1016/j.marchem.2005.09.010>
17. Almasheer WA, Al-Taissan WA, Mohammed MK. Metals accumulation in grey mangrove *Avicennia marina* (Forsk.) vierh. inhabiting Tarut bay, Eastern Saudi Arabia. *J. Agri. Sci*. 2014;6(1):137-149.
DOI: <http://dx.doi.org/10.5539/jas.v6n1p137>
18. Jemal F, Ghorbal MH. Phytoremédiation. *Revue H.T.E.* 2002;122:49-60.
Available:<http://www.anafide.org/doc/HTE%2012%202/122-10.pdf>
19. Wong YS, Lan CY, Chen GZ, Li SH, Chen XR, Liu ZP. Effect of waste-water discharge on nutrient contamination of mangrove soils and plants. *Hydrobiologia*. 1995;29:243-254.
DOI: 10.1007/BF00029131
20. Marchand C. Origine et devenir de la matière organique des sédiments de mangrove de Guyane française. Thèse de Doctorat, Université d'Orléans, Orléans. 2003;521-523.
21. MacFarlane GR, Burchett MD. Toxicity growth and accumulation relationship of copper lead and zinc in the grey mangrove *Avicennia marina* (Forsk.) vierh. *Marine Environmental Research*. 2002;5:65-84.
DOI: [http://dx.doi.org/10.1016/S0141-1136\(02\)00095-8](http://dx.doi.org/10.1016/S0141-1136(02)00095-8)
22. Almeida AAF, Valle RR, Mielke MS, Gomes FP. Tolerance and prospection of phytoremediator woody species of Cd, Pb, Cu and Cr. *Braz. J. Plant Physiol*. 2007;19(2):83-98.
DOI: <http://dx.doi.org/10.1590/S1677-04202007000200001>
23. Kamaruzzaman MC, Ong KCA, Jalal S, Mohd Nor O. *Rhizophora apiculata* from Setui mangrove forest, Terengganu, Malaysia. *J. Env. Biol*. 2009;30(5 Suppl.):821-824.
24. Varz MK, Mohammadikia D, Gharibpour F, Dabbagh AR. Accumulation of heavy metals (Pb, Cd, V) in sediment, roots and leaves of Mangrove species in Sirik Creek along the Sea Coasts of Oman, Iran. *J. Appl. Sci. Environ. Manage*. 2012;16(4):323-326.
25. Ndoutoume C, Michel M. Matériau bois, manuel destiné à la formation académique de niveau universitaire. In: *Projet d'appui à la formation en gestion des ressources naturelles dans le Bassin du Congo*. PFOGRN. Université de Laval. 2012;6.
26. Normand D, Paquis J. Manuel d'identification des bois commerciaux. Tome II. Centre Technique forestier Tropical (CTFT). Nogent-sur-Marne. 1972;144-149.
27. Berrichi M. Détermination des aptitudes technologiques du bois de *Quercus rotundifolia* lamk et possibilités de valorisation. Thèse de Doctorat en Foresterie, Université Abou Bakr Belkaid Tlemcen, Algérie. 2011;40.
28. Safou Tchiama R, Soulonganga P, Engozogho Anris PS, Bikoro Bi Athomo A, Andzi Barhe´ T, De Jeso B, Charrier B, Akagah AG. Understanding the natural durability of some African tropical heartwoods toward *Pycnopus sanguineus* and *Antrodia* sp.: Lignin structure and cellulose morphology control. *J. Ind. Acad. Wood Sci*. 2018;15(2):162–171.
DOI: <https://doi.org/10.1007/s13196-018-0222-5>
29. Itoigawa M, Ito C, Tan HTW, Okuda M, Tokuda H, Nishino H, Furukawa H. Cancer chemopreventive activity of naphthoquinones and their analogs from *Avicennia* plants. *Cancer Lett*. 2001;174:135–139.
30. Ali RM, Houghton PJ, Raman A, Hoult JRS. Antimicrobial and antiinflammatory activities of extracts and constituents of *Oroxylum indicum* (L.) Ven. *Phytomedicine*. 1998;5(5):375-38.
31. Beeckman H, Boeren I, Couralet C, De Ridder M, Schmitz N, Tavernier W, Toirambe B, Verheyden A. Ouvrir la boîte noire du bois africain. In *Science Connection* 18, Mettens P (Ed). Rue de la Science 8 à B: Bruxelles. 2007;12.
32. Boureau E. Anatomie végétale: l'appareil végétatif des phanérogames. Tome 2. Presses Universitaires de France. Paris; 1956.

33. Marchand C, Lallier-Vergès E, Baltzer F, Albéric P, Cossa D, Baillif P. Heavy metals distribution in mangrove sediments along the mobile coastline of French Guiana. *Mar. Chem.* 2006;98(1):1-17.
DOI: <http://dx.doi.org/10.1016/j.marchem.2005.06.001>
34. Balde P. Etude de l'état de référence des plantations de *Rhizophora sp.* du projet pilote océanique dans le bassin du Saloum. Mémoire de fin d'études. Université de Thiès. 2010;29.
35. Braido dos Santos DG. Variation intra-arbre de la croissance radiale de la masse volumique et de la morphologie du trachéide du bois d'épinette noire [*Picea mariana* (Mill) B.S.P.] avant et après traitement de coupes partielles. Mémoire de la maîtrise en Biologie, Université de Québec en Abitibi Temiscamingue, Québec. 2014;22.
36. Détienne P. Cours d'Anatomie des bois. CTFI-CIRAD. Nogent-Sur-Marne, France; 1988.
37. Cheng S. Heavy metals in plants and phytoremediation. *Env. Sci. Pollut Res.* 2003;10(5):335-340.
DOI: <http://dx.doi.org/10.1065/espr2002.11.141.3>
38. Kamaruzzaman BY, Rina Sharlinda MZ, Akbar John B, Siti Waznah A. Accumulation and distribution of lead and copper in *Avicennia marina* and *Rhizophora apiculata* from Balok mangrove forest, Pahang, Malaysia. *Sains Malay.* 2011;40(6):555-560.
Available:<http://docplayer.net/14764567-Sains-malaysiana-40-6-2011-555-560-b-y-kamaruzzaman-m-z-rina-sharlinda-b-akbar-john-a-siti-waznah.html>
39. Mejías CL, Musa JC, Otero J. Exploratory evaluation of retranslocation and bioconcentration of heavy metals in three species of mangrove at las cucharillas marsh, Puerto Rico. *J. Top. Life Sci.* 2013;3(1):14-22.
Available:<http://jtolis.ub.ac.id/index.php/jtolis/article/viewFile/69/86>
40. Erakhrumen AA. Potentials of *Rhizophora racemosa* for bio-indication and dendroremediation of heavy metal contamination in a mangrove forest, Ondo State, Nigeria. *Nig. J. Agri. Food Env.* 2014;10(4):1-5.
Available:http://njafe.org/Njafe2014Vol_10No_4/1_%20Erakhrumen,_A_A.pdf
41. Rashidi O, Razanah R, Zainul MB, Khairusy SHYH, Maheran Y. Ecological indicator agents for inorganic contaminants state monitoring through *Sonneratia alba*, *Avicennia alba* and *Rhizophora apiculata*. *J. Teknol.* 2014;77(30):111-118.
DOI: <http://dx.doi.org/10.11113/jt.v77.6874>
42. Zheng WJ, Chen XY, Lin P. Accumulation and biological cycling of heavy metal elements in *Rhizophora stylosa* mangroves in Yingluo Bay, China. *Marine Ecol. Progr. Ser.* 1997;59:293-301.
Available:<http://www.int-res.com/abstracts/meps/v159/p293-301/>
43. Defew LH, Mair JM, Guzman HM. An assessment of metal contamination in mangrove sediments and leaves from Punta Mala Bay, Pacific Panama. *Marine Poll. Bull.* 2005;50:547-552.
DOI: 10.1016/j.marpolbul.2004.11.047
44. Akshayya S, Gunale VR, Panditn GG. Bioaccumulation of Zn and Pb in *Avicennia marina* (Forsk.) Vierh. and *Sonneratia apetala* Buch. Ham. From urban areas of Mumbai (Bombay), India. *J. Appl. Sci. Envir. Man.* 2007;11(3):109-112.
Available:www.bioline.org.br/ja
45. Necochea R, Valderrama B, Diaz-Sandoval SA, Folch-Mallol JL, Vazquez-Duhalt R, Iturriaga G. Phylogenetic and biochemical characterisation of a recombinant laccase from *Trametes versicolor*. *FEMS Microbiology Letters.* 2005;244:235-241.
46. Teoh YP, Mashitah MD, Salmiah U. Media selection for mycelia growth, antifungal activity against wood-degrading fungi and GC-MS study by *Pycnoporus sanguineus*. *BioResource.* 2011;6(3):2719-2731.
DOI: <https://doi.org/10.15376/biores.6.3.2719-2731>
47. Rowell RM. Handbook of wood chemistry and wood composites, Second Edition. CRC Press; 2012.
48. Jellison J, Connolly J, Goodell B, Doyle B, Illman B, Fekete F, Ostrofsky A. The role of cations wood by the in the biodegradation of brown rot fungi. *Int Biodet & Biodegrad.* 1997;39(2-3):165-179.

Biography of author(s)



Dr. S. B. Mabicka Iwangou

Laboratoire de Recherche et de Valorisation du Matériau Bois (LaReVa Bois), Ecole Normale Supérieure d'Enseignement Technique (ENSET), BP. 3989, Libreville, Gabon and Université de Lorraine, Inra, Laboratoire d'Etudes et de Recherche sur le Matériau Bois (LERMAB), Faculté des Sciences et Technologies Boulevard des Aiguillettes BP 70239. 54506 Vandœuvre lès Nancy Cedex-France.

He has a Ph.D. degree in Wood and Fibers Sciences of the University of Lorraine (France, 2020) and the National School of Water and Forests (ENEF-Gabon, 2020). He obtained a Master of Science Degree in Wood Sciences (ENEF, 2015). He is acting as associated research at the LaReVa Bois the LaReVa Bois (Laboratoire de Recherche et de Valorisation du Matériau Bois) of Gabon where he develops new knowledges on the chemical, anatomical and ecophysiological changes of mangrove trees exposed to mineral and organic pollution.



Dr. P. Soulounganga

Laboratoire de Recherche et de Valorisation du Matériau Bois (LaReVa Bois), Ecole Normale Supérieure d'Enseignement Technique (ENSET), BP. 3989, Libreville, Gabon and Laboratoire Pluridisciplinaire des Sciences, Ecole Normale Supérieure, BP 17009, Libreville, Gabon.

He is assistant Professor (CAMES). He is lecturer at the Ecole Normale Supérieure (ENS) of Libreville (Gabon) since 2004. He obtained a Ph.D. in Industrial Science and Technology at Henri Poincaré University of Nancy I (France, 2002), thereafter he had a postdoctoral position at Laval University (Quebec, Canada). From 2008 to 2019, he was the Head of Department of Life and Earth Sciences at ENS. He is member of the UNESCO Chair in International Hydrological Program (IHP). Since November 2019, he is Director of Training and Research at ENS. He is member of both the LaReVa Bois (Laboratoire de Recherche et de Valorisation du Matériau Bois) of Gabon and the Laboratoire Pluridisciplinaire des Sciences (LAPLUS) of ENS. His researches are focused on wood chemistry, durability, and lignocellulosic fiber-based composite materials stability.



Dr. A. Besserer

Université de Lorraine, Inra, Laboratoire d'Etudes et de Recherche sur le Matériau Bois (LERMAB), Faculté des Sciences et Technologies Boulevard des Aiguillettes BP 70239. 54506 Vandœuvre lès Nancy Cedex-France.

He is an assistant professor in biology and biochemistry at the National Timber Engineering School (ENSTIB, France) since 2012 where he teaches wood sciences especially wood anatomy, degradation and preservation. He teaches also in field

related wood based biorefinery, recycling and chemical valorization of wood wastes and co-products. He is in charge of teaching units and training program in Biorafinery. He is in charge of international affairs at ENSTIB. He is member of the LERMAB (Laboratoire d'Etudes et de Recherche sur le Matériau Bois, Nancy) where he works on wood degradation and deconstruction by microorganisms by fungi and bacteria. Another field of his research is developing innovative processes using various woody biomass (wastes and co products) as starting material to develop new products by biotransformation-based processes in a circular economy context.



Dr. R. Safou Tchiana

Laboratoire de Recherche et de Valorisation du Matériau Bois (LaReVa Bois), Ecole Normale Supérieure d'Enseignement Technique (ENSET), BP. 3989, Libreville, Gabon and Laboratoire de Chimie des Substances Naturelles et de Synthèses Organométalliques, Unité de Recherche en Chimie (URChi), Université des Sciences et Techniques de Masuku, BP. 941, Franceville, Gabon.

He is an assistant Professor (CAMES). He is lecturer at the Polytechnic School of the University of Sciences and Technics of Masuku (USTM) in Gabon since 2008. He obtained a Ph.D. in Wood Sciences at the University of Bordeaux 1 (2005) where he was also graduated in Bachelor and Master in Organic Chemistry. He was Director of Studies and Stages at the National School of Water and Forests (ENEF, Gabon) from 2013 to 2015 and Director of Studies of Engineers Cycle of the Polytechnic School of Masuku from 2010 to 2013 where he was the Head of the Department of General Sciences of Engineers from 2008 to 2010. He is lecturer in organic chemistry, material sciences, wood chemistry and spectroscopic methods for lignocellulosic materials. He is Deputy director of the LaReVa Bois (Laboratoire de Recherche et de Valorisation du Matériau Bois) of Gabon, and member of the LASNOM (Laboratoire des Substances Naturelles et de Synthèses Organométalliques) of USTM. His research topics are fundamental chemistry of wood extracts, lignin, cellulose and hemicelluloses. He is acting in new fields of research dealing with the valorization of African tropical hardwood wastes in biorifinery, green adhesives and wood-based composites.



C. Ndoutoume

Laboratoire de Recherche et de Valorisation du Matériau Bois (LaReVa Bois), Ecole Normale Supérieure d'Enseignement Technique (ENSET), BP. 3989, Libreville, Gabon.

She obtained a Master of Science Degree in Wood Sciences, option Biochemistry at the Ecole Nationale de Génie Rural et des Eaux et Forêts (ENGREF, France) in 1998 and an Engineer Degree in Water and Forests at the National School of Water and Forests (ENEF, Gabon) in 1981. She was Director of Studies of ENEF from 2003 to 2006. She worked as researcher in sylviculture and genetic amelioration of forest trees at the Institut de Recherche Agronomiques et Forestières (IRAF, Gabon). She was scientific advisor of various generations of Gabonese students and teacher of wood anatomy and sylviculture at ENEF. She ended her administrative carrier as Deputy General Secretary (2001-2010) and General Inspector of Services (2011-2014) of the Ministry of Water and Forests of Gabon.



Professor T. Andzi Barhé

Laboratoire de Recherche et de Valorisation du Matériau Bois (LaReVa Bois), Ecole Normale Supérieure d'Enseignement Technique (ENSET), BP. 3989, Libreville, Gabon and Laboratoire de Recherche en Chimie Appliquée (LARCA), Ecole Normale Supérieure (ENS), Université Marien Nguabi, Brazzaville, Congo.

He is a Lecturer-CAMES and Director of Academic Affairs at the University Marien NGOUABI (Brazzaville-CONGO). He obtained a Ph.D. in Engineering Sciences at the University of Poitiers (France), he teaches chemistry. He is member of the director of the Laboratoire de Recherche en Chimie Appliquée (LACRA), Ecole Normale Supérieure (ENS), Université Marien Nguabi, Brazzaville, Congo and associated researcher at the LaReVa Bois (Laboratoire de Recherche et de Valorisation du Matériau Bois) in Gabon. His research topics are the chemistry of natural substances, water treatment, waste management and the impact of chemical pollution in wood growth.



P. Gerardin

Université de Lorraine, Inra, Laboratoire d'Etudes et de Recherche sur le Matériau Bois (LERMAB), Faculté des Sciences et Technologies Boulevard des Aiguillettes BP 70239. 54506 Vandœuvre lès Nancy Cedex-France.

He is Professor in Organic Chemistry at the Faculty of Sciences and Technologies, where he teaches organic chemistry, but also wood sciences especially in the fields of wood chemistry and wood protection. He is in charge of the specialty "Bois Forêt Développement Durable" (Wood, Forest, Sustainable Development) of Master AETPF. His research activities are centered on wood chemistry and wood protection in order to improve and promote wood and wood derived products utilizations. In this context, he's particularly interested in the development of friendly environmentally preservation methods based either on new generation of chemicals or formulations with low toxicity or on thermal and chemical modifications of wood. He also interested in the reasons of natural durability of wood developing researches activities in the field of chemistry of extractives and fungal mechanisms involved in wood degradation. Another aspect of his research concerns circular economy and valorization of extractives aimed to improve wood industries competitively. He is head of LERMAB laboratory since 2011. He has published more than 150 publications in International Peer Reviewed Journals and supervised numerous PhD students.

© Copyright (2020): Author(s). The licensee is the publisher (Book Publisher International).

DISCLAIMER

This chapter is an extended version of the article published by the same author(s) in the following journal.
Int. J. Biol. Chem. Sci., 10(6): 2526-2538, 2016.

London Tarakeswar

Registered offices

India: Guest House Road, Street no - 1/6, Hooghly, West Bengal, PIN-712410, India, Corp. Firm
Registration Number: L77527, Tele: +91 8617752708, Email: director@bookpi.org,

(Headquarters)

UK: Third Floor, 207 Regent Street, London, W1B 3HH, UK

Fax: +44 20-3031-1429 Email: director@bookpi.org,
(Branch office)